# PARALLEL NEUROVASCULAR COUPLING MODELS AND ASSOCIATED SPREADING DEPRESSION

**Allanah Kenny**


A thesis submitted for the Degree of Doctor of Philosophy in Biomedical Engineering at the University of Canterbury.

Feb 2019

# PREFACE

Material covered in Chapters 3 – 7 of this thesis have been published in international, peer-reviewed journals. Co-authorship forms are attached.

*Chapter 3:*

Kenny, A., Zakkaroff, C., Plank, M. J., and David, T. (2018). Massively parallel simulations of neurovascular coupling with extracellular diffusion. Journal of Computational Science, 24, 116 – 124.

*Chapter 4:*

Kenny, A., Plank, M. J., and David, T. (2018). The role of astrocytic calcium and TRPV4 channels in neurovascular coupling. Journal of Computational Neuroscience, 44(1), 97 – 114.

*Chapter 5:*

Mathias, E., Kenny, A., Plank, M. J., and David, T. (2018). Integrated models of neurovascular coupling and BOLD signals: Responses for varying neural activations. NeuroImage, 174(March), 69 – 86. This chapter covers the work of the author of this thesis, Allanah Kenny, based on the section from the paper titled "Comparison of experimental cortical CBF data with simulated data with varying stimulus conditions".

*Chapter 6:*

Kenny, A., Plank, M. J., and David, T. (2018). Macro scale modelling of cortical spreading depression and the role of astrocytic gap junctions. Journal of Theoretical Biology, 458, 78 – 91.

*Chapter 7:*

Kenny, A., Plank, M. J., and David, T. (2019). The effects of cerebral curvature on cortical spreading depression. Journal of Theoretical Biology, 472, 11 – 26.

The foundation model of the neurovascular unit (NVU) extended throughout this thesis is based on the work of Dr. Katharina Dormanns during her doctoral studies at the University of Canterbury under the supervision of Prof. Tim David.

# CONTENTS

# ACKNOWLEDGEMENTS

This thesis has taken almost 3 years to complete and I wouldn't be where I am today without the help of a few important people. First of all I would like to thank my supervisors Prof Tim David and Dr Michael Plank for guiding me throughout this process and providing encouragement when I needed it. This wouldn't be possible without you and I am deeply grateful.

Thanks to Tim and various other funding bodies for providing the opportunity to travel all over the world and attend numerous conferences: the Australasian winter conference on brain research (AWCBR) in Queenstown, NZ in 2016, 2017 and 2018; the Virtual Physiological Human conference in Amsterdam, Netherlands in 2016; the Workshop on Global Sensitivity Analysis in Toronto, Canada in 2017; the annual meeting of the Australasian Neuroscience Society (ANS) in Brisbane, Australia in 2018; the Brain Research New Zealand early career workshop in Dunedin, NZ (2017) and Auckland, NZ (2018). I would also like to thank the University of Canterbury and Brain Research New Zealand for providing funding for this thesis project.

Thank you to the students who have come and gone for providing entertainment as well as valuable input into my research: Kathi Dormanns, Christine McManaman, Jaijus Johny, Elshin Mathias, Stewart Dowding. Special thanks to Angela Armstrong whose admin skills were of immense help in the first years of this thesis.

Thank you to my parents for always supporting me in whatever I want to do, and thank you to my partner Valentin for putting up with my neverending study!

Finally I would like to thank my late grandparents Don and Joane for your continued support from across the globe. Unfortunately you couldn't be around to see my finished thesis, and so I dedicate this to you both.

# ABSTRACT

Neuronal activity evokes a localised increase in cerebral blood flow (CBF) in a response known as neurovascular coupling (NVC). This response is achieved through communication between neurons, astrocytes and vascular cells, together comprising a neurovascular unit (NVU). Impaired NVC is associated with several pathological conditions such as Alzheimer's disease, stroke, and cortical spreading depression (CSD). Although NVC has been widely studied the inner workings and signalling pathways of the brain have yet to be fully elucidated. Mathematical models provide an alternative and complementary method of research, working in tandem with physical experiments and providing a deeper understanding of experimental results as well as guiding future experiments.

This thesis details the extension of a foundational biophysical model of a single NVU with multiple new pathways and compartments allowing for the simulation of both normal and impaired NVC. The single NVU model was first extended with the nitric oxide (NO) pathway, the glutamate induced astrocytic calcium ($Ca^{2+}$) pathway with epoxyeicosatrienoic acid (EET) signalling, and the stretch dependent transient receptor potential vanniloid-related 4 (TRPV4) $Ca^{2+}$ channel on the astrocytic endfoot. It was found that the potassium ($K^+$) pathway governs the fast onset of vasodilation while the NO pathway has a delayed response. Increases in astrocytic $Ca^{2+}$ concentration to levels consistent with experimental data were insufficient for inducing either vasodilation or constriction, in contrast to a number of experimental results. However astrocytic $Ca^{2+}$ was shown to strengthen $K^+$ induced NVC by further opening the big potassium (BK) channel on the astrocytic endfoot.

The model was then extended with a complex neuron submodel and the blood-oxygen-level dependent (BOLD) response, allowing for model validation through comparison with experimental data. The change in CBF due to neural activity in the model showed good agreement with experimental data obtained from the rat barrel cortex. When using an experimental neural input profile, the model compared well for short stimuli but was unable to replicate the double maximum of the experimental CBF profile for longer periods. An additional pathway through the locus coeruleus

(LC) (on a purely phenomenological basis) provided a better comparison with experimental data, further showing that there exist numerous signalling pathways in the NVC process.

The NVU model was then embedded in a large two dimensional (2D) cerebral tissue slice model with a coupled vascular tree, solved in a parallel environment using high performance computing. The tissue slice model was first extended with extracellular Fickian $K^+$ diffusion, allowing for direct communication between adjacent NVUs. It was found that a localised neuronal stimulation resulted in vasodilation with a decreasing gradient in vessel radius from the stimulated to non-stimulated area. During vasomotion there was emergent behaviour in the form of waves of increased vessel radius moving towards the stimulated area. This indicates that communication within the tissue via extracellular ion diffusion has a much greater effect than communication solely through the vascular tree.

Extracellular ion electrodiffusion and an astrocytic gap junction network were added to allow further communication throughout the tissue. It was found that under pathological CSD conditions, $K^+$ waves could propagate radially outwards from a stimulated area with a wave of vasoconstriction followed by slight vasodilation comparing well with murine experiments. Extracellular Fickian diffusion was insufficient for allowing a wave to propagate. An astrocytic gap junction network reduced the duration of the vasoconstrictive wave and the area initially affected. This indicates that communication throughout the extracellular space (ECS) is necessary in the model for allowing a CSD wave to propagate, whereas the communication through the astrocytic gap junction network regulates the vascular response.

The flat 2D tissue slice model could simulate the smooth cortex of murine animals but could not take into account the highly folded nature of the human cortex. The model was extended with a spatial Gaussian curvature mapping which allowed for investigation into how the surface curvature affects the propagation of CSD waves throughout the tissue. It was found that for a surface with spatially varied curvature comparable to a section of human cortex, areas of positive Gaussian curvature inhibited wave propagation due to decreased extracellular diffusion rate, whereas areas of negative curvature promoted propagation. CSD was observed travelling as wave segments (as opposed to radial waves on a flat surface), providing some insight into the differences seen between human and animal experiments.

# LIST OF FIGURES

# LIST OF TABLES

# ABBREVIATIONS

**1D** . . . . . one dimensional

**20-HETE** . . . . 20- hydroxyeicosatetraenoic acid

**2D** . . . . . two dimensional

**AA** . . . . . arachidonic acid

**ACF** . . . . . autocovariance function

**ATP** . . . . . adenosine triphosphate

**BBB** . . . . . blood brain barrier

**BK** . . . . . big potassium

**BOLD** . . . . . blood-oxygen-level dependent

**$Ca^{2+}$** . . . . . calcium

**CaM** . . . . . calmodulin

**CBF** . . . . . cerebral blood flow

**CBV** . . . . . cerebral blood volume

**cGMP** . . . . . cyclic guanosine monophosphate

**CICR** . . . . . $Ca^{2+}$ induced $Ca^{2+}$ release

**$Cl^{-}$** . . . . . chlorine

**$CMRO_2$** . . . . cerebral metabolic rate of $O_2$ consumption

**$CO_2$** . . . . . carbon dioxide

**COX** . . . . . cyclooxygenase enzymes

**CPI-17** . . . . . myosin phosphatase inhibitor protein

**CS** . . . . . conditioning block

**CSD** . . . . . cortical spreading depression

**EC** . . . . . endothelial cell

**ECS** . . . . . extracellular space

**EET** . . . . . epoxyeicosatrienoic acid

**EFS** . . . . . electro field stimulation

**eNOS** . . . . . endothelial nitric oxide synthase

**EPSP** . . . . . excitatory postsynaptic potential

**ER** . . . . . endoplasmic reticulum

**fMRI** . . . . . functional magnetic resonance imaging

**GHK** . . . . . Goldman Hodgkin Katz

**HbO** . . . . . oxyhemoglobin

**HbR** . . . . . deoxyhemoglobin

**HbT** . . . . . total hemoglobin

**IBSI** . . . . . inter-stimulus interval

**$IP_3$** . . . . . inositol trisphosphate

**IPSP** . . . . . inhibitory postsynaptic potential

**$K^+$** . . . . . potassium

**KA** . . . . . transient $K^+$

**KCl** . . . . . potassium chloride

**KDR** . . . . . delayed rectifier $K^+$

**KIR** . . . . . inward rectifying $K^+$

**LC** . . . . . locus coeruleus

**LC-NA** . . . . . noradrenalin locus coeruleus

**mGluR** . . . . . metabotropic glutamate receptor

**MLC** . . . . . myosin light chain kinase

**MPI** . . . . . Message Passing Interface

**MTT** . . . . . mean transit time

**$Na^+$** . . . . . sodium

**NaP** . . . . . persistent $Na^+$

**NaT** . . . . . transient $Na^+$

**NE** . . . . . neuron

**NMDA** . . . . . N-methyl-D-aspartate

**nNOS** . . . . . neuronal nitric oxide synthase

**NO** . . . . . nitric oxide

**NVC** . . . . . neurovascular coupling

**NVU** . . . . . neurovascular unit

**$O_2$** . . . . . oxygen

**OEF** . . . . . $O_2$ extraction fraction

**ODE** . . . . . ordinary differential equation

**P2Y** . . . . . purinergic G protein-coupled

**PDE** . . . . . partial differential equation

**Pg$E_2$** . . . . . prostaglandin $E_2$

**PKC** . . . . . protein-kinase C

**PLC** . . . . . phospholipase-C

**PS** . . . . . probing block

**PVS** . . . . . perivascular space

**SAC** . . . . . stretch activated channel

**SC** . . . . . synaptic cleft

**sGC** . . . . . soluble guanylyl cyclase

**SMC** . . . . . smooth muscle cell

**SR** . . . . . sarcoplasmic reticulum

**TRPV4** . . . . . transient receptor potential vanniloid-related 4

**VOCC** . . . . . voltage operated $Ca^{2+}$ channel

**WSS** . . . . . wall shear stress

# 1

# INTRODUCTION

## 1.1 THE BRAIN

The brain is arguably the most complex and sophisticated organ in the body. It critically relies on the supply of both oxygen ($O_2$) and glucose via the perfusion of blood throughout the cerebral tissue, using 20% of all $O_2$ taken in by the body despite comprising only 2% of the total human body mass [176]. The physiological purpose of the brain is to control the other organs in the body, achieved by generating patterns of muscle activity and releasing hormones. The brain can be divided into three main components: the cerebrum, the cerebellum, and the brainstem comprised of the pons, medulla and midbrain (see Figure 1). The largest and most advanced part is the cerebrum, forming two hemispheres connected by over 200 million neural fibres.

The cerebral cortex forms the outer layer of the cerebrum and is found only in mammals. Based on cortical folding, mammals can be divided into two groups: those with lissencephalic brains where the cortical surface is smooth (such as small rodents), and those with gyrencephalic brains (such as primates, in particular humans) where the cortex is tightly folded forming ridges (gyri) and grooves or valleys (sulci). These folds allow for a greater surface area whilst maintaining a manageable volume within the skull [149, 156]. The level of gyrification (folding) is dependent on species, though it is largely correlated with brain size [156].

### 1.1.1 *Brain tissue composition*

The brain tissue is primarily comprised of neurons and glial cells. Cells are basic structural units consisting of the membrane, the cytoplasm, and organelles such as the nucleus, mitochondria, and endoplasmic reticulum (ER). The membrane separates the inside of the cell from the external environment and acts as a capacitor as it can support a potential difference (the so called "membrane potential") due to the distribution of charged particles (ions). The cytoplasm is the intracellular

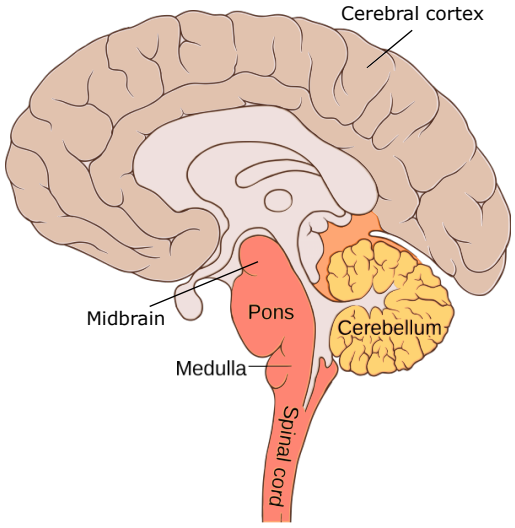


Figure 1: Main components of the human brain. Adapted from Wikimedia Commons[1]

[1] https://commons.wikimedia.org

fluid containing a complex mixture of substances such as ions and molecules dissolved in water, and makes up the bulk of the cell. The mitochondria utilise $O_2$ and glucose to generate energy for the cell in the form of adenosine triphosphate (ATP), a complex chemical required in many biological processes. The ER has a wide range of functions depending on the specific cell type; one such function in vascular cells is to act as an internal store of ions such as calcium ($Ca^{2+}$).

Cells can transport ions or other molecules from the cytosol through channels, pumps or gap junctions. Channels are membrane proteins with selective permeability that allow ions to pass through according to their electrochemical gradient (or concentration gradient for non charged molecules). Pumps move ions or molecules against their concentration gradient through active transport, primarily using ATP as an energy source. Channels and pumps can be gated by voltage (membrane potential), ion concentration, and mechanical stretch among others. Gap junctions are specialised intercellular connections which directly connect the cytosol of two cells, allowing various ions or molecules to pass through.

#### 1.1.1.1 *Neurons*

A human brain contains approximately 100 billion neurons which are connected to one another via synapses. These connections form neural pathways and circuits, capable of sending and receiving information within, to and from the brain.

A neuron consists of a cell body (soma), dendrites and an axon. The dendrites are thin processes extending from the soma, often for hundreds of micrometres. Most neurons receive signals from

other neurons via the dendrites, and send signals via the axon, a single process that can extend up to 1 metre in humans or even further in other species.

Neurons are electrically excitable due to the difference in intracellular and extracellular ion concentrations, maintained primarily by ATP driven ion pumps. This allows for inter-cell communication via electrical impulses known as action potentials. An action potential is generated when the membrane potential changes by a large enough amount, and this change propagates rapidly along the neuron's axon and reaches the synapse. If the synapse is chemical (the most abundant type) the axon releases neurotransmitters to communicate with other cells through binding to postsynaptic receptors [148]. The other type of synapse is electrical and is not considered further in this research.

#### 1.1.1.2 *Astrocytes*

Glial cells known as astrocytes were originally thought to be passive cells whose main function was to provide structural support for neurons, however it is now known that astrocytes play a key role in maintaining the neuronal environment [107, 167]. Astrocytes are star shaped cells with long processes and are the most abundant form of glial cells, occupying between 25% to 50% of the brain volume. The astrocytic processes surround neuronal synapses, astrocytic synapses, and vascular smooth muscle cells (SMCs). One important function of astrocytes is the buffering of extracellular ions and other neurotransmitters. In particular, astrocytes are able to take potassium ($K^+$) from the extracellular space (ECS) and various synapses and transport this $K^+$ to the processes surrounding the vasculature. The $K^+$ is then released from the astrocytic processes and subsequently taken up by the SMCs of the perfusing arteriole.

## 1.2 THE CIRCULATORY SYSTEM

The primary function of the circulatory system is to provide nutrients to cells in need. There are four main arteries (two pairs of internal carotid arteries and vertebral arteries) supplying oxygenated blood and glucose to the brain. These arteries have thick muscular walls to facilitate rapid blood flow under high pressure. Pial arteries ($200 - 1000$ μm wide [12]) lie on the cerebral surface within the subarachnoid space, from which penetrating arteries ($100 - 400$ μm wide [119]) enter the brain tissue perpendicular to the surface (see Figure 2). These arteries then branch into smaller arterioles ($5 - 100$ μm wide [141]) which are surrounded by the endfeet of astrocytic

processes and contain a thin layer of SMCs lining the cell wall. The arterioles then terminate as capillaries ($5-10$ µm wide [141]) which have very thin walls to allow for the exchange of nutrients between the vasculature and the tissue. After the blood has perfused the tissue it is collected by venules and transported back to the heart via progressively larger veins in order to remove carbon dioxide and metabolic waste products. The research presented in this thesis is focussed primarily on the arteriole and the comprising vascular cells: SMCs and endothelial cells (ECs).

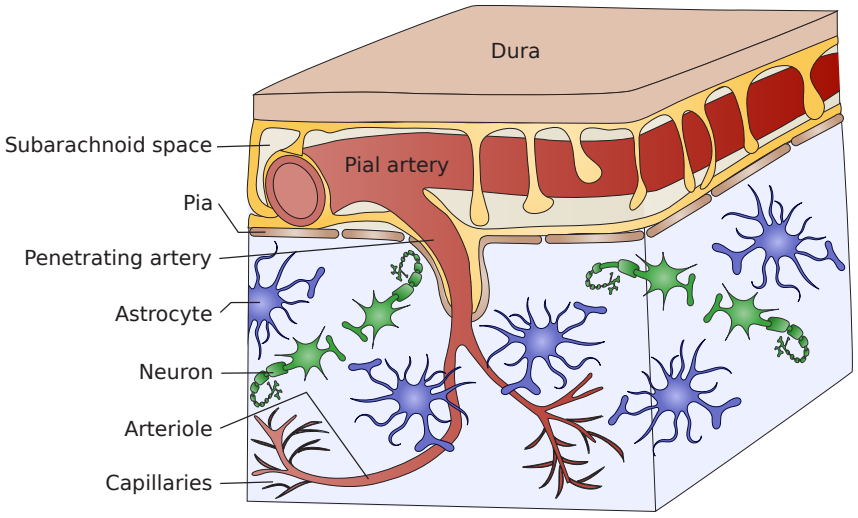


Figure 2: The cerebral vasculature. Pial arteries lie on the surface of the brain, from which penetrating arterioles enter the brain tissue at right angles. Arterioles and capillaries perfuse the tissue, and astrocytic processes surround the arterioles. Adapted from Zlokovic [176].

### 1.2.1 *Vascular cells*

The outer layer of the arteriole is comprised of a thin layer of SMCs, cells which act as the contractile units of the vessel. The SMCs are aligned in the circumferential direction and are able to contract and relax via actin-myosin cross bridge formation in order to vary the diameter of the arteriole. This contraction is involuntary and is primarily dependent on the intracellular $Ca^{2+}$ concentration in the SMC. The $Ca^{2+}$ interacts with calmodulin, a $Ca^{2+}$ binding messenger protein, and stimulates the phosphorylation of the myosin light chain kinase (MLC) causing muscular contraction [80, 175]. The capillaries do not contain SMCs; instead any change in capillary diameter is passive and the rate of blood flow is controlled by the upstream arterioles. SMCs contain a specific type of ER called the sarcoplasmic reticulum (SR), primarily used for storing and releasing $Ca^{2+}$ into the cytosol.

The inner layer of the arteriole is comprised of a single layer of ECs. These cells line the entire circulatory system and their primary function is to prevent diffusion of large molecules, while smaller molecules such as $O_2$ can pass through. These cells can also detect changes in wall shear stress (WSS) induced by blood flow, which can affect the production rate of ATP and the messenger molecule inositol trisphosphate ($IP_3$) [5]. Together with SMC these cells form the blood brain barrier (BBB), a highly selective semi-permeable barrier that protects the brain from unwanted chemical substances in the blood. Finally, the vessel interior is called the lumen; this is the space through which blood flows.

## 1.3 NEUROVASCULAR COUPLING

The cerebral cortex contains a multitude of blood vessels that regulate blood supply in response to local changes in a process known as functional hyperaemia. This process is characterised by an increase in neuronal activity followed by a rapid dilation of local blood vessels. This leads to increased blood supply providing $O_2$ and glucose to cells in need, under the assumption of constant systemic pressure.

The study of functional hyperaemia began over a century ago with the work of Roy and Sherrington [152], although the exact cellular and chemical pathways involved in this process are still unknown. Initially it was believed that an increase in cerebral blood flow (CBF) was triggered by a metabolic signal such as lower $O_2$ or higher carbon dioxide ($CO_2$) levels in the blood. However investigations over the last few decades have indicated that functional hyperaemia is controlled through the process of neurovascular coupling (NVC), an intercellular communication system based on ion exchange through pumps and channels between neurons, astrocytes, SMCs, ECs, and the spaces between these cells: the synaptic cleft (SC) between the neuron and astrocyte, and the perivascular space (PVS) between the astrocyte and SMC [50, 5, 83, 95]. In addition, the ECS surrounding the cells of the neurovascular unit (NVU) comprises approximately 20% of the cerebral tissue [164]. Diffusion of various substances in the ECS play an important role in both functional intercellular communication and during pathological conditions such as cortical spreading depression (CSD) [99, 26]. Together these components comprise a NVU, see Figure 3. The exchange of ions contribute to changes in ionic concentrations (both intra- and extracellular) and cell membrane potentials.

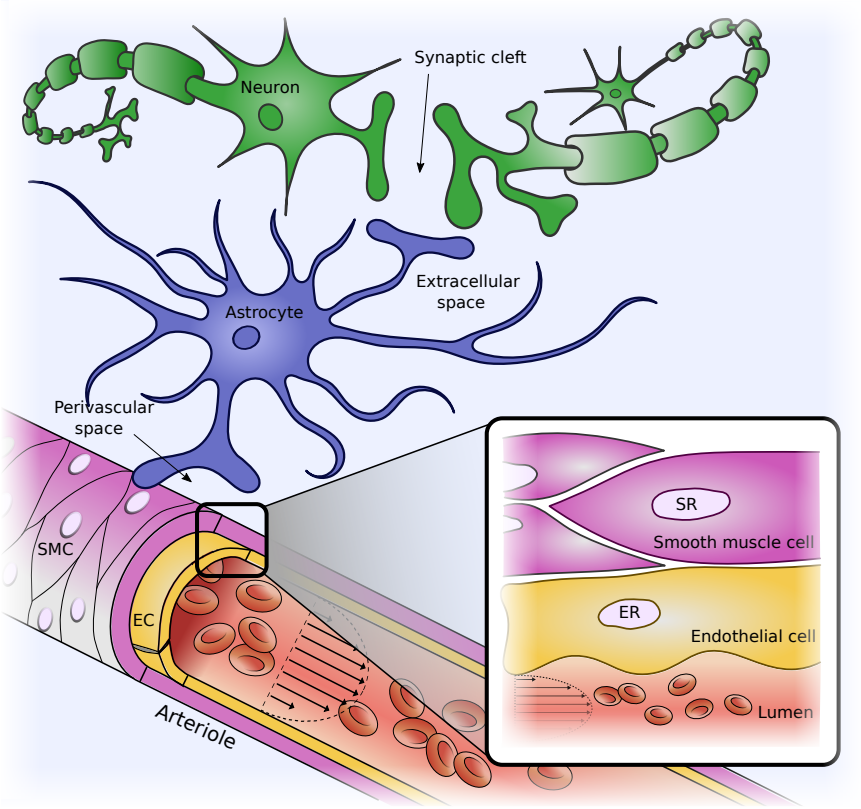


Figure 3: A schematic representation of the neurovascular unit (NVU). Communication between these cells controls the process of neurovascular coupling (NVC).

The process of NVC begins with the release of $K^+$ and the neurotransmitter glutamate into the SC and ECS due to neuronal activity, initiating multiple pathways. The first major well known pathway is via $K^+$. During neural activity $K^+$ is released from the neuron into the ECS and SC. This $K^+$ is taken up by the astrocyte and extruded into the PVS, causing further release of $K^+$ from the adjacent SMC and hyperpolarisation of the SMC membrane. This leads to decreased $Ca^{2+}$ concentration in the SMC and hence SMC relaxation, dilating the arteriole and resulting in increased blood flow [5, 59, 130].

The second major pathway is via nitric oxide (NO), a potent cerebral vasodilator. Synaptic glutamate causes an increase in neuronal NO production, and this NO can diffuse to the SMC where it leads to SMC relaxation and increased blood flow [47]. It should be noted that there are other mechanisms present for which NVC is thought to be achieved. One such mechanism is via pericytes, contractile cells that wrap around capillaries and are thought by some to be the primary method for vasodilation during NVC. However as shown in the papers of Hall et al. [81] and Hill et al. [89] there is still some controversy concerning the role of pericytes. Another well known mechanism for NVC is the astrocytic $Ca^{2+}$ pathway, which is initiated by glutamate and results in the opening of the astrocytic big potassium (BK) channel. However, as with pericytes, there

are conflicting views on the importance of this pathway in the literature [7]. The astrocytic $Ca^{2+}$ pathway is discussed further in Chapter 4.

## 1.4 CORTICAL SPREADING DEPRESSION

CSD is the occurrence of slowly propagating waves (travelling between $1-10$ mm $min^{-1}$ [18]) of high extracellular $K^+$ concentration (over $30-50$ mM) and neuronal depolarisation in the grey matter of various species [115]. It typically arises in metabolically compromised tissue as in ischemia [49] and is associated with several neurological disorders such as migraine, traumatic brain injury, Alzheimer's disease, stroke, and hypertension [69, 158, 114, 27]. Cell damage or death during ischemia results in reduced supply of $O_2$ and glucose to brain cells [94]. This decreases ATP production and leads to the failure of the neuronal $Na^+/K^+$ ATPase pump, which in turn leads to increased extracellular $K^+$ levels, elevated neuronal sodium ($Na^+$) concentration, cell swelling, and neuronal depolarisation [54]. In these conditions a decrease in CBF is often observed followed by a slight increase and slow return to the baseline [30, 161]. These waves of depolarisation are then followed by a short period of neuronal inactivity.

## 1.5 MOTIVATION

Impaired NVC resulting in reduced blood supply to brain tissue is associated with several pathological conditions such as Alzheimer's disease, atherosclerosis, stroke, hypertension, traumatic brain injury, and CSD [14, 69, 114, 146, 176]. These pathologies all begin with an altered relationship between neural activity and the CBF. These alterations limit the delivery of crucial nutrients such as $O_2$ and glucose, and impair the removal of waste metabolic products such as $CO_2$ [175]. Reduced flow to areas in need can result in chronic brain injury associated with cognitive impairment, whereas complete interruption of CBF for more than a few minutes (as can occur during stroke) leads to severe brain damage and possible death [96].

While research into the brain has increased the collective understanding over the years, the inner workings and signalling pathways of the brain have yet to be elucidated. Mathematical models provide an alternative and complementary method of research, working in tandem with *in vivo* or *in vitro* experiments. Numerical models consist of a set of equations with parameters based

on experimental data sets. The output of these models can be validated through experimental comparison, and new results are produced which can provide insight into physical experiments and guide future experiments. This method is non-invasive and allows for novel experiments by measuring certain quantities or isolating specific pathways which are either difficult or impossible in the wet-lab. This provides clinicians and physiologists with an experimentally validated test-bed.

This research aims to move towards a numerical model of the regulated blood supply perfusing the cerebral cortex, including the complex cell to cell signalling both within the single NVU and the entire brain tissue. Simulation results provide a non-invasive means for investigating NVC, overcoming some of the limitations of physical experiments. The goal of the model is to obtain a better understanding of the various processes involved in NVC, and in particular the methods of communication and various pathways in the brain during normal and impaired NVC. The long term objective of this work is to further understanding of the causes, symptoms and effects of degenerative diseases and pathogenic conditions in the brain.

# 2

# METHODOLOGY: MATHEMATICAL MODELLING AND NEUROVASCULAR COUPLING MODELS

In this chapter the experimental methods used to measure neurovascular coupling (NVC) are detailed, followed by the limitations encountered in physical experiments. Next is a brief overview of mathematical modelling (cell modelling in particular) and the various concepts used to construct model equations (such as mass conservation and Kirchhoff's Law). This is followed by a review of relevant existing cell models. Lastly the foundation neurovascular unit (NVU) model of Dormanns et al. [48] is described as well as the large scale NVC model of Dormanns et al. [46] and its implementation; these foundation models are later extended throughout this thesis.

## 2.1 EXPERIMENTAL METHODS

### 2.1.1 *fMRI BOLD response*

Functional magnetic resonance imaging (fMRI) is a widely used non-invasive imaging technique that measures brain activity by detecting changes associated with blood flow. The most common form of fMRI uses the blood-oxygen-level dependent (BOLD) response. This technique relies on the fact that, under normal circumstances, brain activity is closely followed by a localised increase in blood flow (i.e. NVC). The change in blood flow causes an increase in the relative levels of oxyhemoglobin and decrease in the levels of deoxyhemoglobin, where hemoglobin is the iron-containing protein that transports oxygen ($O_2$) in red blood cells. These proteins can be detected as deoxyhemoglobin is paramagnetic (weakly attracted to magnetic fields) and oxyhemoglobin exhibits diamagnetism (weakly repulsed from magnetic fields).

### 2.1.2 *Experimental limitations*

In physical experiments, blood perfusion can be measured using optical reflectance imaging [30], cell membrane potential can be measured using voltage clamping techniques [144], and changes in intracellular concentration of ions such as calcium ($Ca^{2+}$), potassium ($K^{+}$) or sodium ($Na^{+}$) can be estimated using fluorescent indicators [120, 150]. However there are important experimental variables that are either difficult or impossible to measure. These include ion concentrations in the internal stores of cells (e.g. the endoplasmic reticulum (ER) or sarcoplasmic reticulum (SR) in the endothelial cell (EC) and smooth muscle cell (SMC) respectively), the open probability of certain channels on a cell membrane, or the flux of a certain species through a channel or pump.

Both *in vitro* and *in vivo* experiments have certain limitations. *In vitro* procedures are widely performed on both animal and human tissue (for example, single cells or brain slices) but these are not fully representative of human physiology as the cells are treated outside of their "natural" environment (e.g. no surrounding tissue, vasculature providing nutrients through blood flow, or neighbouring cell network).

The majority of *in vivo* experiments are performed on animals rather than humans, primarily due to the obvious ethical limitations. However, the results of these animal experiments may not accurately predict the behaviour of humans [154]. In addition, these *in vivo* experiments are generally performed when the animal is sedated, potentially leading to skewed results due to the effects of anaesthesia on cell dynamics [66].

## 2.2 MATHEMATICAL MODELLING

Numerical models of blood regulation provide insight into the interaction of the cellular-level and macro-scale phenomena studied *in silico*, a term referring to computer simulations of the dynamics of complex biological systems as opposed to *in vivo* or *in vitro* experimental studies. These *in silico* simulations can be a useful tool for guiding future experiments and providing a deeper understanding of physiological processes. Mathematical modelling provides a number of key benefits, in particular the ability to measure quantities and isolate signalling pathways that are difficult or impossible to implement in a wet lab environment.

Cells and spatial domains such as the neuron or synaptic cleft (SC) can be represented as single compartments. Complex models may consider the difference in species concentration or other

variables throughout the compartment, such as the electrodiffusive model for astrocytic and neuronal ion concentrations by Halnes et al. [82] or the arterial blood flow model of Chakravarty and Sannigrahi [24]. However most mathematical models are assembled using a lumped parameter approach. This means that the distribution of various species inside the compartment is considered to be homogeneous, and any spatial gradients within the compartment are negligible. Hence at any point in time there is a single value for each variable in each compartment; this simplifies the mathematical description of the physiological processes considerably.

### 2.2.1 *Ordinary differential equations*

The main variables of a physiological cell model are molecular concentrations and cell membrane potential. Molecular concentration is measured in molar (denoted 'M') and describes the amount of a substance per volume within a compartment. The membrane potential is usually measured in millivolts (denoted 'mV'). The changing behaviour of a variable as a function of time is described by an ordinary differential equation (ODE).

#### 2.2.1.1 *Mass conservation*

The ODEs of a cell model are primarily based on two concepts: mass conservation and Kirchhoff's law. Mass conservation implies that the rate of change of a certain species is equal to the flux entering ($J_{in}$) minus the flux leaving the compartment ($J_{out}$). For a species concentration c this can be written as follows:

$$\frac{dc}{dt} = \frac{1}{VR_{io}}(J_{in} - J_{out}) + \text{other terms}, \tag{2.1}$$

where $VR_{io}$ is the volume ratio of the inner compartment to the outer compartment (usually the extracellular space (ECS)), and the other terms can be production, reaction or degradation terms.

#### 2.2.1.2 *Kirchhoff's Law*

Kirchhoff's law states that the sum of all currents into any junction is zero; this implies that the membrane potential $V_m$ of a cell containing one or more ions can be found through the following equation:

$$\frac{dV_m}{dt} = \sum_{ion} -\frac{g_{ion}}{C_m}(V_m - E_{ion}), \tag{2.2}$$

where $g_{ion}$ is the ion conductance, $C_m$ is the cell capacitance, and $E_{ion}$ is the ionic Nernst potential: the equilibrium potential at which there is no net flow of that particular ion through the membrane.

#### 2.2.1.3 *Open probability of ion channels*

Ion channels may open and close in response to voltage (membrane potential), ion concentration, and mechanical stretch among others. The average open/close state (where 1 denotes open and 0 denotes closed) of many channels of a specific channel type is termed the open probability $w$ generally given by:

$$\frac{dw}{dt} = \frac{1}{\tau_w}(w_\infty - w), \tag{2.3}$$

where $w_\infty$ is the equilibrium state open probability and the time constant $\tau_w$ is a characteristic time scale indicating how long $w$ takes to approach $w_\infty$. These two terms can be functions of other variables which depends on how the specific ion channel is gated (e.g. membrane potential $V_m$, ion concentration c etc.).

## 2.3 EXISTING CELL MODELS

There exist a wide variety of models describing one or more cellular compartments of the NVU, however very few models describe the full NVU including the neuron, astrocyte and vascular cells.

Chang et al. [26] developed a mathematical model containing neuronal soma/axon, dendrite, and ECS components. The purpose of this model was to study the effects of perfusion and hypoxia on cortical spreading depression (CSD) and was implemented as a one dimensional (1D) model simulating a row of cells. They used a neuron model based on Kager et al. [99] and were able to simulate neuronal depolarisation and high extracellular $K^+$ levels that occur during CSD. They were also able to simulate the resulting vasoconstriction and $O_2$ depletion. However the vascular submodel was comprised of a single ODE for vessel radius dependent solely on extracellular $K^+$ concentration. Hence they did not include the full NVU system with astrocytes, SMCs, ECs or the myosin-actin wall mechanics.

There are a variety of models detailing only the neuron/astrocyte subsystem [137, 140, 94, 35] while excluding the vascular dynamics of the NVU. As an example, the mathematical model of

Østby et al. [137] is composed of neuron, astrocyte, and extraneural space compartments. They investigated the phenomenon of extracellular space shrinkage during neuronal activity, as a result of $K^+$ clearance followed by osmotically driven water uptake by the astrocyte. The model of Conte et al. [35] is also composed of neuron, astrocyte, and ECS compartments. The purpose of their model was to explore the mechanisms responsible for the initiation and propagation of CSD and focussed on the role of extracellular $K^+$ and glutamate.

Finally, in order to model spatial phenomena such as CSD these cell models can be extended into one or two dimensions. There are many 1D models simulating a row or array of cells [26, 94, 135, 35], however two dimensional (2D) models simulating the dynamics of the brain are mostly limited to simple reaction-diffusion systems with few variables [108].

## 2.4 FOUNDATION NVU MODEL

In this research the mathematical model of a NVU developed by Dormanns et al. [48] is extended. This model is originally based on Farr and David [56] and is able to model the entire NVC process, but did not include the complex neuron/ECS dynamics necessary for modelling pathologies such as CSD. It is based on three existing models: the astrocyte/SC submodel describes the crucial biochemical processes within the astrocyte, based on Østby et al. [137] and reviewed by Donk and Kock [44]; the SMC/EC submodel describes the behaviour and main ion fluxes within the vascular cells and is based on the model of Koenigsberger et al. [111]; finally the wall mechanics submodel describes the relationship between the cytosolic $Ca^{2+}$ concentration in the SMC and the contraction and dilation of the SMC by myosin phosphorylation and cross bridge formation, based on the models of Hai and Murphy [80] and Kelvin Voigt [17].

The experimentally validated NVU model by Dormanns et al. [48] consists of several basic compartments: the neuron, astrocyte, SMC, SR, EC, ER, the SC between the neuron and astrocyte, the perivascular space (PVS) between the astrocyte and SMC, and the lumen.

These compartments are represented in the model by different subdomains, assembled using a lumped parameter approach where spatial variation within each compartment is negligible. These subdomains are assumed to have differing volumes and contain a number of homotypic cells; however, they are each considered to be an aggregate of cells and therefore act as a single entity. Each compartment contains various channels allowing for the transport of ions such as $K^+$ and $Ca^{2+}$, and messenger molecules such as inositol trisphosphate ($IP_3$), detailed by ODEs. Other

equations detail cell membrane potentials, the open probability and gating variables of various channels, the actin-myosin cross bridge dynamics describing the vessel wall mechanics, and the vessel radius. The model contains what are believed to be the crucial components of NVC but allows for the inclusion of additional pathways.

A schematic diagram of this NVU model is found in Figure 4. For a full list of all equations and parameters of this model see Appendix A.3. In this model, during neuronal stimulation $K^+$ is released into the SC, leading to an influx of $K^+$ into the astrocyte via $Na^+/K^+$ pumps on astrocytic processes adjacent to the SC. Consequently the astrocyte depolarises, leading to a large $K^+$ efflux into the PVS through the big potassium (BK) channel on the astrocytic endfoot [33]. The rise in perivascular $K^+$ concentration leads to a further influx of $K^+$ through the inward rectifying $K^+$ (KIR) channel from the SMC into the PVS, hyperpolarising the SMC membrane. As a result the voltage operated $Ca^{2+}$ channels (VOCCs) on the SMC close, preventing an influx of $Ca^{2+}$. The decrease in $Ca^{2+}$ concentration causes a decrease in the rate constants $K_1$ and $K_6$ for the phosphorylation of free and attached cross bridges, respectively. Overall the change in the actin-myosin cross bridge formation relaxes the SMC, dilating the vessel which results in increased blood flow. This $K^+$ induced NVC pathway is well known [5, 59, 130]. There are other signalling pathways present in NVC such as the nitric oxide (NO) pathway and astrocytic $Ca^{2+}$ pathway, however the focus of this model was primarily to investigate the $K^+$ dynamics during NVC.

The flow of blood through the lumen provides convection of agonists such as adenosine triphosphate (ATP). ATP activates the purinergic G protein-coupled (P2Y) receptors on the luminal side of the ECs, providing an $IP_3$ signalling pathway via the membrane bound enzyme phospholipase-C (PLC) [101]. In the model this is simulated via a constant flux of $IP_3$ into the EC termed $J_{PLC}$ and has a qualitative effect on the dynamics of the NVU (see Figure 5). $J_{PLC}$ invokes an increase in the $IP_3$ concentration in the EC and hence the SMC through EC-SMC coupling. The high $IP_3$ concentration in the SMC causes a greater influx of $Ca^{2+}$ into the cytosol from the SR through the $IP_3$ receptor ($IP_3R$) channel. At the resting state (i.e. with no neuronal stimulation), for $J_{PLC}$ values in the range of 0.25 to 0.5 $\mu Ms^{-1}$ the additional flux of $IP_3$ from the EC into the SMC induces the $Ca^{2+}$ in the SMC (and other variables such as the vessel radius) to oscillate, causing vasomotion [48]. In the activated state (i.e. when the NVU is neuronally stimulated) the radius increases for low levels of $J_{PLC}$ and the oscillatory area shifts to the right. The oscillatory area is bordered by two supercritical Hopf bifurcations (black square) where the stable state (solid line) becomes unstable (dashed line) and generates a set of periodic orbits corresponding to oscillations.

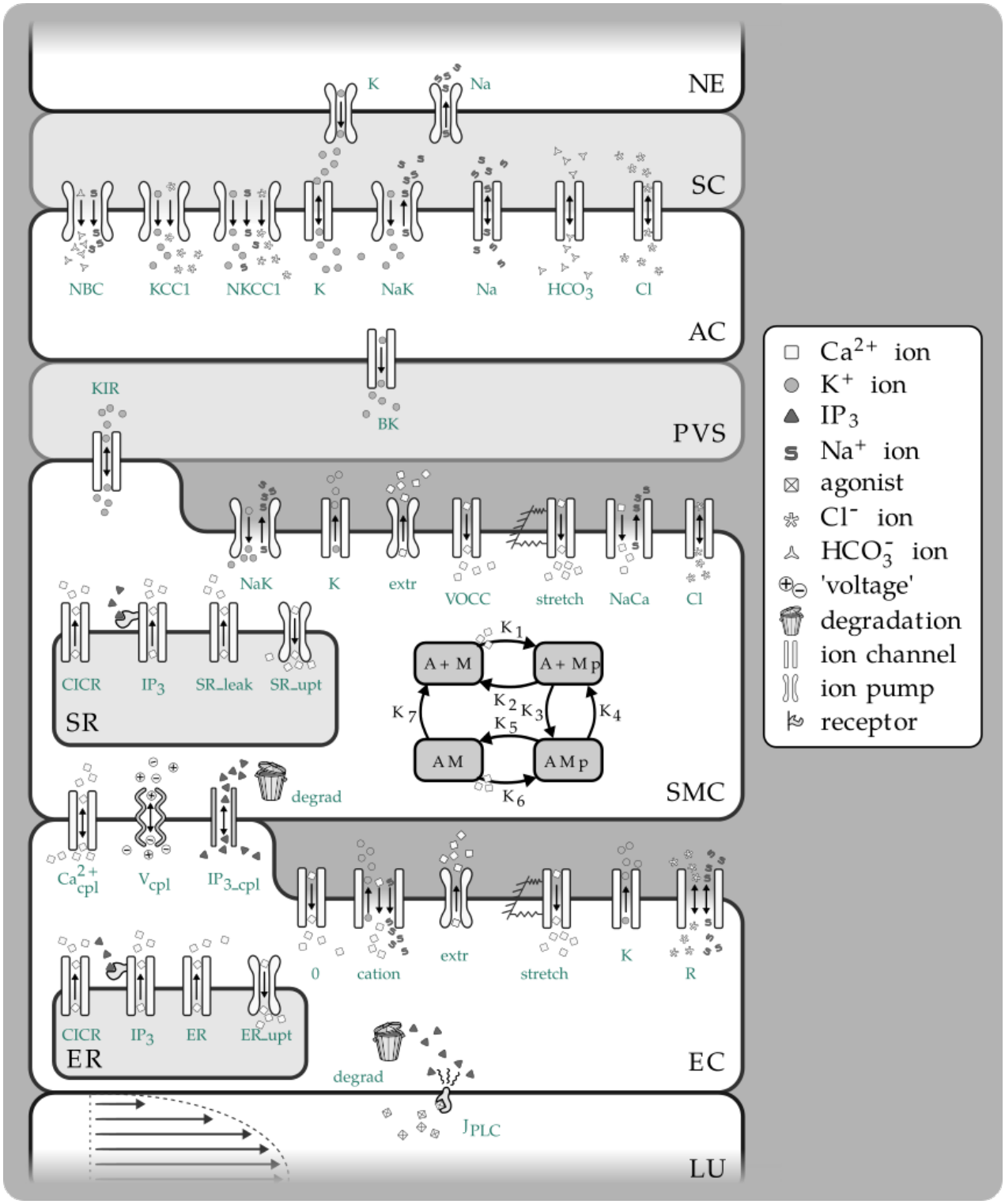


Figure 4: A schematic representation of the foundation NVU model of Dormanns et al. [48]. NE: neuron, SC: synaptic cleft, AC: astrocyte, PVS: perivascular space, SMC: smooth muscle cell, SR: sarcoplasmic reticulum, EC: endothelial cell, ER: endoplasmic reticulum, LU: lumen. $K_1$ to $K_7$: wall mechanics reaction rate constants, M: free nonphosphorylated cross bridges, Mp: free phosphorylated cross bridges, AMp: attached phosphorylated cross bridges, AM: attached dephosphorylated latch bridges, KIR: inwardly rectifying potassium channel, BK: large conductance potassium channel, VOCC: voltage operated calcium channel, CICR: calcium induced calcium release channel, $J_{PLC}$: phospholipase-C dependent $IP_3$ flux. Adapted from Dormanns et al. [48].

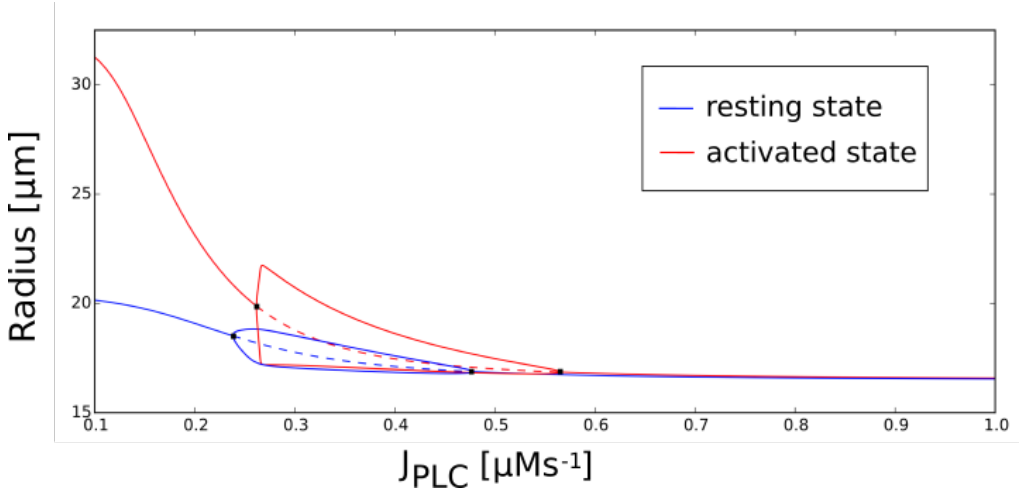


Figure 5: Radius bifurcation diagram for varied $J_{PLC}$ denoting the magnitude of the $IP_3$ flux into the EC as a result of luminal agonists such as ATP. As $J_{PLC}$ increases the vessel radius decreases, for $J_{PLC}$ between 0.25 to 0.5 $\mu Ms^{-1}$ the radius oscillates in the resting state, and for $J_{PLC}$ between 0.28 to 0.56 $\mu Ms^{-1}$ the radius oscillates in the activated state. Blue: resting state, red: activated (neuronally stimulated) state. Solid line: stable state, dashed line: unstable state, black square: supercritical Hopf bifurcation. Adapted from Dormanns [45].

### 2.4.1 *Tissue slice model*

The blood supply within the cerebral cortex begins at the pial arteries, bifurcating inwards with penetrating arteries which eventually perfuse the capillary bed. Therefore the cerebral vasculature can be thought of as a bifurcating tree of blood vessels comprising up to 20 or more bifurcation levels, corresponding to millions of vessels in the tree [65]. Variation in vessel resistance can modify blood flow in a highly localised manner. Due to the connectivity of the tree a change in resistance of one blood vessel can result in a change in local pressure (and hence blood flow) throughout the vascular tree [46].

The single NVU model of Dormanns et al. [48] has been implemented on the macro scale as described by Dormanns et al. [46] via a space filling binary H-tree simulating a perfusing arterial tree (vasculature). The H-tree is a tree of blood vessels which repeatedly bifurcate from a root vessel into vessels with smaller radius and shorter length. This vascular tree is coupled to a 2D slice comprised of tissue blocks with each block corresponding to a single NVU. The leaves of the vascular H-tree are each coupled with a corresponding NVU block via stretch-activated $Ca^{2+}$ channels in the SMC and EC that depend on the vascular blood pressure. Figure 6 gives an overview of the macro scale model.

### 2.4.2 *Vascular tree model*

The bifurcating H-tree contains the radius, conductance (reciprocal of resistance), blood flow for each branch, and dynamic pressure at each internal node. At each bifurcation, the radius $r$ of the daughter vessels is a factor of $\sqrt{2}$ of the radius of the parent, while the length $l$ is divided by 2 every second bifurcation. These scalings are within the biologically realistic limits described by the binary tree algorithm of Ottesen et al. [139]. The radius is non-dimensionalised with respect to a characteristic arteriolar radius of 20 µm and the length with respect to a characteristic length of 200 µm. The radii are only dynamic at the leaves of the tree and are determined by the dynamics of the corresponding coupled NVU within the tissue slice and the pressure drop over the leaf.

Because most of the systemic pressure drop occurs over the small arterioles, the leaves of the tree have their pressure fixed at a constant capillary bed pressure $p_{cap}$. The pressure at the root of the tree is set at a (possibly) time dependent $p_0(t)$ (Figure 7), however in the following simulations $p_0(t)$ is constant.

The structure of an H-tree of N levels is represented as a directed graph via an $m \times n$ adjacency matrix $A$ where $m$ is the number of internal nodes not including the leaves ($m = 2^{N-1} - 1$) and $n$ is the number of edges/vessels ($n = 2^N - 1$). The entries of the matrix are $a_{ij} = -1$ if edge $j$ enters node $i$, $a_{ij} = 1$ if edge $j$ exits node $i$, and 0 otherwise. There are $2^{N-1}$ leaves and the same number of corresponding coupled NVU blocks in the tissue slice.

The Reynolds and Womersley numbers in small arterioles are very small, with the Reynolds number approximately 1 [112] and the Womersley number less than 1 [65]. Therefore, at the scale

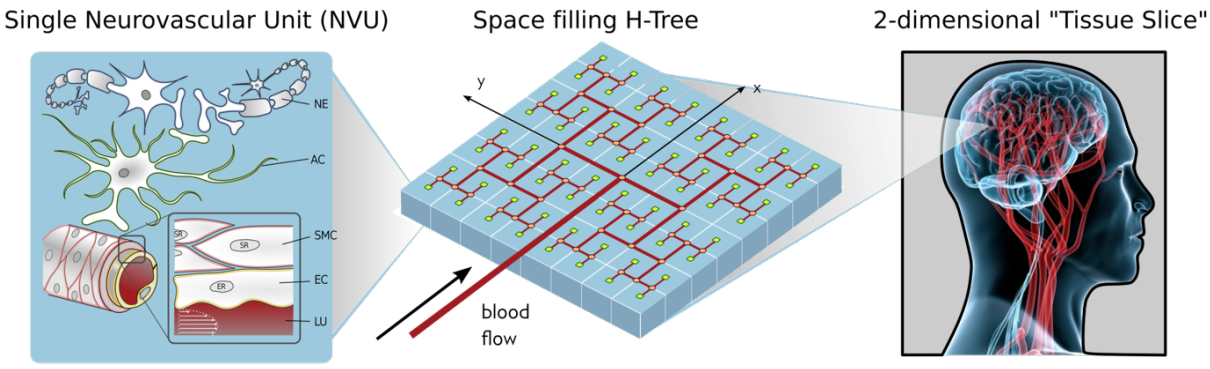


Figure 6: Overview of the tissue slice model of Dormanns et al. [46]. A 2D cerebral tissue slice is comprised of multiple NVUs coupled to a vascular H-tree simulating the blood flow and pressure of the cerebral vasculature.

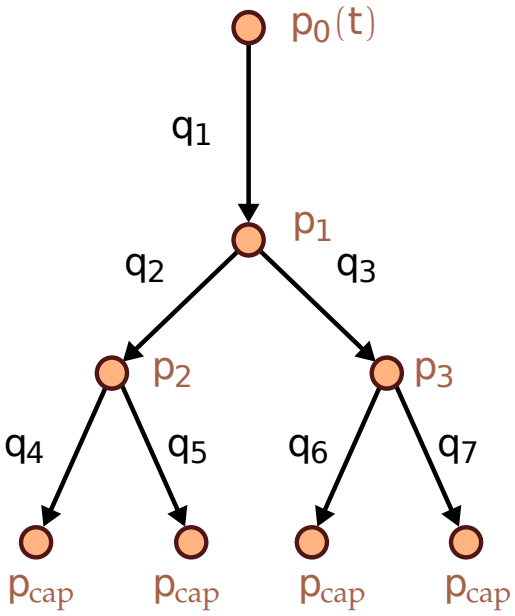


Figure 7: Indexing scheme for a vascular bifurcating H-tree with $N = 3$ levels. The pressure $p$ and the blood flow $q$ are shown for each node and branch respectively. The nodes and branches are ordered breadth first. The pressure at the terminating arterioles (leaves) is fixed at $p_{cap}$.

of the model Hagen-Poiseuille flow can be readily assumed. Hence, the non-dimensional flow $q$ through a blood vessel is given by

$$q = gv, \quad \text{where} \quad g = \frac{r^4}{l}. \tag{2.4}$$

The non-dimensional conductance of the vessel is given by $g$ and the pressure drop over the vessel is given by $v = p_{up} - p_{down}$. Hence, the vector of flows at each vessel is given by

$$\mathbf{q} = G\mathbf{v}, \tag{2.5}$$

where $\mathbf{q} \in \mathbb{R}^n$ is the vector of flows at each vessel, $G = \operatorname{diag} \mathbf{g} \in \mathbb{R}^{n\times n}$, and $\mathbf{v} \in \mathbb{R}^n$ is the vector of pressure drops over each vessel. With imposed flow boundary conditions the following is obtained:

$$\mathbf{v} = A^T\mathbf{p} + \mathbf{b}, \tag{2.6}$$

where $\mathbf{p} \in \mathbb{R}^m$ is the vector of pressures at each internal node of the tree, and $\mathbf{b} \in \mathbb{R}^n$ incorporates the boundary conditions. Due to flow conservation, $A\mathbf{q} = 0$. Hence, from Eq. (2.5) and (2.6) the vector of pressures is given by the positive definite linear system:

$$AGA^T\mathbf{p} = -AG\mathbf{b}. \tag{2.7}$$

Eq. (2.4), (2.5), (2.6) and (2.7) determine the dynamics of the vascular tree and are solved in unison with the NVU tissue slice model according to Brown and David [16], Dormanns et al. [46], and briefly described in the following section.

### 2.4.3 *Implementation*

The model has been designed to run on parallel architectures with a view of building simulation size up to macro scale tissue slices. The parallel implementation follows the work of Brown and David [16]. Combining the individual ODE systems for all NVUs in the tissue slice produces a large system of ODEs of the form

$$\frac{d\mathbf{x}}{dt} = \mathbf{f}(\mathbf{x}, \mathbf{p}, t), \quad \mathbf{x} \in \mathbb{R}^k, \; k \in \mathbb{N}, \tag{2.8}$$

where $\mathbf{x}$ is the vector of state variables of the large ODE system of size $k$; for example using a tree of 13 levels requires 4096 coupled NVUs, producing a vector $\mathbf{x}$ of size $k = 4096 \times 25 = 102400$. The differential equations depend on the pressure $\mathbf{p}$ of the vascular tree, and the conductances of the tree are algebraically dependent on the radius variable of the NVU so that $\mathbf{g} = \mathbf{g}(\mathbf{x})$. Therefore Eq. (2.7) and (2.8) define a semi explicit index-1 differential algebraic system of equations. This can be transformed into the form

$$\frac{d\mathbf{x}}{dt} = \mathbf{f}(\mathbf{x}, (AG(\mathbf{x})A^T)^{-1}AG(\mathbf{x})\mathbf{b}(t), t). \tag{2.9}$$

The system is stiff, requiring the computation of the Jacobian matrix. However, the Jacobian is dense, precluding the traditional implicit methods used for numerically solving differential equations. This is remedied by taking a block diagonal Jacobian approximation, allowing for the use of an implicit method while still retaining the solution time scaling properties of explicit solvers. Additionally, this method lends itself to significant parallelisation. The simulated tissue slice is split into rectangular domains with each domain corresponding to a single computational node, whereas the H-tree is partitioned into subtrees with a root subtree. The system is solved using a C implementation of a fixed-step Backward Euler method with Newton iteration due to stiffness.

Numerical scaling experiments by Dormanns et al. [46] showed that strong scaling (where the problem size stays fixed and the number of processors is increased) provides a near ideal profile. Weak scaling results (where the problem size and number of processors are both increased so that

the problem size per processor remains constant) indicate that the wall clock time increases above 10% when the number of processors is increased from 8 to 256. This small increase again indicates that the parallel algorithm is near optimal parallelisation. Further details on the solver used can be found in Brown and David [16] and Dormanns et al. [46].

# 3

# THE EFFECTS OF EXTRACELLULAR DIFFUSION VS THE VASCULATURE

## 3.1 INTRODUCTION

The numerical neurovascular unit (NVU) model of Dormanns et al. [48] has been implemented on the macro scale as described by Dormanns et al. [46] via a space filling binary H-tree simulating a perfusing arterial tree (vasculature) as discussed in Chapter 2. The H-tree is a tree of blood vessels which repeatedly bifurcate from a root vessel into vessels with smaller radius and shorter length. This vascular tree is coupled to a two dimensional (2D) slice comprised of tissue blocks with each block corresponding to a single NVU. The leaves of the vascular H-tree are each coupled with a corresponding NVU block via stretch-activated calcium ($Ca^{2+}$) channels in the smooth muscle cell (SMC) and endothelial cell (EC) that depend on the vascular blood pressure. For further details on this model refer to Chapter 2.

The extracellular space (ECS) surrounding the cells of the NVU comprises approximately 20% of the cerebral tissue [164]. Diffusion of various substances in the ECS play an important role in both functional intercellular communication and during pathological conditions such as cortical spreading depression (CSD) [99, 26].

The work of Dormanns et al. [46] contains no direct communication between the adjacent NVUs. In this chapter a more physiologically correct neurovascular coupling (NVC) model is presented with an added ECS compartment, and extracellular potassium ($K^+$) diffusion throughout the ECS between neighbouring tissue blocks in the macro scale simulations to enable direct NVU to NVU communication.

## 3.2 METHOD AND MODEL DEVELOPMENT

This section describes the ECS compartment of the proposed NVU model, and the method for simulating extracellular $K^+$ diffusion throughout the macro-scale cerebral tissue slice consisting of multiple NVUs. Finally the large-scale parallel implementation of the NVC is presented along with the simulation details.

A schematic representation of the proposed model is found in Figure 8 for reference, and all relevant equations and parameters can be found in Appendix A.4.

### 3.2.1 *Extracellular space compartment*

Transport of $K^+$ between the ECS and synaptic cleft (SC) compartments of a single NVU is implemented via a linear diffusion term $J_{diff}$ based on Fick's law (where ions move from high to low concentrations) such that

$$J_{diff} = \frac{1}{\tau_s}(K_e - K_s), \tag{3.1}$$

where $J_{diff}$ is added to or subtracted from the differential equation for the $K^+$ concentration in the SC ($K_s$) and the $K^+$ concentration in the ECS ($K_e$) respectively. $\tau_s$ is the characteristic time in seconds that is needed for $K^+$ to diffuse over some distance $\Delta x$ such that

$$\tau_s = \frac{(\Delta x)^2}{2D_K}, \quad D_K = \frac{D_{free}}{\lambda_0^2}. \tag{3.2}$$

Here $D_K$ is the effective diffusion coefficient of $K^+$, $D_{free}$ is the diffusion coefficient of $K^+$ in a free medium, and $\lambda_0$ is a non-dimensional tortuosity factor which is necessary since diffusion is hindered by the narrow confines of the ECS [157]. For extracellular diffusion the tortuosity has been reported as $\lambda_0 = 1.6$ [157]. For diffusion between the ECS and SC, $\tau_s = 2.8$ s based on an average astrocyte length (across two astrocyte arms) of $\Delta x = 100$ µm.

It is proposed here that any transport of $K^+$ between the ECS and perivascular space (PVS) compartment is excluded from the model, for the following reasons: it is assumed that the PVS volume is orders of magnitude smaller than the ECS as the astrocytic endfoot closely surrounds the arteriole [171]. In addition, by including a diffusive flux between the PVS and ECS in the model, the astrocytic $K^+$ uptake and extrusion pathway that occurs following neuronal stimulation is effectively short circuited via the ECS and the astrocyte is bypassed. As such it is more physiologically

realistic to model the PVS and ECS as completely separate spaces with no ion transport between them.

The ECS is directly connected to the SMC via a $Ca^{2+}$ mediated $K^+$ channel and $Na^+/K^+$ adenosine triphosphate (ATP)-ase pump (with fluxes denoted by $J_K$ and $J_{NaK}$ respectively) given by:

$$J_K = G_K w_i (v_i - v_K) \tag{3.3}$$

$$J_{NaK} = F_{NaK}, \tag{3.4}$$

where $J_{NaK}$ is simplified to a constant hyperpolarising flux according to Parthimos et al. [142]. $G_K$ is the whole SMC conductance for $K^+$ efflux, $w_i$ is the open state probability of the $Ca^{2+}$ mediated $K^+$ channel, $v_i$ is the SMC membrane potential, $v_K$ is the Nernst potential for $K^+$ in the SMC, and $F_{NaK}$ is the rate of $K^+$ influx into the SMC via the $Na^+/K^+$ ATPase pump [110].

### 3.2.2 *Extracellular diffusion in the tissue slice*

The macro scale simulations incorporate $K^+$ diffusion between the ECS of adjacent NVU tissue blocks via a linear diffusion term as in Eq. (3.1) with characteristic time $\tau_e$. Dormanns et al. [46] originally estimated a tissue block size of side length 400 μm. However, arterioles of the cortex perfuse a cylindrical volume of diameter 140 to 320 μm [84]. Assuming that the cube shaped tissue blocks of the proposed model each containing a leaf of the H-tree (arteriole) perfuse the same volume as a cylindrical volume of diameter 140 μm, the side length of a single cubic tissue block will be 124 μm by volume equivalence. Therefore the characteristic time based on Eq. (3.2) for $K^+$ to travel through the ECS from one tissue block to another is $\tau_e = 4.3$ s based on $\Delta x = 124$ μm.

Diffusion between adjacent NVU tissue blocks is implemented using linear diffusion via the Laplace operator. Diffusion is not implemented for tissue blocks on a diagonal. For a single NVU tissue block with coordinates $i, j$ the differential equation for $K_e$ is given by

$$\frac{dK_e^{i,j}}{dt} = J_{K_i}^{i,j} - J_{NaK_i}^{i,j} - J_{diff}^{i,j} - \frac{1}{\tau_e}\left(4K_e^{i,j} - K_e^{i-1,j} - K_e^{i+1,j} - K_e^{i,j-1} - K_e^{i,j+1}\right), \tag{3.5}$$

with $J_{K_i}$ and $J_{NaK_i}$ defined in Eq. (3.3) and (3.4) respectively. Zero flux boundary conditions are implemented on the edges of the tissue slice.

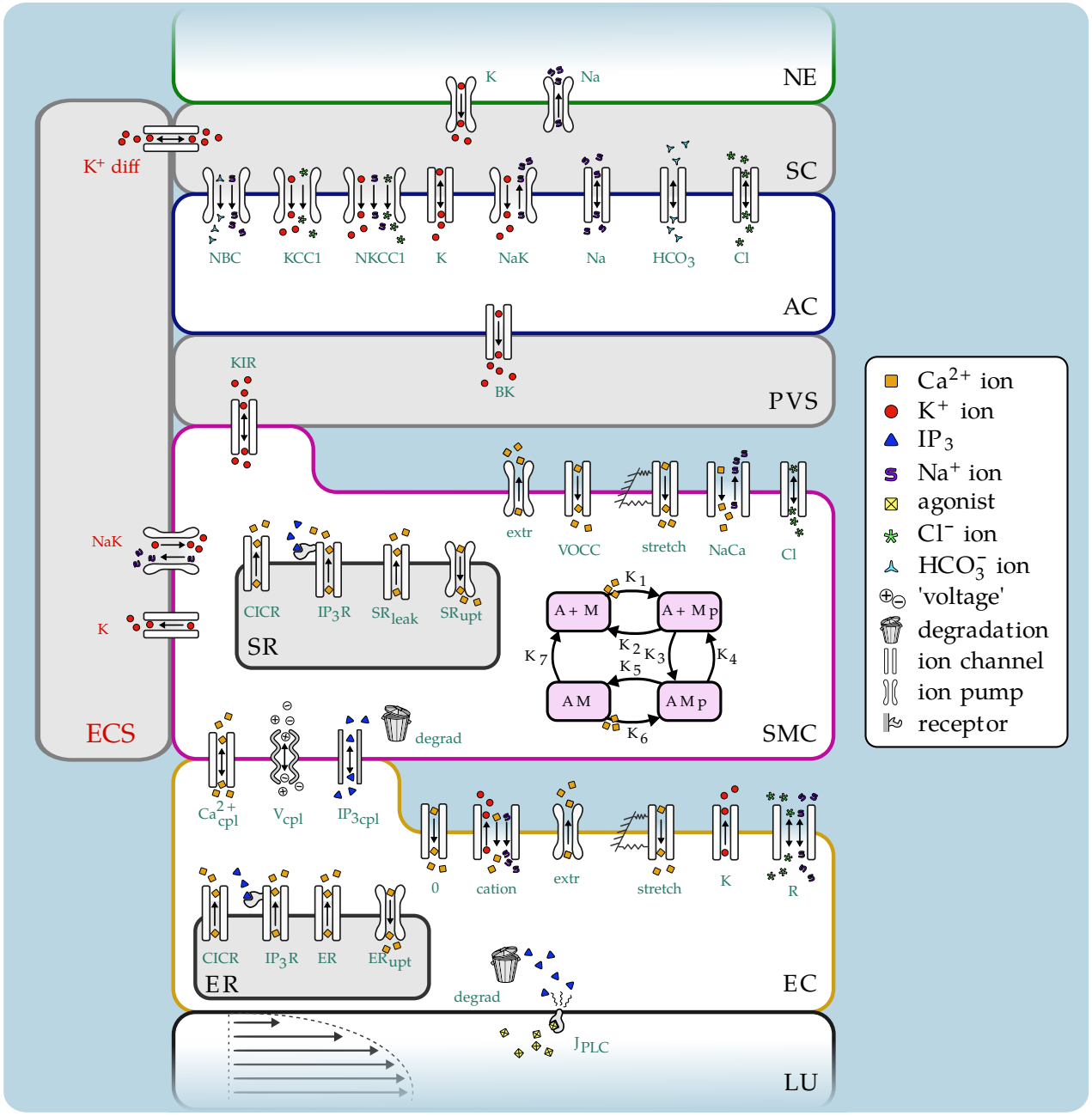


Figure 8: A schematic representation of the proposed NVC model with added ECS compartment. NE: neuron, SC: synaptic cleft, AC: astrocyte, PVS: perivascular space, SMC: smooth muscle cell, SR: sarcoplasmic reticulum, EC: endothelial cell, ER: endoplasmic reticulum, LU: lumen, ECS: extracellular space. $K_1$ to $K_7$: wall mechanics reaction rate constants, M: free nonphosphorylated cross bridges, Mp: free phosphorylated cross bridges, AMp: attached phosphorylated cross bridges, AM: attached dephosphorylated latch bridges, KIR: inwardly rectifying potassium channel, BK: large conductance potassium channel, VOCC: voltage operated $Ca^{2+}$ channel, CICR: $Ca^{2+}$ induced $Ca^{2+}$ release channel, $IP3_R$: inositol trisphosphate ($IP_3$) receptor $Ca^{2+}$ channel, $J_{PLC}$: phospholipase-C dependent $IP_3$ flux, NaK: $Na^+/K^+$ ATPase pump, K: $Ca^{2+}$ activated potassium channel. The ECS compartment and fluxes $J_{diff}$, $J_{NaK}$ and $J_K$ shown in red are new additions to the NVU model.

### 3.2.3 *Implementation*

The Message Passing Interface (MPI) is used for the communication between tissue blocks in a multi-core architecture. For the implementation of extracellular diffusion, at each time step the state variables from the blocks along the edges of the domains are passed to the adjacent blocks in the neighbouring domain. Communication between domains and the corresponding boundary conditions enforcement within a single domain is implemented following the mesh ghost block communication pattern [78].

For the neuronal activation simulations, the simulated vascular H-tree contained $N = 13$ levels coupled with 4096 NVU tissue blocks corresponding to a 7.9 mm $\times$ 7.9 mm 2D cerebral tissue slice. The initial conditions were homogeneous over the entire tissue slice.

The ordinary differential equation (ODE) set and solution was implemented on a 56 core Intel Xeon E5-4660 v3 server with 128 GB of memory and clock speed of 2.10 GHz. The numerical simulations for the neuronal stimulation experiments were executed on 32 cores with 128 NVU tissue blocks allocated to each core. All simulations were performed for a total of 300 physiological seconds. Each iteration corresponding to one physiological second took approximately 4 minutes of wall clock time to complete.

A neuronal input signal was applied to the lower left corner of the tissue slice in the form of a $K^+$ influx to the SC from the neuron at $t_0 = 100$ s. The input function $K(t)$ mimics phenomenologically the $K^+$ efflux from the neuron during neuronal stimulation followed by the neuronal uptake of $K^+$ after stimulation ends. The piecewise function has the temporal form of a beta distribution followed by a simple block input according to the work of Østby et al. [137]:

$$K(t) = \begin{cases} K_{input} \dfrac{(\alpha_n + \beta_n - 1)!}{(\alpha_n - 1)!(\beta_n - 1)!} \left(\dfrac{t_\beta - (t - t_0)}{\Delta t}\right)^{\beta_n - 1} \left(\dfrac{t - t_0}{\Delta t}\right)^{\alpha_n - 1}, & \text{for } t_0 \leqslant t < t_0 + \Delta t \\ -K_{input}, & \text{for } t_1 \leqslant t \leqslant t_1 + \Delta t \\ 0. & \text{otherwise} \end{cases} \tag{3.6}$$

This form ensures that the integral of the function over all time equals zero; in other words, the amount of input $K^+$ from the neuron into the SC is equal to the amount taken back by the neuron at $t_1 = 200$ s. The input duration is $\Delta t = 10$ s. The constants of the beta distribution are $\alpha_n = 2$ and $\beta_n = 5$ as determined by Østby et al. [137]. This function is added to the ODE for synaptic

$K^+$ concentration (see Dormanns et al. [48] for further details). Figure 9 shows the form of the input function $K(t)$ and the area of the tissue slice that is stimulated.

Simulations were performed with both $J_{PLC} = 0.18\ \mu Ms^{-1}$ for steady state dynamics and $J_{PLC} = 0.4\ \mu Ms^{-1}$ for oscillatory dynamics (vasomotion).

## 3.3 RESULTS

In this model neuronal stimulation is simulated by an influx of $K^+$ from the neuron into the SC. With the addition of the ECS compartment, following neuronal stimulation $K^+$ is able to diffuse out of the SC into the ECS ($J_{diff}$) causing an increase in extracellular $K^+$ concentration ($K_e$). The $K^+$ then diffuses into the ECS of adjacent NVUs in the tissue slice, causing a spatial gradient in $K_e$ as the $K^+$ diffuses outward from the stimulated area (see Figure 10). This extracellular $K^+$ is then able to diffuse into the SC, indirectly stimulating the NVUs adjacent to the directly stimulated area.

The fluxes from the SMC into the ECS through the $Ca^{2+}$ mediated $K^+$ channel and $Na^+/K^+$ ATPase pump ($J_K$ and $J_{NaK}$ respectively) are orders of magnitude smaller than the diffusive flux from the SC into the ECS. Therefore there is very little effect on the dynamics from these two fluxes and the majority of the $K^+$ flux is from the SC compartment.

The effect of extracellular $K^+$ diffusion on the resulting radial dynamics of the vasculature is shown for two cases: $J_{PLC} = 0.18\ \mu Ms^{-1}$ (without vasomotion) and $J_{PLC} = 0.4\ \mu Ms^{-1}$ (with vasomotion). These correspond respectively to low and high luminal agonist concentration. These two cases are chosen as the underlying dynamics of the system are qualitatively different, namely steady state and oscillatory.

### 3.3.1 *Without vasomotion*

Figure 11a shows the normalised radius and blood flow of the vascular tree following neuronal activation when the luminal agonist concentration is low ($J_{PLC} = 0.18\ \mu Ms^{-1}$) so the dynamics of the NVU are steady state (without vasomotion). Figure 11b shows the normalised vessel radii of 3 NVUs in distinct areas of the tissue slice: in the stimulated area, the boundary of the stimulated area, and non stimulated area. In the single NVU model with $J_{PLC} = 0.18\ \mu Ms^{-1}$, neuronal

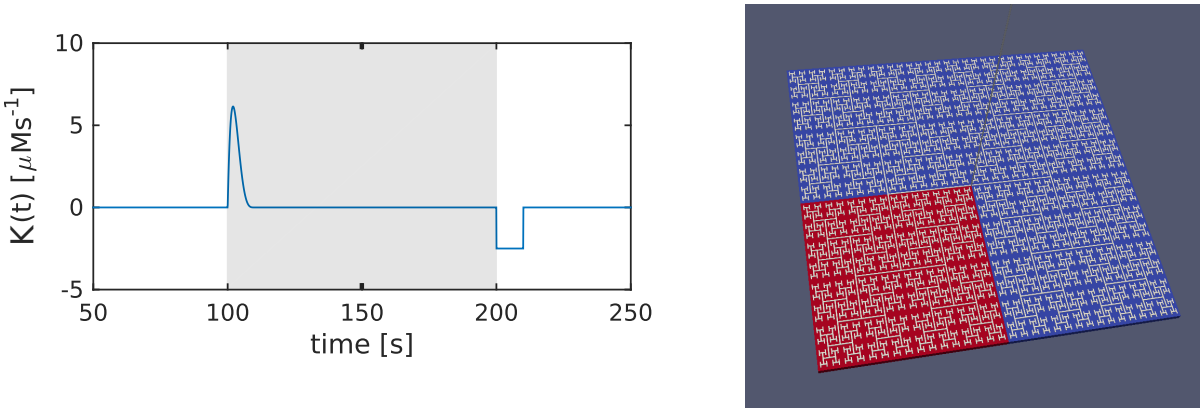


Figure 9: Left: The input function $K(t)$ in $\mu Ms^{-1}$ simulating the input of $K^+$ into the SC during neuronal activation and uptake of $K^+$ following activation, see Eq. (3.6). Grey area: period of neuronal activation. Right: The area of the tissue slice that is neuronally activated (red) via an input $K(t)$ of $K^+$ into the SC. Blue: non activated area, white: vascular tree.

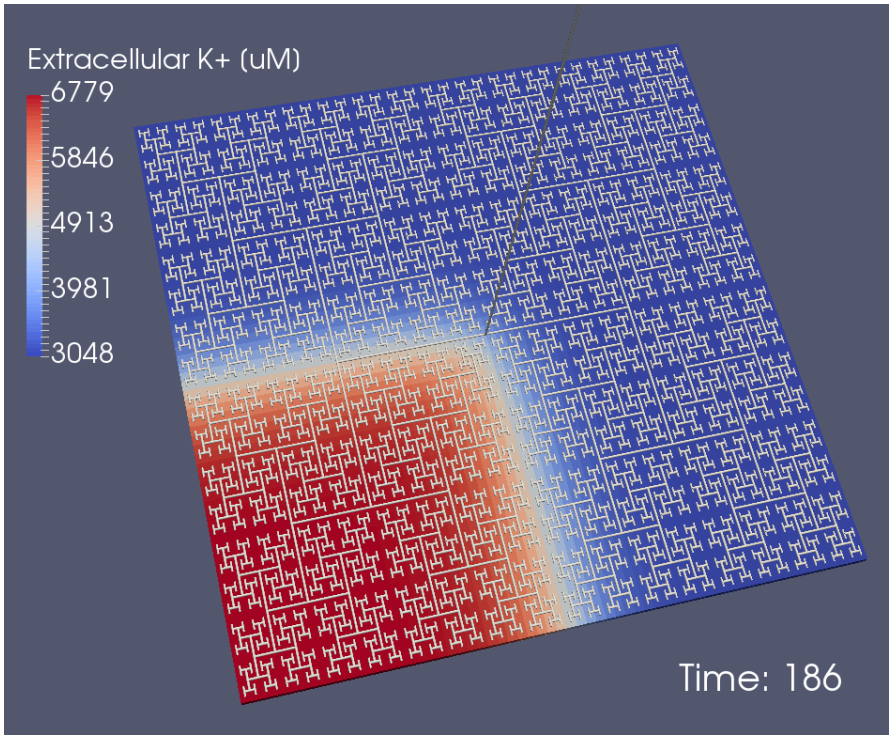


Figure 10: Extracellular $K^+$ concentration in a neuronal activation simulation snapshot of a 7.9 mm $\times$ 7.9 mm cerebral tissue slice including 4096 NVU blocks globally coupled via a space filling H-tree and diffusion of $K^+$ through the ECS. The extracellular $K^+$ concentration is shown in $\mu M$ at $t = 186$ s following neuronal activation in the lower left corner at $t = 100$ s. Stimulation causes an increase in SC $K^+$ concentration. This $K^+$ diffuses out of the SC into the ECS which then diffuses into the ECS of adjacent NVUs and outward throughout the tissue slice. White: vascular tree.

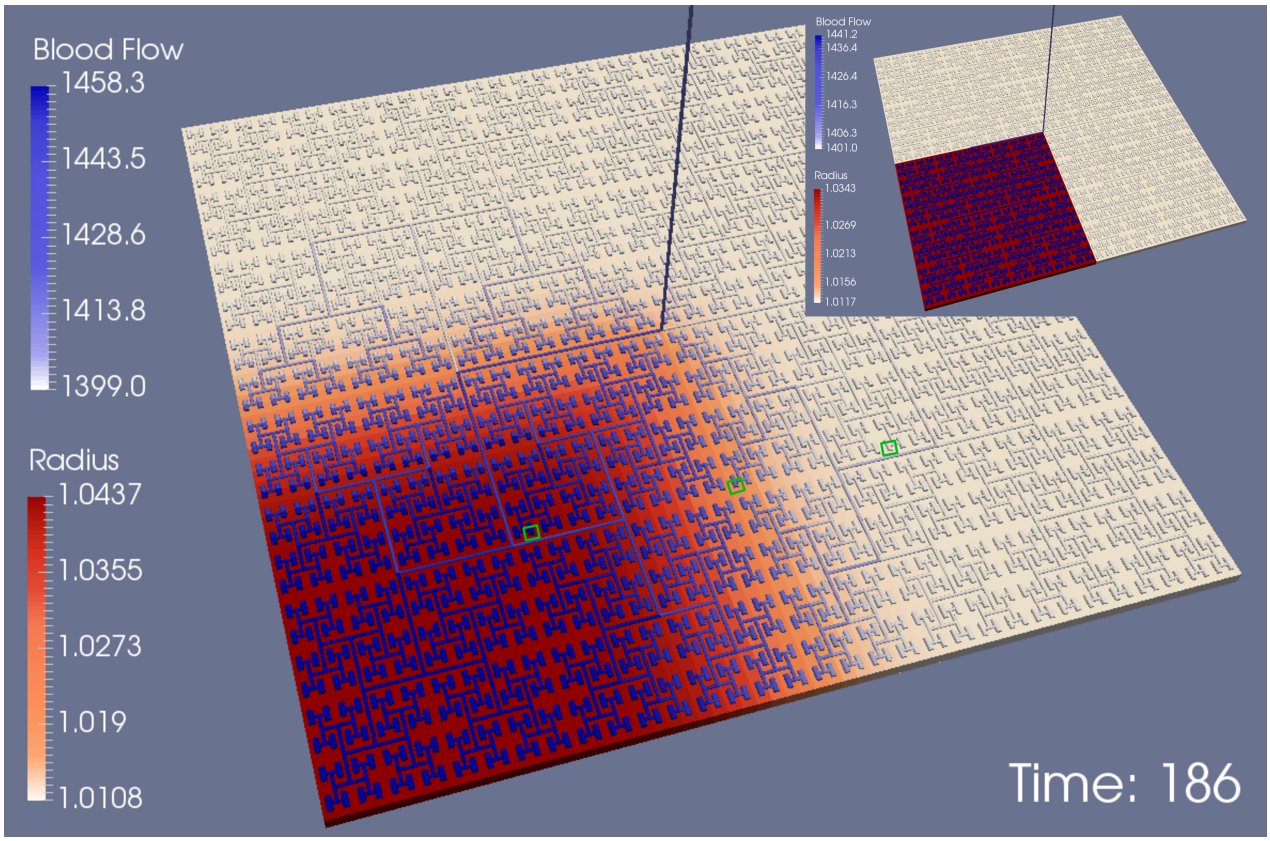


(a) Radius and blood flow of a tissue slice snapshot following neuronal activation. Video available online

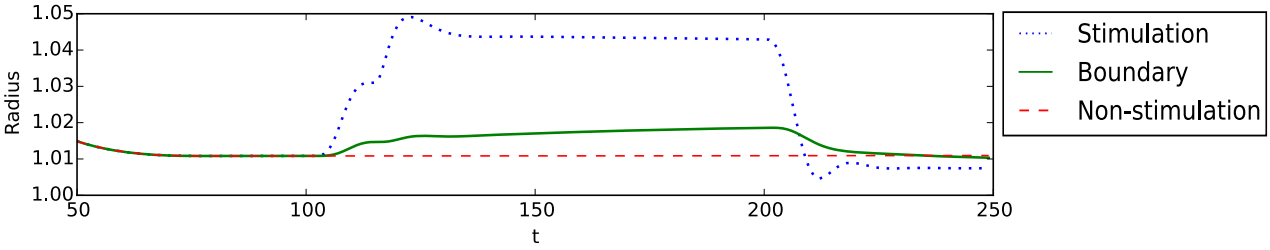


(b) Normalised vessel radii in 3 different areas of the tissue slice.

Figure 11: (a) Normalised radius and blood flow of the neuronal activation simulation of Figure 10, with steady state dynamics (without vasomotion). The colour of the tissue blocks represents the vessel radius and the colour of the vascular tree represents the blood flow. The basic model without extracellular diffusion is shown in the top right corner. The lower left corner of the tissue slice was stimulated by neuronal input from t = 100 to 200 s causing the local dilation of blood vessels and increased blood flow. The diffusion of $K^+$ through the ECS of neighbouring NVU tissue blocks results in the weak dilation of blood vessels in adjacent areas not directly stimulated by the neuronal input.
(b) Shown are the normalised radii of vessels in 3 distinct areas of the tissue slice highlighted in green in a). The plots are shown with time starting at t = 50 s to disregard any transient behaviour. Boundary refers to a vessel adjacent to the stimulated area. When $J_{PLC} = 0.18\ \mu Ms^{-1}$ the vessel in the directly stimulated area experiences a large increase in radius, while the radius of a boundary vessel slightly increases. In the basic model the behaviour of vessels on the boundary and non stimulated areas are the same. Video available online (https://youtu.be/Se1L_4VVBZk)

activity simulated by an increase in synaptic $K^+$ concentration $K_s$ results in a radial increase [48], so the radius is a function of $K_s$.

In the simulations of the basic model with no extracellular diffusion, the vessels in the stimulated area experience an increase in radius and hence vasodilation (Figure 11a, top right). However, the adjacent NVU blocks on the boundary of the stimulated area receive no stimulation, resulting in a clear divide in vessel radius and blood flow between the two areas. This is physiologically unrealistic as adjacent cells should have some effect on one another.

In the proposed model with extracellular diffusion, the $K^+$ from the SC of the NVUs in the stimulated area diffuses into the ECS and outward throughout the tissue slice. This $K^+$ then weakly stimulates the adjacent NVUs, resulting in slight dilation of vessels adjacent to the stimulated area (see Figure 11b). Therefore there is a physiologically realistic gradient of vessel radius and blood flow from the area of stimulation to non stimulation. The vessel dilation remains sufficiently spatially localised over larger time scales. As a result of the outward diffusion of $K^+$, NVUs in the stimulated area will have an overall slightly lower radial increase.

### 3.3.2 *With vasomotion*

Figure 12a shows the normalised radius and blood flow of the vascular tree following neuronal activation when the luminal agonist concentration is high ($J_{PLC} = 0.4\ \mu Ms^{-1}$) so the dynamics of the NVU are oscillatory (vasomotion). Figure 12b shows the normalised vessel radii of 3 NVUs in distinct areas of the tissue slice: in the stimulated area, the boundary of the stimulated area, and non stimulated area. In the single NVU model with $J_{PLC} = 0.4\ \mu Ms^{-1}$, neuronal activity simulated by an increase in synaptic $K^+$ concentration $K_s$ results in an increase in the amplitude and period (reciprocal of frequency) of radial oscillations [48]. Therefore the amplitude and period are functions of $K_s$.

In the basic model with no extracellular diffusion, the NVUs in the stimulated area and non stimulated area have no direct communication so their individual oscillatory dynamics are independent.

In the present model with extracellular diffusion, the vessels in the stimulated area experience an increase in the amplitude and period of radial oscillations. $K^+$ from the SC of the NVUs in the stimulated area diffuses into the ECS and outward throughout the tissue slice as in Figure 10. This $K^+$ then weakly stimulates the adjacent NVUs. This weak stimulation causes a slight increase in

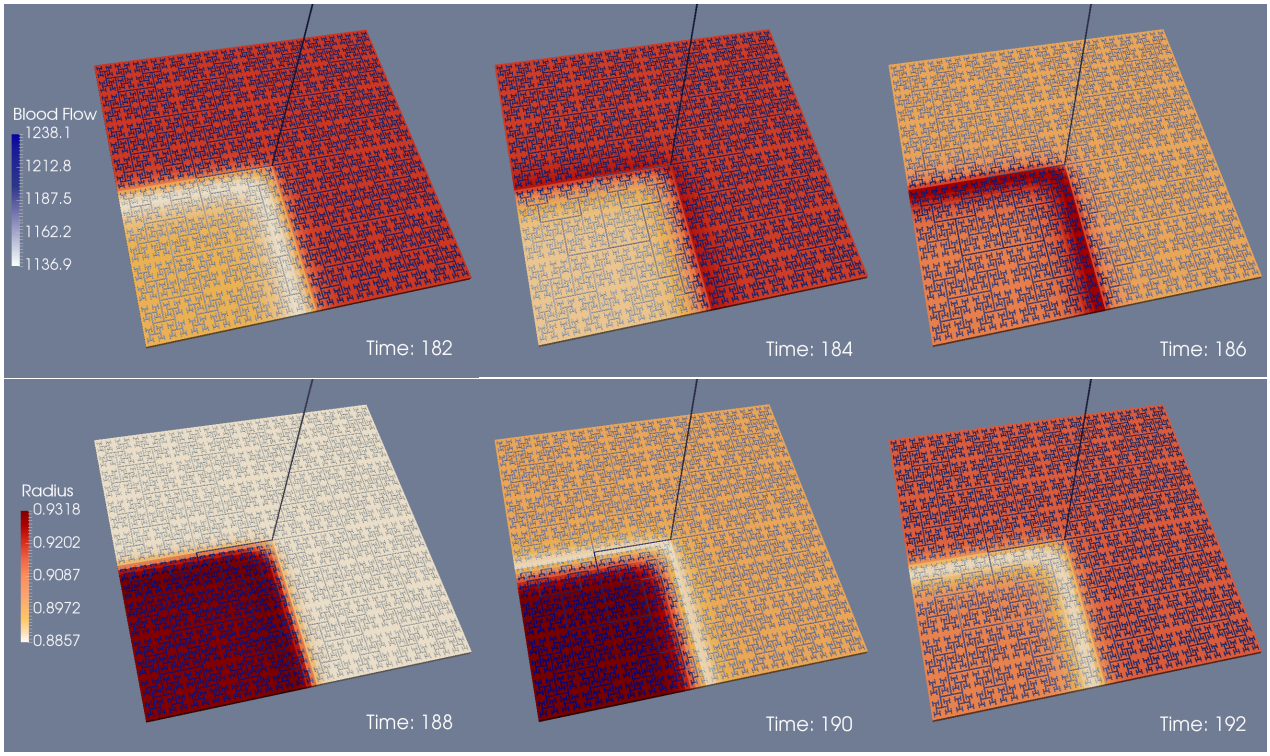


(a) Tissue slice snapshots of the proposed model following neuronal stimulation.

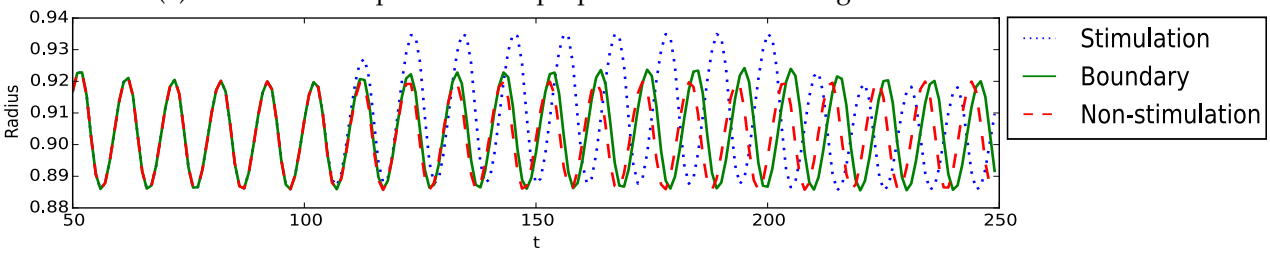


(b) Normalised vessel radii in 3 different areas of the tissue slice.

Figure 12: (a) Neuronal activation simulation snapshots of a 7.9 mm $\times$ 7.9 mm cerebral tissue slice including 4096 NVU blocks globally coupled via a space filling H-tree and diffusion of $K^+$ through the ECS, with oscillatory dynamics (with vasomotion). The colour of the tissue blocks represents the normalised vessel radius and the colour of the vascular tree represents the blood flow. The lower left corner of the tissue slice was stimulated by neuronal input from $t = 100$ to 200 s causing the local dilation of blood vessels and increased blood flow. The diffusion of $K^+$ through the ECS of neighbouring NVU tissue blocks results in the weak stimulation of NVUs adjacent to the activation area, resulting in an decreasing gradient in amplitude and period of oscillations from the stimulated to non stimulated area. The spatial variation in the period of oscillations causes the vessels to oscillate out of sync, resulting in what look like waves of increased radius moving towards the stimulated area.
(b) The normalised radii of vessels in 3 distinct areas of the tissue slice are shown. The plots are shown with time starting at $t = 50$ s to disregard any transient behaviour. Boundary refers to a vessel adjacent to the stimulated area. When $J_{PLC} = 0.4$ $\mu Ms^{-1}$ the amplitude and period of radial oscillations of an NVU in the directly stimulated area increases. An NVU on the boundary experiences a slight increase in amplitude and period of radial oscillations. The non stimulated area experiences no change. After the stimulation ends at $t_1 = 200$ s the NVUs remain out of phase. In the basic model the behaviour of vessels on the boundary and non stimulated areas are the same. Video available online (https://youtu.be/7jepHw_7xCE)

amplitude and period for NVUs on the boundary of the stimulated area, clearly seen in Figure 12b.

This difference in the period of oscillations of vessels in the stimulated, boundary and non stimulated areas causes the vessels to oscillate out of phase, resulting in what appear to be waves of increased radius moving towards the stimulated area. This is an example of emergent behaviour that persists when the neuronal stimulation is removed since the oscillating NVUs remain out of phase.

The dynamics of the SMC in the NVU are oscillatory, therefore the flux through the $Ca^{2+}$ mediated $K^+$ channel $J_K$ into the ECS also oscillates due to its dependence on the SMC membrane potential $v_i$. This will induce the $K^+$ concentration in the ECS to also oscillate. However, the magnitude of the flux $J_K$ is comparatively small so the amplitude of $K^+$ oscillations in the ECS are negligible.

## 3.4 DISCUSSION

The implementation of the macro scale model of neurovascular coupling combined with the vascular tree provides a platform for the study of blood supply regulation in the brain; in particular the addition of extracellular $K^+$ diffusion allows for further study in relation to pathological conditions such as cortical spreading depression.

With the addition of extracellular $K^+$ diffusion the proposed model is able to simulate NVC in a more physiological manner. When the tissue slice has low luminal agonist concentration ($J_{PLC} = 0.18\ \mu Ms^{-1}$), a spatially localised stimulus results in vasodilation with a decreasing gradient in vessel radius and blood flow from the area of neuronal stimulation to non stimulation. In contrast, with the basic model, vessels on the boundary of the neurally stimulated area received no stimulation at all. This results in a physiologically unrealistic clear divide in the vessel radius and blood flow between the two areas.

When vasomotion is present for high agonist concentration ($J_{PLC} = 0.4\ \mu Ms^{-1}$), a localised neuronal stimulus results in vasodilation with an increase in the amplitude and period of radial oscillations. There is a decreasing gradient in the amplitude and period of radial oscillations from stimulated to non stimulated area. This spatial variation in the period causes the NVUs in adjacent tissue blocks to oscillate out of phase, resulting in emergent behaviour in the form of waves of increased radius moving inward toward the stimulated area. This behaviour persists when the

neuronal stimulation is removed as the oscillating NVUs remain out of phase. Hence, the model is able to produce fundamentally new behaviour when simulated on the macro scale.

Due to flow conservation, the changes in flow at the leaves of the vascular tree following a localised neuronal stimulation have an effect on the blood flow through the higher level branches. This effect is minor as the higher level branches are of relatively low resistance, so changes in pressure due to a downstream flow perturbation are very small. Hence, there is minimal influence on other downstream vessels, and the majority of influence on non-stimulated NVUs within the tissue slice is via extracellular diffusion.

The increase in blood flow in response to neuronal stimulation remains sufficiently spatially localised over larger time scales. This is necessary as neurovascular coupling is the spatially localised response of the blood vessels to neuronal activation in an area of the cortex.

## 3.5 CONCLUSIONS

A numerical NVC model containing a vascular H-tree coupled with multiple NVUs comprising a cerebral tissue slice is extended via extracellular potassium diffusion, allowing for direct communication between adjacent NVUs. The model simulates NVC on the macro scale in a parallel environment using high performance computing. A localised neuronal stimulation results in vasodilation with a decreasing gradient in vessel radius from the stimulated to non-stimulated area. The dilation remains sufficiently spatially localised over larger time scales. During vasomotion, there is emergent behaviour in the form of waves of increased vessel radius moving towards the stimulated area. Results indicate that communication within the tissue is more important than communication via the vascular tree.

# 4

# THE ROLE OF ASTROCYTIC CALCIUM AND THE TRPV4 CHANNEL IN NEUROVASCULAR COUPLING

## 4.1 INTRODUCTION

There has been significant work done on the vascular response to neuronal activity and astrocytic inputs [10, 58, 56, 48] but little has been done to investigate the effect that the vasculature has on astrocytes. Moore and Cao [127] hypothesised that the cerebral vasculature has an important effect on neural function through various mechanisms. Witthoft et al. [171] suggested that one indirect mechanism is through astrocytic mechanosensation of vascular motions. Their bidirectional signalling model includes the astrocyte response to vascular function via the transient receptor potential vanniloid-related 4 (TRPV4) channel, a mechanosensitive calcium ($Ca^{2+}$) channel on the astrocytic endfoot [9]. The model was validated using experimental data from Cao [23] who provided evidence that vessel dilation provokes astrocytic $Ca^{2+}$ increase and membrane depolarisation. Dunn et al. [52] have also shown that TRPV4-mediated $Ca^{2+}$ influx contributes to the astrocytic endfoot response to neuronal activation, enhancing vasodilation.

There is some debate as to the importance of astrocytic $Ca^{2+}$ towards neurovascular coupling (NVC) [7]. Zonta et al. [177] observed experimentally that glutamate activated astrocytic endfoot $Ca^{2+}$ increases were well-timed with vascular changes; these observations were the first evidence that astrocytes may contribute towards NVC. An increase in astrocytic $Ca^{2+}$ can result in the production of arachidonic acid (AA) which is subsequently metabolised to epoxyeicosatrienoic acids (EETs) and prostaglandin $E_2$ ($PgE_2$), a derivative of cyclooxygenase enzymes (COX) [21]. These metabolites may act directly on smooth muscle cells (SMCs) [5] or directly on the astrocytic endfeet to modulate potassium ($K^+$) currents [87]. Numerous *in vivo* experimental results [133, 15, 159] indicate that NVC can occur independently of large astrocytic $Ca^{2+}$ signalling. Whereas various *in situ* experimental results [59, 155, 68] support the hypothesis that astrocytic endfoot $Ca^{2+}$ is a critical factor for NVC. In particular, Girouard et al. [68] examined the effect of astrocytic $Ca^{2+}$

on the vascular response with brain slices. The $Ca^{2+}$ concentration was elevated by either electro field stimulation (EFS) or by uncaging $Ca^{2+}$ in the astrocytic endfeet. They found that, regardless of the elevation method, moderate increases in $Ca^{2+}$ concentration resulted in vasodilation while large increases resulted in constriction (see Figure 13).

A mathematical model of a single neurovascular unit (NVU) has been presented in Chapter 3 and is based on the model of Dormanns et al. [48]. This model describes the synaptic $K^+$ induced NVC pathway, where synaptic $K^+$ is taken up by the astrocyte and extruded into the perivascular space (PVS), culminating in vasodilation via the relaxation of the SMC.

In this chapter the model is extended to include nitric oxide (NO) dynamics, where NO is a neurotransmitter primarily produced in both the neuron and endothelial cell (EC) and able to diffuse into the SMC where it acts as a potent cerebral vasodilator. The model is also extended to include glutamate mediated astrocytic $Ca^{2+}$ dynamics, the subsequent production of EETs, and their combined effect on the big potassium (BK) channel on the astrocytic endfoot. It is assumed that the EETs do not diffuse through the PVS to the arteriole, but act primarily upon the astrocytic BK channel. It is possible that EETs or other AA-derived metabolites act on the SMCs themselves [5], but it is assumed, in keeping with the findings of Higashimori et al. [87], that EETs act directly upon the astrocytic endfoot. The model does not yet include the COX - $PgE_2$ pathway, although findings from Metea and Newman [125] suggest that it is EETs rather than $PgE_2$ that result in vasodilation.

Finally, the model has been extended to include a stretch dependent TRPV4 channel on the astrocytic endfoot based on the model of Witthoft et al. [171], allowing for the direct study of the influence of this bidirectional coupling of the astrocyte and vasculature. The relative efficacy of these different pathways on the process of NVC can be examined using the complex and more comprehensive NVU model.

## 4.2 METHOD AND MODEL DEVELOPMENT

This section details the extensions to the single NVU model, in particular the addition of the NO pathway, astrocytic $Ca^{2+}$ pathway and TRPV4 channel. A schematic diagram of the proposed model containing the various extensions is found in Figure 14, and all relevant equations and parameters can be found in Appendix A.5.

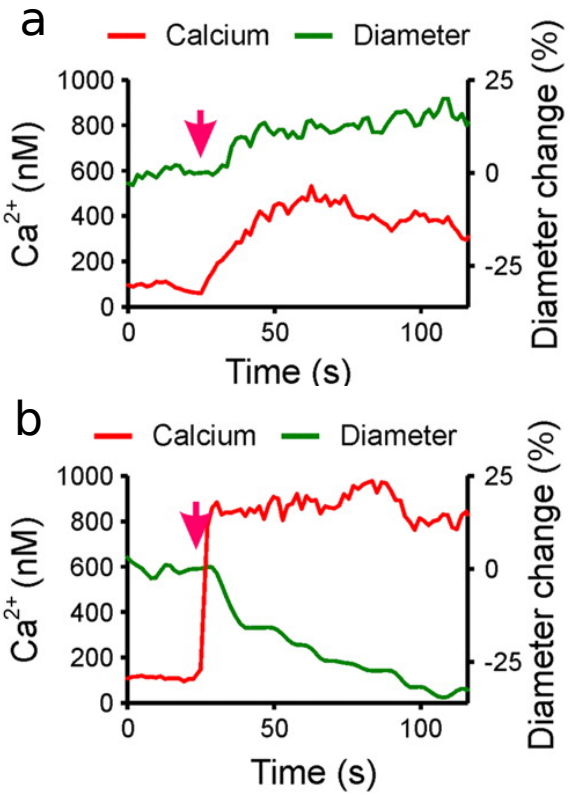


Figure 13: Experimental *in situ* results of Girouard et al. [68] show that a) moderate increases in $Ca^{2+}$ concentration in the astrocytic endfoot up to $0.324 \pm 0.016$ μM results in vasodilation, whereas b) high $Ca^{2+}$ levels of $0.732 \pm 0.041$ μM result in vasoconstriction. Adapted from Girouard et al. [68].

### 4.2.1 *NVU model: potassium pathway*

The current NVU model was previously described in Chapter 3. However as the focus of this chapter is on the contribution of the various signalling pathways within the NVU, the $K^+$ pathway is briefly described here as follows.

During neuronal stimulation $K^+$ is released into the synaptic cleft (SC), leading to an influx of $K^+$ into the astrocyte via $Na^+/K^+$ pumps on astrocytic processes adjacent to the SC. Consequently the astrocyte depolarises, leading to a large $K^+$ efflux into the PVS through the BK channel on the astrocytic endfoot [33].

The rise in perivascular $K^+$ concentration leads to a further influx of $K^+$ through the inward rectifying $K^+$ (KIR) channel from the SMC into the PVS, hyperpolarising the SMC membrane. As a result the voltage operated $Ca^{2+}$ channels (VOCCs) on the SMC close, preventing an influx of $Ca^{2+}$. The decrease in $Ca^{2+}$ concentration causes a decrease in the rate constants $K_1$ and $K_6$ for the phosphorylation of free and attached cross bridges, respectively. Overall the change in the

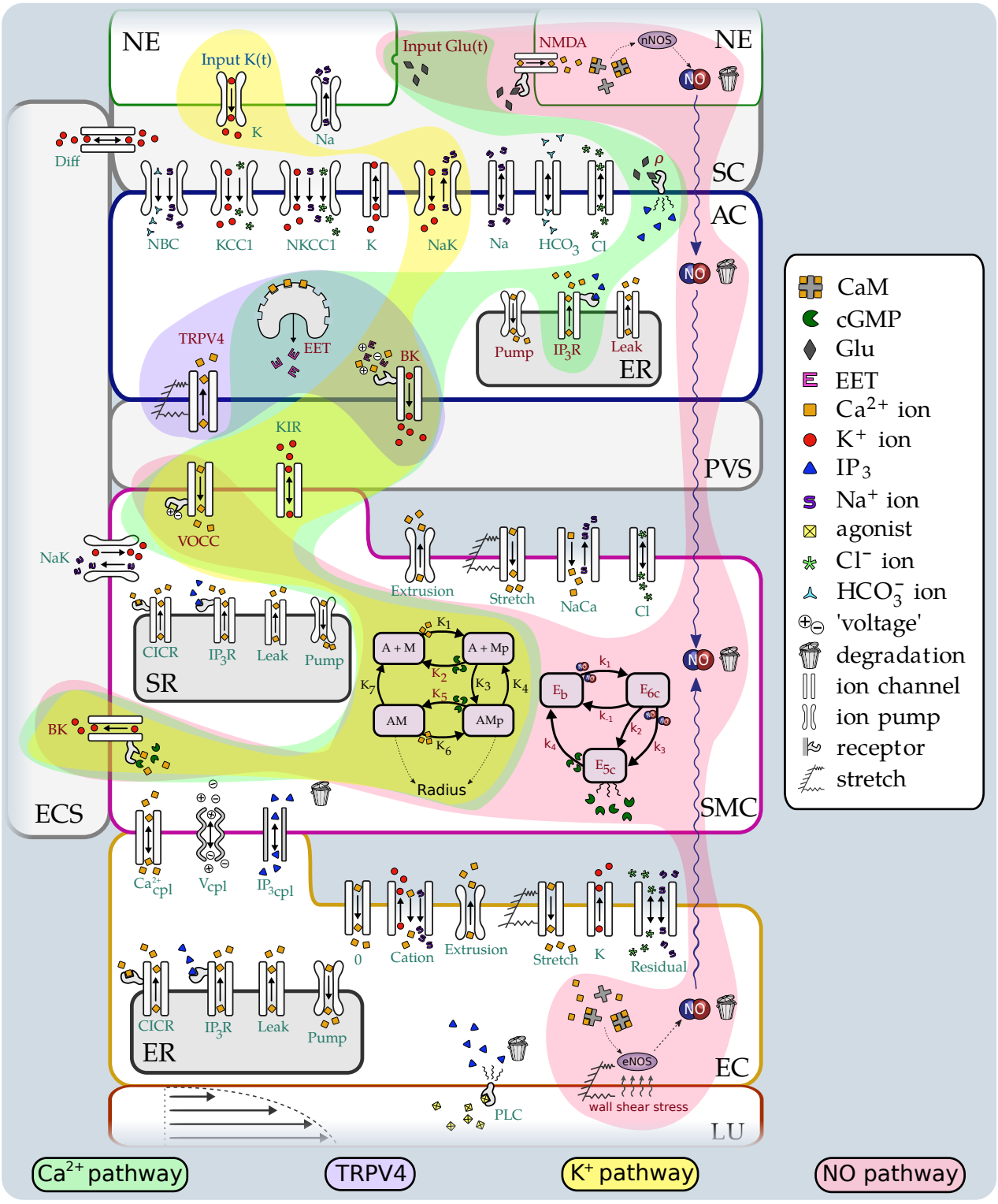


Figure 14: A schematic representation of the proposed NVC model with added NO pathway (pink), astrocytic $Ca^{2+}$ pathway (green), and TRPV4 channel (purple). NE: neuron, SC: synaptic cleft, AC: astrocyte, PVS: perivascular space, SMC: smooth muscle cell, SR: sarcoplasmic reticulum, EC: endothelial cell, ER: endoplasmic reticulum, LU: lumen, ECS: extracellular space. NMDA: N-methyl-D-aspartate receptor channel, $E_b, E_{6c}, E_{5c}$: fraction of soluble guanylyl cyclase (sGC) in the basal state, intermediate form, and fully activated form respectively, $k_{-1}$ to $k_4$: sGC rate constants, Pump: $Ca^{2+}$ uptake pump, Leak: $Ca^{2+}$ leak channel, $IP3_R$: inositol trisphosphate ($IP_3$) receptor $Ca^{2+}$ channel. Components that have been added or modified are labelled in dark red.

actin-myosin cross bridge formation relaxes the SMC, dilating the vessel which results in increased blood flow. This $K^+$ induced NVC pathway is well known [5, 59, 130] and is highlighted in yellow in Figure 14.

### 4.2.2 *Nitric oxide model of Dormanns et al. [47]*

The NO signalling pathway described by Dormanns et al. [47] has been integrated into the current model. NO is a neurotransmitter known to act as a potent cerebral vasodilator. The biochemical reaction that synthesises NO is catalysed by the enzyme family of NO synthases (NOS): neuronal (nNOS), endothelial (eNOS), and inducible (iNOS), found in neurons, ECs and multiple cell types respectively [61]. The production rate of NO is dependent on the concentration of activated NOS. nNOS and eNOS are thought to be the most influential NO producers, hence it is assumed NO production is in only the neuron and EC compartments and no production in the other cell types. However NO is able to diffuse rapidly into other compartments. NO production in the EC is catalysed by eNOS and mediated by wall shear stress (WSS) and endothelial $Ca^{2+}$ concentration, where WSS is dependent on the radius. Endothelial NO is produced continuously and independent of neuronal activity.

During neuronal stimulation, glutamate is released from the neuron into the SC. The glutamate concentration in the SC is described by the time dependent input function $\mathrm{Glu}(t)$ as given by

$$\mathrm{Glu}(t) = \mathrm{Glu}_{\max}\left[0.5\tanh\left(\frac{t-t_0}{\theta_L}\right) - 0.5\tanh\left(\frac{t-t_1}{\theta_R}\right)\right] \tag{4.1}$$

where $\mathrm{Glu}_{\max}$ is the maximum glutamate concentration corresponding to the release of one vesicle, and $\theta_L$, $\theta_R$ are slope scaling factors. The profile of the function $\mathrm{Glu}(t)$ is shown in Figure 15.

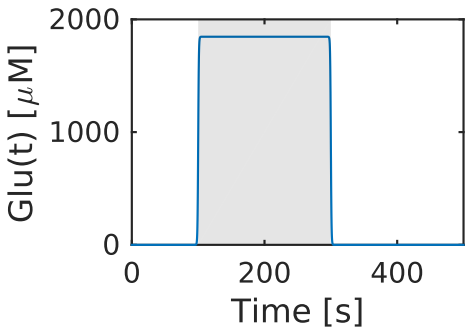


Figure 15: The input function $\mathrm{Glu}(t)$ simulating the rise of glutamate concentration during neuronal stimulation. Grey area: period of neuronal stimulation.

The rise in synaptic glutamate concentration induces a $Ca^{2+}$ influx into the neuron through N-methyl-D-aspartate (NMDA) receptor channels. The $Ca^{2+}$ binds with calmodulin (CaM) to form $CaM/Ca^{2+}$ complexes, which act to increase nNOS production and hence increase neuronal NO production.

When NO diffuses into the SMC it regulates intracellular enzyme activation and induces SMC relaxation as follows. NO activates soluble guanylyl cyclase (sGC), an enzyme which catalyses the formation of the secondary messenger cyclic guanosine monophosphate (cGMP). The increase in cGMP causes an increase in the rate of dephosphorylation of free and attached cross bridges. cGMP also acts to open the BK channel so that both the SMC $K^+$ concentration and membrane potential decrease, closing the VOCC channel. As a result the SMC $Ca^{2+}$ concentration decreases and hence the rate of phosphorylation of free and attached cross bridges decreases. Overall this leads to a decrease in the proportion of attached cross bridges and hence the SMC relaxes, i.e. the addition of the NO pathway to the model has a vasodilatory effect. This pathway is highlighted in pink in Figure 14.

### 4.2.3 *Astrocytic $Ca^{2+}$ pathway*

The first extension to the NVU model is of the astrocytic $Ca^{2+}$ pathway and based on the model of Farr and David [56]. This pathway is highlighted in green in Figure 14. The release of glutamate in the SC induces an $IP_3$ release into the astrocyte, causing the release of $Ca^{2+}$ from the endoplasmic reticulum (ER) into the cytosol, which in turn leads to the production of EETs. The membrane potential, EET concentration and $Ca^{2+}$ concentration regulate the opening of the BK channel, allowing further $K^+$ release into the PVS.

The ratio $\rho$ of bound to unbound metabotropic receptors on the astrocytic process adjacent to the SC is dependent on the synaptic glutamate release according to the following proposed relation:

$$\rho = \rho_{min} + \frac{\rho_{max} - \rho_{min}}{Glu_{max}} Glu(t) \tag{4.2}$$

where $Glu(t)$ is the smooth pulse function in Eq. (4.1), $\rho = \rho_{min}$ when $Glu(t) = 0$ and $\rho = \rho_{max}$ when $Glu(t) = Glu_{max}$. The ratio $G$ of active to total G-protein due to metabotropic glutamate receptor (mGluR) binding on the astrocytic endfoot surrounding the SC is then given by

$$G = \frac{\rho + \delta}{K_G + \rho + \delta} \tag{4.3}$$

where $K_G$ is the G-protein disassociation constant and $\delta$ is the ratio of the activities of the bound and unbound receptors, which allows for background activity in the absence of any stimulus [11]. The glutamate attachment at metabotropic receptors induces an increase in astrocytic $IP_3$ concentration $IP3_k$ according to the following ordinary differential equation (ODE):

$$\frac{dIP3_k}{dt} = r_h G - k_{deg}\, IP3_k \tag{4.4}$$

where $r_h$ is the $IP_3$ production rate and $k_{deg}$ is the degradation rate.

The astrocytic cytosolic $Ca^{2+}$ ($Ca_k$) comes from both the ER through various channels and from the PVS via the TRPV4 channel:

$$\frac{dCa_k}{dt} = B_{cyt}\left(J_{IP3_k} - J_{pump_k} + J_{ERleak_k} - \frac{J_{TRPV_k}}{r_{buff}}\right) \tag{4.5}$$

where the flux through the TRPV4 channel ($J_{TRPV_k}$) is described in Eq. (4.21), the fluxes $J_{IP3_k}$, $J_{pump_k}$, and $J_{ERleak_k}$ are described below, and $r_{buff}$ is a ratio describing the rate of $Ca^{2+}$ buffering at the astrocytic endfoot compared to the main body. Similarly the $Ca^{2+}$ concentration in the astrocytic ER ($s_k$) is given by

$$\frac{ds_k}{dt} = \frac{-B_{cyt}}{VR_{ERcyt}}\left(J_{IP3_k} - J_{pump_k} + J_{ERleak_k}\right) \tag{4.6}$$

where $VR_{ERcyt}$ is the volume ratio between the ER and the astrocytic cytosol. Fast $Ca^{2+}$ buffering is described with the steady state approximation as detailed by Fink et al. [60]:

$$B_{cyt} = \left(1 + BK_{end} + \frac{K_{ex} B_{ex}}{(K_{ex} + Ca_k)^2}\right)^{-1} \tag{4.7}$$

where $BK_{end}$ is the ratio of the endogenous buffer concentration to the endogenous disassociation constant, $K_{ex}$ is the disassociation constant of exogenous buffer, and $B_{ex}$ is the constant concentration of exogenous buffer.

The ER has 3 mechanisms for $Ca^{2+}$ transport: $IP_3R$ channels that release $Ca^{2+}$ in response to $IP_3$, an uptake pump, and a leak channel. The flux of $Ca^{2+}$ through the $IP_3R$ channel is:

$$J_{IP3_k} = J_{max}\left[\left(\frac{IP3_k}{IP3_k + K_i}\right)\left(\frac{Ca_k}{Ca_k + K_{act}}\right)h_k\right]^3\left(1 - \frac{Ca_k}{s_k}\right) \tag{4.8}$$

where $J_{max}$ is the maximum rate, $K_i$ is the dissociation constant for $IP_3R$ binding, and $K_{act}$ is the dissociation constant for $Ca^{2+}$ binding to an activation site on the $IP_3R$. The inactivation variable $h_k$ is given by

$$\frac{dh_k}{dt} = k_{on}\left[K_{inh} - (Ca_k + K_{inh})h_k\right] \tag{4.9}$$

where $k_{on}$ and $K_{inh}$ are the $Ca^{2+}$ binding rate and dissociation constant, respectively. The flux of $Ca^{2+}$ through the uptake pump is given by

$$J_{pump_k} = V_{max}\frac{Ca_k^2}{Ca_k^2 + k_{pump}^2} \tag{4.10}$$

where $V_{max}$ is the maximum pump rate and $k_{pump}$ is the pump constant. The flux of $Ca^{2+}$ through the leak channel is given by

$$J_{ERleak_k} = P_L\left(1 - \frac{Ca_k}{s_k}\right) \tag{4.11}$$

where $P_L$ is the steady state balance constant.

The ODE for the astrocytic EET concentration ($eet_k$) is assumed to have the form of

$$\frac{deet_k}{dt} = V_{eet}(Ca_k - c_{k_{min}}) - k_{eet}eet_k \tag{4.12}$$

where $V_{eet}$ is the EET production rate, $c_{k_{min}}$ is the minimum $Ca^{2+}$ concentration required for EET production, and $k_{eet}$ is the decay rate.

#### 4.2.3.1 *BK channel*

The following equations are modified from Dormanns et al. [48] to include astrocytic $Ca^{2+}$ dynamics following the work of Farr and David [56]. Astrocytic $Ca^{2+}$, EET concentration, and membrane

potential $v_k$ all have an opening effect on the astrocytic BK channel on the endfeet adjacent to the PVS. The flux of $K^+$ through the astrocytic BK channel is given by

$$J_{BK_k} = \frac{g_{BK_k}}{R_k F} w_k (v_k - E_{BK_k}) \tag{4.13}$$

where $g_{BK_k}$ is the channel conductance per unit area, $F$ is Faraday's constant, and $R_k$ is the astrocytic volume-area ratio (see Dormanns et al. [48] for further details on this variable). The Nernst potential of the BK channel is given by

$$E_{BK_k} = \frac{R_g T}{z_K F} \ln\left(\frac{K_p}{K_k}\right) \tag{4.14}$$

where $R_g$ is the universal gas constant, $z_K$ is the ionic valence for $K^+$, and $K_p$ and $K_k$ are the perivascular and astrocytic $K^+$ concentrations respectively (see Dormanns et al. [48] for further details on these two variables).

The open probability $w_k$ of the voltage, $Ca^{2+}$ and EET mediated BK channel (Eq. (4.13)) is given by

$$\frac{dw_k}{dt} = \phi_n (w_\infty - w_k) \tag{4.15}$$

The time constant associated with the opening of the BK channel is given by

$$\phi_n = \psi_n \cosh\left(\frac{v_k - v_3}{2v_4}\right) \tag{4.16}$$

where $\psi_n$ is the characteristic time constant and $v_4$ is a measure of the spread of the open probability. The equilibrium state BK channel is written as

$$w_\infty = 0.5\left(1 + \tanh\left(\frac{v_k + eet_{shift} eet_k - v_3}{v_4}\right)\right) \tag{4.17}$$

where $eet_{shift}$ determines the EET-dependent shift of the channel. Finally the voltage associated with half open probability is given by

$$v_3 = -\frac{v_5}{2} \tanh\left(\frac{Ca_k - Ca_3}{Ca_4}\right) + v_6 \tag{4.18}$$

where $v_5, v_6, Ca_3$ and $Ca_4$ are constants.

The BK channel submodel of Farr and David [56] used parameters from Gonzalez-Fernandez and Ermentrout [74], however some of these parameters were more suited to a cell model such

as a neuron where the membrane potential depolarises and becomes positive. As such the profile of the steady state open probability $w_\infty$ had a sharp incline between $-50$ mV and 20 mV (see Figure 16). However in the model the astrocyte only depolarises from $-87$ mV up to a maximum of $-54$ mV. This range is consistent with the experimental results of Meeks and Mennerick [124] who found that the astrocyte membrane potential varied from approximately $-90$ to $-60$ mV for extracellular $K^+$ between 3 and 8 mM (as occurs during regular NVC).

Cox [36] modelled a BK channel in the neuron and found that increasing the $Ca^{2+}$ concentration shifted the profile of the open probability to the left. However, even at very high $Ca^{2+}$ concentrations the open probability was not high unless the cell was depolarised.

BK channels represent a diverse group of channels mediated by accessory subunits ($\beta 1 - \beta 4$) that alter the biophysical properties and pharmacology of these channels [166]. In addition, similar ion channels often behave differently in different organs leading to organ-specific model parameterisations. It is not unreasonable, therefore, to assume BK channels in the neuron and astrocyte have distinct properties.

Based on the open probability profile at differing $Ca^{2+}$ concentrations in Cox [36] and the range of $v_k$ that is seen in the model, the parameters of BK channel open probability have been modified (see Figure 16).

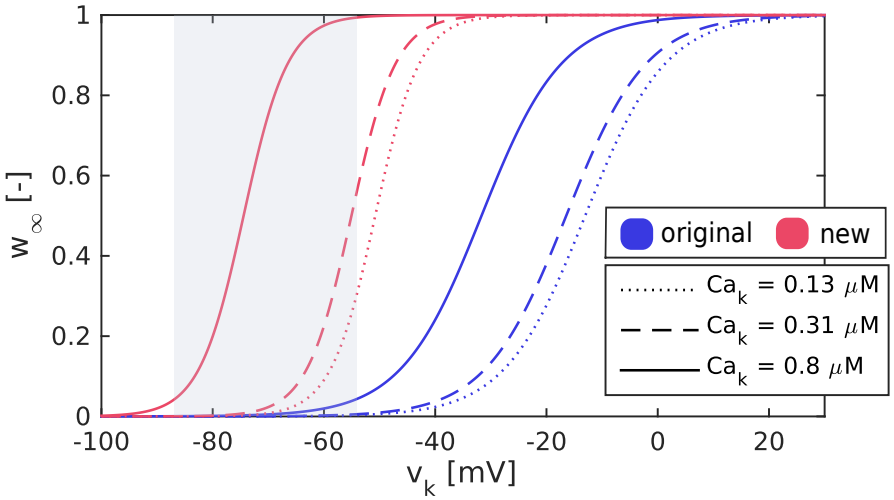


Figure 16: BK steady state open probability $w_\infty$ varied with astrocytic membrane potential ($v_k$) at differing astrocytic $Ca^{2+}$ concentration levels ($Ca_k$), for the original model parameters (blue) and new parameters (red). Grey area: range of $v_k$ in the astrocyte.

### 4.2.4 *TRPV4 channel*

The second extension to the NVU model is the inclusion of the TRPV4 channel on the astrocytic endfoot adjacent to the PVS and is based on the bidirectional model of Witthoft et al. [171]. This pathway is highlighted in purple in Figure 14. In this model vessel dilation activates the TRPV4 channels, allowing an influx of $Ca^{2+}$ from the PVS into the cytosol and hence increasing the astrocytic $Ca^{2+}$ concentration. As the model does not contain any $Ca^{2+}$ in the SC, including TRPV4 channels on the astrocytic endfoot facing the SC was not considered.

The perivascular $Ca^{2+}$ concentration $Ca_p$ is given by

$$\frac{dCa_p}{dt} = \frac{J_{TRPV_k}}{VR_{pa}} + \frac{J_{VOCC_i}}{VR_{ps}} - Ca_{decay_p}(Ca_p - c_{min_p}) \tag{4.19}$$

where $VR_{pa}$ and $VR_{ps}$ are volume ratios, $Ca_{decay_p}$ is the $Ca^{2+}$ decay rate, and $c_{min_p}$ is the resting state equilibrium $Ca^{2+}$ concentration in the PVS. Here $J_{VOCC_i}$ is the flux of $Ca^{2+}$ through the VOCC which connects the SMC to the PVS. When the membrane of the SMC hyperpolarises this channel closes and the flux is given by

$$J_{VOCC_i} = G_{Cai}\frac{v_i - v_{Ca1}}{1 + \exp\left[-(v_i - v_{Ca2})/R_{Cai}\right]} \tag{4.20}$$

where $G_{Cai}$ is the whole cell conductance, $v_{Ca1}$ is the reversal potential, $v_{Ca2}$ is the half point of the VOCC activation sigmoidal, $R_{Cai}$ is the maximum slope of the activation sigmoidal, and $v_i$ is the variable SMC membrane potential.

The flux of $Ca^{2+}$ through the TRPV4 channel is given by

$$J_{TRPV_k} = G_{TRPV_k} m_k (v_k - E_{TRPV_k}) c_{unit} \tag{4.21}$$

where $G_{TRPV_k}$ is the whole cell conductance for TRPV4 channels and $c_{unit}$ is a conversion factor. The Nernst potential of the TRPV4 channel is given by

$$E_{TRPV_k} = \frac{R_g T}{z_{Ca} F} \log\left(\frac{Ca_p}{Ca_k}\right) \tag{4.22}$$

where $z_{Ca}$ is the ionic valence for $Ca^{2+}$.

The open probability of the TRPV4 channel is modelled as an ODE that decays to its equilibrium state $m_{\infty_k}$ according to

$$\frac{dm_k}{dt} = \frac{m_{\infty_k} - m_k}{t_{TRPV_k}} \tag{4.23}$$

where $t_{TRPV_k}$ is the characteristic time constant, and the equilibrium state of the TRPV4 channel is described by the Boltzmann equation [170]

$$m_{\infty_k} = \Gamma_m \left[ \frac{1}{1 + H_{Ca_k}} \left( H_{Ca_k} + \tanh\left( \frac{v_k - v_{1,TRPV}}{v_{2,TRPV}} \right) \right) \right] \tag{4.24}$$

where $v_{1,TRPV}$ and $v_{2,TRPV}$ are voltage gating constants. The material strain gating term is given by

$$\Gamma_m = \frac{1}{1 + \exp\left( -\frac{\eta - \eta_0}{\kappa_k} \right)} \tag{4.25}$$

where $\eta_0$ is the local radial strain on the arteriole required for half activation and $\kappa_k$ is a strain constant. The strain on the perivascular endfoot of the astrocyte is taken as approximately equal to local radial strain on the arteriole given that the endfoot surrounds the arteriole, and is given by

$$\eta = \frac{R - R_{passive}}{R_{passive}} \tag{4.26}$$

where $R_{passive}$ is the resting radius. The $Ca^{2+}$ inhibitory term is given by

$$H_{Ca_k} = \frac{Ca_k}{\gamma_{Cai}} + \frac{Ca_p}{\gamma_{Cae}} \tag{4.27}$$

where $\gamma_{Cai}$ and $\gamma_{Cae}$ are constants associated with intracellular and extracellular $Ca^{2+}$, respectively.

The astrocytic membrane potential $v_k$ equation is modified from the foundation model to include the TRPV4 channel:

$$v_k = \frac{g_{Na_k} E_{Na_k} + g_{K_k} E_{K_k} + \ldots + g_{TRPV_k} m_k E_{TRPV_k}}{g_{Na_k} + g_{K_k} + \ldots + g_{TRPV_k} m_k} \tag{4.28}$$

where $g_{TRPV_k}$ is the TRPV4 channel conductance per unit area (note: not the same as $G_{TRPV_k}$).

### 4.2.5 *Minor model corrections*

The direction of the $Ca^{2+}$ flux through the stretch channels in the SMC and EC compartments was incorrect due to a misprint in the work of Koenigsberger et al. [111]; this has now been fixed.

This shifted the bifurcation diagram of the parameter $J_{PLC}$ (see Figure 5 in Chapter 2) to the left so that the model now oscillates for lower values of $J_{PLC}$. Consequently a lower $J_{PLC}$ value of 0.11 $\mu M\ s^{-1}$ is used from here onwards to simulate steady state conditions.

### 4.2.6 *Implementation*

A total of 42 coupled ODEs make up the entire single NVU system and are solved in Matlab using the stiff solver 'ode15s' due to domains of stiffness encountered in the foundation model of Dormanns et al. [47]. The initial conditions were chosen so that the system is initially at a steady state.

A single NVU is neuronally stimulated via an input of $K^+$ and glutamate into the SC in order to produce a vascular response through the process of NVC. These input functions are given by $K(t)$ (described in Chapter 3) and $Glu(t)$ (described in Section 4.2.2) respectively. However with multiple pathways and components in the NVU the vascular response should vary based on which pathways are active, where the pathways are: $K^+$, NO, astrocytic $Ca^{2+}$, and the TRPV4 channel shown in Figure 14. The effects of each pathway are examined, in particular the contribution of astrocytic $Ca^{2+}$ and the TRPV4 channel. It is important to note that mathematical models are able to shut off or isolate individual pathways which are impossible to do in a wet lab.

The four pathways are activated or deactivated as follows. The $K^+$ pathway is controlled via the input function $K(t)$ so that when there is no input (i.e. $K_{input} = 0$) the pathway is deactivated. The astrocytic $Ca^{2+}$ pathway is controlled via the input function $Glu(t)$ in a similar manner ($Glu_{max} = 0$). The NO pathway is activated through the input function $Glu(t)$ and deactivated by setting the rates of nNOS and eNOS production to zero, so that no NO can be produced. Finally the TRPV4 channel is deactivated by setting the open probability of the channel to zero so there is no $Ca^{2+}$ flux.

The stimulation input functions are from 100 to 300 s simulation time (indicated by a grey box in the following figures), primarily for the NO pathway as it has a delayed response.

## 4.3 RESULTS

### 4.3.1 *Astrocytic $Ca^{2+}$ pathway and TRPV4 channel*

The effects of the astrocytic $Ca^{2+}$ pathway and the TRPV4 channel implemented in isolation and together are shown in Figure 17. Note the small scale on the y axis for $w_k$.

When only the $Ca^{2+}$ pathway is active, the glutamate release from neuronal stimulation induces a fast release of $IP_3$ into the astrocyte via metabotropic receptors. Consequently there is an influx of $Ca^{2+}$ into the cytosol through the $IP_3$ mediated $Ca^{2+}$ channel on the ER. The level of astrocytic $Ca^{2+}$ ($Ca_k$) increases to 0.31 $\mu$M, consistent with the experimental results of Girouard et al. [68] (see Figure 13). The rise in $Ca_k$ induces an increase in EET concentration ($eet_k$), and the increase in $Ca_k$ and $eet_k$ both cause a very minor increase in the open probability of the BK channel ($w_k$). Therefore the flux of $K^+$ through the BK channel has a corresponding small increase, as does the perivascular $K^+$ concentration ($K_p$) and radius of only 0.002% from the baseline. This radial increase is negligible (results not shown).

When the $Ca^{2+}$ pathway is deactivated and the TRPV4 channel active, the TRPV4 channel induces a small constant $Ca^{2+}$ flux into the astrocyte which slightly increases the resting $Ca_k$ and $eet_k$ by a small amount. The astrocytic membrane potential $v_k$ also slightly increases due to the $Ca^{2+}$ ion influx to the cell. This constant $Ca^{2+}$ influx is minor as the TRPV4 channel is stretch dependent and the resting basal radius is small.

The $Ca^{2+}$ pathway and TRPV4 channel together produce the largest increase in $w_k$, however this increase is still negligible. The increase in $w_k$ is small because the open probability is also strongly voltage dependent (clearly seen in Figure 16), and there is no significant increase in $v_k$ during stimulation associated with the $Ca^{2+}$ pathway and/or TRPV4 channel. Hence the $K^+$ flux through the BK channel is not large enough to significantly raise $K_p$ and have any effect on the radius.

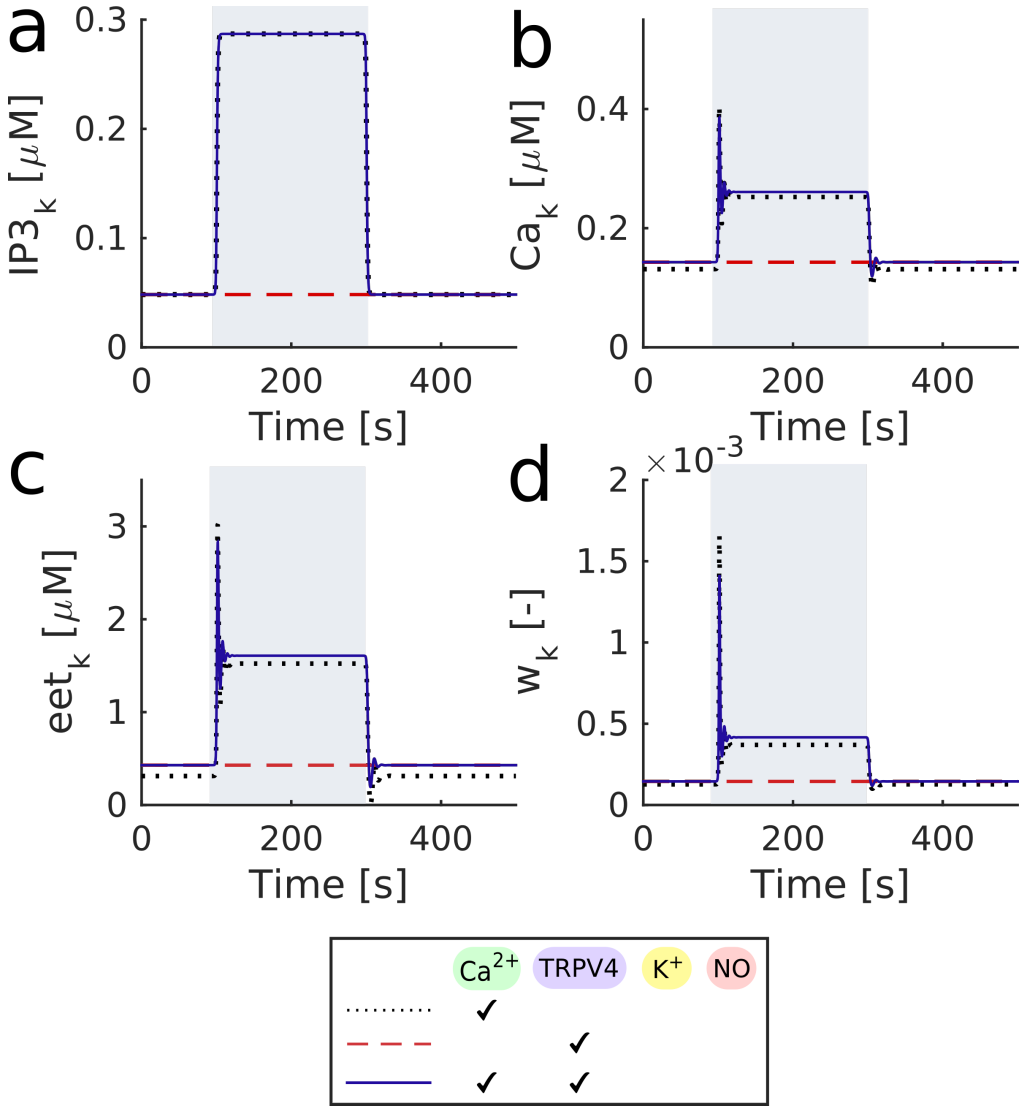


Figure 17: The effects of the astrocytic $Ca^{2+}$ pathway and TRPV4 channel both individually and together. a) astrocytic $IP_3$ concentration, b) astrocytic $Ca^{2+}$ concentration, c) astrocytic EET concentration, and d) open probability of the astrocytic BK channel.

### 4.3.2 *Potassium pathway*

The effects of the $K^+$ pathway with and without the astrocytic $Ca^{2+}$ pathway and TRPV4 channel are shown in Figure 18. The two variable components of the BK flux equation are the open probability $w_k$ and the term $v_k - E_{BK_k}$ (see Eq. (4.13)).

When only the $K^+$ pathway is active, the release of $K^+$ into the SC is taken up by the astrocyte. This influx of positive ions depolarises the astrocyte and $v_k$ increases. Even though there is no increase in either $Ca_k$ or $eet_k$, the strong voltage dependency of the BK channel means that $w_k$ increases significantly up to 0.05 and the magnitude of the flux (via the term $v_k - E_{BK_k}$) is large.

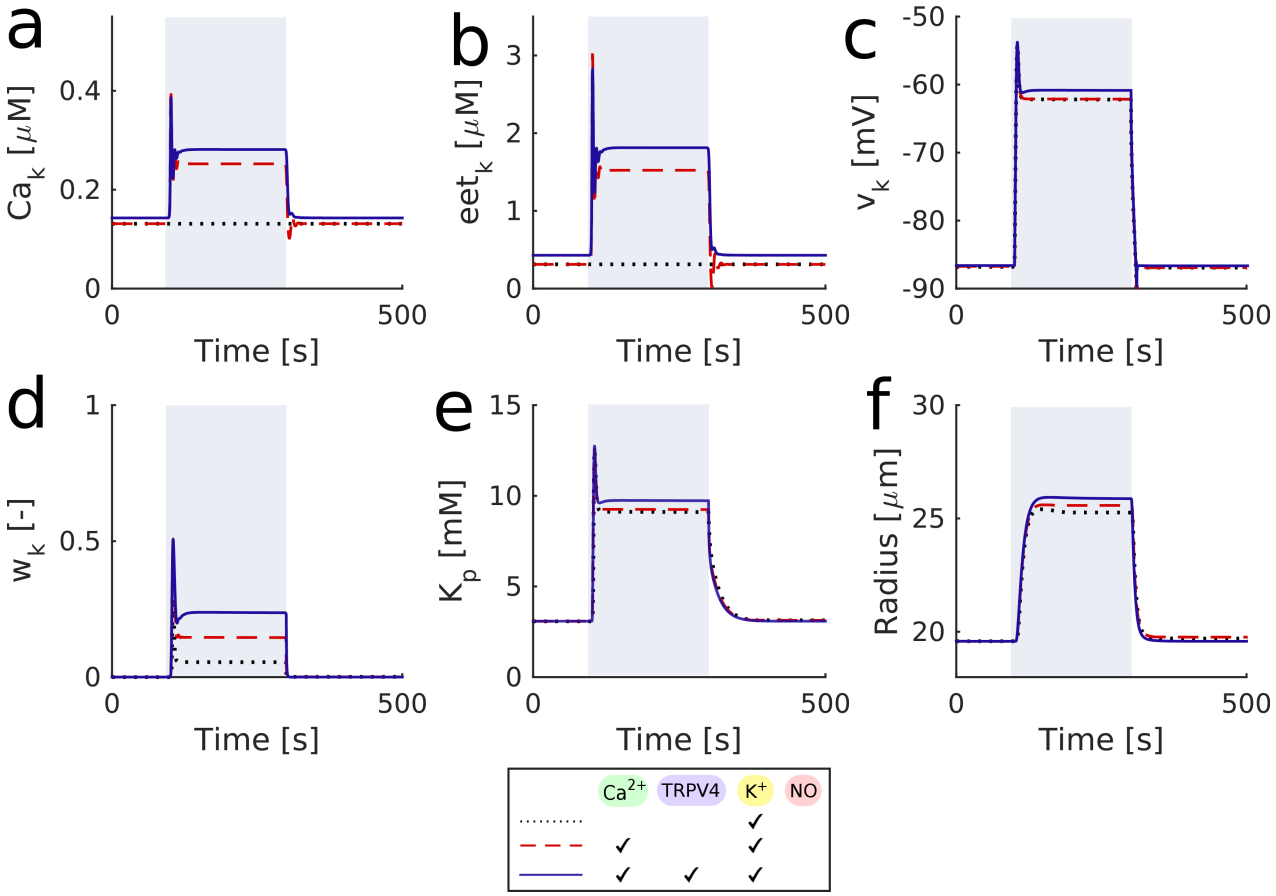


Figure 18: The effects of the $K^+$ pathway with the $Ca^{2+}$ pathway and TRPV4 channel. a) astrocytic $Ca^{2+}$ concentration, b) astrocytic EET concentration, c) astrocytic membrane potential, d) open probability of the astrocytic BK channel, e) perivascular $K^+$ concentration, and f) arteriolar radius.

Consequently the flux through the BK channel is large and $K_p$ increases, leading to a maximal radial increase of 29% from the baseline.

When both the $K^+$ and $Ca^{2+}$ pathways are active, the increase in $Ca_k$ and $eet_k$ cause $w_k$ to increase up to 0.15, leading to increased $K_p$ and a maximal radial increase of 31% from the baseline. It is important to note that the increase in $w_k$ from the $Ca^{2+}$ pathway is not linearly additive, due to the profile of the steady state open probability $w_\infty$ in Figure 16. By itself the $Ca^{2+}$ pathway is only able to induce a very small increase in $w_k$, but when the astrocyte is depolarised via the $K^+$ pathway, $Ca^{2+}$ results in a comparatively large increase in $w_k$.

When the TRPV4 channel is activated in addition to the $K^+$ and $Ca^{2+}$ pathways, $Ca_k$ increases further to 0.34 μM. The TRPV4 channel has a larger effect on $Ca_k$ than in the case without $K^+$ in Figure 17 because of its stretch dependency; when the radius is increased the TRPV4 $Ca^{2+}$ flux also increases, providing a positive feedback loop. The membrane potential $v_k$ slightly increases further due to the influx of positive $Ca^{2+}$ ions through the TRPV4 channel from the PVS into the astrocyte. The increase in $Ca_k$, $eet_k$ and $v_k$ causes $w_k$ to increase to 0.24 and the magnitude of

the BK flux (via term $v_k - E_{BK_k}$) to increase, opening the BK channel further and resulting in an increased maximal radius of 32% of the baseline.

Therefore the $Ca^{2+}$ pathway and TRPV4 channel are able to strengthen NVC induced by the $K^+$ pathway by increasing the open probability of the BK channel and hence allowing more $K^+$ into the PVS.

### 4.3.3 *Nitric oxide pathway*

The NO pathway is independent of the dynamics in the astrocyte. When the NO pathway is active, the glutamate release into the SC during neuronal stimulation induces neuronal NO production. The NO from both the neuron and EC diffuses into the SMC where it increases the production of cGMP and eventually induces vasodilation. The $Ca^{2+}$ pathway and TRPV4 channel have no effect on the NO pathway because they only affect the astrocytic BK channel. Consequently the $Ca^{2+}$ and TRPV4 channel have a negligible effect as in the case without NO (Figure 17) and do not strengthen NO induced NVC.

### 4.3.4 *All pathways*

The accumulative effects of all four model pathways ($K^+$, NO, astrocytic $Ca^{2+}$, and the TRPV4 channel) on the vascular response (i.e. the arteriolar radius) are shown in Figure 19. The $K^+$ pathway (dotted line) has fast radial dynamics that begin 3 seconds after neuronal stimulation begins, reaching the maximal radius in approximately 30 seconds. The radius then slightly decreases before reaching a steady state approximately 100 seconds after stimulation starts. However there is also rapid decay almost directly after stimulation ceases, with the radius reaching the baseline within 30 seconds.

When only the NO pathway is active (dashed line) the radial baseline is 23.2 μm, 18% higher due to the vasodilatory effect of the NO continuously produced in the EC. In contrast to the $K^+$ pathway the dynamics are much slower and the response is delayed. The vascular response to neuronal stimulation begins approximately 8 seconds after stimulation starts. The radius continuously increases at a slow rate until approximately 15 seconds after stimulation has ceased. The radius profile then slowly decays, reaching the baseline after approximately 150 seconds.

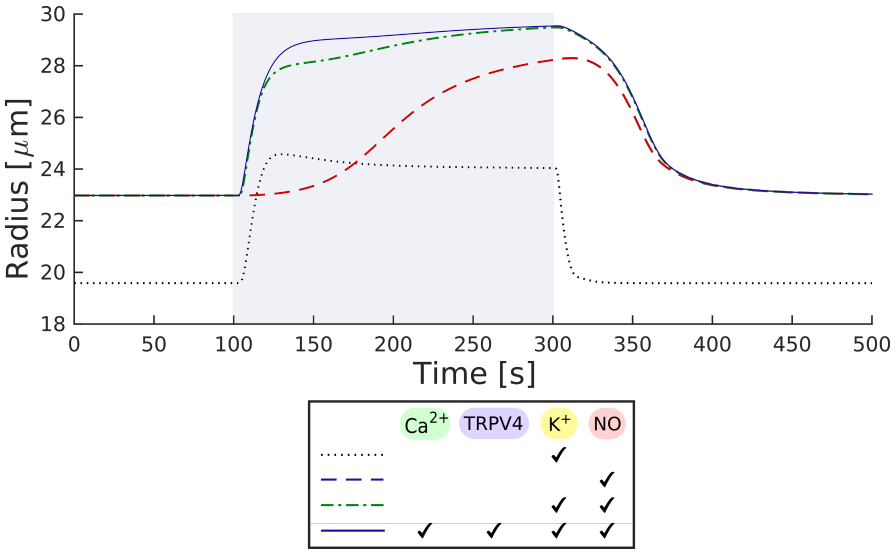


Figure 19: The effects of both $K^+$ and NO pathways with the astrocytic $Ca^{2+}$ pathway and TRPV4 channel on the arteriolar radius.

When both the $K^+$ and NO pathways are active (dot-dashed line) the radius experiences a fast initial increase for approximately 30 seconds, before continuously increasing at a slower rate until approximately 5 seconds after stimulation ceases. The radius then slowly decreases back to the baseline over approximately 150 seconds.

When all four components are active ($K^+$, NO, $Ca^{2+}$ and TRPV4, solid line), the radius increases at a fast rate for approximately 40 seconds, reaching a higher initial maximum than the case without $Ca^{2+}$ and TRPV4. The radius continues to slowly increase and reaches a slightly higher maximal radius approximately 5 seconds after stimulation ceases, and the radius decays to the baseline over 150 seconds. Hence the $Ca^{2+}$ pathway and TRPV4 channel increase the maximal radius of the vascular response due to their effects on the astrocytic BK channel which in turn strengthen the $K^+$ induced NVC pathway.

### 4.3.5 *$Ca^{2+}$ induced vasoconstriction*

Various studies have suggested that, in contrast to glutamate induced NVC where a moderate increase in $Ca^{2+}$ concentration can cause vasodilation, larger increases in $Ca^{2+}$ can result in vasoconstriction [68, 52, 51]. As an example, Du et al. [51] performed experiments with glutamatergic neurons which exude only glutamate upon activation. They suggest that NO and the neuropeptide vasopressin mediate NVC through different pathways. Vasopressin leads to a rapid and significant increase in astrocytic $Ca^{2+}$ concentration [173]. According to their data, high concentrations

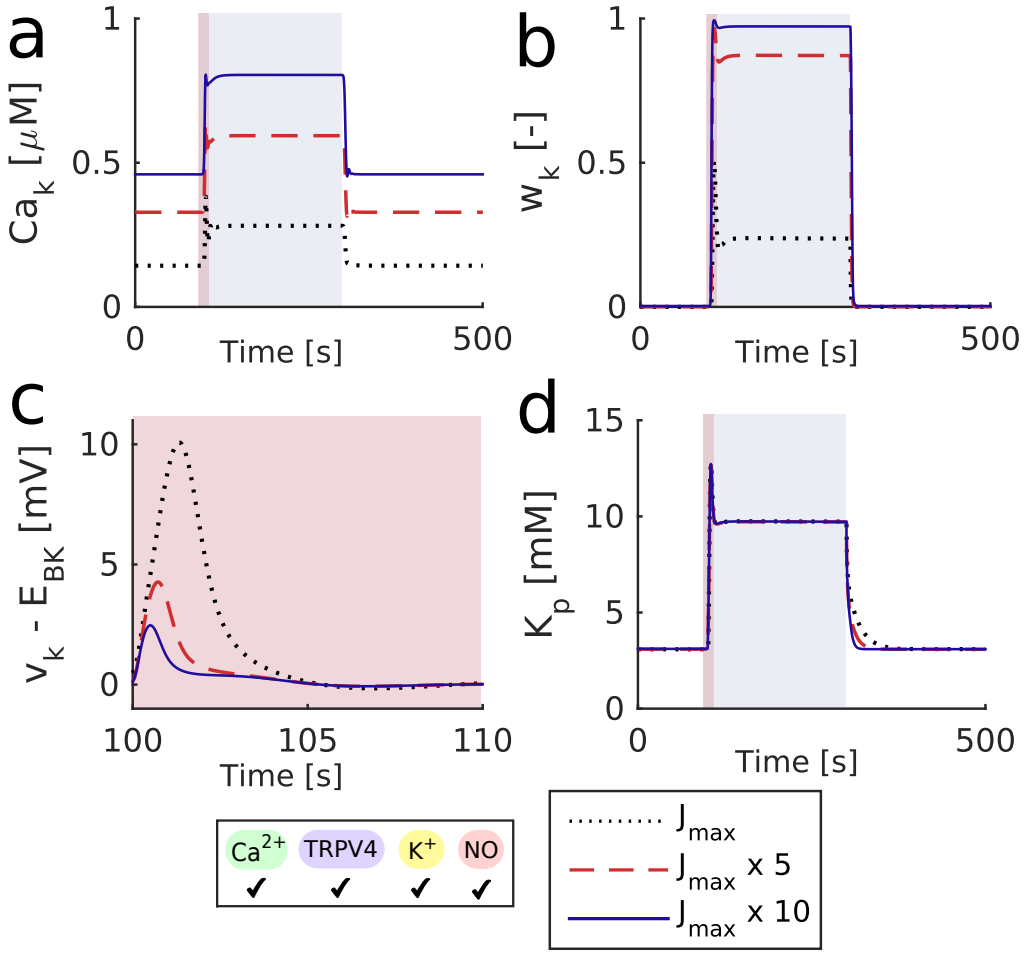


Figure 20: The effects of high astrocytic $Ca^{2+}$ concentration $Ca_k$ via increased $IP_3$ induced $Ca^{2+}$ release ($J_{max}$) in the astrocyte. a) astrocytic $Ca^{2+}$ concentration, b) open probability of the BK channel $w_k$, c) the component $v_k - E_{BK}$ of the BK flux, and d) the perivascular $K^+$ concentration $K_p$.

of $Ca^{2+}$ (through the release of vasopressin) results in vasoconstriction, NO causes vasodilation, and when released together there is brief vasodilation followed by constriction.

As Du et al. [51] studied glutamatergic neurons specifically, the rates of various ion channels and amount of $Ca^{2+}$ released during stimulation may differ from the generic NVU model presented here. To account for this, the maximum rate $J_{max}$ of the $IP_3R$ $Ca^{2+}$ channel on the ER is varied in order to simulate much larger releases of $Ca^{2+}$ from the ER into the astrocyte. However, as shown in Section 4.3.1, in the model increased $Ca^{2+}$ levels have a negligible effect on the radius without the astrocytic depolarisation caused by the $K^+$ pathway. In fact, even unphysiologically high $Ca^{2+}$ levels of over 4 μM still have no significant effect (results not shown). Therefore the effects of high $Ca^{2+}$ are examined with the $K^+$ pathway active. The behaviour of the NVU in response to high astrocytic $Ca^{2+}$ concentration with all components active is shown in Figure 20.

By increasing $J_{max}$ by a factor of 5, the $Ca^{2+}$ concentration $Ca_k$ during stimulation increases up to 0.6 μM. Whereas increasing $J_{max}$ by a factor of 10 causes $Ca_k$ to increase up to 0.8 μM.

This $Ca^{2+}$ concentration is at a similar level to that in the experiment of Girouard et al. [68] which induced vasoconstriction (see Figure 13). As the astrocyte is depolarised from the $K^+$ pathway, this high $Ca^{2+}$ level causes the BK channel to almost fully open ($w_k$ almost 1). Consequently the BK flux has a high initial magnitude of $K^+$ moving into the PVS. But this means that the BK Nernst potential $E_{BK}$ is quick to increase due to the fast increase in perivascular $K^+$ concentration, so that the term $v_k - E_{BK}$ becomes smaller more quickly. Hence the BK flux will be quick to decrease in magnitude. Conversely, when the open probability is low, the BK flux has a lower initial magnitude and $E_{BK}$ takes longer to increase, so the BK flux will take longer to decrease in magnitude.

Therefore if the channel is only slightly open, the $K^+$ flux will be of lower magnitude over a longer time, whereas if the channel is almost fully open the $K^+$ flux will be of higher magnitude over a shorter time. Regardless, over the period of stimulation the total amount of $K^+$ through the BK channel will be almost the same, so the effect of increasing $w_k$ is minor. Hence while increasing the $Ca^{2+}$ levels increases the open probability of the BK channel, the effect is counteracted by the fast increase in Nernst potential.

These results show that in the model the only way to significantly increase the amount of $K^+$ going through the BK channel in order to cause further dilation or vasoconstriction is by increasing the astrocytic membrane potential $v_k$ further; increases in astrocytic $Ca^{2+}$ alone are not sufficient. This suggests that either there is some important component missing from the model, or that the increase in astrocytic $Ca^{2+}$ that occurs at the same time as vasodilation or constriction is irrelevant to the vascular response of NVC.

## 4.4 DISCUSSION

The addition of astrocytic $Ca^{2+}$ and the TRPV4 channel to the foundation model of Dormanns et al. [47] allows for a comparison of the contribution of various different pathways present in the NVU ($K^+$, NO, astrocytic $Ca^{2+}$, and the TRPV4 channel). Changing the BK submodel parameters to fit the astrocyte dynamics rather than neuronal dynamics results in a more physiologically realistic open probability that naturally ranges from 0 to 1 rather than 0 to 0.002.

The $K^+$ signalling pathway induced by neuronal $K^+$ release governs the fast onset of vasodilation during neuronal stimulation, while the NO signalling pathway induced by neuronal glutamate release is responsible for maintaining the dilation longer with a slow decline to the basal state

following stimulation. The NO produced in the EC increases the basal radius due to constant WSS induced eNOS production.

The TRPV4 channel provides a bidirectional signalling pathway between the astrocyte and the vasculature. The pathway results in an increase in astrocytic $Ca^{2+}$ concentration proportional to the level of vasodilation during neuronal stimulation.

The astrocytic $Ca^{2+}$ pathway induced by glutamate results in a significant increase in the astrocytic $Ca^{2+}$ concentration up to levels consistent with the experimental results of Girouard et al. [68], but the effect on the astrocytic BK channel (mediated by $Ca^{2+}$, EET and strongly mediated by membrane potential) is negligible on the basis of the model. When the TRPV4 channel is active alongside the $Ca^{2+}$ pathway there is a slight increase in the astrocytic $Ca^{2+}$ concentration, but the effect is minimal as the channel is stretch dependent and the radius change is small. Even with an unrealistically high $Ca^{2+}$ concentration, the magnitude of the BK flux is still insignificant to induce either vasodilation or constriction. This is because according to the model the magnitude of the BK flux is strongly dependent on the astrocytic membrane potential, but the membrane potential has little to no change from the $Ca^{2+}$ pathway and TRPV4 channel.

Figure 21 demonstrates how the BK flux changes with both astrocytic $Ca^{2+}$ ($Ca_k$) and the membrane potential ($v_k$). Note the small scale on Figure 21a. Recall that at the resting state the NVU has $Ca_k = 0.14$ μM and $v_k = -86.5$ mV. Increasing $Ca_k$ from 0.14 μM even up to unrealistically high concentrations of 0.9 μM (while keeping $v_k$ at the resting state of $-86.5$ mV) produces only a very small increase in flux. Whereas increasing $v_k$ from the resting state up to the stimulated state at $-60$ mV (while keeping $Ca_k$ at the constant resting state at 0.14 μM) produces a large increase in flux. Therefore it is clear that, in the model with astrocytic $Ca^{2+}$ and EET signalling, the astrocyte must depolarise in order for the BK channel flux to increase in magnitude. Hence astrocytic $Ca^{2+}$ with EET signalling does not produce any noticeable vascular response, and on the basis of the model this pathway is insufficient for NVC.

However when the $K^+$ signalling pathway is active, the release of neuronal $K^+$ results in astrocytic depolarisation. Consequently the open probability of the BK channel increases and the magnitude of the BK flux is large (see Figure 21), resulting in vasodilation. When the $Ca^{2+}$ pathway and/or TRPV4 channel are activated alongside the $K^+$ pathway, the high astrocytic $Ca^{2+}$ and EET concentrations have a noticeable effect on the open probability of the BK channel, opening the channel further and providing a larger flux of $K^+$ into the PVS. This results in a significant radial increase compared to when only the $K^+$ pathway is active.

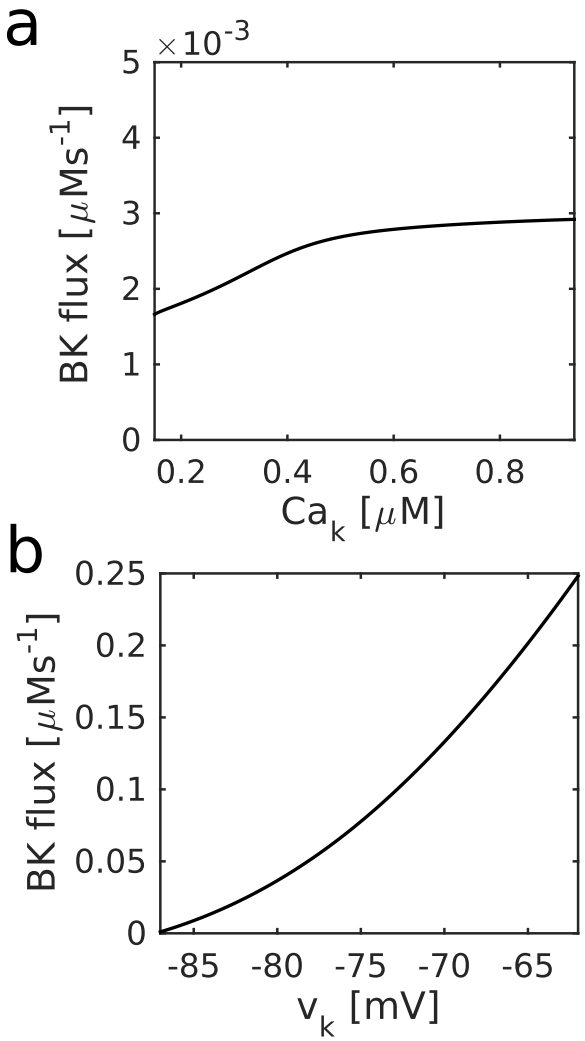


Figure 21: The effect on the BK flux of a) astrocytic $Ca^{2+}$ ($Ca_k$) when the astrocytic membrane potential ($v_k$) is at a constant resting state of $-86.5$ mV, and b) $v_k$ when $Ca_k$ is at a constant resting state of 0.14 μM.

When the astrocytic $Ca^{2+}$ pathway and TRPV4 channel are activated alongside the NO pathway, there is no difference in the vascular response to neuronal stimulation. The $Ca^{2+}$ pathway and TRPV4 channel affect the astrocytic BK channel, but the NO pathway is essentially independent of the dynamics in the astrocyte.

When all pathways present in the model are active, during neuronal stimulation the arteriolar radius increases by approximately 20% from the baseline value. This increase is consistent with experimental results such as those of Chen et al. [28], who observed rapid dilation of $17-29\%$ upon fore and hind paw stimulation.

In summary, on the basis of the model, by themselves astrocytic $Ca^{2+}$ and EETs have no significant effect on the BK channel and hence no effect on the vasculature. Due to the high dependence of the BK channel on the membrane potential, the astrocyte must depolarise (for example through the $K^+$ signalling pathway) in order to produce a significant $K^+$ flux into the PVS and provide a

vascular response. Only then can astrocytic $Ca^{2+}$ enhance the vascular response by opening the BK channel further.

There are conflicting views on the importance of the astrocytic $Ca^{2+}$ pathway in the literature. Dunn et al. [52], Girouard et al. [68] and Filosa et al. [59] among others claim that $Ca^{2+}$ is an important factor for NVC. However, Gordon et al. [76] state that there are problems regarding the data interpretation presented by Filosa et al. [59]. One such problem is that the thromboxane $A_2$ agonist U46619 used in their experiments increases extracellular $PgE_2$ [75], engaging the prostaglandin pathway and shifting the balance of other pathways to be observed.

In addition, Otsu et al. [138] using genetically encoded $Ca^{2+}$ sensors in astrocytes examined NVC in the olfactory bulb. Their results indicated only small $Ca^{2+}$ concentrations are seen in the astrocyte and even then are in the processes rather than the astrocyte body. However these increases were extremely small. They observed vasodilation so it may be that these small $Ca^{2+}$ transients come from the stretch dependent TRPV4 channel which are situated on the astrocytic processes. In addition the adult mice that were part of the experiment do not have the mGluR receptor, so $IP_3$ is most likely unavailable for intracellular $Ca^{2+}$ release. Overall their results seems to suggest that $K^+$ is the main NVC mechanism.

One possible reason for the discrepancy in results between the work presented here and experimental data is that, in all papers mentioned prior, the astrocytic $K^+$ concentration or membrane potential are not explicitly measured. Therefore it is possible that experiments showing vasodilation or vasoconstriction following astrocytic $Ca^{2+}$ increase may be ignoring the contribution of $K^+$ or the astrocytic membrane potential towards the vascular response. Consequently the results of this chapter can be considered consistent with those of Girouard et al. [68] and others as they say nothing about the influence of astrocytic $K^+$ or membrane potential. This highlights one of the key benefits of mathematical modelling, namely the ability to examine specific components and measure quantities that are difficult or impossible to measure experimentally.

## 4.5 CONCLUSIONS

Although NVC has been widely studied the exact mechanisms that mediate this response remain unclear; in particular the role of astrocytic $Ca^{2+}$ is controversial. Mathematical modelling can be a useful tool for investigating the contribution of various signalling pathways towards NVC and for analysing the underlying cellular mechanisms. The lumped parameter model of a neurovascular

unit with both $K^+$ and NO signalling pathways and comprised of neurons, astrocytes, and vascular cells has been extended to include the glutamate induced astrocytic $Ca^{2+}$ pathway with EET signalling and the stretch dependent TRPV4 $Ca^{2+}$ channel on the astrocytic endfoot.

Results show that the $K^+$ pathway governs the fast onset of vasodilation while the NO pathway has a delayed response, maintaining dilation longer following neuronal stimulation. Increases in astrocytic $Ca^{2+}$ concentration via the $Ca^{2+}$ signalling pathway and/or TRPV4 channel to levels consistent with experimental data are insufficient for inducing either vasodilation or constriction, in contrast to a number of experimental results. It is shown that the astrocyte must depolarise in order to produce a significant $K^+$ flux through the astrocytic BK channel. However astrocytic $Ca^{2+}$ is shown to strengthen $K^+$ induced NVC by opening the BK channel further, consequently allowing more $K^+$ into the perivascular space. The overall effect is vasodilation with a higher maximal vessel radius.

# 5

# EXPERIMENTAL MODEL VALIDATION: CEREBRAL BLOOD FLOW AND THE BOLD RESPONSE

## 5.1 INTRODUCTION

During the last two decades functional magnetic resonance imaging (fMRI) has proven to be an established tool in studying the human brain. This is especially true in the case of the blood-oxygen-level dependent (BOLD) signal, where changes in blood oxygen ($O_2$) levels can be detected [136]. However due to the constraint on the resolution of BOLD, fMRI methodology has not been used extensively to study the underlying cellular neural architecture and their associated cerebral functions. Complex models that address this important relationship and constructing a detailed compartmental model with the relevant cell types involved will allow simulations relating certain brain functions performed in a region to its fMRI BOLD response. The neurovascular coupling (NVC) mechanism, the cerebral metabolic rate of $O_2$ consumption ($CMRO_2$), and the cerebral blood volume (CBV) are known to contribute to the fMRI BOLD response [19], however a thorough understanding of these factors has yet to be fully established.

The BOLD response is sensitive to the changes in cerebral blood flow (CBF), $CMRO_2$, and CBV, the set of physiological responses that are referred to collectively as the hemodynamic response to activation. CBV is defined as the volume of blood in a given amount of tissue (usually measured as mL of blood per 100 g of tissue) and can be calculated as a function of CBF. Following increased neural activity in the brain, the local CBF increases much more than the $CMRO_2$, and as a result the $O_2$ extraction fraction (OEF) decreases with activation [62]. Because the local blood is more oxygenated, there is less deoxyhemoglobin present, the magnetic field distortions are reduced, and the local MR signal increases slightly. This small BOLD signal change is the mapping signal used in most fMRI applications [19].

In this chapter the single neurovascular unit (NVU) model presented in Chapter 4 is extended with a complex neuron submodel based on the work of Mathias et al. [122]. This submodel details

the dynamics in the soma/axon, dendrite, and extracellular space (ECS) and is extended to include an additional sodium ($Na^+$) channel expressed in the neuron. The model is also extended with a fMRI BOLD submodel along with the associated metabolic and blood volume responses.

This present model is based on the hypothesis that the potassium ($K^+$) signalling mechanism of NVC is the primary contributor to the vascular response and the sodium potassium ($Na^+/K^+$) exchange pump in the neuron is the primary consumer of $O_2$ during neural activation. The simulated CBF change is compared to that of experimental data from Zheng et al. [174] from the rat barrel cortex and provided a simulation of the associated BOLD signal. The motivation for the comparison between simulated and experimental CBF changes in the cortex is primarily for model validation, as well as to investigate whether the neurovascular response due to the assumed primary $K^+$ signalling mechanism for a hippocampal neuron model is sufficient to represent the blood flow response in any other region.

## 5.2 MODEL DEVELOPMENT

This section details the extensions to the single NVU model, in particular the addition of the complex neuron submodel and the BOLD response. Subsections 5.2.1 and 5.2.2 are the work of Dr. Elshin Mathias (see Mathias et al. [121]) and are included here for reference; all subsequent sections in this chapter are the work of the author of this thesis, Allanah Kenny. A schematic diagram of the proposed model is found in Figure 22, and all relevant equations and parameters can be found in Appendix A.6.

### 5.2.1 *The neuron model*

The neuron model of Mathias et al. [122] was based on the model of Chang et al. [26]. They had only considered ion channels that contribute to cortical spreading depression (CSD) and hence did not include the voltage dependent transient $Na^+$ (NaT) channel which is one of a number of primary $Na^+$ channels in neurons. The effect of not including this channel on the neural membrane potential dynamics is substantial as its gating properties enable action potential generation. To quantify the effects of neural activity on the BOLD signal, Mathias et al. [121] included this channel based on the work of Kager et al. [99]. The model is used to describe

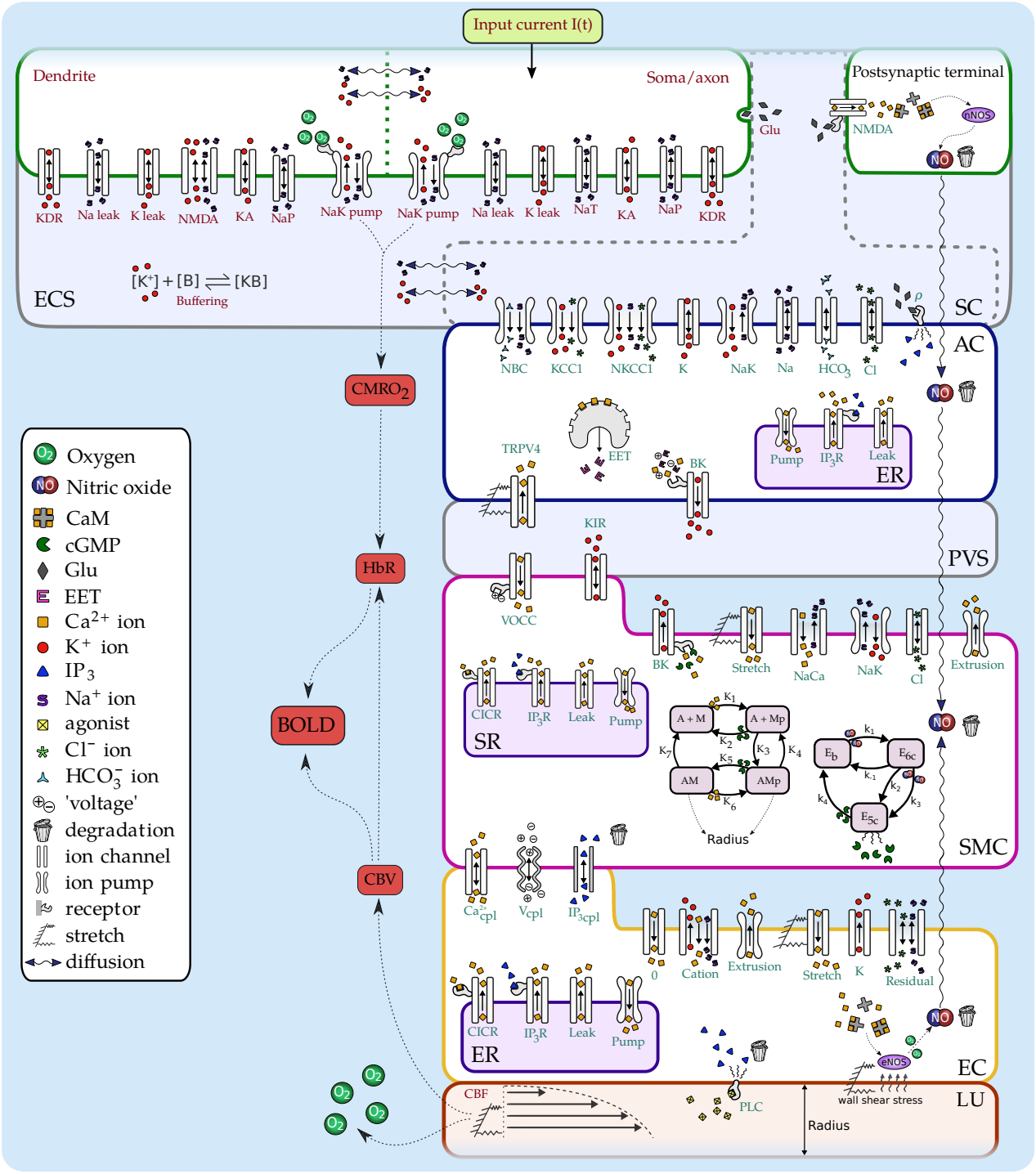


Figure 22: A schematic representation of the proposed NVC model with added neuron/ECS dynamics and the BOLD signal. Neuronal activity is initiated by a current $I(t)$ leading to neuronal depolarisation and an efflux of $K^+$ from the neuron into the ECS and SC. The increase in synaptic $K^+$ concentration leads to an influx of $K^+$ into the astrocyte and consequent efflux into the PVS through the big potassium (BK) channel on the astrocytic endfoot [5]. The rise in perivascular $K^+$ concentration leads to a further influx of $K^+$ through the inward rectifying $K^+$ (KIR) channel from the SMC into the PVS, hyperpolarising the SMC membrane and closing the voltage operated calcium ($Ca^{2+}$) channels (VOCCs) preventing an influx of $Ca^{2+}$ [59]. The decrease in $Ca^{2+}$ concentration relaxes the SMC via actin-myosin cross bridge formation, dilating the vessel which results in increased blood flow [130]. This behaviour may change in response to varied stimuli or pathological conditions. SC: synaptic cleft, AC: astrocyte, PVS: perivascular space, SMC: smooth muscle cell, SR: sarcoplasmic reticulum, EC: endothelial cell, ER: endoplasmic reticulum, LU: lumen, ECS: extracellular space. Components that have been added or modified are labelled in dark red.

neural activation, restoration of ionic gradients and consumption of the $Na^+/K^+$ ATPase pump. The model assumes no interaction between the ECS and the vasculature, synaptic cleft (SC) or astrocyte (only extracellular $K^+$ buffering).

The neuron is divided into two components: the soma/axon (including the main cell body and pre-synaptic terminal) and the dendrite. The model also includes the post-synaptic terminal of an adjacent neuron containing a N-methyl-D-aspartate (NMDA) receptor channel used in the nitric oxide (NO) submodel described in Chapter 4.

The membrane potential of the soma/axon ($v_{sa}$) and dendrite ($v_d$) compartments are given by

$$C_m \frac{dv_{sa}}{dt} = -I_{tot_{sa}} + \frac{1}{2R_a\delta_d^2}(v_d - v_{sa}) + I_{input} \tag{5.1}$$

$$C_m \frac{dv_d}{dt} = -I_{tot_d} + \frac{1}{2R_a\delta_d^2}(v_{sa} - v_d) \tag{5.2}$$

where $C_m$ is the membrane capacitance, $R_a$ is the input resistance of the dendritic tree, $\delta_d$ is the half length of the dendrite, $I_{input}$ is a time dependent rectangular input function which stimulates the neuron, and $I_{tot_*}$ is the sum of all currents into the compartment. The ion concentrations ($K^+$, $Na^+$) of the two neuron compartments are given by

$$\frac{d[ion]_{sa}}{dt} = -\frac{A_s}{FV_s} I_{ion,tot_{sa}} + \frac{D_{ion,n}(V_d + V_s)}{2\delta_d^2 V_s}([ion]_d - [ion]_{sa}) \tag{5.3}$$

$$\frac{d[ion]_d}{dt} = -\frac{A_d}{FV_d} I_{ion,tot_d} + \frac{D_{ion,n}(V_d + V_s)}{2\delta_d^2 V_d}([ion]_{sa} - [ion]_d), \tag{5.4}$$

where $A_s, V_s, A_d, V_d$ are the surface area and volume of the soma/axon and dendrite compartments respectively, $I_{ion,tot_*}$ is the sum of all currents of a particular ion into the compartment, and $D_{ion,n}$ is the ionic intracellular diffusion rate.

The soma/axon compartment of the model contains a persistent $Na^+$ (NaP) channel, delayed rectifier $K^+$ (KDR) channel, transient $K^+$ (KA) channel, NaT channel, and $K^+$ and $Na^+$ leak channels. The dendrite compartment also contains these channels (except the NaT) as well as an NMDA receptor mediated channel which allows a flux of both $K^+$ and $Na^+$. The leak channels are modelled by a Hodgkin-Huxley equation given by

$$I_{ion,*,leak} = g_{ion,leak}(v_* - E_{ion,*}), \tag{5.5}$$

where $*$ is either $sa$ for somatic or $d$ for dendritic, $g_{ion,leak}$ is the channel conductance, and $v_*$ is the membrane potential of the soma/axon or dendrite. The Nernst potential of the channel is given by

$$E_{ion_*} = \frac{\phi}{z_{ion}} \ln\left(\frac{[ion]_e}{[ion]_*}\right), \tag{5.6}$$

where $\phi = R_g T/F$ ($R_g$ is the universal gas constant, $T$ is absolute temperature, and $F$ is Faraday's constant), $z_{ion}$ is the ionic valence, and $[ion]_e$ is the ion concentration in the ECS. The cross-membrane currents of the remaining ion channels are modelled using the Goldman Hodgkin Katz (GHK) equation given as

$$I_{ion,*,GHK} = m^p h^q \frac{g_{ion,GHK} F v_* \left[[ion]_* - \exp\left(\frac{-v_*]}{\phi}\right)[ion]_e\right]}{\phi\left[1 - \exp\left(\frac{-v_*}{\phi}\right)\right]} \tag{5.7}$$

where $p$ and $q$ are channel dependent parameters. The fraction of activation and inactivation gates in the open state for a certain channel are denoted $m$ and $h$ respectively and are modelled by the differential equations

$$\frac{dm}{dt} = (\alpha_m(1-m) - \beta_m m) \tag{5.8}$$

$$\frac{dh}{dt} = (\alpha_h(1-h) - \beta_h h)\,. \tag{5.9}$$

The open rates $\alpha_m, \alpha_h$ and close rates $\beta_m, \beta_h$ are functions that are channel dependent (see the Appendix A.6).

The $K^+$ and $Na^+$ concentrations in the ECS are given by

$$\frac{dK_e}{dt} = \frac{1}{Ff_e}\left(\frac{A_s I_{K,tot_{sa}}}{V_s} + \frac{A_d I_{K,tot_d}}{V_d}\right) - \frac{dBuff_e}{dt} \tag{5.10}$$

$$\frac{dNa_e}{dt} = \frac{1}{Ff_e}\left(\frac{A_s I_{Na,tot_{sa}}}{V_s} + \frac{A_d I_{Na,tot_d}}{V_d}\right) \tag{5.11}$$

where $f_e$ is the volume ratio between the ECS and the neuron. A phenomenological $K^+$ buffer is added to regulate $K^+$ concentration in the ECS ($K_e$), where the rate of change of buffer $Buff_e$ is given by the differential equation

$$\frac{dBuff_e}{dt} = \mu(B_0 - Buff_e)\frac{K_e}{1 + \exp\left(\frac{-(K_e - 5.5)}{1.09}\right)} - \mu Buff_e \tag{5.12}$$

where $B_0$ is the initial buffer concentration.

#### 5.2.1.1 *The tissue $O_2$ submodel*

Oxygen is delivered to the neuron via the perfusing arteriole and is a function of the arteriolar radius, the blood flow rate and the $O_2$ concentration in the blood. It is assumed that the main component of $O_2$ consumption in the neuron is the $Na^+/K^+$ exchange pump and is a function of the intracellular $Na^+$ (both dendrite $Na_d$ and soma/axon $Na_{sa}$) and the extracellular $K^+$ ($K_e$) concentrations. The tissue $O_2$ concentration ($O_2$) is given by

$$\frac{dO_2}{dt} = J_{O_2\,vascular} - J_{O_2\,background} - J_{O_2\,pump}. \tag{5.13}$$

The vascular supply of $O_2$ is given by

$$J_{O_2\,vascular} = J\frac{O2_b - O_2}{O2_b - O2_0}, \tag{5.14}$$

where J is the change in $O_2$ concentration due to CBF described in Eq. (5.24), $O2_b$ is the arterial oxygen concentration at steady state, and $O2_0$ is the baseline tissue oxygen concentration. The background $O_2$ consumption is given by

$$J_{O_2\,background} = J_0 P_{O2}(1 - \gamma_{O2}), \tag{5.15}$$

where $J_0$ is the equilibrium change in $O_2$ concentration due to CBF, $P_{O2}$ is the normalised $Na^+/K^+$ pump rate described below, and $\gamma_{O2}$ is the fraction of $O_2$ consumed by the $Na^+/K^+$ pump. The consumption of $O_2$ by the $Na^+/K^+$ ATPase pump which is active during neural activation is given by

$$J_{O_2\,pump} = J_0 P_{O2}\gamma_{O2}\frac{J_{pump1_{sa}} + J_{pump1_d}}{J_{pump1_{sa_0}} + J_{pump1_{d_0}}}, \tag{5.16}$$

where $J_{pump1_{sa}}, J_{pump1_d}$ are the $O_2$ independent terms of the $Na^+/K^+$ ATPase pump in the soma/axon and dendrite respectively (described below), and $J_{pump1_{sa_0}}, J_{pump1_{d_0}}$ are their respective steady state values. The normalised pump rate is given by

$$P_{O2} = \frac{J_{pump2}(O_2) - J_{pump2}(0)}{J_{pump2}(O2_0) - J_{pump2}(0)}. \tag{5.17}$$

where $J_{pump2}$ is the oxygen dependent term of the ATPase pump described below. The $O_2$ independent terms of the ATPase pump are given by

$$J_{pump1_*}(K_e, Na_*) = \left(1 + \frac{K_{e,0}}{K_e}\right)^{-2} \left(1 + \frac{Na_{*,0}}{Na_*}\right)^{-3} \tag{5.18}$$

where $*$ is either $sa$ for somatic or $d$ for dendritic, and $K_{e,0}$ and $Na_{*,0}$ are the baseline concentrations of extracellular $K^+$ and intracellular $Na^+$ respectively. This expression describes that the action of the pump depends on the concentrations of extracellular $K^+$ and intracellular $Na^+$. The second term of the ATPase pump represents the $O_2$ dependent production of adenosine triphosphate (ATP) by the mitochondria [34, 85] taking the form

$$J_{*,pump,2}(O_2) = 2\left(1 + \frac{O2_0}{(1-\alpha)O_2 + \alpha O2_0}\right)^{-1} \tag{5.19}$$

where $\alpha$ is the percentage of ATP production that is independent of $O_2$. This expression indicates that the pumping rate will be reduced whenever there is a decrease in the $O_2$ level in the tissue. The total current due to the $Na^+/K^+$ exchange pump in the soma and dendrite is given by

$$I_{*,pump} = I_{max} J_{pump1_*}(K_e, Na_*) J_{*,pump,2}(O_2) \tag{5.20}$$

where $*$ is either $sa$ for somatic or $d$ for dendritic and $I_{max}$ is the maximum pumping rate of the pump. The $K^+$ and $Na^+$ pump currents in the soma and dendrite are then given by

$$I_{*,K,pump} = -2I_{*,pump} \tag{5.21}$$

$$I_{*,Na,pump} = 3I_{*,pump} \tag{5.22}$$

where $*$ is either $sa$ for somatic or $d$ for dendritic.

The blood flow in the perfusing arterioles can be modelled as Poiseuille type [172] where the volume flow rate is proportional to the perfusing arterial radius to the fourth power. The CBF is given by the equation

$$CBF = CBF_0 \frac{R^4}{{R_0}^4} \tag{5.23}$$

where $R_0$ and $CBF_0$ are the steady state values of the perfusing arteriolar radius and CBF respectively. The equation for the radius $R$ is given by the numerical model described in the earlier

chapters. J is the rate of change in $O_2$ concentration in the blood due to CBF for neuronal activation above a resting state given by

$$J = J_0 \frac{CBF}{CBF_0} \tag{5.24}$$

In this case $J_0$ is the rate of change in $O_2$ concentration under non-activated conditions. The $CMRO_2$ is given simply by the sum of the consumption of $O_2$ by the pump and other active processes

$$CMRO_2 = J_{O_2\,background} + J_{O_2\,pump} \tag{5.25}$$

For further details on the neuron and tissue $O_2$ submodel see Mathias et al. [122]; all equations and parameters are also presented in Appendix A.6.

### 5.2.2 *The BOLD model*

The simulation of the BOLD signal is based on the work of Buxton et al. [19] and is used to provide a time-dependent response determined by the NVC model. The response depends on the changes in CBF, $CMRO_2$ and CBV and is based on the experimental finding that CBF increases $2-3$ times more than the $CMRO_2$, decreasing the $O_2$ extraction fraction [62, 90] and providing a variable delay in CBF and BOLD responses after the stimulus. The model simulates the experimental observations such as the initial "dip" and the post stimulus undershoot. The initial dip is a transient decrease in the BOLD signal generally believed to originate from a change in oxygenation (due to an increase in metabolism) prior to any increase in CBF. This initial dip has been reported in a variety of studies [92] but there are conflicting views about the associated mechanisms and due to its elusive nature the existence of the initial dip is still under debate [91].

The model uses normalised CBF and $CMRO_2$ profiles derived from the NVC model considering the venous compartment as a balloon and describing the non dimensionalised deoxyhemoglobin (HbR), and CBV, by mass conservation equations [20, 19]. The rate of change of HbR concentration is simply the difference between that generated by the consumption of $O_2$ by the neuron and that flowing into the varying volume (or balloon) given by

$$\frac{dHbR}{dt} = \frac{1}{\tau_{MTT}} \left( \frac{CMRO_2}{CMRO_{20}} - \frac{HbR}{CBV} f_{out} \right) \tag{5.26}$$

where the quantity $CMRO_{20}$ is the steady state value of $CMRO_2$. Here $\tau_{MTT}$ is the mean transit time (MTT) defined as the time a specified volume of blood spends in the capillary circulation. The MTT is assumed to be constant and is estimated by the ratio between the resting venous volume fraction and steady state blood flow.

The rate of change of CBV is the difference between the non-dimensional blood flow into a varying volume and that flowing out given by $f_{out}$ with the characteristic time scale of $\tau_{MTT}$, hence

$$\frac{dCBV}{dt} = \frac{1}{\tau_{MTT}}\left(\frac{CBF}{CBF_0} - f_{out}\right) \tag{5.27}$$

The time-dependent outflow $f_{out}$ from the venous compartment which is transiently different from CBF is composed of two parts, namely the relationship between blood flow and the blood volume and the rate at which the blood volume changes due to viscous effects of the vessel wall. Hence the outflow is defined as

$$f_{out} = CBV^{\frac{1}{d}} + \tau\frac{dCBV}{dt} \tag{5.28}$$

where $d$ gives an empirical relationship between blood flow and volume, and the transient adjustment required is controlled by the time constant $\tau$.

The net extraction fraction of $O_2$ ($E$) is given by

$$E = E_0\frac{CMRO_2}{J} \tag{5.29}$$

where $E_0$ is the steady state value of the extraction fraction of $O_2$. The BOLD signal change from its steady state value is a linear combination of the normalised HbR content (normalised with respect to its initial steady state value, denoted $HbR_N$) and normalised venous volume (similarly given by $CBV_N$) so that

$$BOLD_{signal} = V_0[a_1(1 - HbR_N) - a_2(1 - CBV_N)] \tag{5.30}$$

where $V_0$ is the resting venous blood volume fraction of the tissue voxel, and $a_1, a_2$ are dimensionless parameters based on several experimental and physiological conditions [134]. To correspond with definitions used in other publications the plotted BOLD signal is defined as a percentage change from the resting BOLD signal such that

$$\Delta BOLD\ \% = \left(\frac{BOLD_{signal}}{BOLD_{rest}} - 1\right) \times 100 \tag{5.31}$$

where $BOLD_{rest}$ is the BOLD signal during the resting state.

Given the numerical values of HbR, CBV and $f_{out}$, time dependent profiles can be derived for both normalised oxyhemoglobin (HbO) and normalised total hemoglobin (HbT). $HbT_N$ can be evaluated in a similar method to Boas et al. [13] using

$$HbT_N = \frac{HbR_N \; CBF_N}{CMRO_{2N}} \tag{5.32}$$

where CBF and $CMRO_2$ are defined in Eq. (5.23) and (5.25) respectively. Finally the normalised HbO content is determined by conservation such that

$$HbO_N = HbT_N - HbR_N + 1 \tag{5.33}$$

### 5.2.3 *Integration with the NVU model*

The neuron model developed by Mathias et al. [121, 122] is integrated into the single NVU model described in the earlier chapters. As the neuron model of Mathias et al. [121] based on the work of Chang et al. [26] already contained a complex ECS compartment submodel, the simple ECS compartment described in Chapter 3 has been replaced. Hence the previous equation for extracellular $K^+$ (Eq. (3.5)) is replaced with Eq. (5.10), and the flux $J_{diff}$ (Eq. (3.1)) has been removed.

The glutamate input $Glu(t)$ is replaced by a function $Glu(K_e)$ based on the assumption that glutamate is released when extracellular $K^+$ ($K_e$) levels are raised [99]. The glutamate concentration is given by the following equation:

$$Glu = \frac{Glu_{max}}{2}\left(1 + \tanh\left(\frac{K_e - K_{e_{switch}}}{Glu_{slope}}\right)\right) \tag{5.34}$$

where $Glu_{max}$ is the maximum glutamate concentration corresponding to the release of one vesicle, $K_{e_{switch}}$ is the threshold past which glutamate is released, and $Glu_{slope}$ is the slope of the sigmoidal function.

For the neuron model to communicate with another neuron and to facilitate synaptic transmission (when functioning normally by spiking or bursting), the action potential has to travel along the axon until it reaches the synapse. This causes ionic efflux and influx at the SC which can then communicate with the astrocyte effectively as the astrocytes express a high density of ion channels near the synapses [132]. In the NVU model the flux of $K^+$ from the neuron into the SC

and opposite flux of $Na^+$ from the SC to the neuron are modelled via an input function $K(t)$. This is modified so that the coupling between the astrocyte and the neuron is done by assuming that the flux from the neuron into the synaptic space is equal to fraction of the scaled flux from the neuron into the ECS. The scaling factor $k_{syn}$ is given by the ratio of the extracellular volume ($V_e$) to synaptic volume ($V_s$) multiplied by the fraction $f_{AS}$ of synapses activated near the astrocytic end process. Then the number N of $K^+$ and $Na^+$ ions in the SC are given by

$$\frac{dN_{s,K}}{dt} = k_{syn}\frac{dK_e}{dt}R_s - J_{K^+,SC\to AC} \tag{5.35}$$

$$\frac{dN_{s,Na}}{dt} = -k_{syn}\frac{dK_e}{dt}R_s - J_{Na^+,SC\to AC}, \tag{5.36}$$

where $R_s$ is the volume to area ratio of the SC compartment, $J_{ion,SC\to AC}$ is the net flux of ions from the SC to the astrocyte as defined by the NVU model described in earlier chapters, and $k_{syn}$ is the scaling factor which represents the total volume of synapses which are associated with an astrocyte process.

Neuronal activity is initiated by a current $I_{input}$ leading to neuronal depolarisation and an efflux of $K^+$ from the neuron into the ECS and SC. The increase in synaptic $K^+$ concentration leads to an influx of $K^+$ into the astrocyte and consequent efflux into the perivascular space (PVS) through the BK channel on the astrocytic endfoot [5]. The rise in perivascular $K^+$ concentration leads to a further influx of $K^+$ through the KIR channel from the smooth muscle cell (SMC) into the PVS, hyperpolarising the SMC membrane and closing the VOCCs preventing an influx of $Ca^{2+}$ [59]. The decrease in $Ca^{2+}$ concentration relaxes the SMC via actin-myosin cross bridge formation, dilating the vessel which results in increased blood flow [130]. This behaviour may change in response to varied stimuli or pathological conditions.

## 5.3 COMPARISON OF EXPERIMENTAL CORTICAL CBF DATA WITH VARYING STIMULUS CONDITIONS

Zheng et al. [174] performed NVC experiments by stimulating the rat barrel cortex and investigated the results using concurrent multichannel electrophysiology and laser Doppler flowmetry. To investigate if the proposed model can be utilised with other areas of the brain, the simulated CBF change of the model is compared to the experimentally derived CBF change in the rat barrel cortex using the data of Zheng et al. [174] for different stimulus conditions. For these experimental data

electrical stimulation of the whisker pad was delivered in 5 Hz trains with each pulse having an intensity of 1.2 mA and an individual pulse width of 0.3 ms (see Figure 23). CBF measurements were made by a laser doppler probe inserted in the animal's cortex at an average depth equivalent to layer IV.

Experimental protocols were designed to have a conditioning block (CS) of stimulation followed closely in time by a probing block (PS) separated by an inter-stimulus interval (IBSI) for each trial. This particular protocol was used to investigate neural adaptation and recovery characteristics and was chosen to ensure that any mathematical models of NVC were capable of simulating the CBF response with respect to not only the conditioning block but also the probing block of stimulation, whose onset occurs well within the return-to-baseline period of the CBF response to the conditioning block. The experiment used up to 11 animals with each trial performed up to 10 times covering 21 different conditioning and probing block protocols. The experimental data shows a considerable variation in peak CBF values with a standard deviation sometimes being up to 100% of the average signal (see Figure 24). This indicates that there exists a substantial variation between animals in terms of their neuronal activity, however the rate at which CBF changes occur vary by no more than approximately $25-30\%$. The NVC model is stimulated with a variety of input profiles and the numerical output is compared with the experimental CBF data of Zheng et al. [174].

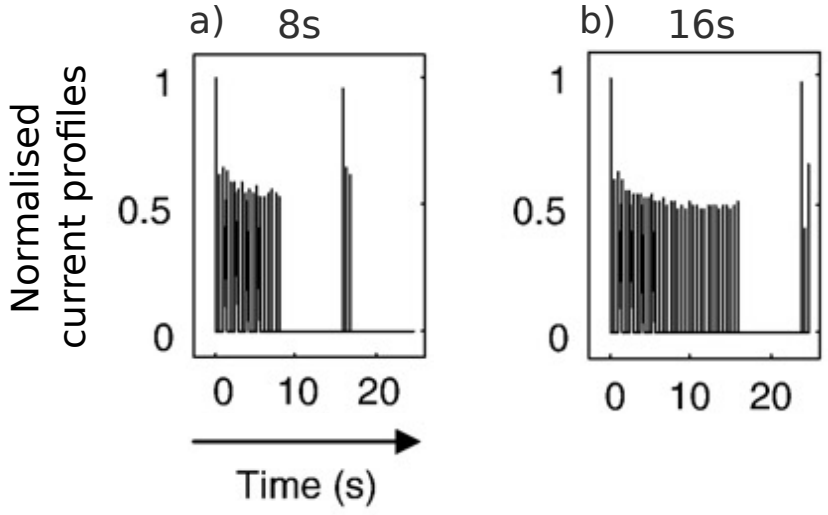


Figure 23: Normalised current profiles of Zheng et al. [174] for a) CS = 8 s and b) CS = 16 s. For both figures IBSI = 8 s, PS = 1 s. The current profiles exhibit a large spike at the beginning of stimulation followed by a drop to approximately 60% of the initial strength.

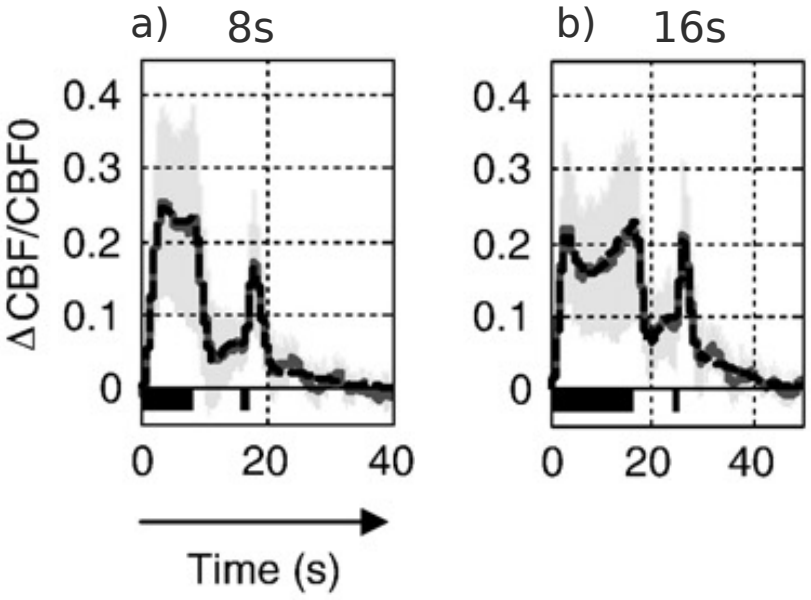


Figure 24: Averaged (over animal and trial) fractional change in CBF observed in the experiments of Zheng et al. [174] for a) CS = 8 s and b) CS = 16 s. For both figures IBSI = 8 s, PS = 1 s. The light grey band is $\pm 1$ standard deviation of the data.

### 5.3.1 *Input current using neural activity data*

In order to obtain a CBF profile in the model that correlates with the experimental CBF profile of Zheng et al. [174], the experimental stimulus data (see Figure 23) is used to provide the input current profile for the cases of CS $=$ 8 and 16 s. The normalised current profiles in Figure 23 exhibit a large initial spike quickly followed by a lower current of approximately $50-60\%$ of the initial value. Hence a large maximum current strength of $I_{strength} = 4.2 \times 10^{-2}$ mA cm$^{-2}$ is used to scale the normalised input profiles so that the majority of the current input is approximately $2.4 \times 10^{-2}$ mA cm$^{-2}$; this value is sufficient for inducing neuronal oscillations corresponding to neuronal activity.

The numerical model has the ability to provide not only CBF but also the BOLD response and time-dependent profiles of HbR, HbO, and HbT. Figure 25 shows the simulated BOLD signal, hemodynamics, and CBF profiles compared with experimental CBF in the cortex from Zheng et al. [174] for IBSI $=$ 8 s, PS $=$ 1 s, and CS either 8 or 16 s.

For the case of CS $=$ 8 s (Figure 25a, b, c) the simulated CBF provides reasonable agreement with the experiment where the initial rate of increase of the blood flow is simulated reasonably well, however the return to basal levels takes longer than the experimental data suggests. This may be due to a number of reasons. One possibility as noted below is the inactivation variable of

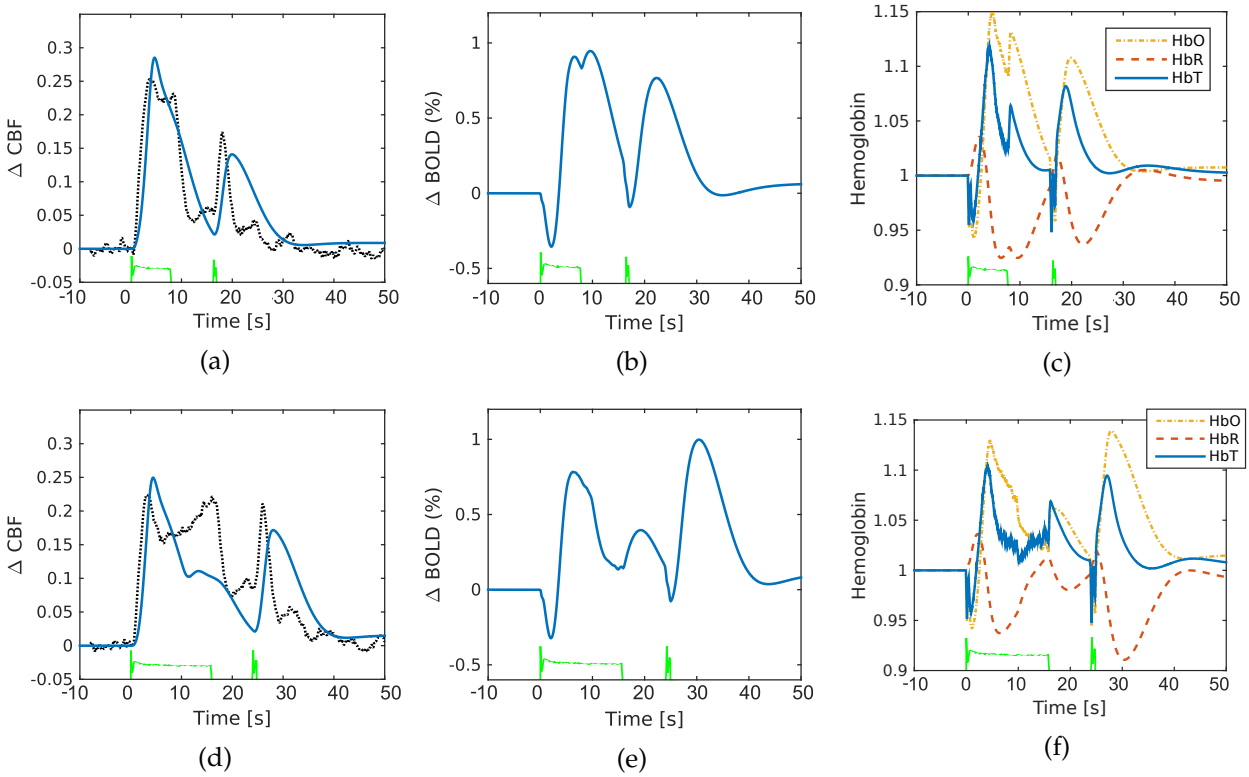


Figure 25: (a,d) CBF profiles (solid line) compared with experimental CBF (dashed line) in the cortex from Zheng et al. [174], (b,e) simulated BOLD signal, (c,f) hemodynamics. Top row: CS = 8 s, bottom row: CS = 16 s. For all figures IBSI = 8 s, PS = 1 s. The soma of the neuron is stimulated with a depolarising current with profile (green) given by Zheng et al. [174].

the NaP channel. Another possibility is the vessel dynamics since the original data for the radius parameters utilised a porcine carotid artery, whereas the murine dynamics may be much faster.

The associated BOLD response for CS $= 8$ s shows an initial negative signal (occurring for half the stimulation period) followed by a positive and then a slightly larger second positive signal, out of phase with the experimental and simulated CBF. The initial dip is due to the metabolic rate increasing before the radius of the perfusing vessel has changed significantly. This then forces the resulting peak BOLD signals to be approximately 2.5 seconds later than the experimental CBF. The BOLD signal returns to baseline after approximately 30 seconds after the PS simulation due to (possibly) the long characteristic time of the inactivation variable of the NaP pump.

The hemoglobin profiles for CS $= 8$ s show as expected an increase in HbR during the short stimulus period since the radius has yet to increase, with a concomitant decrease in HbO. After approximately 2 seconds HbO increases by 12% where the delay compares very well with the work by Boas et al. [13]. This delay is primarily caused by the rate at which the vasculature reacts to neuronal stimulation and is effectively a constant derived from the vessel wall mechanics and SMC $Ca^{2+}$ concentration. During the 2 seconds post stimulus HbT reduces by approximately 5%.

Although this is rarely seen in experiment it is a consequence of the conservation of hemoglobin as given by Eq. (5.33). Post stimulus undershoot exists for both HbO and HbT whilst the converse is evident for HbR. Again this correlates well with experimental results (see Figure 2 of Boas et al. [13]).

For the case of CS = 16 s (Figure 25d, e, f) the initial rate of change of simulated CBF compares very well with the experimental data, however as in the previous case the first peak CBF value is higher (approximately 10% in this case). The simulated CBF profile does not show a 2nd local maximum in the profile compared to the experiment; instead the CBF profile reduces immediately after the peak.

The corresponding BOLD profile again has the initial dip occurring during the 16 s CS period but only for 30% of the period. Indeed the time for the BOLD initial dip is the same for the two cases of CS and indicates the phase lag between the production of $CMRO_2$ and the vessel dilation, independent of the length of the conditioning block.

The increased oxygenated blood produces a second peak of BOLD signal. The probing block stimulation produces a third peak of BOLD followed by a slow return to baseline, again occurring because of excess $K^+$ in the ECS. As in the previous case of CS = 8 s, post stimulus HbT and HbO reduces as $CMRO_2$ increases before the NVC effect dominates. The time over which HbT reduces is similar to that found for the 8 s simulation.

For the neuron model used in these simulations the neuron develops high frequency oscillations in the membrane potential during stimulation (as one would expect for this model) which is reflected in the time-dependent $CMRO_2$ profile, and hence these oscillations are also shown in the profile of HbT (Figure 25c, f).

### 5.3.2 *Input current utilising the locus coeruleus pain pathway*

In its present form the model could not replicate the second local maximum in the profile of the experimental CBF. Zheng et al. [174] suggested that this form was due to the combined effects of a contraction and dilation of the perfusing vessels - the dilation caused by excitatory postsynaptic potential (EPSP) and constriction by inhibitory postsynaptic potential (IPSP) (no experimental evidence for this hypothesis has been found). NO might be a possible player in the formation of the second maximum in the profile [125], however sensitivity analysis (data not shown) indicated

that this was not the case (it could produce the required increase after stimulation but its effects continued too far in time after the end of stimulation).

The experimental stimulation protocol of 16 s is quite long whilst the current injection of 1.2 mA is relatively high. It is possible that an additional pathway from the whisker pad to the somatosensory cortex is being utilised during the stimulation. This pathway is hypothesised to include the locus coeruleus (LC) and recruits a network of both cortical excitatory and inhibitory neurons resulting in substantial cortical activity and increased CBF, essentially a neuromodulatory effect. Work by Toussay et al. [162] showed that the noradrenalin locus coeruleus (LC-NA) pathway activated both pyramidal and interneurons whilst noting that noradrenalin does not have a significant effect on SMCs. In the light of this, from a purely phenomenological viewpoint an additional stimulation current is introduced that models the temporally increasing activity of pyramidal and interneurons.

The LC stimulus is approximated via a polynomial function as follows:

$$I_{LC}(t) = \begin{cases} 0.0006t^2 + 0.1, & \text{for } t_0 \leqslant t < t_0 + \Delta t \\ 0.1, & \text{for } t_1 \leqslant t \leqslant t_1 + 2 \\ 0, & \text{otherwise} \end{cases} \tag{5.37}$$

where $t_0$ is the start time of stimulation, $\Delta t$ is the initial stimulus duration (either 2, 8 or 16 s), and $t_1$ is the start of the second stimulus (either 0.6, 1, 2, 3, 4, 6, or 8 s gap from the end of the first stimulus).

The total stimulation current $I_{total}$ is the linear combination of the initial (whisker pad) stimulation $I_{Wh}$ and the LC-NA pathway $I_{LC}$ given by

$$I_{total}(t) = \alpha I_{Wh}(t) + \beta I_{LC}(t) \tag{5.38}$$

where $\alpha$ and $\beta$ are scaling parameters, in this case set at 1. The three currents are shown in Figure 26. This current profile is scaled by the maximum current strength given by $I_{strength} = 3.5 \times 10^{-2}$ mA cm$^{-2}$.

Figure 27 shows CBF, BOLD and hemoglobin profiles for a 16 second CS stimulation where the input stimulation current is given by the total current $I_{total}$ given by Eq. (5.38). The CBF simulation profile now correctly follows a double maximum shape, however (as in the previous cases) the slow return of the radius forces the CBF profile to be out of phase with the experimental data.

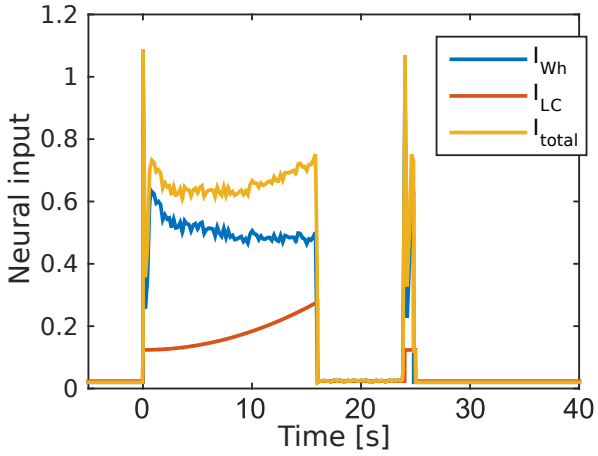


Figure 26: Normalised time profiles of the currents for LC-NA pathway $I_{LC}(t)$ (given by a simple polynomial function), whisker pad stimulation $I_{Wh}(t)$ (experimental profile given by Figure 5 of Zheng et al. [174]) and total current $I_{total}(t)$. CS = 16 s, IBSI = 8 s, PS = 1. The actual input current is given by $I_{strength} \times I_{total}$ in mA cm$^{-2}$.

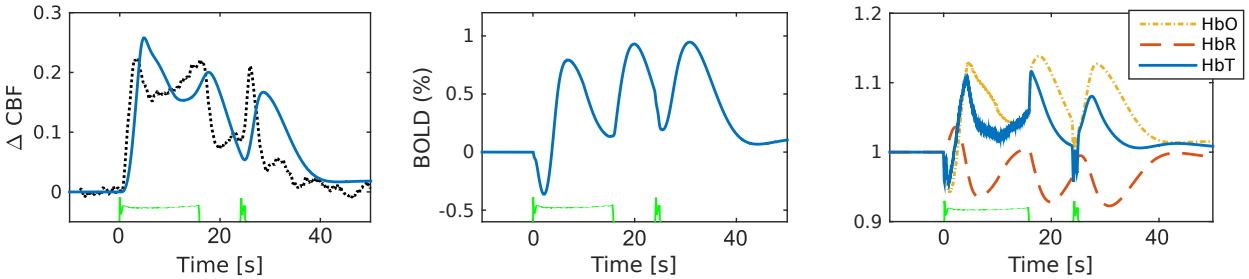


(a) (b) (c)

Figure 27: (a) CBF profile (solid line) compared with experimental CBF (dotted line) in the cortex from Zheng et al. [174], (b) simulated BOLD signal, (c) hemodynamics. CS = 16 s, IBSI = 8 s, PS = 1 s. The soma of the neuron is stimulated with a depolarising current (green) with profile given by $I_{total}$.

The CBF is therefore of substantial size during the "quiescent" period between CS and PS stimulations, the consequence of which is an enlarged BOLD signal during this period. The hemoglobin profiles are of a similar form to that found for the single stimulation current apart from the higher values in the "quiescent" period.

## 5.4 DISCUSSION

The motivation for the comparison between simulated CBF and the experimental CBF changes in the cortex is primarily for model validation, as well as to investigate whether the neurovascular response due to the assumed primary $K^+$ signalling mechanism for a hippocampal neuron model is sufficient to represent the blood flow response in any other region of the cortex. The comparison

shows that for the two stimulation periods the numerical model provides a reasonably good match to the CBF data of Zheng et al. [174]. However for the longer stimulus the second peak of the conditioning block is not represented well when only the experimental stimulus current is used.

Zheng et al. [174] as a result of their experiments hypothesised that the dual peak appearing in the CBF profile for stimuli of 16 seconds was due to "competing" dilation and constriction components of the NVC phenomenon. They cited both Filosa and Blanco [57] and Metea and Newman [125] as showing that there existed simultaneous dilation and constriction functions. They indicated that both epoxyeicosatrienoic acid (EET) and 20- hydroxyeicosatetraenoic acid (20-HETE) could be working at the same time but no evidence exists to show that the two pathways have a time lag. The model of Zheng et al. [174] was developed from a third order system to "prevent oscillations in the output". No physiological data was used to support the third order system model. By the use of impulse response functions they reduced their parameter set from 9 to 3 varying parameters, and using the CBF data, fitted these parameters to the data. Their results showed the fitted and experimental data but did not show the associated functions for dilation or constriction. This would have given some indication as to whether the system was operating in a physiologically correct sense.

An alternative hypothesis is put forward in that it is assumed that there exist two sensory pathways due to the prolonged stimulation and the relatively large current used to stimulate the whisker pad of the animal. Using a phenomenological representation of the LC-NA pathway and combining that with the experimental input stimuli the numerical model simulation provides a good comparison with the experimental data. However for the numerical model results, the return to baseline of the radius (and hence CBF) is too slow. There exist a variety of reasons why this should be, including the kinetic model of Hai and Murphy [80] and the slow release of $K^+$ from the ECS. Further investigation is required to understand the physiological reasons for the double maximum profile induced by the stimulation of the murine whisker pad. It should be noted that this phenomenon has also been observed in other experiments (see Figure 4A of Takuwa et al. [160]).

The integration of the new neuron model has allowed for the study of the BOLD signal and hemoglobin dynamics for short input stimulations in this chapter; however input stimulations of longer duration produce profiles for some variables that do not correspond well with the previous model in Chapter 4. In addition, the oscillations of membrane potential in the neuron are on the order of milliseconds whereas the rest of the model is on the order of seconds, producing a two

timescale problem that takes far longer to solve than the previous model in Chapter 4. These drawbacks of the model are discussed in detail in Section 8.3.3 of Chapter 8.

## 5.5 CONCLUSIONS

A state-of-the-art integrated model of NVC with complex neuron dynamics and the BOLD signal is presented with the ability to simulate the fMRI BOLD responses along with the underlying complex vascular coupling. Comparison of the model with experimental data shows good agreement. The model compares well for stimuli of 8 s with the model unable to replicate the double maximum of the experimental CBF profile for longer periods. An introduction of an additional pathway through the locus coeruleus (on a purely phenomenological basis) provided a better comparison with experimental data.

# 6

# THE EFFECTS OF ASTROCYTIC GAP JUNCTIONS AND EXTRACELLULAR ELECTRODIFFUSION ON CORTICAL SPREADING DEPRESSION

## 6.1 INTRODUCTION

Cortical spreading depression (CSD) is the occurrence of slowly propagating waves of high extracellular potassium ($K^+$) concentration (over $30-50$ mM) and neuronal depolarisation in the grey matter of various species [115]. It typically arises in metabolically compromised tissue as in ischemia [49] and is associated with several neurological pathologies such as migraine, subarachnoid and intracranial haemorrhage, Alzheimer's disease, stroke, traumatic brain injury, and hypertension [69, 158, 114, 27]. Cell damage or death during ischemia results in reduced supply of oxygen ($O_2$) and glucose to brain cells [94]. This decreases adenosine triphosphate (ATP) production and leads to the failure of the neuronal $Na^+/K^+$ ATPase pump, which in turn leads to increased extracellular $K^+$ levels, elevated neuronal sodium ($Na^+$) concentration, cell swelling, and neuronal depolarisation [54]. In these conditions a decrease in cerebral blood flow (CBF) is often observed followed by a slight increase and slow return to the baseline [30, 161]. Indeed, numerous studies have documented that small increases in extracellular $K^+$ concentration can lead to vasodilation, whereas high concentrations lead to vasoconstriction [72, 123, 53, 22, 113]. The massive rise in extracellular $K^+$ to levels sufficient for depolarising adjacent cells is the main factor for allowing the spread of depolarisation throughout the tissue [6, 54]. These waves of depolarisation are then followed by a short period of neuronal inactivity.

Pathologies such as CSD can occur when the normal regulation of extracellular $K^+$ fails [165]. Astrocytes are able to regulate the extracellular $K^+$ concentration via a process known as spatial buffering. Astrocytes can take up $K^+$ via ion channels and distribute it further to neighbouring astrocytes via gap junctions. The neuroprotective role of astrocytic gap junctions during diseased states has been under debate (see Chen and Swanson [31], Chew et al. [32] for review). Some

studies indicate that gap junction communication may increase ischemic damage by allowing the propagation of pre-apoptotic signals between dying and viable astrocytes [116]. On the other hand, Nakase et al. [131] demonstrated that reduced expression of Cx43 (the most widely expressed gap junction protein) in astrocytes led to a significant increase in the size of ischemic infarcts, suggesting that gap junctions play a critical role in the regulation and removal of ions. Ma et al. [118] demonstrated both experimentally and numerically that a syncytium of coupled astrocytes can distribute excess $K^+$ and maintain a physiological membrane potential in the presence of elevated extracellular $K^+$ concentration.

In Chapter 3 a previous neurovascular unit (NVU) model was implemented on the macro scale by embedding multiple NVUs in a two dimensional (2D) tissue slice. Each NVU was coupled to its nearest four neighbours by extracellular $K^+$ diffusion and globally coupled via a space filling binary H-tree simulating a perfusing arterial tree (vasculature). This NVU model did not contain the nitric oxide (NO) signalling pathway [47], astrocytic calcium ($Ca^{2+}$) dynamics [105], complex neuron/extracellular space (ECS) dynamics or the blood-oxygen-level dependent (BOLD) response.

In this chapter, the proposed complex NVU model of Chapter 5 has been implemented on the macro scale and extended by the addition of astrocyte to astrocyte communication via $K^+$ gap junctions. In addition, extracellular electrodiffusion of $K^+$ and $Na^+$ has been implemented rather than the simpler approximation of Fickian diffusion. This state of the art model is the first of its kind to be able to simulate spatial phenomena such as CSD and astrocytic spatial buffering in a 2D tissue slice while also containing the complex dynamics of the NVU. Importantly, it contains full neuron/ECS dynamics and the vascular dynamics which in turn control the vessel radius and hence the rate of perfusion. This is in contrast to various models detailing only the neuron/ECS subsystem [26], neuron/astrocyte subsystem [140, 94, 35], or in particular the previous spatial neurovascular coupling (NVC) model from Chapter 3 which did not include the complex neuron/ECS dynamics necessary for modelling pathologies such as CSD. In addition, the model is embedded in a 2D tissue slice which allows for the simulation of 2D propagating wavefronts; as CSD waves travel across the cortical surface [115], this is preferable to simpler one dimensional (1D) models simulating a row or array of cells [26, 94, 135, 35].

## 6.2 METHOD AND MODEL DEVELOPMENT

The implementation of a tissue slice containing multiple NVUs on the macro scale is given below, with an explanation of the two extensions to the model: extracellular electrodiffusion and astrocytic gap junctions. A schematic overview of communication within the tissue slice is given in Figure 28; a schematic diagram of the single NVU model can be found in Figure 22. All relevant equations and parameters can be found in Appendix A.7.

### 6.2.1 *Astrocytic gap junctions*

The majority of astrocytic gap junction currents are likely to be carried via $K^+$ and chlorine ($Cl^-$) due to their high cytosolic concentrations [97]. Astrocytes are also known to transfer $Ca^{2+}$ and $Cl^-$ through gap junctions [143, 63]. However in the model only $K^+$ transport is considered as the primary interest is in spatial $K^+$ buffering during CSD. In the model $Cl^-$ transport is not considered as the astrocytic $Cl^-$ concentration is found via electroneutrality with the other cytosolic ions ($K^+$, $Na^+$, and $HCO_3^-$), and astrocytic $Ca^{2+}$ transport is not considered as it does not seem to have any significant effect on the dynamics in the model as shown in Chapter 4.

The gap junction $K^+$ flux between two compartments is modelled in the same manner as Jacobsen et al. [97] by using an additive electrodiffusion equation based on the Nernst-Planck equation. This allows us to couple a NVU block to an arbitrary number of neighbours if needed. The gap junctional flux is due to both membrane potential and ion concentration gradients between adjacent blocks. Note that with nonlinear systems there are often multiple forms of discretisation; the method chosen is given below.

The Nernst-Planck equation describes the flux $J_c$ of ion c due to both concentration gradient $\nabla c$ and membrane potential gradient $\nabla V$:

$$J_c = -D\left[\nabla c + \frac{z_c F}{R_g T} c \nabla V\right] \tag{6.1}$$

where $z_c$ is the valence of ion c, $F$ is Faraday's constant, $R_g$ is the gas constant, $T$ is the temperature, and $D$ is the diffusion coefficient (assumed constant). The flux can be simplified for an

assumed linear gradient (i.e. between two blocks) by replacing the differential terms with ratios of differences and the concentration $c$ by the mean concentration of two adjacent blocks $i$ and $j$ [70]:

$$J_{c,i\to j} = -\frac{D}{\Delta x}\left((c_j - c_i) + \frac{z_c F}{R_g T}\frac{c_i + c_j}{2}(V_j - V_i)\right) \tag{6.2}$$

where $\Delta x$ is the distance between the two blocks. Note that each block is symmetric so $\Delta x$ is the same in both 2D coordinates. This gives the flux of ion $c$ from block $i$ into its neighbour $j$. Assuming that the area of interface between adjacent blocks is $\Delta x^2$, the rate of change of ion concentration in block $i$ as a result of the gap junction flux to block $j$ is given by $\frac{J_{i\to j}\times\Delta x^2}{\Delta x^3} = \frac{J_{i\to j}}{\Delta x}$, where $\Delta x^3$ is the volume of the block.

In the macro scale tissue slice model each block corresponding to a NVU has width $\Delta x = 124$ µm [106] and astrocytic $K^+$ gap junctions are implemented for each block's four nearest neighbours (excluding diagonals) shown schematically in Figure 28. Then the total rate of change of $K^+$ due to the sum of diffusive ion fluxes $J$ into the astrocyte of block $i$ via gap junctions is given by

$$Q_{K_k} = -\frac{1}{\Delta x}\sum_j J_{K,i\to j} \tag{6.3}$$

which takes into account each neighbour $j$ of block $i$. This rate of change is added to the conservation equation for the astrocytic $K^+$ concentration $K_k$:

$$\frac{dK_k^i}{dt} = -\frac{1}{\Delta x}\sum_j J_{K,i\to j} - J^i_{K_k} + 2J^i_{NaK_k} + J^i_{NKCC1_k} + J^i_{KCC1_k} \tag{6.4}$$

with gap junctional fluxes given by

$$J_{K,i\to j} = -\frac{D_{gap}}{\Delta x}\left((K_k^j - K_K^i) + \frac{z_K F}{RT}\frac{K_k^i + K_k^j}{2}(v_k^j - v_k^i)\right). \tag{6.5}$$

The effective diffusion coefficient $D_{gap}$ is dependent on the ion permeability through the gap junction, the area of contact between the neighbouring astrocytes, and the volume-area ratio of the astrocyte. The general ion permeability can be found in the literature as $P = 5\times10^{-8}$ m s$^{-1}$ [97], the area of contact between neighbouring astrocytes is taken as the astrocytic endfoot area

$A_{ef} = 3.7 \times 10^{-9}$ m$^2$ [48], and the volume-area ratio of the astrocyte is given by $R_k = 6 \times 10^{-8}$ m [48]. This gives an effective diffusion coefficient of

$$D_{gap} = \frac{PA_{ef}}{R_k} \tag{6.6}$$

where $D_{gap} = 3.1 \times 10^{-9}$ m$^2$s$^{-1}$.

The astrocytic membrane potential $v_k$ was previously evaluated via the Goldman Hodgkin Katz (GHK) method, however for ease of integration of new channels and gap junctions $v_k$ is evaluated via an ordinary differential equation (ODE) given in the form used by Witthoft et al. [171] and Koenigsberger et al. [111] where a parameter $\gamma_v$ relates the net movement of ion fluxes to membrane potential and is inversely proportional to membrane capacitance [142]. Then the ODE for $v_k$ in block $i$ is given by:

$$\frac{dv_k^i}{dt} = \gamma_v \left[ -\frac{1}{\Delta x} \sum_j z_K J_{K,i\to j} + \text{other terms} \right] \tag{6.7}$$

where the "other terms" are all ion fluxes into the astrocyte of block $i$, detailed in Appendix A.7.

### 6.2.2 *Other model changes*

The volume-area ratios for the astrocyte ($R_k$) and synaptic cleft (SC) ($R_s$) were originally implemented by Østby et al. [137] as variables, as they specifically wanted to investigate the effect of NVC on the shrinkage of the extraneural space. This made the model more complicated, as for example the ODEs for ion concentrations in the astrocyte and SC were for the number of ions (in μMm) rather than simple ion concentrations (in μM). This made connecting the astrocyte/SC submodel to the other submodels more complicated due to the difference in units, and made adding new components more difficult. This has been greatly simplified by setting the volume-area ratios as constants (taken as their steady state values when they were variable) where $R_k = 6 \times 10^{-8}$ m, $R_s = 2.79 \times 10^{-8}$ m. These changes have minimal effect on the model (results not shown).

In addition, the astrocytic membrane potential is now evaluated in mV rather than V so that the conversion parameter $c_{unit}$ can be removed. Note that all parameters with units of V have also been converted to mV.

### 6.2.3 *Extracellular electrodiffusion*

In the macro scale model of Chapter 3 the ECS compartment was very simple and contained only $K^+$ diffusion modelled via Fickian diffusion, i.e. $K^+$ moved from high to low concentrations. However Fickian diffusion does not take into account the effect of the electric field due to ion movement within the ECS, and the ECS compartment in the complex model of Mathias et al. [121] described in Chapter 5 contains both $K^+$ and $Na^+$. Therefore in order to produce a more physiologically viable result extracellular electrodiffusion is implemented. It should be noted that $Cl^-$ is also present in the ECS but it is assumed to be found via electroneutrality with the other extracellular ions, so any movement of $Cl^-$ is not considered.

Almeida et al. [4] constructed a mathematical model containing electrodiffusion equations describing the movement of multiple ions in the ECS. This model focused on the dynamics of the neuron (pre and post synapse) and ECS and did not consider the influence or behaviour of the remainder of the NVU. They considered that the extracellular ionic fluxes would be produced by the concentration gradient (Fickian diffusion) and also by the electric field $\nabla V$, where $V$ is the extracellular potential. Almeida et al. [4] hypothesised that the extracellular potential has a component related to a Nernst potential across the ECS. This implies a dynamic equilibrium where the total current in each point is zero. Using the Nernst-Planck equation, the current density for an ion with concentration $c$ is given by

$$I_c = -z_c F D_c \left[ \nabla c + \frac{z_c F}{R_g T} c \nabla V \right]. \tag{6.8}$$

The following dynamic equilibrium can be considered:

$$\sum_n I_n = 0, \tag{6.9}$$

where in this case $n \in \{K^+, Na^+\}$. By using the Nernst-Planck equation (6.1) applied to multiple ions and considering a dynamic equilibrium where the total current in each point of the ECS is zero, Almeida et al. [4] gave the extracellular potential gradient $\nabla V$ as

$$\nabla V = -\frac{R_g T}{F} \frac{\sum_n z_n D_n \nabla n}{\sum_n z_n^2 D_n n} \tag{6.10}$$

where in this case $n \in \{K^+, Na^+\}$. Substituting this into Eq. (6.1) the flux of ion $c$ is given by

$$J_c = -D_c \left[ \nabla c - z_c c \left( \frac{\sum_n z_n D_n \nabla n}{\sum_n z_n^2 D_n n} \right) \right] \tag{6.11}$$

This can be simplified for a linear gradient (i.e. between two compartments, in this case two adjacent NVU blocks in the tissue slice) in the same way as for astrocytic gap junctions in Section 6.2.1, giving the flux $J^e_{c,i\to j}$ of ion concentration $c$ due to extracellular diffusion from compartment $i$ to $j$:

$$J^e_{c,i\to j} = -\frac{D_c}{\Delta x} \left[ (c_j - c_i) - z_c \left( \frac{c_i + c_j}{2} \right) \left( \frac{\sum_n z_n D_n (n_j - n_i)}{\sum_n z_n^2 D_n \frac{n_i + n_j}{2}} \right) \right] \tag{6.12}$$

where the diffusion rates for extracellular $K^+$ ($K_e$) and $Na^+$ ($Na_e$) are given by $D_{K,e} = 3.8 \times 10^{-9}$ $m^2 s^{-1}$ [163] and $D_{Na,e} = 2.5 \times 10^{-9}$ $m^2 s^{-1}$ [157]. Then the total rates of change $Q$ of $K^+$ and $Na^+$ due to the sum of diffusive ion fluxes $J$ into the ECS of block $i$ are given by

$$Q_{K_e,i} = -\frac{1}{\Delta x} \sum_j J^e_{K,i\to j} \tag{6.13}$$

$$Q_{Na_e,i} = -\frac{1}{\Delta x} \sum_j J^e_{Na,i\to j} \tag{6.14}$$

which takes into account each neighbour $j$ of block $i$. These rates of change are added to the conservation equations in NVU block $i$ for $K_e$ and $Na^+$ concentration $Na_e$ respectively; these equations can be found in Appendix A.7. An overview of the communication between NVU blocks in the tissue slice is given in Figure 28.

### 6.2.4 *Implementation*

The single NVU ODE system is solved in Matlab using the solver 'ode15s' due to stiffness. The macro scale tissue slice model is implemented in the same manner as in Chapter 3 (discussed in detail in Section 3.2.3). For all simulations, the simulated vascular H-tree contained $N = 11$ levels coupled with 1024 NVU tissue blocks corresponding to a 4 mm $\times$ 4 mm 2D cerebral tissue slice. The initial conditions were homogeneous over the entire tissue slice. The system used was

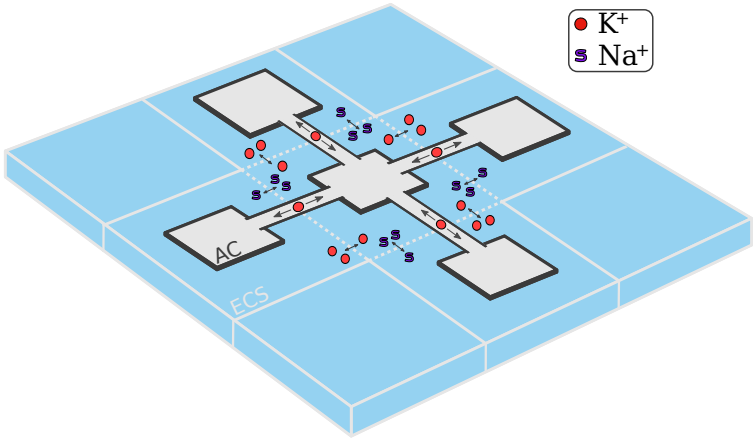


Figure 28: Overview of the communication between NVU blocks in the tissue slice simulation, with extracellular $K^+$ and $Na^+$ electrodiffusion and $K^+$ transport via astrocytic gap junctions. Each block communicates with its four nearest neighbours. AC: astrocyte, ECS: extracellular space.

a 56 core Intel Xeon E5-4660 v3 server with 128 GB of memory and clock speed of 2.10 GHz. The numerical simulations were executed on 32 cores with 32 NVU tissue blocks allocated to each core. All simulations were performed for a total of 35 physiological seconds. Each iteration corresponding to one physiological second took approximately 2 minutes of wall clock time to complete.

## 6.3 RESULTS

While regular NVC leads to vasodilation following neuronal activity, dysfunctional NVC can lead to various pathologies such as CSD where a wave of high extracellular $K^+$ moves throughout the cortex. The parameters of the model were chosen in order to produce a response typical of CSD as follows: the maximum rate of the neuronal $Na^+/K^+$ ATPase pump was set at a lower rate of $I_{max} = 0.013 \times 10^{-2}$ mA cm$^{-2}$ (following the work of Kager et al. [99]), and the number of active synapses per astrocytic process was set as $k_{syn} = 1$ (since communication between the neuron and astrocyte during CSD happens primarily through the ECS rather than the SC). These parameters are used for all simulations in this chapter.

### 6.3.1 *Excitability of the Neuron and ECS*

During pathologies such as CSD, the neuron releases large amounts of $K^+$ into the ECS. This extracellular $K^+$ can diffuse outward, where an increase in extracellular $K^+$ exceeding a critical

threshold concentration (generally around 12 mM) leads to a massive $K^+$ efflux from the neuron and extracellular concentrations over $30-50$ mM, and sometimes as high as 80 mM [6]. This is known as excitable behaviour, and provides the mechanism by which waves of extracellular $K^+$ can propagate. The threshold is known to vary in different species and brain regions, and with age and other factors [6].

To induce excitable behaviour in the single NVU model a rectangular input of $K^+$ is injected into the ECS (with duration 1.5 s). The amplitude of this input is varied between 10 and 11 $mMs^{-1}$ in order to produce two distinct cases of subthreshold and supra-threshold excitable behaviour.

Figure 29 shows the behaviour of the NVU for these two cases. For a 10 $mMs^{-1}$ input of $K^+$ to the ECS, after 1.5 s the extracellular $K^+$ concentration ($K_e$) only reaches 9.5 mM which is below the excitation threshold of 10.2 mM; note that this threshold value depends on the neuron parameters of the model and may change if parameters are varied. Consequently $K_e$ returns to baseline when the input ceases and there is little effect on the rest of the NVU.

In contrast, for a 11 $mMs^{-1}$ input $K_e$ exceeds the threshold of 10.2 mM and quickly increases to approximately 80 mM with concurrent neuronal depolarisation (increase in dendritic membrane potential $v_d$). This excitable behaviour seems to be due to the N-methyl-D-aspartate (NMDA) channel on the dendrite. This is strengthened by the fact that when the NMDA channel is removed from the model the neuron/ECS subsystem is not excitable. The NMDA channel is the only neuron channel with fraction of open activation gates $m$ and fraction of open inactivation gates $h$ dependent on $K_e$. Kager et al. [99] stated that high extracellular $K^+$ enhances the NMDA receptor activation based on findings by Poolos and Kocsis [147].

Once $K_e$ reaches the threshold of 10.2 mM, the NMDA channel on the dendrite opens to allow a significant flux of $K^+$ through the channel from the dendrite into the ECS which causes a further increase in $K_e$. This increase in $K^+$ further opens the NMDA channel in a positive feedback loop. This large efflux of $K^+$ from the neuron is offset by a larger and concurrent influx of $Na^+$ into the neuron (as the NMDA channel allows both $K^+$ and $Na^+$), causing the neuron to depolarise which allows the remaining $K^+$ and $Na^+$ channels and pumps to open. All this leads to a sharp increase in $K_e$ up to a maximum concentration of around 80 mM. This is followed by a drop in both $K_e$ to around 11 mM and neuronal membrane potential to around $-40$ mV due to extracellular $K^+$ buffering and re-uptake of $K^+$ by the neuron. Approximately 20 s after depolarisation the neuron membrane potential drops slightly below baseline (and $K_e$ soon follows) and then slowly returns to baseline. This drop below baseline is important as it inhibits another excitation from occurring

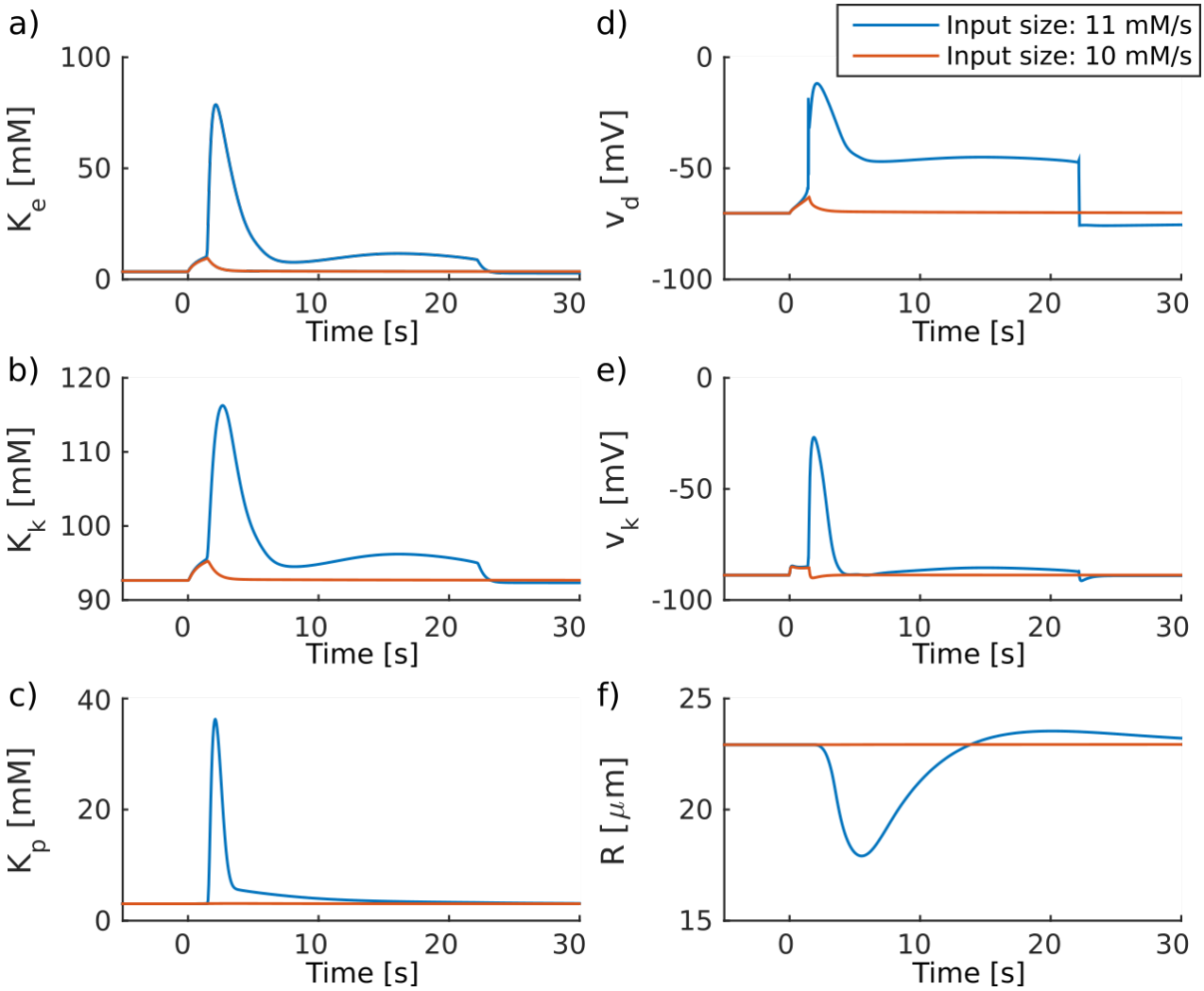


Figure 29: Response to a rectangular input of $K^+$ into the ECS for duration 1.5 s and amplitude 10 $mMs^{-1}$ (subthreshold) and 11 $mMs^{-1}$ (superthreshold) into the single NVU model. For subthreshold stimulation, $K_e$ returns to baseline when the input ceases and there is little effect on the rest of the NVU. For supra-threshold stimulation, $K_e$ increases to 80 mM leading to astrocytic $K^+$ uptake and subsequent efflux into the perivascular space (PVS), leading to vasoconstriction followed by dilation. a) $K_e$: extracellular $K^+$ concentration, b) $K_k$: astrocytic $K^+$ concentration, c) $K_p$: perivascular $K^+$ concentration, d) $v_d$: dendrite membrane potential, e) $v_k$: astrocytic membrane potential, f) R: vessel radius.

too soon after the first excitation. The inhibitory period is present in all excitable systems and prevents propagating waves in an excitable medium from travelling backwards.

The effect on the remainder of the NVU is as follows. The increase in $K_e$ leads to an increase in synaptic $K^+$ concentration and hence astrocytic $K^+$ concentration ($K_k$) up to 117 mM (via $K^+$ flux from the SC). This depolarises the astrocyte (i.e. an increase in astrocytic membrane potential $v_k$) which opens the voltage dependent big potassium (BK) channel leading to a large efflux of $K^+$ from the astrocytic endfoot into the PVS. The rapid increase in perivascular $K^+$ ($K_p$) up to 35 mM leads to constriction of the vessel radius R from 22.9 µm down to 18 µm. As $K_e$ drops both $K_k$ and $v_k$ decrease, which leads to the reversal of the BK channel flux as a result of the difference

between $v_k$ and the BK Nernst potential. This causes $K^+$ to flow out of the PVS and hence a rapid decrease in $K_p$. Once $v_k$ drops below $-85$ mV (at approximately $t = 4$ s) the BK channel closes. At this point $K_p$ is still approximately 5 mM and slowly decays down to the baseline of 3 mM, and the radius undergoes slight vasodilation up to 23.5 μm with a slow return to baseline of 22.9 μm.

### 6.3.2 *Effects of perivascular $K^+$ concentration on the radius*

The behaviour of the vessel radius in response to changes in $K_p$ can be summarised in a bifurcation diagram (Figure 30), where $K_p$ is varied from 3 to 30 mM. This enables us to determine whether the vessel will undergo either vasodilation or constriction depending on $K_p$.

In the model, when the dynamics are initially at a steady state the radius has a resting state of 22.9 μm and $K_p = 3$ mM. Increasing $K_p$ to levels up to 16.8 mM (as can occur during neuronal stimulation in regular non-pathological conditions) results in vasodilation, with a maximal dilation of 28.8 μm at $K_p = 10.8$ mM. However when $K_p$ is between 16.8 and 21.1 mM the vessel radius undergoes oscillations, and for $K_p$ larger than 21.1 mM the vessel is constricted with a minimal radius of 17 μm as $K_p$ increases further.

The inward rectifying $K^+$ (KIR) channel connecting the smooth muscle cell (SMC) to the PVS is the cause of the shift from vasodilation to constriction as $K_p$ increases. The direction of the $K^+$

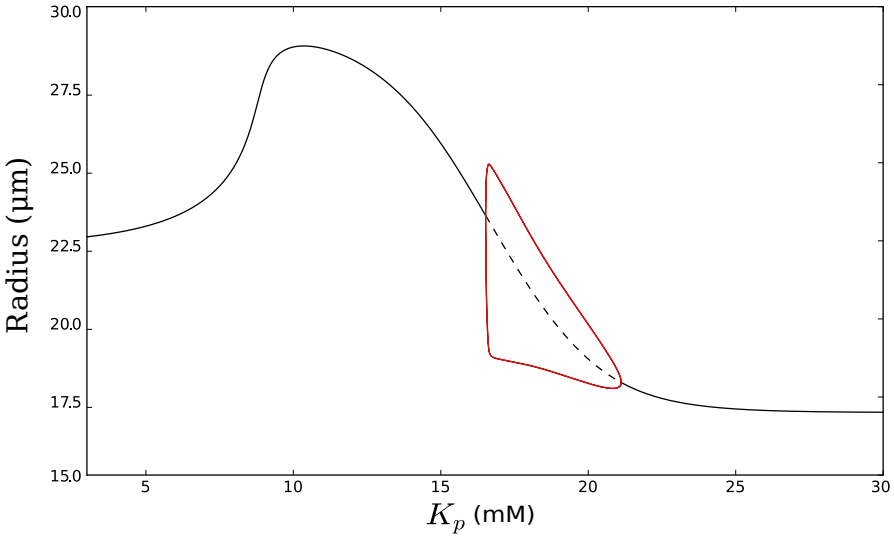


Figure 30: Bifurcation diagram of the radius dynamics with the perivascular $K^+$ concentration ($K_p$) varied as a bifurcation parameter. For $3 < K_p < 16.8$ mM the steady state radius is higher than the baseline of 22.9 μm (i.e. vasodilation), for $16.8 < K_p < 21$ mM the radius tends to oscillatory behaviour, and for $K_p > 21$ mM the steady state radius is below the baseline (i.e. vasoconstriction). Black solid: steady state radius, red solid: minimum and maximum amplitude of radial oscillations. The bifurcation analysis was achieved using the continuation package AUTO [25].

flux through the KIR channel is given by the difference in SMC membrane potential $v_i$ and the resting potential $v_{KIR_i}$ which is proportional to $K_p$ and given by

$$J_{KIR_i} = G_{KIR_i}(v_i - v_{KIR_i}) \tag{6.15}$$

$$v_{KIR_i} = z_1 K_p - z_2 \tag{6.16}$$

where the conductance $G_{KIR_i}$ and parameters $z_1$ and $z_2$ are found in Appendix A.3. When $v_i > v_{KIR}$ the flux is directed into the PVS whereas for $v_i < v_{KIR}$ the flux is directed into the SMC. Hence for large enough $K_p$, $v_{KIR}$ will be greater than $v_i$ and the channel reverses.

For $K_p < 16.8$ mM the $K^+$ flux is directed into the PVS so the SMC membrane hyperpolarises. This closes the voltage operated $Ca^{2+}$ channels (VOCCs) thereby decreasing the SMC $Ca^{2+}$ concentration and resulting in vasodilation. However for $K_p > 18.5$ mM the KIR channel reverses leading to an influx of $K^+$ into the SMC. This depolarises the cell membrane and opens the VOCCs, leading to increased $Ca^{2+}$ concentration and hence vasoconstriction.

The bifurcation diagram shows the steady state values that the radius tends to as a function of $K_p$, however it is important to note that the vascular dynamics are relatively slow, and during neuronal stimulation $K_p$ does not stay at a constant high concentration for long. Therefore even though $K_p$ may briefly reach a maximum concentration such as 11 mM (where the steady state radius is around 29 μm), the radius will not react fast enough to reach such a high value before $K_p$ decreases. It should also be noted that the radius does not drop below 17 μm for higher values of $K_p$ as the open probability of the SMC $Ca^{2+}$ mediated $K^+$ channel $w_i$ reaches its maximal value of 1.

The bifurcation diagram also shows that there are oscillations in the vessel radius when $K_p$ is between 16.5 and 21 mM; the likely underlying physiology causing these oscillations is as follows. The high $K_p$ causes the KIR channel to reverse, resulting in a flux of $K^+$ from the PVS into the SMC. The SMC depolarises, opening the VOCCs and resulting in an influx of $Ca^{2+}$ into the SMC cytosol. Consequently the SMC $Ca^{2+}$ concentration increases. This causes the $Ca^{2+}$ mediated $K^+$ channel on the SMC to pump out more $K^+$ and as a result the SMC hyperpolarises. This reverses the KIR channel so that the flux is from the SMC to the PVS and closes the VOCCs, causing a decrease in $Ca^{2+}$ concentration. These oscillations may provide a mechanism for vasomotion, the rhythmic contraction and dilation of vessels at a frequency of anywhere from 1 to 20 $min^{-1}$ [1] which is thought likely to assist in tissue perfusion during periods of altered metabolism or pathological conditions [79]. Indeed, vasomotion is known to occur in response to increases in extracellular $K^+$

concentration [88], among other causes such as pressure, stretch and vasoconstrictive agonists [79]. However these oscillations are generally not seen in the simulations for the following reasons: the oscillations have a large period from between 10 and 40 s (corresponding to frequencies between 1.5 to 6 $min^{-1}$) depending on the specific value of $K_p$ (not shown), the simulations are generally run for less than 50 seconds, and $K_p$ does not remain at any constant value for a long enough period of time to induce visible oscillations.

### 6.3.3 *Macro scale model*

The behaviour of the single NVU system in response to high extracellular $K^+$ ($K_e$) levels and neuronal depolarisation was discussed in Section 6.3.1. However this model can also be implemented on a large scale by simulating a 2D cortical slice consisting of tissue blocks, where each block corresponds to single NVU and is globally coupled by extracellular diffusion, astrocytic gap junctions, and a vascular H-tree.

#### 6.3.3.1 *Scaling results*

In this chapter further communication between adjacent tissue blocks has been added in the form of both extracellular electrodiffusive ion fluxes (Eq. (6.12)) and astrocytic gap junction fluxes (Eq. (6.2)). This additional communication may have an effect on the scalability, therefore 3 numerical experiments were performed in order to determine the scaling effects of the parallel code which are shown in Figure 31.

The first experiment measured the strong scaling performance of the system with a fixed number of levels in the vascular tree of $N = 13$ corresponding to a problem size of $2^{N-1} = 4096$ NVUs (Figure 31a). The number of processes was varied between 1 and 64 in powers of 2 and the simulation wall clock time was recorded. Strong scaling is ideal up to 16 processes; the wall clock time for the case with 32 processes is less than ideal as the time needed for extra communication between processes is beginning to outweigh the benefit of a smaller problem size per process. With 64 processes the wall clock time is greater than the case with 32 processes; however this is not surprising as the system used only has 56 cores, so one or multiple processes are assigned to each core leading to an increase in computation time.

The second experiment measured the weak scaling performance, where the problem size was increased from $N = 7$ to 13 in proportion to the number of processes varying between 1 and 64.

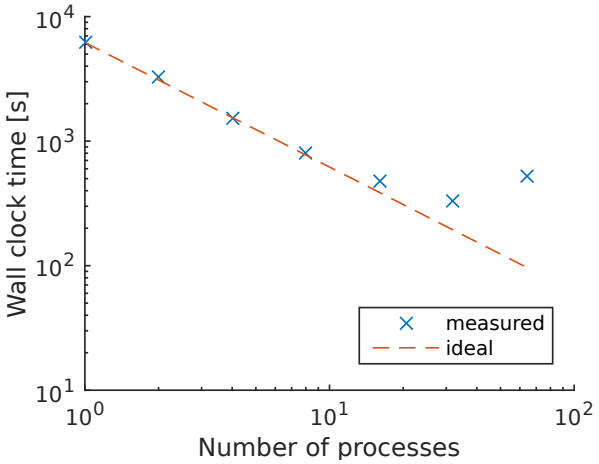


(a) Strong scaling (N = 13, number of processes = 1, 2, . . . , 64)

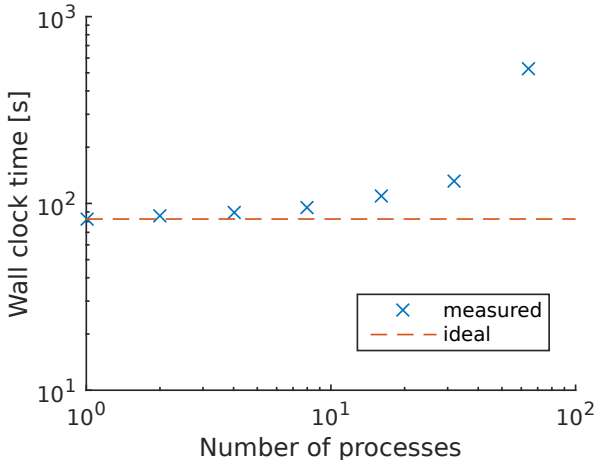


(b) Weak scaling (N = 7, . . . , 13, number of processes = 1, 2, . . . , 64)

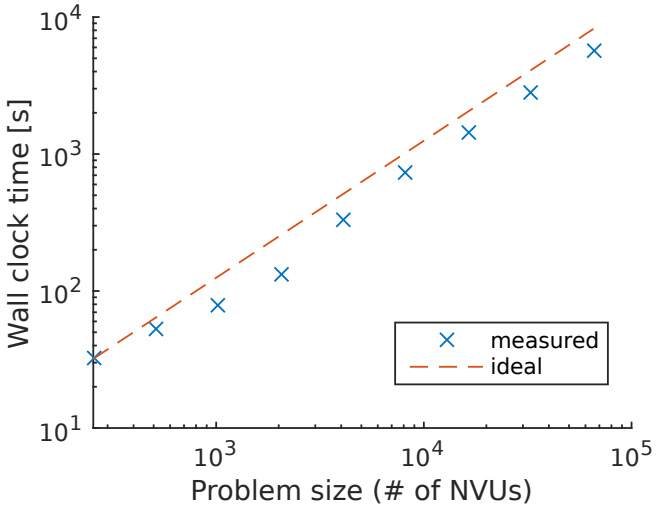


(c) Scaling with problem size (number of processes = 32, N = 9, . . . , 17)

Figure 31: Scaling experiments for the large scale tissue slice model, where N is the number of levels in the H tree and the problem size is the number of NVUs in the tissue slice given by $2^{N-1}$.

Figure 31b shows that the wall clock time increases slightly with problem size and number of processes, up until 64 processes where the wall clock time jumps sharply - again this is a result of the 56 core system. With small problem sizes the relative contribution of communication is accentuated; larger problem sizes would flatten the curve further.

Finally the performance was tested with a fixed number of processes and the problem size varied from N = 9 to 17, shown in Figure 31c. The results show that the scaling with problem size reflects the expected linear performance.

#### 6.3.3.2 *Extracellular diffusion*

A square ($12 \times 12$ NVU blocks, enclosed by the yellow dotted line in the following figures) in the centre of the tissue slice ($32 \times 32$ NVU blocks) is stimulated by a rectangular input current of amplitude $0.6 \times 10^{-2}$ mA cm$^{-2}$ for 1 s which is a sufficient duration for inducing CSD following the work of Kager et al. [99] and Mathias et al. [121]. Time series in the following figures are shown for a block in the centre of the stimulation area (block 496) and blocks which are 1, 2 and 3 blocks out from the stimulation area (blocks 304, 272, 240 respectively). In this section there are no astrocytic gap junctions (i.e. $D_{gap} = 0$) in order to clearly see the effects of extracellular diffusion.

##### FICKIAN DIFFUSION

Figure 32 shows the behaviour in the tissue slice model with Fickian diffusion and without astrocytic gap junctions. The snapshots of the tissue slice (Figure 32e,f) are shown at $t = 4$ s after stimulation. The input current of 1 s stimulates the centre area, causing neuronal depolarisation and a dramatic increase in $K_e$ from 3.5 mM up to 80 mM.

With extracellular Fickian diffusion, $K_e$ diffuses outward from the stimulation area. $K_e$ on the boundary of the stimulation area (block 304) reaches 10.2 mM approximately 1.5 s after the beginning of stimulation; this induces a further quick increase in $K_e$ up to 70 mM according to the dynamics explained in Section 6.3.1 and subsequent increase in $K_e$ up to 65 mM in the neighbouring NVU (block 272). However this is not enough to induce an increase in $K_e$ up to 10.2 mM in the next NVU (block 240, 3 blocks out from the stimulation area), so the wave of extracellular $K^+$ travels no further.

##### ELECTRODIFFUSION

The model has been extended by extracellular electrodiffusion of both $K^+$ and $Na^+$ in the ECS shown in Figure 33. The snapshots of the tissue slice (Figure 33e,f) are shown at $t = 11$ s after stimulation. With electrodiffusion, the flux of $K^+$ (and $Na^+$) throughout the ECS is greater due to the influence of the electric field. As a result, the $K^+$ in the stimulation area diffuses outward at a higher rate so that $K_e$ on the boundary (block 304) reaches the excitation threshold and undergoes a large increase in $K_e$. This $K^+$ diffuses further out and each NVU block is able to induce a rise in $K^+$ above the threshold in its neighbouring block. Consequently a wave of $K^+$ is able to propagate throughout the ECS. This wave travels at a velocity of 6.7 mm min$^{-1}$ based on a block width of

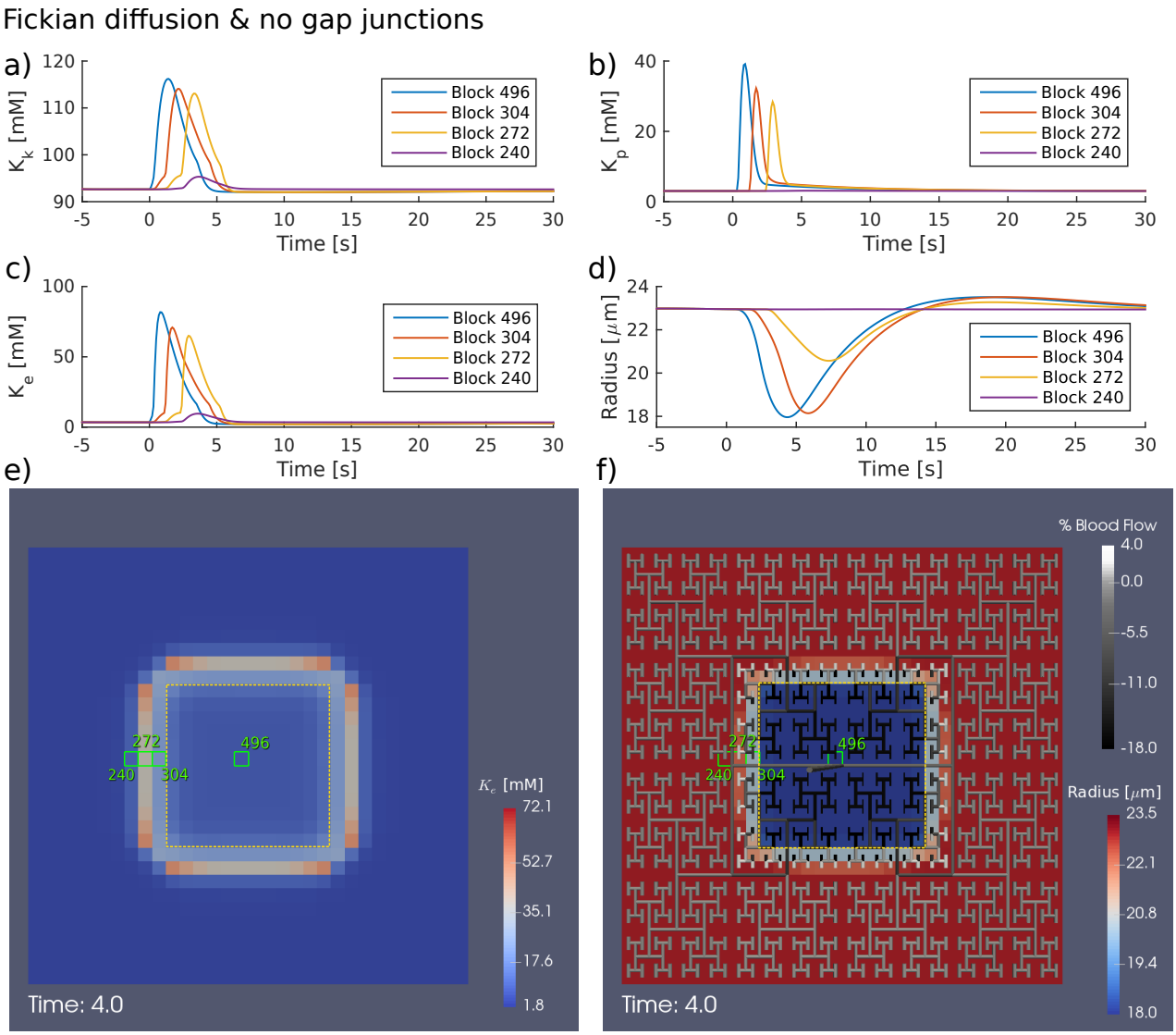


Figure 32: Snapshots and time series for selected blocks (green) in the tissue slice model for a 1 s neuronal stimulation to centre of tissue slice (enclosed by dashed yellow line) under CSD conditions with extracellular Fickian diffusion and no astrocytic gap junctions. The ECS is subexcitable so the $K^+$ wave cannot propagate further than 2 blocks out from the stimulation area. a) astrocytic $K^+$ concentration $K_k$ in mM, b) perivascular $K^+$ concentration $K_p$ in mM, c) extracellular $K^+$ concentration $K_e$ in mM, d) vessel radius in µm, e) snapshot at $t = 4$ s of the extracellular $K^+$ concentration $K_e$, f) snapshot at $t = 4$ s of the percentage change in blood flow through the tree and the radius of the vascular leaf coupled to the NVU block. Video available online (https://youtu.be/nivZ_bSuGrI)

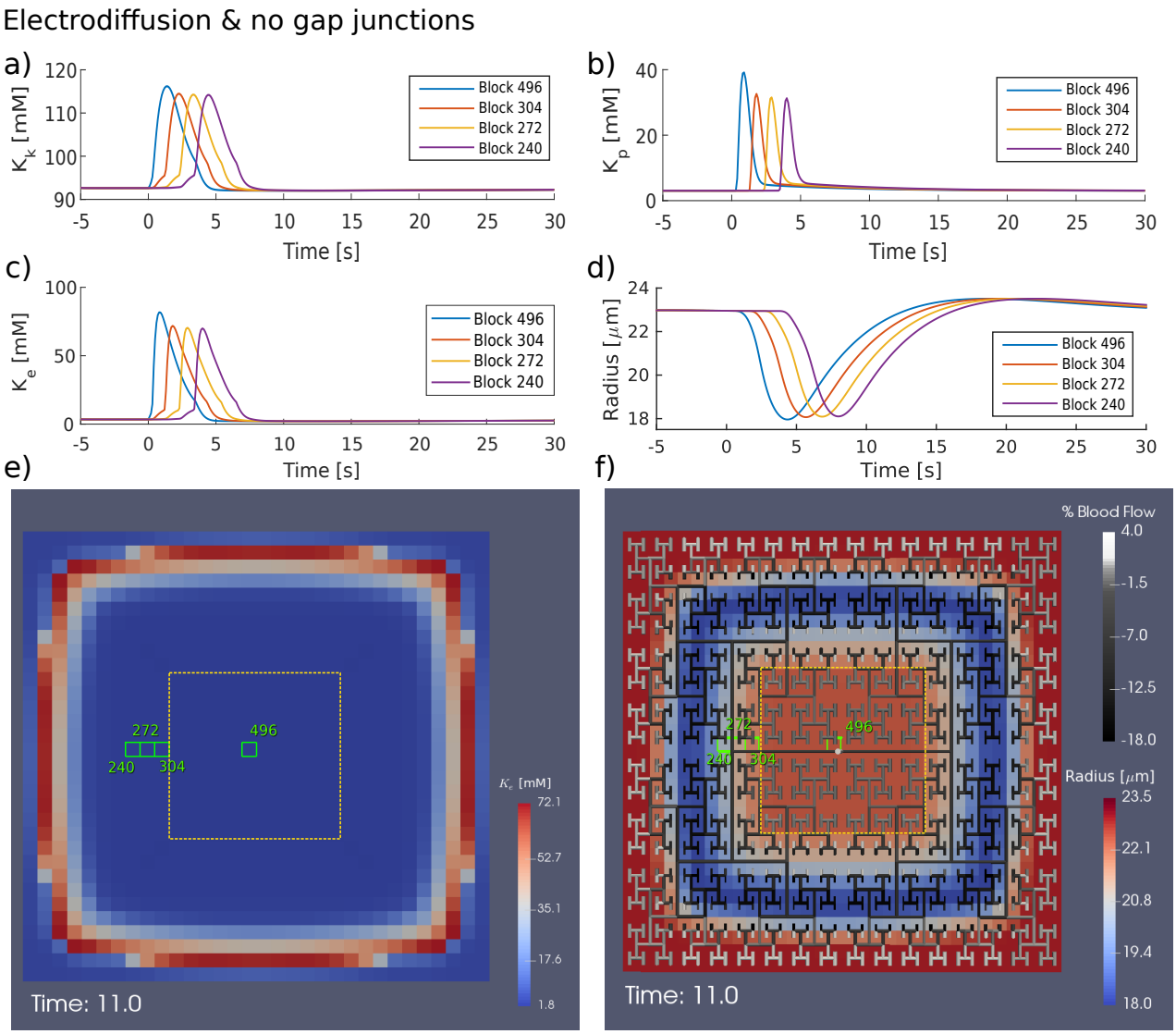


Figure 33: Snapshots and time series for selected blocks (green) in the tissue slice model for a 1 s neuronal stimulation to centre of tissue slice (enclosed by dashed yellow line) under CSD conditions with extracellular electrodiffusion and no astrocytic gap junctions. With electrodiffusion the ECS is excitable and can support a propagating $K^+$ wave that travels at 6.7 mm $min^{-1}$. Without gap junctions, stimulation results in a wave of vasoconstriction and decreased blood flow spreading outwards followed by slight vasodilation. a) astrocytic $K^+$ concentration $K_k$ in mM, b) perivascular $K^+$ concentration $K_p$ in mM, c) extracellular $K^+$ concentration $K_e$ in mM, d) vessel radius in µm, e) snapshot at t = 11 s of the extracellular $K^+$ concentration $K_e$, f) snapshot at t = 11 s of the percentage change in blood flow through the tree and the radius of the vascular leaf coupled to the NVU block. Video available online (https://youtu.be/Mq0EyFRrdCQ)

124 μm given in Section 6.2. As the ECS is able to support a travelling wave the medium is said to be excitable [108].

The dynamics of extracellular $K^+$ for both Fickian and electrodiffusion are clearly seen in simulation videos available online and detailed in the Figure captions.

#### 6.3.3.3 *Vascular response*

In this section the vascular response to a neuronal stimulus during CSD conditions is given for the cases with and without astrocytic gap junctions (i.e. $D_{gap} = 0$) and extracellular electrodiffusion in order to determine the role of these gap junctions during pathological conditions.

##### NO GAP JUNCTIONS

Figure 33 shows the behaviour of the tissue slice without gap junctions. The rise of $K_e$ in the centre (block 496) induces an increase in synaptic $K^+$ concentration with subsequent increase in astrocytic $K^+$ concentration ($K_k$) from 93 mM up to 115 mM via $K^+$ channels connecting the SC and astrocyte. The influx of $K^+$ into the astrocyte causes a rise in the astrocytic membrane potential ($v_k$). This induces a large flux of $K^+$ through the voltage gated BK channel on the astrocytic endfoot adjacent to the PVS, resulting in an increase in perivascular $K^+$ concentration ($K_p$) from 3 mM up to 35 mM. $K_p$ then sharply drops to 5 mM and slowly returns to its baseline value. The radius depends on $K_p$ according to the bifurcation diagram in Figure 30, where vasoconstriction occurs for $K_p$ greater than 16.5 mM and vasodilation for $K_p$ less than 16.5 mM. Hence the large increase in $K_p$ to 35 mM induces a decrease in vessel radius from 22.9 to 18 μm, the sharp drop to 5 mM induces a slight increase in radius up to 23.5 μm, and as $K_p$ returns to baseline the radius slowly decreases.

The propagating wave of $K_e$ induces a similar wave in $K_k$ with amplitude approximately 113 mM, in turn leading to a propagating wave in $K_p$ with amplitude approximately 30 mM. This level of $K_p$ is high enough to induce vasoconstriction, so the propagating wave of $K_p$ induces a subsequent wave of vasoconstriction (minimum radius of 18 μm) with corresponding decrease in blood flow by 18% through the vascular tree. This wave occurs approximately 4 s after the peak of the $K_p$ wave due to the slower response of the vasculature. The wave of vasoconstriction is followed by slight vasodilation with a slight increase in blood flow by 1%, as $K_p$ sharply drops to 5 mM then slowly returns to its baseline value of 3 mM.

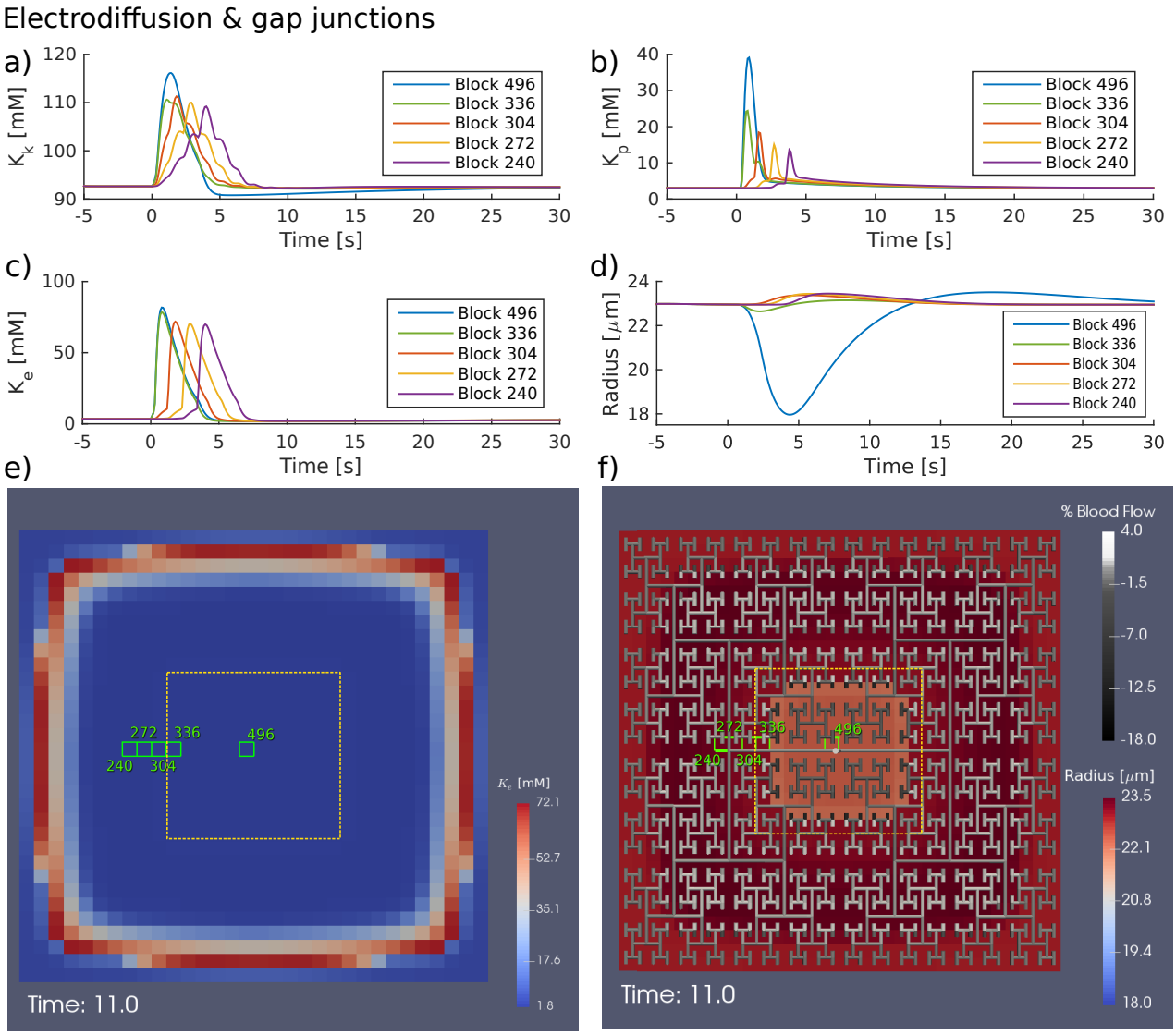


Figure 34: Snapshots and time series for selected blocks (green) in the tissue slice model for a 1 s neuronal stimulation to centre of tissue slice (enclosed by dashed yellow line) under CSD conditions with extracellular electrodiffusion and astrocytic gap junctions. With gap junctions stimulation results in a wave of slight vasodilation, and the area initially affected from vasoconstriction is reduced. a) astrocytic $K^+$ concentration $K_k$ in mM, b) perivascular $K^+$ concentration $K_p$ in mM, c) extracellular $K^+$ concentration $K_e$ in mM, d) vessel radius in μm, e) snapshot at $t = 11$ s of the extracellular $K^+$ concentration $K_e$, f) snapshot at $t = 11$ s of the percentage change in blood flow through the tree and the radius of the vascular leaf coupled to the NVU block. Video available online (https://youtu.be/P9SOj3ljVBI)

### GAP JUNCTIONS

Figure 34 shows the behaviour of the tissue slice with astrocytic gap junctions. The addition of gap junctions does not affect the extracellular $K^+$ dynamics (or neuronal dynamics) in any significant way. This is because in the model the neuron/ECS subsystem feeds into the astrocyte/SC subsystem but this communication is essentially unidirectional. The only effect that the astrocyte and vascular cells have on the neuron/ECS is via the vessel radius which determines the tissue $O_2$ concentration; this in turn affects the behaviour of the neuronal ATPase pumps. However these pumps are also highly dependent on $K_e$, and as $K_e$ rises to very high concentrations during CSD the effect of $O_2$ is comparatively minor.

When the wave of high $K_e$ propagates outwards, the astrocytes take up a large amount of $K^+$ through the SC. With gap junctions the astrocytes are able to transport $K^+$ outwards to neighbouring NVUs so that the amplitude of the $K_k$ wave is lower (around 108 mM). The lower $K_k$ amplitude also means that the resulting wave of membrane potential $v_k$ reaches a lower maximum amplitude. As the BK channel is heavily voltage dependent [105], the magnitude of the $K^+$ flux through the BK channel into the PVS is significantly smaller than the case without gap junctions. Consequently the wave of $K_p$ has a maximum amplitude of only 13 mM (as opposed to 30 mM without gap junctions). Instead of vasoconstriction, this lower $K_p$ induces a wave of slight vasodilation up to 23.5 μm with a corresponding slight increase in blood flow by 1%.

With astrocytic gap junctions, the time series of $K_k$ (Figure 34a) for various NVU blocks in the tissue slice have multiple local maxima or "bumps". This is due to the interaction between $K^+$ diffusion via astrocytic gap junctions throughout the tissue slice and each new influx of $K^+$ via the wave of propagating $K_e$. When the stimulated centre area (block 496) undergoes a large increase in $K_e$ there is a corresponding increase in synaptic $K^+$ concentration and hence an increase in $K_k$ via $K^+$ influx from the SC. The astrocytic $K^+$ diffuses outward via gap junctions to areas of lower $K_k$ (and $v_k$) leading to an increase in $K_k$ in the surrounding area. This increase corresponds to the first local maximum or "bump" in the time series of blocks 304, 272 and 240. As the $K_e$ wave moves outward from the stimulated area it induces a large increase in $K_e$ in the adjacent area (block 304). This leads to another influx of $K^+$ into the astrocyte from the SC, and $K_k$ again diffuses outward through gap junctions, producing another local maximum in the $K_k$ profiles of surrounding blocks. As the $K_e$ wave travels outwards through each block in turn there is a new influx of $K^+$ giving additional local maxima in $K_k$. When the peak of the $K_e$ wave is close to a given block, the $K^+$ flux into the astrocyte is larger and hence the local maximum is steeper than

in a block further from the peak of the wave. When the $K_e$ wave reaches a given block, the final maximum in $K_k$ is induced. As the wave continues to travel past a given block, $K_k$ in that block decreases, with small "bumps" in the $K_k$ profile as a result of further $K^+$ gap junction diffusion from the $K_e$ wave. These "bumps" are likely a result of the discrete nature of the simulated tissue slice containing individual NVU blocks; if the system were essentially homogenised and solved with a set of partial differential equations (PDEs) then it is likely that these bumps would be effectively smoothed out.

The outer edge of the stimulation area (block 336) has a large amount of $K_k$ diffusing outward via gap junctions due to the steep gradient in both $K_k$ and $v_k$ between the stimulated and nonstimulated area. As a result $K_p$ reaches only 24 mM and the vasoconstriction here is brief with a small decrease in radius. Therefore astrocytic gap junctions are able to reduce the size of the initial area that is affected by vasoconstriction in addition to preventing the vasoconstrictive behaviour from travelling further outwards. In contrast, with no gap junctions the entire stimulated area behaves the same (i.e. the profile of the radius for block 496 and 336 are virtually identical).

The behaviour of the tissue slice and vascular tree both with and without astrocytic gap junctions is clearly seen in simulation videos available online and detailed in the Figure captions.

#### 6.3.3.4 *Gap junction density*

Experiments show that the propagating wave of CSD can be slowed or interrupted by pre-existing lesions or areas of high astrocytic density [30], and reduced expression of astrocytic gap junctions significantly increases the size of ischemic infarcts [131]. In areas of high astrocytic density it would follow that there are more gap junction connections between astrocytes [64]. Hence variation in the number of gap junction connections between astrocytes in the tissue slice can be approximated by varying the gap junction diffusion rate $D_{gap}$.

The vascular response to neuronal stimulation during pathological conditions in the model for varied astrocytic gap junction density is shown in Figure 35. A single NVU (block 240) is chosen outside the stimulated area to demonstrate the wave profile of the perivascular $K^+$ concentration $K_p$ and vessel radius. The amount of $K^+$ that is able to be extruded from the astrocyte into the PVS decreases with $D_{gap}$, as stronger coupling between astrocytes means more $K^+$ is able to be diffused outward through the tissue slice. With no gap junctions ($D_{gap} = 0$), $K_p$ reaches 31 mM inducing strong vasoconstriction followed by slight vasodilation (see Figure 33). However with $0.2 \times D_{gap}$, $K_p$ only reaches 26 mM which is still high enough to induce slight vasoconstriction,

and with $0.4 \times D_{gap}$, $K_p$ reaches 21 mM inducing slight vasodilation. With the normal rate of gap junction diffusion $K_p$ reaches only 13 mM inducing vasodilation (see Figure 34).

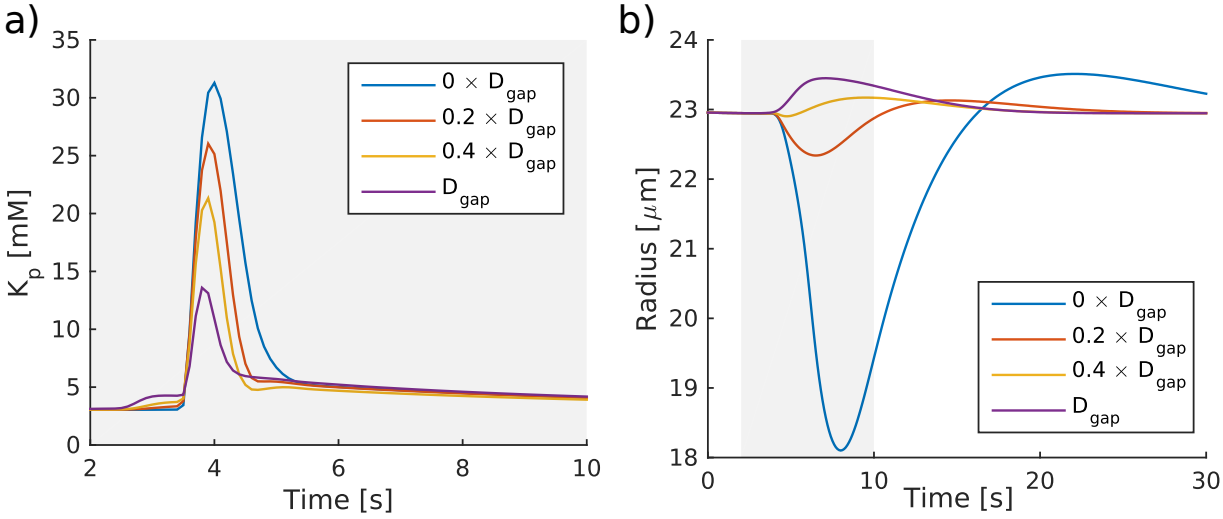


Figure 35: Wave profiles outside the stimulated area for different astrocytic gap junction densities (0%, 20%, 40% and 100% of $D_{gap}$), taken from block 240 in the tissue slice. Increasing the density results in lower $K_p$ and hence reduced vasoconstriction, and for densities over 40% of $D_{gap}$ the radius undergoes vasodilation. a) perivascular $K^+$ concentration $K_p$ in mM, b) vessel radius in µm.

## 6.4 DISCUSSION

The model of a NVU described by Mathias et al. [121] has been implemented on the macro scale via a 2D cerebral tissue slice coupled to a vascular tree. In particular, further communication within the tissue slice has been implemented via extracellular ion electrodiffusion and astrocytic gap junctions. This state of the art model is able to simulate spatial phenomena such as CSD and astrocytic spatial buffering in a 2D tissue slice while also containing the full complex dynamics and multiple pathways of the NVU.

Under pathological conditions the model shows that with extracellular electrodiffusion the medium (i.e. the ECS) is excitable and able to sustain a propagating $K^+$ wave that travels at approximately 6.7 mm $min^{-1}$ (based on block length of 124 µm); experiments generally show a velocity of around $1 - 10$ mm $min^{-1}$ [18] and the model estimate is considered within the bounds of experimental uncertainty. When using normal Fickian diffusion rather than electrodiffusion in the ECS, the medium is subexcitable and the wave of extracellular $K^+$ is not able to travel further than two blocks in the tissue slice. This result still holds when both the stimulation area and duration are increased (results not shown).

In the model, during CSD a rise in extracellular $K^+$ concentration is observed and the vessel radius undergoes vasoconstriction followed by slight vasodilation in the absence of an astrocytic gap junction network. These results can be compared with the work of Chang et al. [26] who utilised a simpler model containing a neuron, ECS and the vessel radius dynamics but did not include the astrocyte, SMC or endothelial cell (EC) compartments. They observed qualitatively similar results, namely a rise in extracellular $K^+$ with vasoconstriction followed by vasodilation. The majority of CSD models do not consider the vascular dynamics so it is difficult to compare the results with a variety of other numerical models, however numerous experimental studies [72, 123, 53, 22, 113] have documented that small increases in extracellular $K^+$ concentration can lead to vasodilation and high concentrations lead to vasoconstriction further supporting the results presented in this chapter.

Pathologies such as CSD can occur when the regulation of $K^+$ via astrocytic gap junctions fails [165]. The model results support this fact, showing that when gap junctions are not present a neuronal stimulus during pathological conditions leads to vasoconstriction in both the stimulated area and in the area surrounding it via a propagating wave, with a corresponding decrease in blood flow through the vascular tree. The vasoconstrictive wave peaks after the extracellular $K^+$ wave due to the delayed vascular response. However with astrocytic gap junctions the vasoconstrictive behaviour is unable to spread, instead inducing slight vasodilation outside the stimulation area (although the extracellular $K^+$ still propagates as with the case without gap junctions) and the constriction remains localised. In addition the gap junctions are able to reduce the size of the initial area that is negatively affected by vasoconstriction by transporting astrocytic $K^+$ outwards.

CSD is said to trigger when a minimum critical volume of brain tissue is stimulated simultaneously so that extracellular $K^+$ levels exceed a critical threshold (experimentally found to be $\sim 12$ mM and given as 10.2 mM in the model). Experiments *in vivo* estimate this minimum critical volume as $\sim 1$ mm$^3$, although this volume is smaller in cortical slices *in vitro* [6]. In the model the minimum area needed to initiate a propagating wave is $4 \times 4$ NVU blocks corresponding to approximately $0.5 \times 0.5$ mm (results not shown), but as the model is only two dimensional a corresponding volume cannot be calculated to compare directly with experiments.

CSD can be initiated experimentally by a number of methods: chemically, via direct application of depolarising substances such as concentrated KCl or NMDA glutamate receptor agonists; electrically, via direct tissue stimulation; or mechanically via pinprick, ultrasound or laser [6]. In the model a wave of high extracellular $K^+$ concentration is observed travelling outwards from the

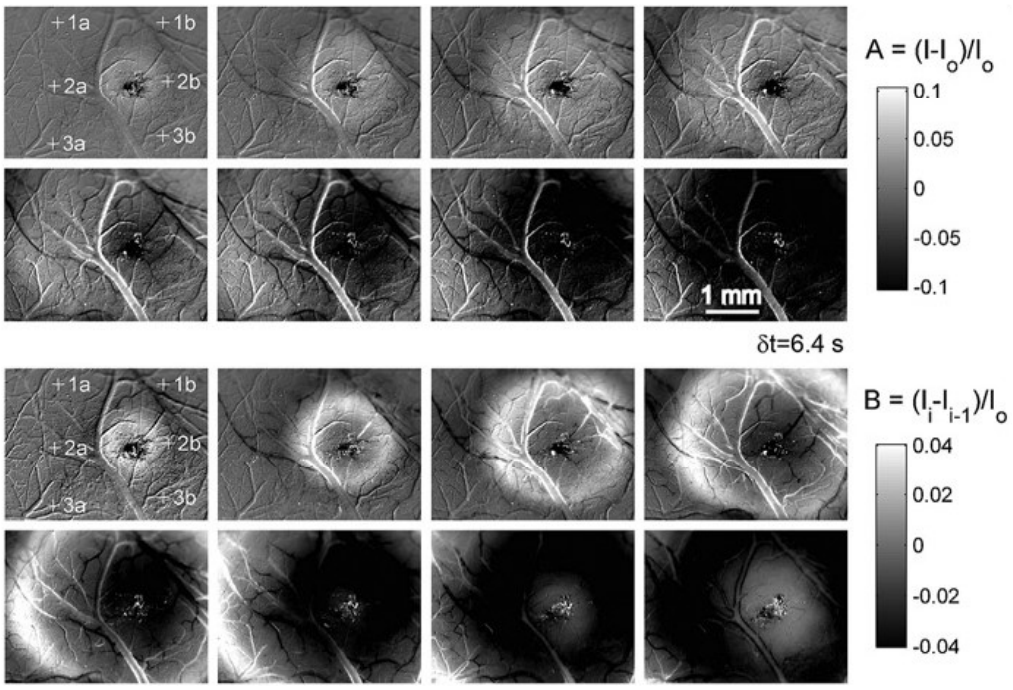


Figure 36: Experimental *in vivo* results of Chen et al. [30] during pinprick induced CSD in a rat cortex. They observed similar behaviour to that found in the model simulations, where a wave of increased reflectance corresponding to decreased perfusion propagated radially outward from the point of origin, followed by widespread decreased reflectance corresponding to increased perfusion. This wave travelled at approximately 5 mm $min^{-1}$ which compares well with the velocity of 6.7 mm $min^{-1}$ found in the model simulations. A: relative reflectance, B: rate of change in reflectance. Modified from Chen et al. [30].

stimulation area which induces vasoconstriction (followed by slight vasodilation) in and around the stimulation area. This behaviour agrees with the experiment performed by Chen et al. [30] as seen in Figure 36. They used optical reflectance imaging to obtain high resolution images of CSD waves based on changes in blood perfusion. A normal rat cortex was induced by a pinprick, resulting in a wave of decreased perfusion (i.e. vasoconstriction) that propagated radially outward from the point of origin regardless of functional or vascular territories. This was followed by hyperperfusion (i.e. vasodilation) then a slow return to normal values. The wave travelled at approximately 5 mm $min^{-1}$ which is comparable with the velocity of 6.7 mm $min^{-1}$ found in the model simulations. Similar results were found in the experiment of Tomita et al. [161] who induced CSD via a concentrated potassium chloride (KCl) solution microinjected into both rat and cat cortex.

Experiments show that CSD propagation can be slowed or interrupted by pre-existing lesions or areas of high astrocytic density [30], and reduced expression of astrocytic gap junctions significantly increases the size of ischemic infarcts [131]. By decreasing the gap junction diffusion rate $D_{gap}$ to 20% of its original value (in order to simulate reduced gap junction density) a propagating wave of slight vasoconstriction is observed shortly followed by slight vasodilation, whereas

with $D_{gap}$ reduced to 40% of its original value only slight vasodilation is observed. This suggests that increasing astrocytic density or gap junction expression reduces the duration of the vasoconstrictive wave prior to vasodilation, and for high enough density (over 40%) the vasoconstrictive behaviour outside of the stimulation area is eliminated.

By increasing the extracellular electrodiffusion rates $D_{K,e}$ and $D_{Na,e}$ the velocity and wave width of the propagating $K^+$ wavefront also increase, as the area in front of the wave takes less time to reach the excitation threshold. Whereas decreasing the diffusion rates by 5% produced a propagating $K^+$ wave that is subexcitable and dies after propagating through a few blocks. Decreasing the diffusion rates further resulted in a nonexcitable medium where an extracellular $K^+$ wave could not propagate at all (results not shown).

## 6.5 CONCLUSIONS

In this chapter, a large scale numerical NVC model of a vascular tree coupled with multiple NVUs comprising a two-dimensional cerebral tissue slice is extended through extracellular $K^+$ and $Na^+$ electrodiffusion and $K^+$ transport via astrocytic gap junctions. An updated NVU model has been utilised that contains complex neuronal and extracellular dynamics and is able to simulate various pathologies such as CSD.

Under pathological conditions (determined by model parameters) and with extracellular electrodiffusion the model is able to simulate a propagating wave of high extracellular $K^+$ travelling at 6.7 mm $min^{-1}$ as can occur in CSD. This wave travels outward from the neuronally stimulated area and is followed by a wave of vasoconstriction (with corresponding decreased blood flow) then slight vasodilation in agreement with multiple experimental results. The vasoconstrictive wave peaks after the $K^+$ wave due to the delayed vascular response. Increasing the density of astrocytic gap junctions reduces the duration of the vasoconstrictive wave and for high enough density the vasoconstrictive behaviour outside the stimulated area is eliminated. Gap junctions also reduce the area that is initially affected by vasoconstriction. This *in silico* model provides a complex and experimentally validated test bed for a variety of neurological phenomena.

# 7

# THE EFFECTS OF CEREBRAL CURVATURE ON CORTICAL SPREADING DEPRESSION

The cerebral cortex of a human is gyrencephalic (composed of tightly folded grey matter), where the outer ridges are known as "gyri" and the depressions or furrows are known as "sulci". Consequently the human cortex contains areas of both strongly negative and positive Gaussian curvature as seen in Figure 37. This is in contrast to a lissencephalic brain which is smooth with very little spatial variation in curvature as found in murine animals. The effective extracellular diffusion rate of various ions and molecules can change depending on the curvature of the medium; areas of negative Gaussian curvature have a higher effective diffusion rate, whereas areas of positive Gaussian curvature have a lower diffusion rate [108, 102]. This may have an effect on the propagation of cortical spreading depression (CSD) waves.

There have been multiple experiments performed on animals with lissencephalic brains (usually murine or feline) where CSD waves are observed to spread radially outwards from a stimulated area [29, 161]. However details on how CSD travels through the gyrencephalic brain such as in a human are not well known; this is considered an important question particularly in migraine research [27]. Indeed, in contrast to radial waves found in murine experiments, it has been suggested that CSD can propagate as a localised wave segment in the human cortex (see Figure 38) [38, 37, 39, 153].

Kenny et al. [102] investigated the effect of curvature on the simple reaction diffusion model of Goldbeter et al. [71]. This model was applied on a torus, a surface with areas of both positive and negative curvature. On a flat surface the only wave solutions are either radial waves or subexcitable wave segments that shrink in length until they cease. However on a curved surface Kenny et al. [102] found a new wave solution in the form of a stable wave segment which could propagate on the inside of the torus (negatively curved surface). They also found that open wave ends produced spiral patterns, a phenomenon often witnessed in excitable media [77, 100, 178].

Dahlem et al. [40] investigated so called cortical "hot spot" and labyrinths, areas of initiation and propagation pathways respectively. They used a generic reaction diffusion model applied to a

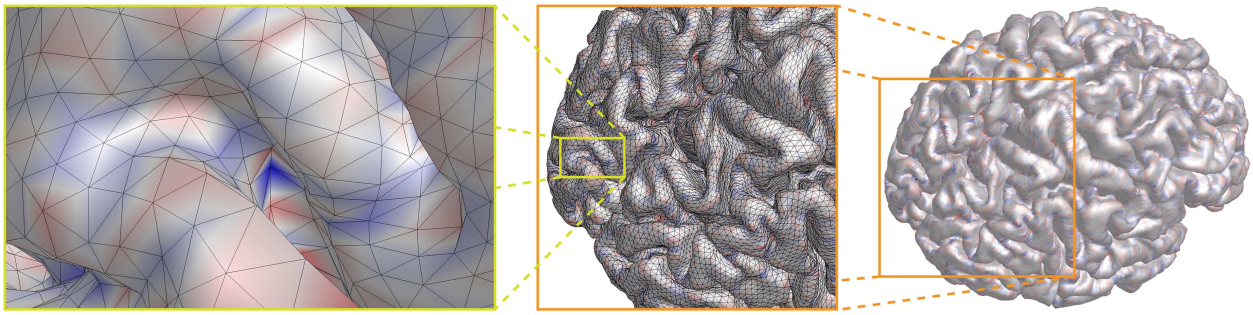

Figure 37: Gaussian curvature on a cortical surface, where red indicates positive curvature and blue indicates negative curvature. Areas of strongly negative curvature can be seen deep in the folds (sulci) of the cortex. Adapted from Dahlem et al. [40].

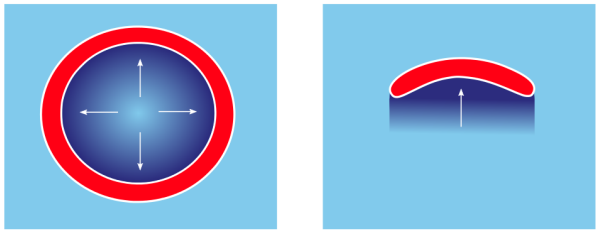

(a) Radial wave (b) Wave segment

Figure 38: Different wave profiles that may occur in reaction-diffusion systems, where red corresponds to the excitation wave and dark blue corresponds to the refractory area.

surface with Gaussian curvature taken from functional magnetic resonance imaging (fMRI) scans, and found that areas of strongly negative curvature (see Figure 37) were likely nucleation sites for CSD waves. However the model they utilised contained only two variables and hence were unable to analyse certain aspects of CSD such as the vascular response.

fMRI is a widely used non-invasive imaging technique, the most common form of which uses the blood-oxygen-level dependent (BOLD) response where changes in blood oxygen ($O_2$) levels can be detected [136]. This technique relies on the fact that, under normal circumstances, brain activity is closely followed by a localised increase in blood flow (i.e. neurovascular coupling (NVC)). Increases in blood flow due to increased neural activity cause a decrease in the levels of deoxyhemoglobin, where hemoglobin is the iron-containing protein that transports $O_2$ in red blood cells. These proteins can then be detected as deoxyhemoglobin is paramagnetic (weakly attracted to magnetic fields). The NVC mechanism, the cerebral metabolic rate of $O_2$ consumption, and the cerebral blood flow (CBF) are all known to contribute to the BOLD response [19].

A complex numerical model of a single neurovascular unit (NVU) has been implemented on the macro scale as described in Chapter 6 by embedding multiple NVUs in a two dimensional (2D) tissue slice. Each NVU was coupled to its nearest four neighbours by extracellular ion electrodiffusion and globally coupled via a space filling binary H-tree simulating a perfusing arterial tree

(vasculature). This lumped parameter model contains compartments for each cell in the NVU and is based on ion exchange with experimentally validated ion channel parameters. The model is able to simulate spatial phenomena such as CSD in a tissue slice while also containing the complex dynamics of the NVU such as the vascular response [104] and in particular the BOLD response implemented using the model of Mathias et al. [121] (see Chapter 5).

In this chapter, the numerical model from Chapter 6 has been extended to include a cerebral Gaussian curvature mapping simulating spatial variation in curvature over a tissue slice [103]. To do so it is assumed each NVU block of the tissue slice is approximated by a portion of a torus, either the inner (negatively curved) or outer area (positively curved), which together comprise a surface of spatially varying curvature. The curvature of a toroidal section can then be directly correlated to the rate of diffusion using an isothermal toroidal coordinate system. The spatial variation in curvature will affect the rate of extracellular diffusion which in turn will affect the initiation, propagation and cessation of extracellular potassium ($K^+$) waves in CSD.

## 7.1 METHOD

### 7.1.1 *Curvature on a torus*

The Gaussian curvature is the product of the two principal curvatures at a given point; if the principal curvatures are in the same direction then the Gaussian curvature is positive, if they are in opposite directions then the Gaussian curvature is negative, and if at least one of the principal curvatures is zero then the Gaussian curvature is zero. To incorporate spatial variation in curvature in the tissue slice model each NVU block is approximated by a section of a torus with a specific Gaussian curvature and diffusion rate, as to a certain degree sections of a torus can approximate the hills and valleys of cortical gyri and sulci [40]. A visualisation of a torus is shown in Figure 39.

A brief review of the properties of a torus is presented here. The surface of a torus in the Euclidean space $\mathbb{R}^3$ can be parameterised by coordinates $(\theta, \varphi)$ as follows:

$$(\theta, \varphi) \mapsto \begin{pmatrix} r(n + \cos\theta)\cos\varphi \\ r(n + \cos\theta)\sin\varphi \\ r\sin\theta \end{pmatrix} = \begin{pmatrix} x \\ y \\ z \end{pmatrix}, \tag{7.1}$$

where $\theta, \varphi \in [0, 2\pi)$ and $n = \frac{R}{r}$ is the ratio of the major ($R$) and minor ($r$) curvature radii. The outside of the torus corresponds to $\theta = 0$ and the inside corresponds to $\theta = \pi$. The Gaussian curvature at a point $(\theta, \varphi)$ on a torus surface is solely a function of $\theta$:

$$\Gamma(\theta) = \frac{\cos\theta}{r^2(n + \cos\theta)} \tag{7.2}$$

and is positive on the outside of a torus $(\theta = 0)$ and negative on the inside of a torus $(\theta = \pi)$.

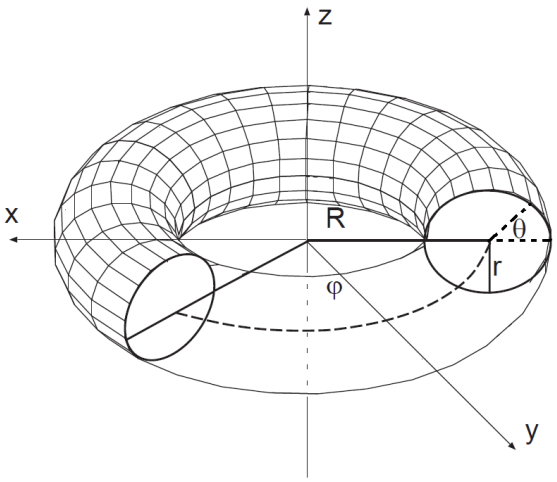


Figure 39: Visualisation of a torus in $\mathbb{R}^3$ with coordinates $(\theta, \varphi)$, where $R$ and $r$ are the major and minor curvature radii [108].

In addition to the coordinates $(\theta, \varphi)$ a torus can also be parameterised by a global isothermal coordinate system referred to as toroidal coordinates $(\tilde{\theta}, \tilde{\varphi})$ where the metric is locally conformal to the Euclidean metric. A full derivation of toroidal coordinates can be found in the work of Kneer et al. [108]. These coordinates are defined as

$$(\tilde{\theta}, \tilde{\varphi}) \mapsto \begin{pmatrix} \dfrac{a \sinh\eta \cos\left(\dfrac{\tilde{\varphi}}{\sinh\eta}\right)}{\cosh\eta - \cos\tilde{\theta}} \\ \dfrac{a \sinh\eta \sin\left(\dfrac{\tilde{\varphi}}{\sinh\eta}\right)}{\cosh\eta - \cos\tilde{\theta}} \\ \dfrac{a \sinh\tilde{\theta}}{\cosh\eta - \cos\tilde{\theta}} \end{pmatrix} = \begin{pmatrix} x \\ y \\ z \end{pmatrix}, \tag{7.3}$$

with

$$a = r\sqrt{n^2 - 1} \tag{7.4}$$

$$\eta = \tanh^{-1}\left(\frac{\sqrt{n^2-1}}{n}\right). \tag{7.5}$$

The coordinate system can also be defined in terms of $(\theta, \varphi)$:

$$\tilde{\theta}(\theta) = \cos^{-1}\left(n - \frac{a^2}{r^2(n + \cos\theta)}\right) \tag{7.6}$$

$$\tilde{\varphi}(\varphi) = \varphi \sinh\eta, \tag{7.7}$$

where both $\tilde{\theta}$ and $\tilde{\varphi}$ are monotonically increasing with $\theta$ and $\varphi$ respectively. In particular, $\tilde{\theta} = 0$ when $\theta = 0$ and $\tilde{\theta} = \pi$ when $\theta = \pi$, i.e. $\tilde{\theta} = 0$ still corresponds to the outside of the torus and $\tilde{\theta} = \pi$ to the inside of the torus. Using Eq. (7.2) and (7.6) the Gaussian curvature can be rewritten in terms of toroidal coordinates:

$$\Gamma(\tilde{\theta}) = \frac{1}{r^2} - \frac{n(n - \cos\tilde{\theta})}{a^2}, \tag{7.8}$$

where the curvature is shown in Figure 40a and is monotonically decreasing with respect to $\tilde{\theta}$.

It can be shown that by using these coordinates the surface of a torus may be mathematically interpreted as a flat medium with a spatial coupling dependent only on $\tilde{\theta}$. For an orthogonal parameterisation $f : \{\alpha^i\} \mapsto \{x^k\}$, the gradient of a scalar field $u$ is given by

$$\nabla u = \frac{1}{h_1}\frac{\partial u}{\partial \alpha^1}\hat{\mathbf{e}}_1 + \frac{1}{h_2}\frac{\partial u}{\partial \alpha^2}\hat{\mathbf{e}}_2, \tag{7.9}$$

where $h_i$ is the scale factor given by $\sqrt{g_{ii}}$, G is the metric tensor with matrix elements $g_{ij}$ which is the product of the transposed Jacobian matrix of $f$ multiplied by the Jacobian of $f$, and $\hat{\mathbf{e}}_i$ is a normalised basis vector. Note that for an orthogonal coordinate system, $g_{ij} = 0$ for $i \neq j$, and for a conformal mapping, $g_{ii} = g_{jj}$ for all $i$ and $j$. Then the gradient operator for an isothermal (meaning orthogonal and conformal) coordinate system is given by

$$\nabla u = \frac{1}{h}\left(\frac{\partial u}{\partial \alpha^1}\hat{\mathbf{e}}_1 + \frac{\partial u}{\partial \alpha^2}\hat{\mathbf{e}}_2\right), \tag{7.10}$$

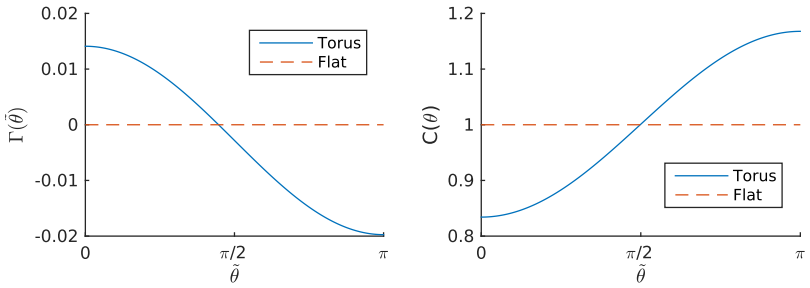


(a) Gaussian curvature $\Gamma$ (b) Diffusive coupling rate $C$

Figure 40: Properties of a torus with minor radius $r = \frac{20}{2\pi}$ and ratio $n = \frac{R}{r} = 6$ compared with a flat surface. a) Gaussian curvature $\Gamma(\tilde{\theta})$ decreases from $\tilde{\theta} = 0$ (outside of torus) to $\tilde{\theta} = \pi$ (inside of torus), b) Diffusive coupling $C(\tilde{\theta})$ increases from $\tilde{\theta} = 0$ to $\tilde{\theta} = \pi$.

where $h = \sqrt{g_{ii}} = \sqrt{g_{jj}}$ is the general scale factor. As shown by Kneer et al. [108], the general scale factor for isothermal toroidal coordinates is

$$h = \sqrt{g_{\tilde{\theta}\tilde{\theta}}} = \sqrt{g_{\tilde{\varphi}\tilde{\varphi}}} \tag{7.11}$$

$$= \frac{a}{\cosh\eta - \cos\tilde{\theta}}. \tag{7.12}$$

Introducing a coupling term $C = \frac{1}{h}$ the gradient of some variable $u$ in toroidal coordinates is given by

$$\nabla u = C\left(\frac{\partial u}{\partial \tilde{\theta}}\hat{\mathbf{e}}_{\tilde{\theta}} + \frac{\partial u}{\partial \tilde{\varphi}}\hat{\mathbf{e}}_{\tilde{\varphi}}\right). \tag{7.13}$$

This is effectively the gradient in Euclidean geometry (i.e. a flat surface) multiplied by a scaling term $C$ given by

$$C(\tilde{\theta}) = \frac{\cosh\eta - \cos\tilde{\theta}}{a}. \tag{7.14}$$

Figure 40b shows that $C(\tilde{\theta})$ is lowest on the outside of the torus ($\tilde{\theta} = 0$) and largest on the inside of the torus ($\tilde{\theta} = \pi$). Using Eq. (7.8) and (7.14) a relationship can be obtained between the Gaussian curvature $\Gamma$ and the coupling term $C$:

$$C(\Gamma) = \frac{\cosh\eta - n}{a} + \frac{a}{n}\left(\frac{1}{r^2} - \Gamma\right) \tag{7.15}$$

which shows that the spatial coupling $C$ decreases as Gaussian curvature $\Gamma$ becomes more positive; in particular, $C < 1$ when $\Gamma > 0$ and $C > 1$ when $\Gamma < 0$.

### 7.1.2 *Electrodiffusive flux on a curved surface*

Recall from Chapter 6 that the electrodiffusive flux of some extracellular ion concentration $c$ is given by

$$J_c = -D_c \left[ \nabla c - z_c c \left( \frac{\sum_n z_n D_n \nabla n}{\sum_n z_n^2 D_n n} \right) \right] \tag{7.16}$$

where $n \in \{K^+, Na^+\}$. Considering the extracellular flux on a curved surface with coordinates conformal to $(\tilde{\theta}, \tilde{\varphi})$, the gradient terms $\nabla c$ and $\nabla n$ can be written in terms of $C$ as in Eq. (7.13). The flux can be simplified for an assumed linear gradient (i.e. between two cells) by replacing the differential terms with ratios of differences and the concentration $c$ by the mean concentration of two adjacent cells $i$ and $j$ [70], giving the flux $J^e_{c,i\to j}$ of ion concentration $c$ due to extracellular diffusion from compartment $i$ to $j$:

$$J^e_{c,i\to j} = -\frac{C}{\Delta x} D_c \left[ (c_j - c_i) - z_c \left( \frac{c_i + c_j}{2} \right) \left( \frac{\sum_n z_n D_n (n_j - n_i)}{\sum_n z_n^2 D_n \frac{n_i + n_j}{2}} \right) \right]. \tag{7.17}$$

where $\Delta x = 124$ μm is the unit distance between the centres of two NVU blocks on a flat surface. This distance is scaled with the curvature, so that two points on a positive curved surface with $C < 1$ will be farther apart than on a flat surface giving a larger distance $\Delta x/C$ between two compartments. The reverse is true for a negatively curved surface with $C > 1$. This means that electrodiffusive fluxes on a negatively curved surface will be greater in magnitude than on a flat surface due to increased coupling $C$, and smaller in magnitude for a positively curved surface.

This can also be seen by calculating the unit surface area element, i.e. the area $dA$ of a toroidal patch defined by $d\tilde{\theta}$ and $d\tilde{\varphi}$. This is found through the following equation using Lagrange's identity:

$$dA = \sqrt{g_{\tilde{\theta}\tilde{\theta}} g_{\tilde{\varphi}\tilde{\varphi}} - g^2_{\tilde{\theta}\tilde{\varphi}}}\, d\tilde{\theta} d\tilde{\varphi} \tag{7.18}$$

$$= \frac{1}{C^2} d\tilde{\theta} d\tilde{\varphi}, \tag{7.19}$$

as $g_{\tilde{\theta}\tilde{\varphi}} = 0$ and $g_{\tilde{\theta}\tilde{\theta}} = g_{\tilde{\varphi}\tilde{\varphi}} = 1/C^2$ from the work of Kneer et al. [108]. This means that for a surface with $C < 1$ (i.e. positively curved) the area of a unit patch will be smaller than on a flat

surface, whereas for a surface with $C > 1$ (i.e. negatively curved) the area will be larger; in other words, the width $dx$ of a unit patch is scaled by a factor of $1/C$.

### 7.1.3 *Effect on the tissue slice model*

In the model, each NVU block of the cortical tissue slice with coordinates $(X, Y)$ is considered locally conformal to the toroidal coordinate system $(\tilde{\theta}, \tilde{\varphi})$ for some section of a torus. This is schematically shown in Figure 41. The $(X, Y)$ coordinates give the centre of a NVU block and are taken as the non-dimensional distance (in terms of blocks) from the centre of the tissue slice. Areas of strongly negative curvature such as the deep folds on the cortex can be approximated by a section of the inner surface of a torus with $\tilde{\theta}$ near $\pi$ (see Figure 39), whereas areas of positive curvature such as the outer areas of the cortex can be approximated by the outer surface of a torus with $\tilde{\theta}$ near $0$. In the following simulations a torus of $r = \frac{20}{2\pi}$ and $n = 6$ is used unless specified otherwise (where decreasing the ratio $n$ would produce a more strongly curved surface).

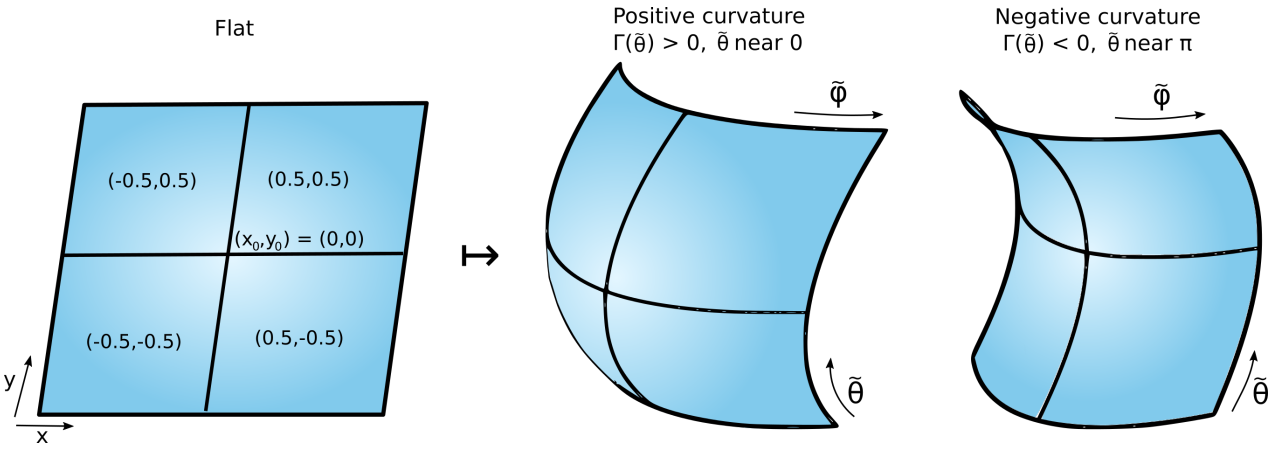


Figure 41: Each NVU block of the large scale tissue slice with coordinates $(X, Y)$ is mapped to a section of a torus with toroidal coordinates $(\tilde{\theta}, \tilde{\varphi})$. The $(X, Y)$ coordinates are given as the distance (in terms of NVU blocks) from the centre of the tissue slice. $\tilde{\theta}$ near $0$ corresponds to the outside of a torus with positive curvature whereas $\tilde{\theta}$ near $\pi$ corresponds to the inside of a torus with negative curvature. The variable $\tilde{\varphi}$ has no effect on the curvature.

To simulate the spatially varied curvature of the cortex in the tissue slice model the $(X, Y)$ coordinates of each NVU are mapped to some $\tilde{\theta}$, i.e. $\tilde{\theta} = \tilde{\theta}(X, Y)$. This will produce a spatial variation in both Gaussian curvature $\Gamma(\tilde{\theta})$ and diffusive coupling rate $C(\tilde{\theta})$, which will in turn affect the magnitude of the electrodiffusive fluxes between the extracellular space of adjacent NVUs. Note that the variable $\tilde{\varphi}$ has no effect on $\Gamma(\tilde{\theta})$ or $C(\tilde{\theta})$ making it irrelevant to the simulations.

Assuming that the area of interface between adjacent blocks is $\Delta x^2$, the rate of change of ion concentration in block $i$ as a result of the gap junction flux to block $j$ is given by $\frac{J_{i\to j} \times \Delta x^2}{\Delta x^3} = \frac{J_{i\to j}}{\Delta x}$,

where $\Delta x^3$ is the volume of the block. Then the total rates of change Q of $K^+$ and $Na^+$ due to the sum of diffusive ion fluxes J into the extracellular space (ECS) of block $i$ with coordinates $(X_i, Y_i)$ and corresponding $\tilde{\theta}_i(X_i, Y_i)$ are given by

$$Q_{K_e,i} = -\frac{C}{\Delta x} \sum_j J^e_{K,i\to j} \tag{7.20}$$

$$Q_{Na_e,i} = -\frac{C}{\Delta x} \sum_j J^e_{Na,i\to j} \tag{7.21}$$

as detailed in Chapter 6, where the sum takes into account each neighbour $j$ of block $i$. Note that the rates of change are effectively scaled by a factor of $C^2$, as the unit distance $\Delta x$ is scaled by a factor of $1/C$ both within the flux J equations (Eq. 7.17) and in the rate of change equations (Eq. 7.20, 7.21). These rates of change are added to the conservation equations in NVU block $i$ for extracellular $K^+$ concentration $K_e$ and $Na^+$ concentration $Na_e$ respectively.

### 7.1.4 *Implementation*

The macro scale tissue slice model has been designed to run on parallel architectures and is discussed in detail in Section 3.2.3 of Chapter 3. The simulated tissue slice is split into rectangular domains with each domain corresponding to a single computational node, whereas the H-tree is partitioned into subtrees with a root subtree. The system is solved using a C implementation of a fixed-step Backward Euler method with Newton iteration due to stiffness.

Message Passing Interface (MPI) is used for the communication between tissue blocks in a multi-core architecture. For the implementation of extracellular diffusion and gap junction communication, at each time step the state variables from the blocks along the edges of the domains are passed to the adjacent blocks in the neighbouring domain. Communication between domains and the corresponding boundary conditions enforcement within a single domain is implemented following the mesh ghost block communication pattern [78].

The system used was a 56 core Intel Xeon E5-4660 v3 server with 128 GB of memory and clock speed of 2.10 GHz. The numerical simulations were executed on 32 cores. For the simulations shown in Sections 7.2.2 and 7.2.3, each iteration corresponding to one physiological second took approximately 2 minutes of wall clock time to complete. For the larger simulations shown in Section 7.2.4 each iteration took approximately 4 minutes of wall clock time to complete.

## 7.2 RESULTS

### 7.2.1 *Dynamics and excitability of the NVU model*

A brief review is presented here of the excitability of the extracellular $K^+$ ($K_e$) dynamics that allows for wave propagation, as well as the effect on the vascular dynamics. For a thorough explanation see Section 6.3.1 of Chapter 6. Note that in Chapter 6 the effect of an astrocytic gap junction network was investigated, however in this chapter it is assumed that this network is dysfunctional due to the pathological conditions which promote CSD.

If a section of the tissue slice is stimulated by a current input under pathological conditions, this leads to neuronal depolarisation and an efflux of $K^+$ from the neuron into the surrounding ECS. When $K^+$ in the ECS reaches the threshold of 10.2 mM it undergoes a rapid increase up to $70-80$ mM followed by a decrease below baseline ($\sim$ 2 mM) and slow rise back to baseline ($\sim$ 3.5 mM) over approximately 40 seconds. This drop below baseline is known as the refractory period and is the reason why waves are not able to travel backwards, and why $K_e$ waves are followed by a trail of decreased $K_e$. In the model $K^+$ waves are able to propagate due to $K^+$ electrodiffusion between the ECS of neighbouring blocks. If the diffusive flux is large enough then the wave is able to provide enough $K^+$ into neighbouring blocks so that they reach the threshold and undergo a large increase in $K_e$, providing the method of propagation.

The large increase in $K_e$ causes a corresponding increase in synaptic $K^+$ concentration. This $K^+$ is taken up by the astrocyte and extruded into the perivascular space (PVS), where the high concentration reverses the inward rectifying $K^+$ (KIR) channel connecting the PVS and smooth muscle cell (SMC). This results in an influx of $K^+$ into the SMC, depolarising the SMC and opening the voltage operated calcium ($Ca^{2+}$) channels (VOCCs), leading to increased SMC $Ca^{2+}$ concentration and hence vasoconstriction and decreased blood flow. As $K_e$ decreases this induces a corresponding decrease in perivascular $K^+$ concentration, reversing the KIR channel back to its original direction (SMC to PVS), hyperpolarising the SMC and leading to slight vasoconstriction and increased blood flow.

Note that CSD only occurs in the model under pathological conditions where the pump rate of the neuronal $Na^+/K^+$ ATPase pump is decreased (such as during hypoxic conditions), so that less $K^+$ is able to be pumped back into the neuron and $K^+$ is able to accumulate in the ECS. During normal conditions a current input will induce NVC, as the ATPase pump is more active

so the extracellular $K^+$ concentration does not reach such a high level. Instead the lower $K^+$ concentration leads to vasodilation and increased blood flow to the stimulated area but does not propagate outwards.

### 7.2.2 *Surfaces of constant curvature*

In this section a tissue slice is simulated with spatially constant Gaussian curvature $\Gamma$: either negative curvature, positive curvature, or a flat surface. In the following simulations $\tilde{\theta} = 1.2$ is used for positive curvature ($\Gamma = 0.004, C = 0.94$) and $\tilde{\theta} = 2.2$ for negative curvature ($\Gamma = -0.012, C = 1.1$).

A small rectangular area at the bottom of the tissue slice (see Figure 42) is stimulated with an input current ($I_{strength} = 0.006$ mA cm$^{-2}$) in order to see if an outward travelling wave will propagate. Figure 43 shows the results. An outward travelling wave of extracellular $K^+$ ($K_e$) is produced following an input to the bottom of the tissue slice. For a flat or negatively curved surface the wave continues to propagate, travelling at approximately 6.7 mm min$^{-1}$ on a flat surface and approximately 8.5 mm min$^{-1}$ on the negatively curved surface. The wave travels faster when the surface is negatively curved due to increased coupling C and hence larger electrodiffusive $K^+$ flux from block to block. However for a positively curved surface (with spatial coupling $C < 0.95$ corresponding to Gaussian curvature $\Gamma > 0.002$) the magnitude of the electrodiffusive flux is too

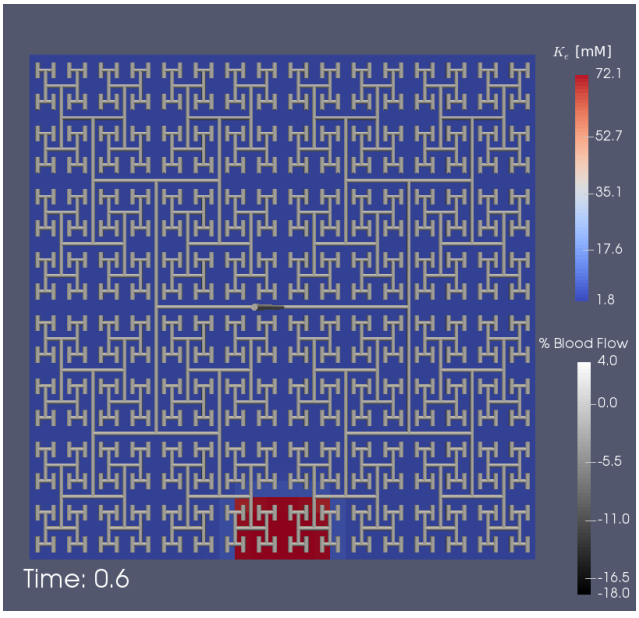


Figure 42: Input stimulus to the bottom of the tissue slice, as an initial condition for the simulations on either a positively curved, negatively curved, or flat surface.

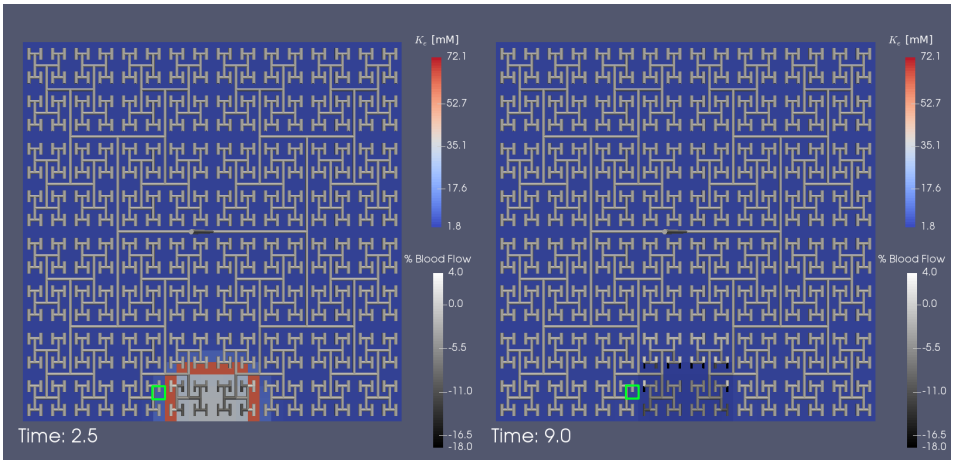


(a) Positive curvature, $\Gamma = 0.004$

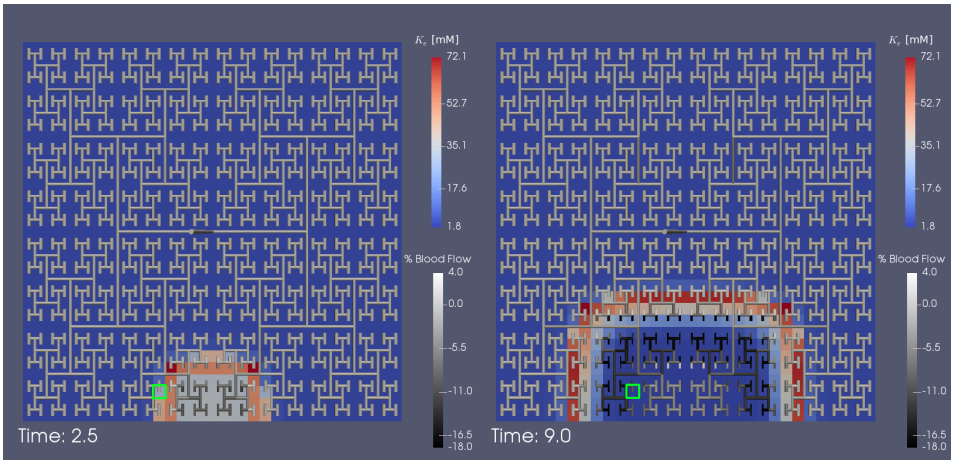


(b) Flat surface, $\Gamma = 0$

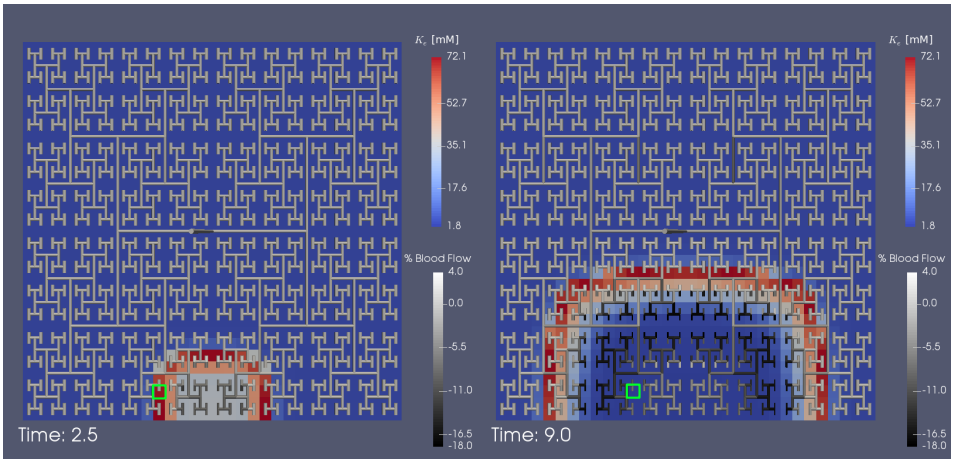


(c) Negative curvature, $\Gamma = -0.012$

Figure 43: Spatially constant Gaussian curvature over the tissue slice with $32 \times 32$ NVUs (11 levels in the H-tree and corresponding to a 4mm $\times$ 4mm tissue slice). An outward travelling wave of extracellular $K^+$ ($K_e$) is produced following an input to the bottom of the tissue slice with a maximum of approximately 70 mM. For a flat or negatively curved surface the wave continues to propagate (travelling faster when more negatively curved due to increased coupling and hence larger electrodiffusive $K^+$ flux from block to block), but for a positively curved surface (with spatial coupling $C < 0.95$ corresponding to Gaussian curvature $\Gamma > 0.002$) the magnitude of the electrodiffusive flux is too low to allow a propagating wave. The decrease in blood flow of approximately 18% follows the peak of the $K_e$ wave due to the delayed vascular response. Videos available online (https://youtu.be/WuqfPTU5Vhg, https://youtu.be/pkVdOOEi6e8, https://youtu.be/X6C2WbPCR_o)

low to allow a propagating wave. The decrease in blood flow below the baseline follows the $K_e$ wave due to the delayed vascular response.

The $K_e$ and blood flow profiles for a selected block near to the stimulated area (highlighted in green in Figure 43, given by coordinates $(X, Y) = (-5.5, -14.5)$) are shown in Figure 44. For a flat or negatively curved surface ($\Gamma < 0.002$) $K_e$ reaches the threshold of 10.2 mM and quickly rises to approximately 70 mM. The surface with negative curvature has greater diffusive flux due to higher spatial coupling C, so the $K_e$ in the highlighted block rises faster and reaches a slightly higher peak compared to a flat surface. The large increase in $K_e$ induces vasoconstriction and decreased blood flow below baseline of approximately 18%, followed by slight vasodilation and increased blood flow above baseline of approximately 2%. However for a positively curved surface ($\Gamma > 0.002$) the diffusive flux of $K^+$ into the highlighted block is not enough to reach the critical threshold, and the small increase in $K_e$ is not enough to induce any significant change in blood flow.

In addition to extracellular $K^+$ concentration and blood flow, the BOLD response can be examined within the tissue slice. The BOLD response decreases with increased deoxyhemoglobin (HbR) levels and $O_2$ consumption, and increases with increased CBF (see Chapter 5 for further details). Following increased neural activity in the brain during pathological conditions, the cerebral metabolic rate of $O_2$ consumption ($CMRO_2$) increases while the blood flow decreases [62]. Because the local blood is less oxygenated, there is more HbR present which gives a negative change in BOLD signal. In contrast, during non-pathological conditions the blood flow increases following neural stimulation which outweighs the neuronal $O_2$ consumption, and the change in BOLD signal is positive (generally $2-4\%$ above baseline).

Figure 45 shows the percentage change from baseline of the BOLD response in a tissue slice with spatially constant curvature (corresponding to the simulations shown in Figure 43), and the time series for a selected block in the tissue slice (highlighted in green) for negative, positive and zero curvature. The BOLD response decreases with increased $O_2$ consumption in the neuron and with decreased blood flow (both occurring during the CSD wave). For a flat or negatively curved surface ($\Gamma < 0.002$) the BOLD response decreases down to 10.3% below baseline. The BOLD response then undergoes a slight increase of 1% as the vessel radius dilates with a slow return to baseline. The wave of decreased BOLD is concurrent with the vasoconstrictive wave. For a positively curved surface, there is not enough $K^+$ in the highlighted block to induce a propagating CSD wave and

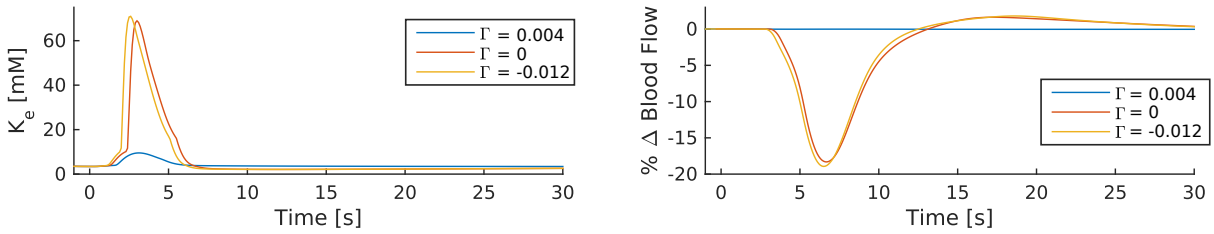


(a) Extracellular $K^+$ concentration $K_e$ (b) Percentage change in blood flow

Figure 44: Extracellular $K^+$ concentration $K_e$ and the change in blood flow for the block highlighted in green in Figure 43, for spatially constant positive, negative and zero Gaussian curvature Γ. a) For a flat or negatively curved surface ($\Gamma < 0.002$) $K_e$ reaches the threshold of 10.2 mM and quickly rises to around 70 mM. The surface with negative curvature has greater diffusive flux due to higher spatial coupling C, so the $K_e$ in the highlighted block rises faster and reaches a slightly higher peak than on a flat surface. However for a positively curved surface ($\Gamma > 0.002$) the diffusive flux of $K^+$ into the highlighted block is not enough to reach the critical threshold. b) For a flat or negatively curved surface the large increase in $K_e$ induces vasoconstriction and decreased blood flow of approximately 18%. This is followed by slight vasodilation and increased blood flow of approximately 2%. For a positively curved surface the small increase in $K_e$ is not enough to induce any significant change in blood flow.

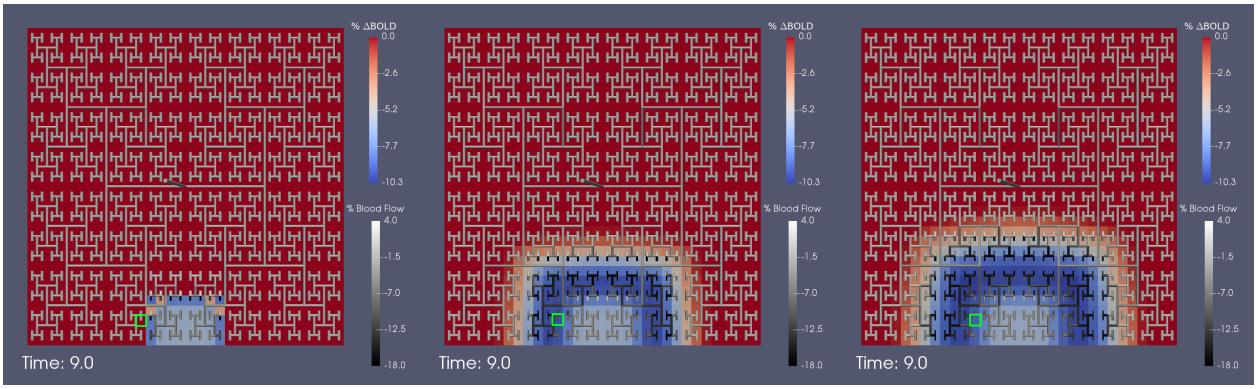


(a) Positive curvature, $\Gamma = 0.004$ (b) Flat surface, $\Gamma = 0$ (c) Negative curvature, $\Gamma = -0.012$

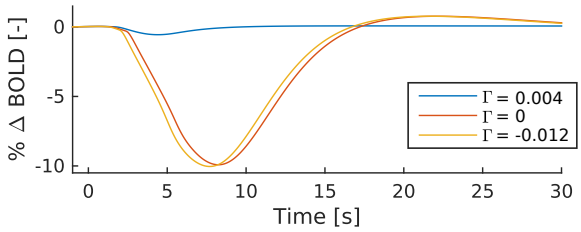


(d) Percentage change in BOLD response

Figure 45: a-c) The BOLD response for a tissue slice with $32 \times 32$ NVUs and spatially constant positive, negative and zero Gaussian curvature Γ, and d) the BOLD response for the block highlighted in green. The BOLD response decreases with increased $O_2$ consumption in the neuron and with decreased blood flow (both occurring during the CSD wave). For a flat or negatively curved surface ($\Gamma < 0.002$) the BOLD response decreases with a maximum decrease of 10.3% below baseline. The BOLD response then undergoes a slight increase of 1% as the vessel radius dilates with a slow return to baseline. The wave of decreased BOLD is concurrent with the vasoconstrictive wave. For a positively curved surface, there is not enough $K^+$ in the highlighted block to induce a propagating CSD wave and vasoconstriction so there is only a minor decrease in BOLD from the $O_2$ consumption in the neuron. Videos available online (https://youtu.be/WuqfPTU5Vhg,https://youtu.be/pkVdOOEi6e8,https://youtu.be/X6C2WbPCR_o)

vasoconstriction so there is only a minor decrease in BOLD from the $O_2$ consumption in the neuron.

### 7.2.3 *Simulating cortical sulci (folds)*

In this section a simple mapping is utilised with $\tilde{\theta}$ varying as a function of the X coordinate so that a "valley" is obtained that corresponds to a cortical sulcus, surrounded by positive curvature (corresponding to ridges or gyri) in the middle of the tissue slice (see Figure 46). The spatial mapping of $\tilde{\theta}$ is given as

$$\tilde{\theta}(X,Y) = \theta_{range}\left(\frac{1}{2}\tanh\left(\frac{X+\frac{X_w}{2}}{X_s}\right) - \frac{1}{2}\tanh\left(\frac{X-\frac{X_w}{2}}{X_s}\right)\right), \tag{7.22}$$

where $\theta_{range}$ determines the curvature of the sulcus, $X_w$ determines the width and $X_s = 1.3$ determines the "slope" of the sulcus wall. This mapping corresponds to a sulcus between two ridges or gyri (positively curved), where the sulcus can be flat or curved downwards (negatively curved) as shown in Figure 46. For a flat sulcus, $\theta_{range} = \frac{\pi}{2}$ to obtain a spatial profile where $\theta = \frac{\pi}{2}$ in the centre (flat) and $\theta = 0$ elsewhere (positively curved). For a negatively curved sulcus, $\theta_{range} = \pi$ to obtain a spatial profile where $\theta = \pi$ in the centre (negatively curved) and $\theta = 0$ elsewhere (positively curved).

Cortical sulci are generally in the range of $0.5 - 3$ mm wide, although this width can increase with age (at a rate of approximately 0.7 mm/decade) [109]. In the following simulations two sulcus widths of $X_w = 6$ (approximately 0.75 mm) and $X_w = 10$ (approximately 1.25 mm) are chosen in order to analyse the effect of wave size on wave propagation, where wave size is defined as the activated area with $K_e$ above the critical threshold 10.2 mM.

A rectangular area at the bottom of the tissue slice is stimulated with an input current in the same manner as in Figure 42. The results for a flat sulcus are shown in Figure 47. With a sulcus width of $X_w = 6$ the input stimulus results in a wave that cannot propagate into the positively curved area due to the low coupling C and hence a lower diffusion rate. This creates a travelling wave segment that is subexcitable and eventually ceases. The wave segment is subexcitable as a result of the small wave size as there is insufficient $K^+$ to continue the wave propagation; wave size is known to have this effect when the system is weakly excitable [108].

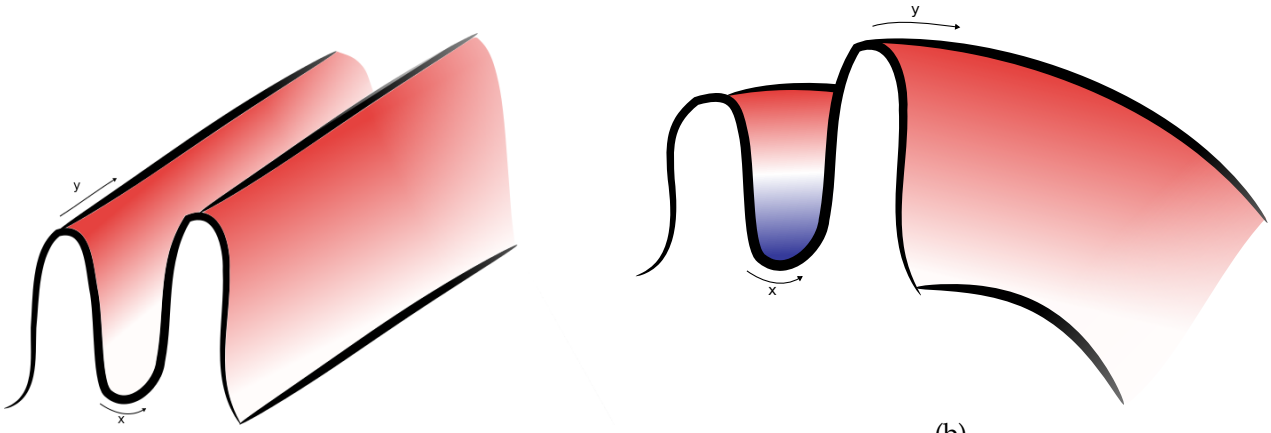


Figure 46: Surfaces that correspond to a sulcus or fold in the cortex between two ridges or gyri, where blue denotes negative curvature and red denotes positive curvature. a) a sulcus with flat curvature, b) a sulcus that curves downward giving it negative curvature.

With a larger sulcus width of $X_w = 10$ the input stimulus results in a larger wave segment with sufficient size to allow propagation at a rate of 6.7 mm $min^{-1}$ (a minimum width of $X_w = 8$ is required for wave propagation under these conditions in the model, results not shown).

The results for a negatively curved sulcus are shown in Figure 48. With a sulcus width of $X_w = 6$ an input stimulus results in a wave segment with small wavesize. The strongly negative curvature in the centre results in high coupling C and hence a higher diffusion rate. This means that although the wave segment is small (causing it to cease propagation in a flat sulcus as in Figure 47), the high diffusion rate means the wave segment is able to continue to propagate.

With a larger sulcus width of $X_w = 10$ the resulting wave segment propagates at a high rate of 9.7 mm $min^{-1}$. This is faster than a wave segment travelling in a flat sulcus (Figure 47) due to higher coupling C. The wave segment is slightly curved due to the spatial curvature gradient. For a more strongly curved surface (i.e. larger range in Gaussian curvature) the gradient in curvature is higher so the wave segment is more curved, and the curvature is more negative in the centre so the wave segment travels faster (results not shown).

### 7.2.4 *Randomly generated surface*

Lastly, in order to simulate the complexity of the human cortical surface a random Gaussian surface is generated with a corresponding Gaussian curvature that determines the spatial coupling C. This is achieved on a larger tissue slice of $64 \times 64$ NVUs (13 levels in the H-tree).

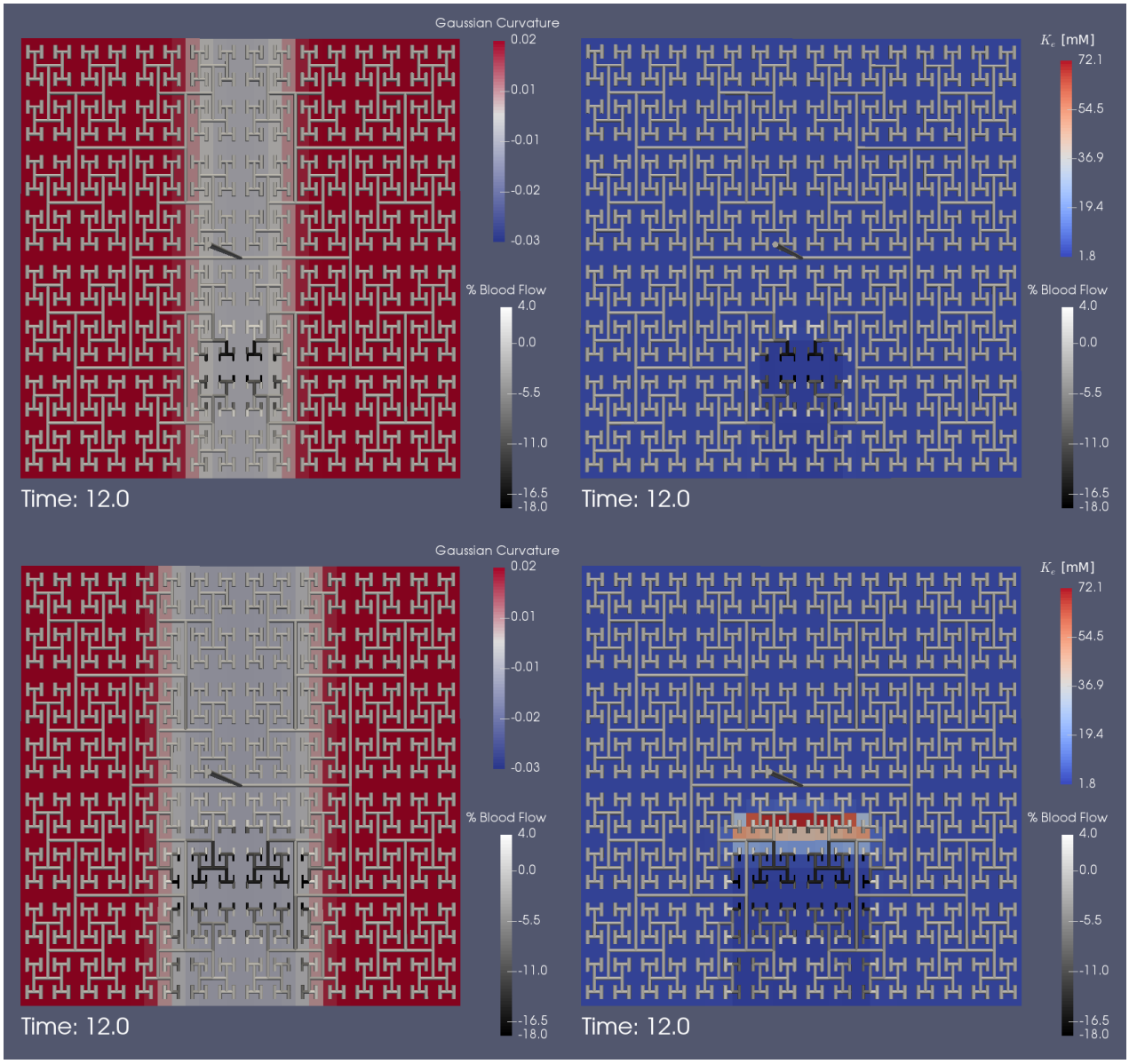


Figure 47: Gaussian curvature (left), percentage change in blood flow and the extracellular $K^+$ concentration ($K_e$, right) in a tissue slice with $32 \times 32$ NVUs (11 levels in the H-tree and corresponding to a 4mm $\times$ 4mm tissue slice) corresponding to a flat sulcus in the cortex shown in Figure 46a. Top row: $X_w = 6$, the resulting wave segment is subexcitable and eventually ceases. Bottom row: $X_w = 10$, the wave segment is large enough that it is able to propagate. Videos available online (https://youtu.be/mwNuptgCatA, https://youtu.be/gul7qDFSx8M)

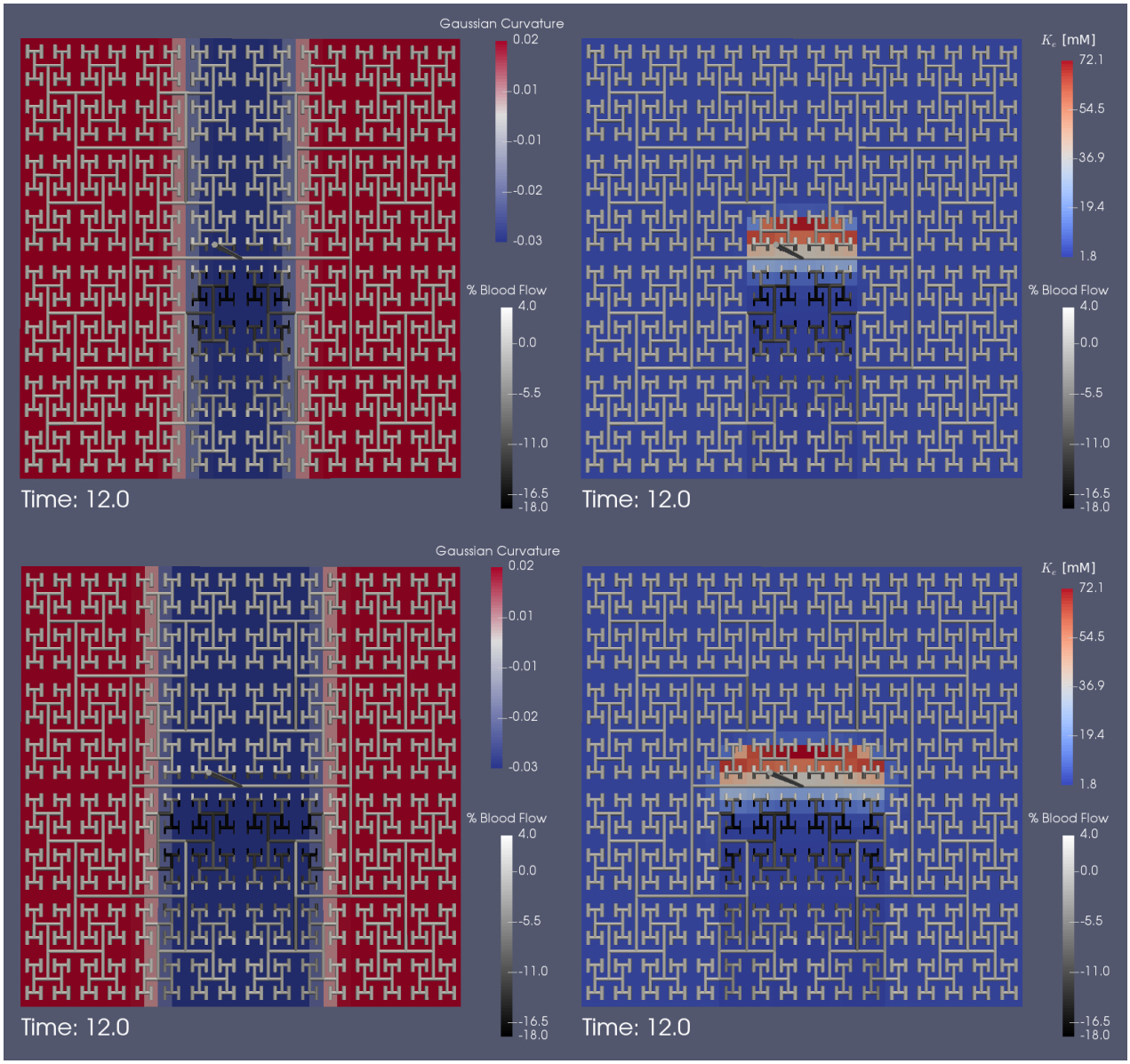


Figure 48: Gaussian curvature (left), percentage change in blood flow and the extracellular $K^+$ concentration ($K_e$, right) in a tissue slice with $32 \times 32$ NVUs (11 levels in the H-tree and corresponding to a 4mm $\times$ 4mm tissue slice) corresponding to a downward curving sulcus in the cortex shown in Figure 46b. Top row: $X_w = 6$, the resulting wave segment is able to propagate (despite the small wave size) due to the highly negative curvature and strong spatial coupling C. Bottom row: $X_w = 10$, the larger wave segment can propagate. Videos available online (https://youtu.be/afLhB7ZHCA0,https://youtu.be/0DcQpSxtY58)

Random surfaces can be generated using a method outlined by Garcia and Stoll [67], where a distribution of surface points using a random number generator (i.e. white noise) is convolved with a Gaussian filter to achieve correlation. This convolution is most efficiently performed using the discrete fast Fourier transform algorithm. The surface has a Gaussian height distribution and an exponential autocovariance function (ACF) which describes the covariance (correlation) of the surface with translationally shifted versions.

If $M_{rand}$ is a $64 \times 64$ matrix of randomly distributed numbers, the correlation of $M_{rand}$ with a covariance function gives the height of the surface $Z(X, Y)$:

$$Z(X, Y) = \mathcal{F}^{-1}\left(\mathcal{F}(V_{cor}) \cdot \mathcal{F}(M_{rand})\right) \tag{7.23}$$

where $\mathcal{F}$ and $\mathcal{F}^{-1}$ denote the Fourier and inverse Fourier transforms respectively. This covariance function $V_{cor}(X, Y)$ is given as

$$V_{cor}(X, Y) = \exp\left(\frac{-(X^2 + Y^2)}{2L_{cor}^2}\right), \tag{7.24}$$

where $L_{cor}$ is the nondimensional correlation length, i.e. the typical distance between two similar features (hills or valleys corresponding to gyri or sulci). Dahlem et al. [40] stated that Gaussian curvature in the cortex changes sign approximately every two millimetres, although larger domains of connected polarity (either negative or positive curvature) exist. Based on this assumption and with a unit block width of 124 µm in the model, $L_{cor} = 5$.

The surface used in the following simulations is shown in Figure 49 with a corresponding Gaussian curvature determined via the Matlab function "surfature". This function determines the curvature of a surface $Z(X, Y)$ by using the ratio of the determinants of the second and first fundamental forms [2]. These forms define the principal curvatures of a surface and are represented as symmetric matrices, with elements determined by the second and first partial derivatives respectively.

The coupling C is found with Eq. (7.15), using $n = 3$ and $r = \frac{20}{2\pi}$ (i.e. a strongly curved torus in order to allow for a large range in curvature $\Gamma$). The current input in the following simulation is a Gaussian plateau with maximum given by $I_{strength} = 0.006$ mA cm$^{-2}$ and centred in the area of negative curvature at $(X, Y) = (6, 5)$. Similar simulations are also performed with the current input centred in an area of positive curvature ($(X, Y) = (20, 22)$) and a relatively flat area ($(X, Y) = (18, -20)$) in order to see if a stimulus in these areas will produce a CSD wave.

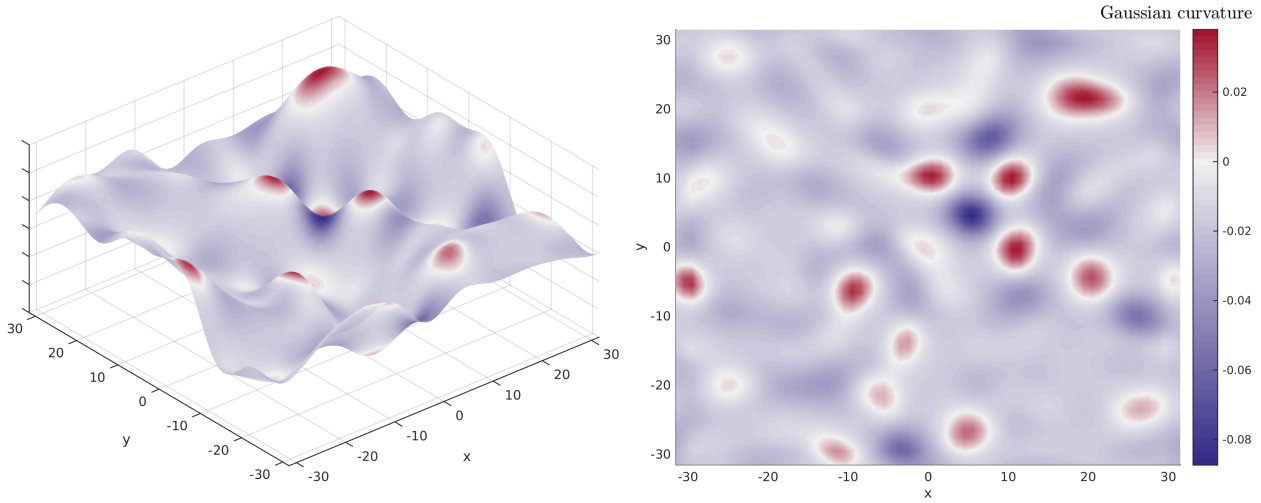


(a) Randomly generated surface

(b) Gaussian curvature $\Gamma$

Figure 49: A randomly generated Gaussian surface with corresponding Gaussian curvature, simulating the structure of a cortical tissue slice with $64 \times 64$ NVUs and corresponding to a 8mm $\times$ 8mm tissue slice.

Figure 50a shows the extracellular $K^+$ concentration and percentage change in blood flow from baseline, and Figure 50b shows the Gaussian curvature for selected time steps following a current input to a negatively curved area (blue in Figure 50b). The $K_e$ wave starts propagating outwards and is followed by a wave of vasoconstriction and then slight vasodilation. At $t = 7$ s the wave attempts to travel through 3 circular areas of positive curvature (red in Figure 50b) corresponding to hills or ridges on the surface. The low spatial coupling in the positively curved areas breaks the wave, leaving 2 small wave segments that cease and one larger wave segment that continues to propagate. At $t = 21$ s the surviving wave segment then collides with another area of positive curvature, producing a large and small wave segment (the small one ceases). At $t = 26$ s the larger wave segment propagates upwards and grows from the open ends, forming loose spirals at $t = 35$ s as the wave cannot travel back into the refractory area. These spirals are often seen in reaction-diffusion systems and in the dynamics of the cortex [73, 93, 153]. As wave segments go through negatively curved areas they grow from the ends; it has been found that a curvature of $\Gamma < -0.009$ is necessary for open wave ends to grow in the model (results not shown). At open ends, the surrounding blocks only receive an influx of $K^+$ from 1 or 2 neighbours. If this smaller flux is sufficient (as is the case in a negatively curved area with high coupling C) then the wave will grow and form spirals.

Figure 51 shows the percentage change from baseline of the BOLD response and blood flow for selected time steps following a current input to a negatively curved area, corresponding to the simulation shown in Figure 50. The wave of vasoconstriction is concurrent with a decrease in the

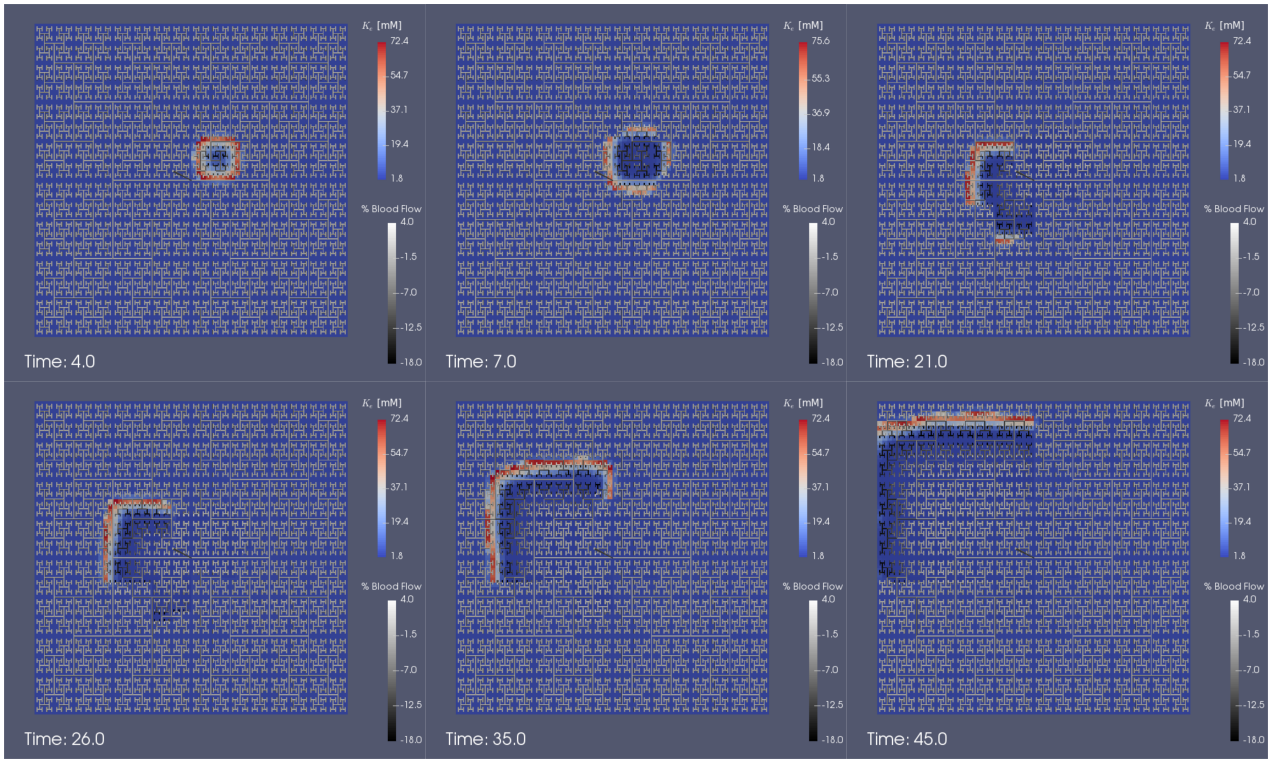


(a) Extracellular $K^+$ concentration $K_e$ in mM

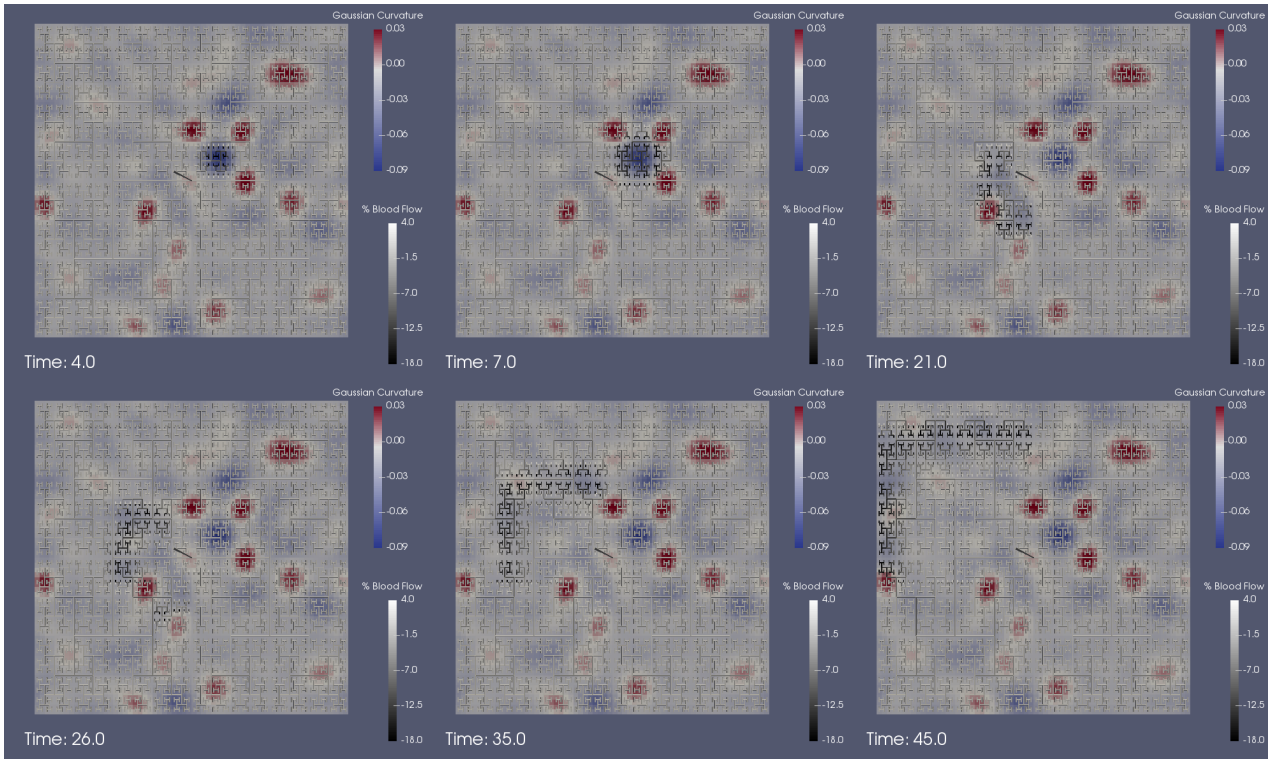


(b) Gaussian curvature $\Gamma$ and change in blood flow

Figure 50: Input stimulus to an area of negative curvature centred at $(X, Y) = (6, 5)$, on a tissue slice with randomly generated surface properties and spatially varied Gaussian curvature. The wave initially travels radially outwards and breaks when it enters areas of positive curvature (red), producing travelling wave segments that can grow and form loose spirals. The $K_e$ wave is followed by a wave of vasoconstriction. Video available online (https://youtu.be/pa5nfAHmRuM)

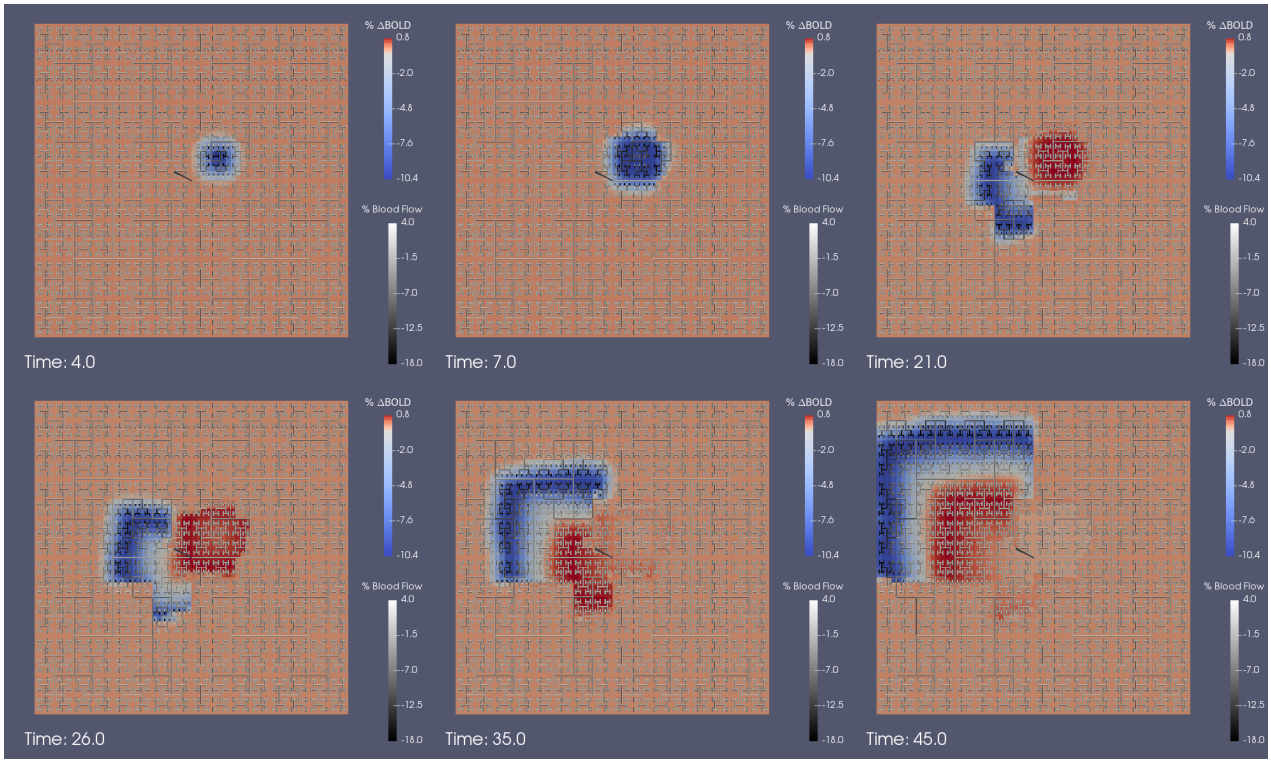


Figure 51: The percentage change from baseline of the BOLD response in a tissue slice with randomly generated surface properties and spatially varied Gaussian curvature, following a stimulating current input to an area centred at $(X, Y) = (6, 5)$. The wave of vasoconstriction is concurrent with a decrease in the BOLD response of approximately 10% due to decreased blood flow and neuronal $O_2$ consumption. Following this is a wave of slight vasodilation and increased BOLD response of approximately 1% due to the increased blood flow and because the neurons stop consuming $O_2$. Video available online (https://youtu.be/4B0lX22UpPI)

BOLD response of approximately 10% due to decreased blood flow and neuronal $O_2$ consumption. Following this is a wave of slight vasodilation and increased BOLD response of approximately 1%. This slight increase in BOLD is due to the increased blood flow and decrease in $O_2$ consumption by the neurons (the $K_e$ wave is in the refractory stage meaning there is no neuronal activity).

An input to a relatively flat area (Figure 52) has a similar effect: a wave of extracellular $K^+$ and vasoconstriction travels outwards from the input stimulus. The wave breaks when it reaches areas of positive curvature producing multiple wave segments which either grow (possibly forming spirals) or cease depending on the curvature and wavesize. Following an input into an area of positive curvature the spatial coupling is insufficient for allowing a wave to propagate (results not shown, however videos are available online at https://youtu.be/IkJifJVafoA,https://youtu.be/5aff5EDe6eo).

Increasing the level of gyrification in the tissue slice (i.e. decreasing $L_{cor}$, the typical distance between two similar features) results in a mapping with many small areas of positive curvature with little distance between them. When an area is stimulated on a flat or negatively curved section

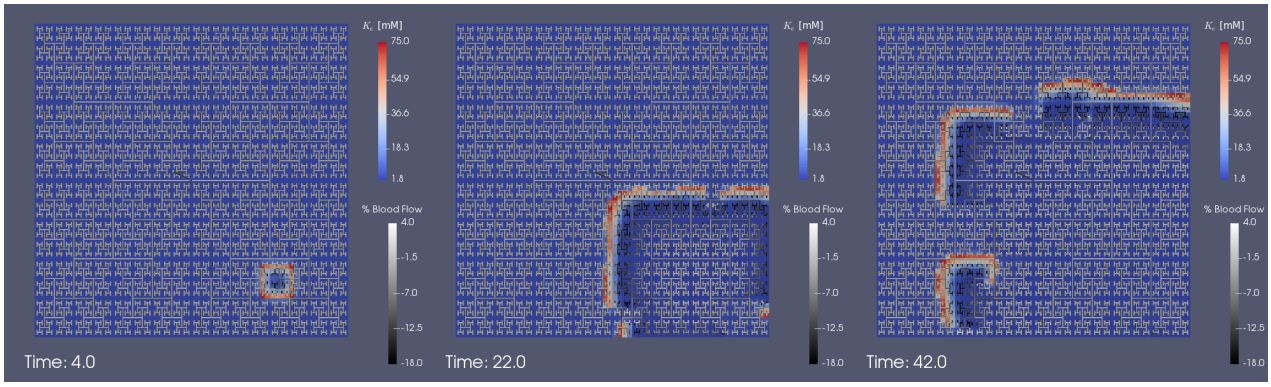


(a) Extracellular $K^+$ concentration $K_e$ in mM

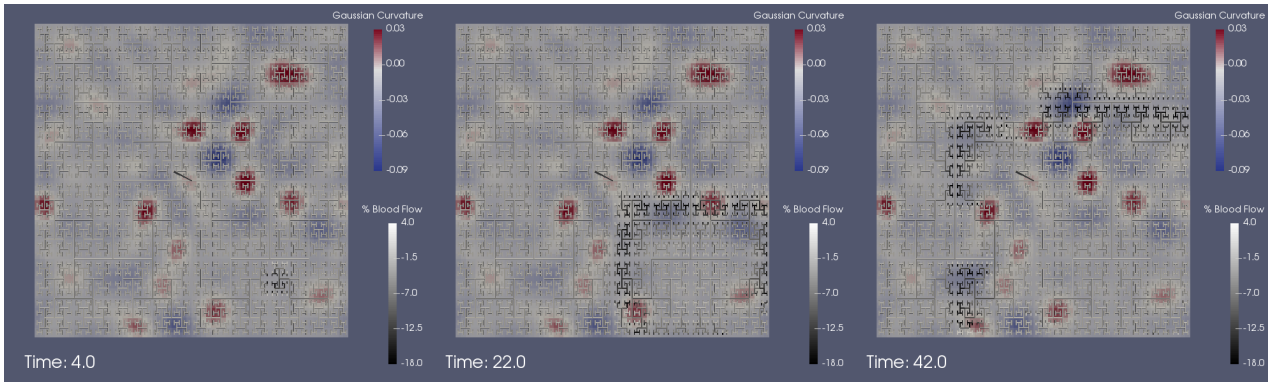


(b) Gaussian curvature $\Gamma$ and change in blood flow

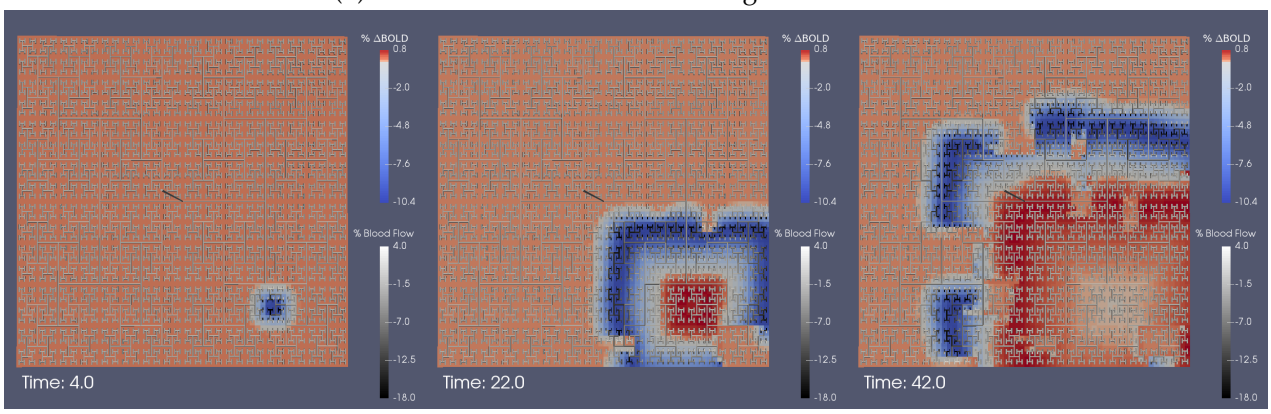


(c) Percentage change in BOLD response

Figure 52: Input stimulus to a relatively flat area centred at $(X, Y) = (18, -20)$, on a tissue slice with randomly generated surface properties and spatially varied Gaussian curvature. The $K_e$ and vasoconstrictive wave travels outwards from the input stimulus. The wave breaks when it reaches areas of positive curvature producing multiple wave segments which either grow (possibly forming loose spirals) or cease depending on the curvature and wavesize. Videos available online (https://youtu.be/1C3nv3d0fH0,https://youtu.be/u_V0ajeYhPk)

of the tissue slice a wave of $K^+$ spreads outwards but is soon broken into multiple smaller waves which are generally not large enough to continue propagating, leading to the cessation of the CSD wave (results not shown). Hence for a more strongly curved surface (corresponding to a more strongly folded cortex) a CSD wave is less able to propagate outwards and cause cellular damage via vasoconstriction and decreased $O_2$ levels.

## 7.3 DISCUSSION

The numerical NVU model of a 2D cerebral tissue slice coupled to a vascular tree from Chapter 6 has been extended with a cerebral Gaussian curvature mapping to simulate spatial variation in curvature over the tissue slice. This state of the art model is able to simulate phenomena such as CSD while also containing the full complex dynamics and multiple pathways of the NVU.

Under pathological conditions radial CSD waves (i.e. with no open ends) will propagate outwards from a stimulated area on a flat or negatively curved surface (in the model when the Gaussian curvature $\Gamma < 0.002$ and diffusive coupling $C > 0.95$). However waves are not able to propagate on a positively curved surface ($\Gamma > 0.002$). These results complement those of Dahlem et al. [40] who stated that CSD initiation is most likely in areas of negative curvature. Waves will travel faster when the curvature $\Gamma$ is more negative as this means the coupling $C$ is higher and hence the rate of extracellular electrodiffusion is greater. For example, on a flat surface a wave will travel at approximately 6.7 mm $\text{min}^{-1}$ while on a negatively curved surface with $\Gamma = -0.012$ a wave will travel at approximately 8.5 mm $\text{min}^{-1}$.

Stable wave segments can travel without shrinking or growing from open ends only when there is a gradient in curvature such that the surface is more positively curved at the wave ends (e.g. if a wave segment travels along a sulcus or fold in the cortex). For a wave segment travelling through a flat sulcus surrounded by positively curved ridges (see Figure 46a), if the resulting wave segment is too small then the wave will be subexcitable and eventually cease propagation, but if the wave size is large enough (approximately 1 mm across) then the wave segment is able to propagate. For a wave segment travelling in a sulcus that curves downward (negatively curved, see Figure 46b) the segment will travel fastest in the centre where the surface is most negative, causing the wave to have a curved shape. The steeper the curvature gradient, the more curved the wave. A wave segment will propagate regardless of wave size when the sulcus is sufficiently negatively curved, in this model when $\Gamma < -0.009, C > 1.06$. This is the curvature at which a wave segment can grow from open ends and form loose spirals, as this is when the flux from a single tissue block is sufficient to induce excitation in a neighbouring block. Note that these results should be considered on a qualitative basis only; specific values of $\Gamma$ and $C$ are given but are only valid for the numerical model presented here with its particular set of model parameters.

Based on cortical folding, mammals can be divided into two groups: those with lissencephalic brains where the cortical surface is smooth (such as small rodents), and those with gyrencephalic

brains (such as primates, in particular humans) where the cortex is tightly folded to provide a greater surface area whilst maintaining a manageable volume within the skull [149, 156]. The level of gyrification (folding) is dependent on species, though it is largely correlated with brain size [156]. As a result the smooth murine cortex may be considered as approximately flat, or at most slightly positively curved. In contrast, the human cortex contains areas of both strongly negative and positive curvature. This difference in curvature may provide some insight for the difference observed in various experimental results, detailed below.

Ayata and Lauritzen [6], Chen et al. [30] and Tomita et al. [161] performed experiments on mice, rats and cats and observed a propagating spreading depression wave radiating outwards from the initiation point, consistent with the results on a flat surface (Figure 43). This is in contrast to various experimentalists [38, 37, 39, 153] who suggest that in the human cortex CSD is likely to propagate via wave segments rather than radial waves. We have shown in the model that wave segments may only travel as a stable segment when there is a gradient in curvature present on the surface. This would be unlikely on a smooth murine cortical surface, but a highly folded human cortex has a large spatial variation in curvature providing a medium for wave segments to travel.

## 7.4 CONCLUSIONS

In this chapter a large scale numerical NVC model of multiple NVUs is coupled to a vascular tree simulating a two-dimensional cerebral tissue slice. This model is extended with a spatial Gaussian curvature mapping that can simulate the highly folded nature of the human cortex. For a flat surface comparable to a lissencephalic cortex the model can simulate propagating waves of high extracellular $K^+$ travelling radially outwards from a stimulated area at approximately 6.7 mm $min^{-1}$, corresponding well with multiple experimental results. The high $K^+$ concentration induces a corresponding wave of vasoconstriction (with decreased blood flow) then slight vasodilation, achieved through cellular communication within the NVU. The BOLD response decreases below baseline by approximately 10% followed by an increase of 1%.

For a surface with spatially varied curvature comparable to a section of gyrencephalic cortex, areas of positive Gaussian curvature inhibit wave propagation due to decreased extracellular diffusion rate. Whereas areas of negative curvature promote propagation. Consequently extracellular $K^+$ is observed travelling as wave segments (as opposed to radial waves) through flat or negatively curved "valleys" corresponding to folds (sulci) in the cortex. If the wave size (defined as the

activated area of high $K^+$ concentration) is too small or diffusion rate too low then wave segments can cease propagation. If the diffusion rate is high enough the wave segments can grow from open ends forming loose spiral waves. These results may provide some insight into the differences seen between human and animal experiments.

# 8

# CONCLUDING REMARKS

Neuronal activity evokes a localised increase in cerebral blood flow (CBF) providing oxygen ($O_2$) and glucose necessary for cellular function in a response known as neurovascular coupling (NVC). This response is achieved through communication between neurons, astrocytes and vascular cells, together comprising a neurovascular unit (NVU). Recent studies suggest that the NVC response in the diseased or aging brain may be altered [175], including changes in both the chemical mediators of NVC, ion channel behaviour, and the dynamics of the vascular system. For example, in Alzheimer's disease the production of nitric oxide (NO) is shown to be inhibited [117], hypertension and diabetes can alter smooth muscle cell (SMC) ion channels [95], and aging results in reduced vascular elasticity and hence limited vasoconstriction/dilation [43].

Numerical models provide insight into the interaction of the cellular-level and macro-scale phenomena studied *in silico*, a term referring to computer simulations of the dynamics of complex biological systems as opposed to *in vivo* or *in vitro* experimental studies. These *in silico* simulations can provide a deeper understanding of experimental results.

The aim of the present research was to obtain a better understanding of the various processes involved in NVC, and in particular the methods of communication and various pathways in the brain during normal and impaired NVC. This was accomplished in two parts. The first part focuses on communication within the NVU and involved extending a biophysical model of a single NVU with multiple new pathways and compartments. This allowed for the simulation of both normal and impaired NVC, providing a comprehensive and experimentally validated test bed for a variety of neurological pathologies. The second part focuses on communication between NVUs and in particular communication throughout the extracellular space (ECS). The single NVU model was embedded in a two dimensional (2D) cerebral tissue slice model with a coupled vascular tree, solved in a parallel environment using high performance computing. The presented model is currently one of the most complex models of its kind as it is able to simulate the entire NVC process in a 2D environment, allowing for the simulation of complex spatial phenomena such as cortical spreading depression (CSD).

## 8.1 SINGLE NVU MODEL

The mathematical foundation model developed by Dormanns et al. [48] describes the NVC process in a single NVU and is based on the potassium ($K^+$) signalling pathway. In order to analyse the role of different signalling pathways within the NVC process, this model was extended with a simple ECS compartment, the NO pathway developed by Dormanns et al. [47], the glutamate induced astrocytic calcium ($Ca^{2+}$) pathway with epoxyeicosatrienoic acid (EET) signalling [56], and the stretch dependent transient receptor potential vanniloid-related 4 (TRPV4) $Ca^{2+}$ channel on the astrocytic endfoot [170].

The results of Chapter 4 showed that in the model the $K^+$ pathway governs the fast onset of vasodilation while the NO pathway has a delayed response, maintaining dilation longer following neuronal stimulation. Increases in astrocytic $Ca^{2+}$ concentration via the $Ca^{2+}$ signalling pathway and/or TRPV4 channel to levels consistent with experimental data were found to be insufficient for inducing either vasodilation or constriction, in contrast to a number of experimental results. However astrocytic $Ca^{2+}$ was shown to strengthen $K^+$ induced NVC by further opening the big potassium (BK) channel on the astrocytic endfoot, consequently allowing more potassium into the perivascular space (PVS). These results showed that in the model $K^+$ signalling is the primary pathway for NVC and astrocytic $Ca^{2+}$ is insufficient by itself. This may suggest that the model could be missing one or more components of the $Ca^{2+}$ pathway such as the influence of $Ca^{2+}$ channels between the astrocyte and synaptic cleft (SC)/ECS; in the model $Ca^{2+}$ in the astrocyte is only altered through release from the internal stores or through the TRPV4 channel. The limitations of the astrocytic $Ca^{2+}$ submodel are discussed further in Section 8.3.

The model was later extended with a complex neuron submodel and the blood-oxygen-level dependent (BOLD) response. This allowed for model validation through comparison with experimental data; in particular the introduction of a CBF variable allowed for comparison with experiments using laser doppler flowmetry, and the BOLD submodel allows for comparison with functional magnetic resonance imaging (fMRI) BOLD scans. The results of Chapter 5 showed that the change in CBF due to neural activity in the model showed good agreement with the experimental data of Zheng et al. [174] obtained from the rat barrel cortex. When using the neural input profile of Zheng et al. [174] the model compared well for stimuli of 8 s but the model was unable to replicate the double maximum of the experimental CBF profile for longer periods. An introduction of an additional pathway through the locus coeruleus (LC) (on a purely phenomenological

basis) provided a better comparison with experimental data, further supporting the notion that there exist numerous signalling pathways in the NVC process.

## 8.2 TISSUE SLICE MODEL

Cells in the cerebral cortex exhibit complex signalling pathways not only within the NVU but also throughout the tissue. This communication can be via extracellular ion diffusion, complex cell networks connected by gap junctions, or via the vasculature which perfuses the entirety of the tissue. The foundation NVU model of Dormanns et al. [48] was implemented on the macro scale following the work of Dormanns et al. [46] where a cerebral tissue slice comprised of multiple NVUs is coupled to a vascular H-tree. This model was then extended with extracellular Fickian $K^+$ diffusion, allowing for direct communication between adjacent NVUs.

The results of Chapter 3 showed that a localised neuronal stimulation resulted in vasodilation with a decreasing gradient in vessel radius from the stimulated to non-stimulated area. The dilation remained sufficiently spatially localised over larger time scales, and during vasomotion there was emergent behaviour in the form of waves of increased vessel radius moving towards the stimulated area. These results indicate that communication within the tissue via extracellular ion diffusion has a much greater effect than communication solely through the vascular tree, however this model could not simulate several phenomena such as CSD as the neuron model used was too simplified.

In order to model complex phenomena such as CSD, this large scale model was then extended by implementing the additional pathways (NO, astrocytic $Ca^{2+}$ and the TRPV4 channel), neuron submodel, and BOLD response described in Chapters 4 and 5. In addition, extracellular ion electrodiffusion and an astrocytic gap junction network were added to allow further communication throughout the tissue. The results of Chapter 6 showed that under pathological conditions, CSD waves in the form of high extracellular $K^+$ could propagate radially outwards from a stimulated area with a wave of vasoconstriction followed by slight vasodilation comparing well with murine experiments. An astrocytic gap junction network reduced the duration of the vasoconstrictive wave and the area initially affected. These results show that communication throughout the ECS is necessary in the model for allowing a CSD wave to propagate, and the communication through the astrocytic gap junction network regulates the vascular response.

The flat 2D tissue slice model could simulate the smooth cortex of murine animals but could not take into account the highly folded nature of the human cortex. Therefore the model was extended with a spatial Gaussian curvature mapping which allowed for investigation into how the surface curvature affects the propagation of CSD waves throughout the tissue. The results of Chapter 7 showed that for a surface with spatially varied curvature comparable to a section of human cortex, areas of positive Gaussian curvature inhibited wave propagation due to decreased extracellular diffusion rate, whereas areas of negative curvature promoted propagation. CSD was observed travelling as wave segments (as opposed to radial waves on a flat surface), providing some insight into the differences seen between human and animal experiments.

## 8.3 LIMITATIONS AND FUTURE WORK

### 8.3.1 *Signalling pathways*

In Chapter 4 the glutamate induced $Ca^{2+}$ pathway with EET signalling in the astrocyte is shown in the model to be insufficient for NVC. However, in addition to their effect on the astrocytic BK channel, EETs produced in the astrocyte may also have a direct vasodilatory effect on the SMC [11, 5, 145]. Astrocytes are also able to produce other vasoactive agents following an increase in $Ca^{2+}$ concentration such as the vasoconstrictor 20- hydroxyeicosatetraenoic acid (20-HETE) and cyclooxygenase enzymes (COX) derived prostaglandins, which can be either vasodilating or vasoconstricting [125, 129]. Pfister et al. [145] hypothesized that EETs could diffuse to the SMC and activate BK channels leading to $K^+$ efflux. In turn this would cause hyperpolarisation, closing off the voltage operated $Ca^{2+}$ channels (VOCCs) and causing relaxation. Fang et al. [55] indicated that 14,15 EETs increased vascular SMC $Ca^{2+}$ concentration through mediated L-type $Ca^{2+}$ channels via some form of secondary messenger. Although they used human bronchial SMCs, Morin et al. [128] expressed a second pathway for EETs to relax SMCs. In contrast to the activation of myosin light chain kinase (MLC), this second pathway was possibly due to the activation of protein-kinase C (PKC)-dependent phosphorylation of myosin phosphatase inhibitor protein (CPI-17) to maintain tone, thus assuming that dephosphorylation produced relaxation. Finally it should be recognised that EET-induced dynamics resulting in dilation/constriction vary significantly with species and vascular beds. Further work is required to determine the importance of these vasoactive agents (EETs, 20-HETE, and prostaglandins) and their influence on SMC dynamics.

Mishra et al. [126] provided both *in vitro* and *in vivo* evidence for different pathways for NVC corresponding to either capillary or arteriolar dilations. The astrocytic $Ca^{2+}$ pathway mediated pericyte contraction whilst the NO pathway mediated arteriolar dilation. The $Ca^{2+}$ pathway was not, as is usually assumed, to come from metabotropic glutamate receptor (mGluR)-5 (which are lacking in mature murine species) but from the activation of the adenosine triphosphate (ATP) receptor P2X1 after release of ATP following neuronal activation. In addition the astrocyte generates arachidonic acid (AA) via phospholipase D2 rather than A2. Finally they indicated that arteriolar dilation depended on N-methyl-D-aspartate (NMDA) receptor activation and the generation of NO via the $Ca^{2+}$ pathway by interneurons. The current model contains only arterioles and no pericytes. The role of pericytes in NVC has not yet been fully determined with any certainty; further experiments could provide more insight.

### 8.3.2 *Experimental model validation*

The model has been compared with experimental data taken from experiments on anaesthetised animals. Anaesthesia is known to have drastic effects on the BOLD signals by changing the neural processing, vascular reactivity and basal metabolism. In evaluating both CBF and cerebral metabolic rate of $O_2$ consumption ($CMRO_2$) normalised values with respect to their baseline conditions are used. At the moment the specific mechanisms through which anaesthesia can affect the relationship of baseline conditions are not modelled. However it can be hypothesised that changing the baseline values of sodium ($Na^+$) and $K^+$ in the ATPase pump of the neuron provide a possible way of simulating anaesthetic conditions. This is a broad area for future research as different anaesthetic agents (fentanyl or isoflurane) are known to have different effects on the BOLD response [3].

The use of experimentally derived parameters arising from variations in animal models requires careful consideration of a number of parameters that appear in the presented numerical model. The model itself has a significant number of parameters (over 270 parameters in the latest iteration) mostly taken from relevant experiments carried out on a variety of animals under different conditions. It would not be surprising if the parameters had different probability distributions for different species. For example the rate at which the cerebro-vasculature of a murine species changes its vessel radii would not necessarily be the same as that found for a porcine or human model. Therefore care must be taken in making hypotheses about a particular result based on

either dissimilar animal or mixed animal models. Sensitivity analyses on the numerical model allows us to correctly determine the "dominant parameters" for a specific quantity of interest such as the rate of change of radius post-stimulation. However this analysis requires a significant effort (both analytically and computationally) due primarily to the non-linearity and complexity of the phenomena being modelled. Work by the research group and collaborators has begun in this area and is an area of interesting potential research.

### 8.3.3 *Neuron submodel*

There are several issues with the neuron model implemented in Chapter 5. The neuron submodel is integrated with the remainder of the NVU by assuming that the flux from the neuron into the SC is equal to a fraction of the scaled flux from the neuron into the ECS:

$$\frac{dK_s}{dt} = c_{unit} k_{syn} \frac{dK_e}{dt} + \frac{1}{VR_{sk}} \left( J_{K_k} - 2J_{NaK_k} - J_{NKCC1_k} - J_{KCC1_k} \right), \tag{8.1}$$

where $K_s$ is the synaptic $K^+$ concentration and the fluxes scaled by the volume ratio $VR_{sk}$ are between the SC and the astrocyte. During neuronal stimulation, extracellular $K^+$ ($K_e$) increases up to 7 mM then reaches a stable state of approximately 6 mM, then drops slightly below baseline when neuronal stimulation ends as shown in Figure 53a. As the rate of change of $K^+$ in the SC is dependent on the rate of change of $K_e$ it follows a similar profile with an initial peak of approximately 14 mM (a higher peak than the ECS as the SC has a smaller volume and the $K^+$ influx is scaled by the parameter $k_{syn}$). However as $K_s$ increases the $K^+$ is taken up by the astrocyte, causing $K_s$ to drop much lower than its initial value down to approximately 6 mM. This produces a rapid large initial spike that is not physiologically realistic (see Figure 53b).

This large initial spike causes other issues within in the model when looking at the behaviour during longer stimulation periods, seen clearly through comparison with the previous model iteration shown in Chapter 4. Figure 54 shows the results with a 200 s stimulation for the simpler neuron model of Chapter 4 compared with the new neuron model shown in Chapter 5 with varied current input strength. The NO pathway is excluded in these results so that the long term effects of the neuronal input are clearly seen. In the old model (red), there is a small initial spike in $K_s$ (Figure 54b) with a steady concentration of 8.7 mM for the duration of the stimulation, causing an uptake of $K^+$ into the astrocyte and hence increase in astrocytic membrane potential ($v_k$) up to

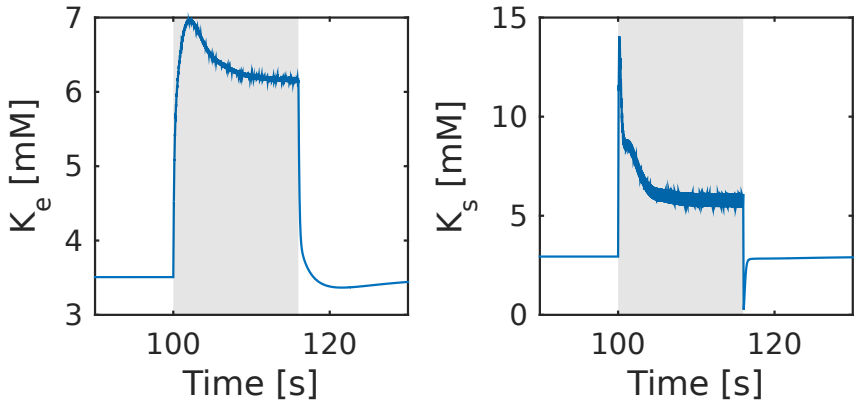


Figure 53: The $K^+$ concentration in the ECS ($K_e$) and SC ($K_s$) in mM. Grey area indicates neuronal stimulation.

−60 mV (Figure 54e) . This causes the BK channel to open (Figure 54f), increasing the perivascular $K^+$ concentration ($K_p$) to 8.7 mM and causing the radius to increase to 26 μm.

In contrast, the initial spike of $K_s$ in the new model using a current input strength of $2.2 \times 10^{-2}$ mA $cm^{-2}$ (blue) is higher than that of the old model (Figure 54b) but the value that it tends to for the duration of the stimulation is lower (6.5 mM in the new model compared to 8.7 mM in the old model). As for the other long term behaviour (disregarding the transient behaviour due to the spike), there is less $K^+$ taken up by the astrocyte and $v_k$ only reaches −74 mV, and so the BK channel has a low open probability ($w_k$) of approximately 0.01 (Figure 54f) according to the heavily voltage-dependent dynamics of the BK channel shown in Figure 16 in Chapter 4. As a result $K_p$ reaches only 6.5 mM and hence the radius has an increase up to 20 μm.

If the current input strength is increased to $3.2 \times 10^{-2}$ mA $cm^{-2}$ (yellow) so that the long term value of $K_s$ during the duration of the stimulation reaches a similar concentration as in the old model (approximately 8.7 mM), then the long term behaviour of the models after a 200 s stimulation are similar. Note that in the new model $K_e$ (and hence $K_s$, $v_k$ $w_k$ and $K_p$) are slowly increasing over the stimulation period rather than reaching a stable state as the neuron is being continuously stimulated by the input current. However, due to the large initial spike present in the new model, $K_s$ initially increases up to 35 mM, causing a brief but large increase in $v_k$, $w_k$, and $K_p$ also up to 35 mM. The PVS is connected to the SMC via a inward rectifying $K^+$ (KIR) channel which reverses direction at high $K^+$ concentrations (discussed in detail in Section 6.3.2 of Chapter 6 and shown clearly in Figure 30). Hence the SMC depolarises and leads to vasoconstriction following the initial spike. This initial vasoconstriction lasting approximately 10 s is unlikely to occur during regular NVC. As Chapter 5 focussed on input stimulations with a duration of 16 s

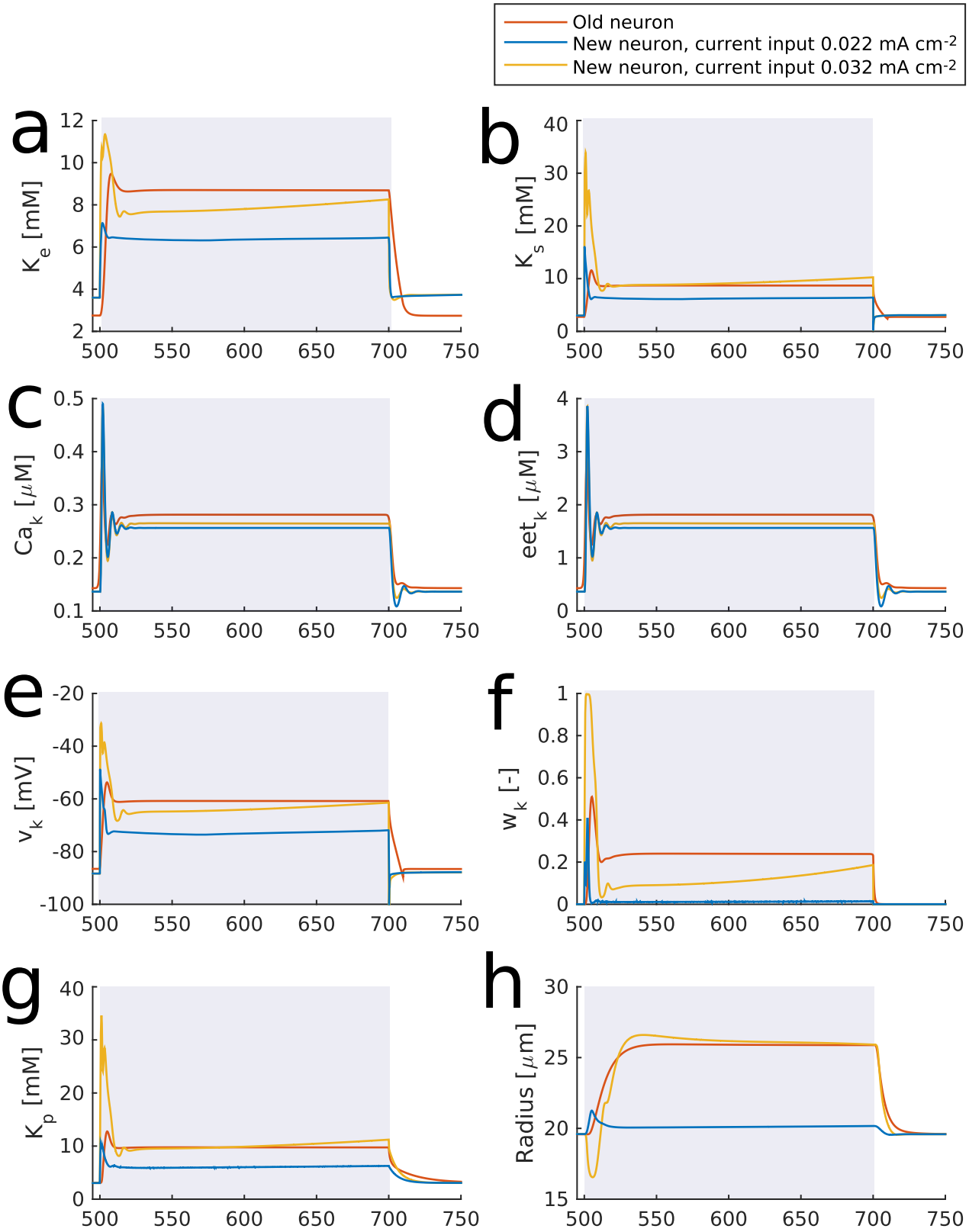


Figure 54: Comparison of the model from Chapter 4 (red) with the updated model from Chapter 5 containing a new neuron submodel, with a standard current input strength of $2.2 \times 10^{-2}$ mA cm$^{-2}$ (blue) and higher input strength of $3.2 \times 10^{-2}$ mA cm$^{-2}$ (yellow). a) extracellular $K^+$ concentration, b) synaptic $K^+$ concentration, c) astrocytic $Ca^{2+}$ concentration, d) astrocytic EET concentration, e) astrocytic membrane potential, f) open probability of the astrocytic BK channel, g) perivascular $K^+$ concentration, and h) arteriolar radius.

or less, the current input strength was kept at $2.2 \times 10^{-2}$ mA cm$^{-2}$ in order to avoid any initial vasoconstriction in the results.

During neural stimulation the neuron submodel oscillates on the order of milliseconds due to the fast open and close rates of several ion channels on the soma/axon and dendrite. However the rest of the model operates on the order of seconds, producing a two time scale problem. A neuronal stimulation of 16 physiological seconds takes minutes of wall clock time to solve using the stiff solver ode15s in Matlab. This is in contrast to the foundation model described in Chapter 2 which used a very simple neuron submodel with no fast mechanics; in this model a neuronal stimulation of 16 physiological seconds took less than a second to solve.

One possible solution to these problems is the introduction of a simplified neuron model such as the population model of Wilson and Cowan [169]. This model describes the dynamics of a spatially localised population of both excitatory and inhibitory neurons. In addition, neurons are likely to be stimulated as a population rather than individually. The input from the neuron into the remainder of the NVU (i.e. an input of $K^+$ and glutamate to the SC) can then be taken as a function of the percentage of neurons in an excited state. Note that a simpler neuron model such as this would not be ideal for describing pathologies such as CSD which propagates primarily through the ECS compartment; instead a model like this would be suited to analysis of astrocyte dynamics or the vascular response.

### 8.3.4 *Cortical spreading depression*

The large $K^+$ efflux from the neuron into the ECS that occurs during CSD is reciprocated by $Na^+$ and chlorine ($Cl^-$) influx that also pulls in water, leading to neuronal swelling and in turn decreases the volume of the ECS [6]. In the model the volume ratio of the ECS to the neuron is given by the parameter $f_e = 0.15$, taken from the model of Kager et al. [99]. During CSD neuronal swelling is observed leading to a decreased volume ratio of 0.05 [98]. In the model decreasing the parameter $f_e$ to 0.05 amplifies extracellular $K^+$ changes, meaning the $K^+$ concentration reaches a higher peak and decreases more quickly following stimulation, but does not qualitatively alter the behaviour. However in reality the volume ratio would not be constant, instead decreasing during the CSD wave as the neurons swell then returning to baseline following the wave. Hence to further study the effects of cell swelling on CSD would require dynamic rather than constant volumes, and is an area of possible future research.

Astrocytic gap junctions are generally known to aid in spatial buffering, where astrocytes take up large amounts of $K^+$ from the ECS and move it away via gap junctions with neighbouring astrocytes [8]. In the CSD simulations of Chapter 6 the astrocytic $K^+$ does spread out from the stimulated area via gap junctions, but this has little effect on the extracellular $K^+$ as there is no direct link between the astrocyte and ECS present in the model. Instead there are multiple channels and pumps connecting the astrocyte with the SC, modelled as a subspace of the ECS. Rather than affecting the extracellular $K^+$ directly, the decrease in astrocytic $K^+$ lowers the perivascular $K^+$ concentration leading to slight vasodilation rather than vasoconstriction. This behaviour is not directly predicted by experiments, although to date no study has fully described the relative contribution of gap junctions to the phenomenon of CSD [151]. KIR channels are highly expressed on astrocytic endfeet adjacent to the synaptic cleft, and $K_{2p}$ channels, $Na^+/K^+/2Cl^-$ transporters and $Na^+/K^+$ ATPase pumps are also expressed on astrocytes [86, 41]. These channels and pumps may provide further uptake of $K^+$ from the ECS and their inclusion in the model is a possible area of future research.

### 8.3.5 *Cerebral curvature*

For a high resolution fMRI scan the voxel size is on average 1 $mm^2$ [42]; the largest simulations in this thesis of a 8 mm $\times$ 8 mm tissue slice would contain approximately 64 voxels. However the brain is much larger than this single tissue slice, and future work could involve larger scale simulations in order to model significant portions of the cerebral cortex.

Wang et al. [168] found that the tension on the cortical surface decreases with age, meaning that the cortex becomes less folded, and the effect is more pronounced in individuals with Alzheimer's disease. The results of Chapter 7 complement this: less folding corresponds to a surface with less spatial variation in curvature meaning CSD waves are more able to propagate and spread (as there are less obstacles in the form of areas of positive curvature). This suggests that debilitating CSD waves would be more likely in the aged or diseased brain due to the decrease in cortical folding. An interesting future research question would be whether this physiological decrease in tension or cortical folding is sufficient to allow CSD waves to propagate more freely.

Dahlem et al. [40] investigated the effects of cerebral curvature on CSD initiation and propagation. They used a generic reaction diffusion model with 2 variables applied to a surface with Gaussian curvature taken from fMRI scans. The model presented in this thesis is more complex,

including the full NVC pathway with neuronal, extracellular, astrocytic and vascular dynamics as well as the BOLD response. Utilising the model with real human brain fMRI scans could provide extensive insight into CSD propagation dynamics in individual brains which are known to differ drastically in their morphology based on a multitude of factors such as age, sex, and disease [168]. This is an interesting area of potential future research.

# A

# APPENDIX

The foundation neurovascular unit (NVU) model of Dormanns et al. [48] (originally developed by Farr and David [56]) has been extended multiple times throughout this thesis, beginning with 24 ordinary differential equations (ODEs) and ending with 67 ODEs and a large number of algebraic variables and parameters. The equations and parameters are divided into sections corresponding to each chapter with different model extensions. The parameters are given for ordinary neurovascular coupling (NVC) conditions.

## A.1 MODEL CODE

The model code for the latest version of the single NVU model detailed in Chapter 5 can be found at `https://github.com/BlueFern/OO-NVU/releases/tag/v2.1`. The code is run in Matlab. The model code for the latest version of the large scale tissue slice model detailed in Chapter 7 can be found at `https://github.com/BlueFern/parbrain/releases/tag/v2.1`. The main source code is written in C and the program to convert the output binary data into .vtu/.vtp files for viewing in Paraview is written in C++.

## A.2 GLOBAL CONSTANTS

| Parameter | Description | Value |
|---|---|---|
| $F$ | Faraday's constant | 96.485 C mmol$^{-1}$ |
| $\tilde{F}$ | Faraday's constant (in different units) | 96485 C mol$^{-1}$ |
| $R_g$ | Gas constant | 8.315 J mol$^{-1}$ K$^{-1}$ |
| $T$ | Temperature constant | 300 K |
| $\phi$ | $R_g T/F$ | 26.7 mV |
| $z_K$ | Ionic valence for potassium ($K^+$) | 1 |
| $z_{Na}$ | Ionic valence for sodium ($Na^+$) | 1 |

| | | |
|---|---|---|
| $z_{Cl}$ | Ionic valence for chlorine ($Cl^-$) | $-1$ |
| $z_{NBC}$ | Effective valence of the NBC cotransporter complex | $-1$ |
| $z_{Ca}$ | Ionic valence for calcium ($Ca^{2+}$) | 2 |
| $c_{unit}$ | Conversion constant | $10^3$ |
| $\gamma_v$ | Change in membrane potential by a scaling factor | 1970 mV $\mu$M $^{-1}$ |

Table 1: Global constants used in the NVU model.

## A.3 FOUNDATION MODEL OF DORMANNS ET AL. (2015)

The foundation NVUs model of Dormanns et al. [48] originally based on the model of Farr and David [56] is described in Chapter 2; a schematic diagram can be found in Figure 4.

### A.3.1 *Astrocyte, SC and PVS*

#### A.3.1.1 *Input to the model*

The input function $K(t)$ of $K^+$ into the synaptic cleft (SC) ($\mu$M m s$^{-1}$):

$$K(t) = \begin{cases} K_{input} \dfrac{(\alpha_n+\beta_n-1)!}{(\alpha_n-1)!(\beta_n-1)!} \left(\dfrac{t_\beta-(t-t_0)}{\Delta t}\right)^{\beta_n-1} \left(\dfrac{t-t_0}{\Delta t}\right)^{\alpha_n-1}, & \text{for } t_0 \leqslant t < t_0+\Delta t \\ -K_{input}, & \text{for } t_1 \leqslant t \leqslant t_1+\Delta t \\ 0, & \text{otherwise} \end{cases} \tag{A.1}$$

#### A.3.1.2 *ODEs*

Astrocyte volume-area ratio (m):

$$\frac{dR_k}{dt} = L_p\left(Na_k + K_k + Cl_k + HCO3_k - Na_s - K_s - Cl_s - HCO3_s + \frac{X_k}{R_k}\right) \tag{A.2}$$

The number of $K^+$ ions per unit area in the astrocyte ($\mu$M m):

$$\frac{dN_{K_k}}{dt} = -J_{K_k} + 2J_{NaK_k} + J_{NKCC1_k} + J_{KCC1_k} - J_{BK_k} \tag{A.3}$$

The number of $Na^+$ ions per unit area in the astrocyte ($\mu$M m):

$$\frac{dN_{Na_k}}{dt} = -J_{Na_k} - 3J_{NaK_k} + J_{NKCC1_k} + J_{NBC_k} \tag{A.4}$$

The number of $HCO_3^-$ ions per unit area in the astrocyte (µM m):

$$\frac{dN_{HCO3_k}}{dt} = 2J_{NBC_k} \tag{A.5}$$

The number of $Cl^-$ ions per unit area in the astrocyte (µM m):

$$\frac{dN_{Cl_k}}{dt} = \frac{dN_{K_k}}{dt} + \frac{dN_{Na_k}}{dt} - \frac{dN_{HCO3_k}}{dt} \tag{A.6}$$

The number of $K^+$ ions per unit area in the SC (µM m):

$$\frac{dN_{K_s}}{dt} = J_{K_k} - 2J_{NaK_k} - J_{NKCC1_k} - J_{KCC1_k} + K(t) \tag{A.7}$$

The number of $Na^+$ ions per unit area in the SC (µM m):

$$\frac{dN_{Na_s}}{dt} = J_{Na_k} + 3J_{NaK_k} - J_{NKCC1_k} - J_{NBC_k} - K(t) \tag{A.8}$$

The number of $HCO_3^-$ ions per unit area in the SC (µM m):

$$\frac{dN_{HCO3_s}}{dt} = -2J_{NBC_k} \tag{A.9}$$

The open probability of the big potassium (BK) channel (-):

$$\frac{dw_k}{dt} = \phi_n(w_\infty - w_k) \tag{A.10}$$

$K^+$ concentration in the perivascular space (PVS) (µM):

$$\frac{dK_p}{dt} = \frac{J_{BK_k}}{R_k VR_{pk}} + \frac{J_{KIR_i}}{VR_{pi}} - K_{decay_p}(K_p - K_{min_p}) \tag{A.11}$$

### A.3.1.3 *Algebraic variables*

Membrane voltage of the astrocyte (V):

$$v_k = \frac{g_{Na_k}E_{Na_k} + g_{K_k}E_{K_k} + g_{Cl_k}E_{Cl_k} + g_{NBC_k}E_{NBC_k} + g_{BK_k}w_kE_{BK_k} - J_{NaK_k}\tilde{F}/c_{unit}}{g_{Na_k} + g_{K_k} + g_{Cl_k} + g_{NBC_k} + g_{BK_k}w_k} \tag{A.12}$$

The number of $Cl^-$ ions per unit area in the SC (μM m):

$$N_{Cl_s} = N_{Na_s} + N_{K_s} - N_{HCO_{3_s}} \tag{A.13}$$

SC volume-area ratio (m):

$$R_s = R_{tot} - R_k \tag{A.14}$$

Ion concentration in either the astrocyte compartment $(k)$ or SC $(s)$ (μM):

$$ion_* = \frac{N_{ion_*}}{R_*} \tag{A.15}$$

Astrocytic $K^+$ flux through the $K^+$ channel (μM m $s^{-1}$):

$$J_{K_k} = \frac{g_{K_k}}{\tilde{F}} (v_k - E_{K_k}) c_{unit} \tag{A.16}$$

Astrocytic $Na^+$ flux through the $Na^+$ channel (μM m $s^{-1}$):

$$J_{Na_k} = \frac{g_{Na_k}}{\tilde{F}} (v_k - E_{Na_k}) c_{unit} \tag{A.17}$$

Astrocytic $Na^+$ and $HCO_3^-$ flux through the NBC channel (μM m $s^{-1}$):

$$J_{NBC_k} = \frac{g_{NBC_k}}{\tilde{F}} (v_k - E_{NBC_k}) c_{unit} \tag{A.18}$$

Astrocytic $Cl^-$ and $K^+$ flux through the KCC1 channel (μM m $s^{-1}$):

$$J_{KCC1_k} = \frac{g_{KCC1_k}}{\tilde{F}} \frac{R_g T}{\tilde{F}} \ln\left(\frac{K_s Cl_s}{K_k Cl_k}\right) c_{unit} \tag{A.19}$$

Astrocytic $Na^+$, $K^+$ and $Cl^-$ flux through the NKCC1 channel (μM m $s^{-1}$):

$$J_{NKCC1_k} = \frac{g_{NKCC1_k}}{\tilde{F}} \frac{R_g T}{\tilde{F}} \ln\left(\frac{Na_s K_s {Cl_s}^2}{Na_k K_k {Cl_k}^2}\right) c_{unit} \tag{A.20}$$

Flux through the astrocytic $Na^+/K^+$ adenosine triphosphate (ATP)-ase pump (μM m $s^{-1}$):

$$J_{NaK_k} = J_{NaK_{max}} \frac{{Na_k}^{1.5}}{{Na_k}^{1.5} + {K_{Na_k}}^{1.5}} \frac{K_s}{K_s + K_{K_s}} \tag{A.21}$$

$K^+$ flux through the BK channel ($\mu M\ m\ s^{-1}$):

$$J_{BK_k} = \frac{g_{BK_k}}{\tilde{F}} w_k \left(v_k - E_{BK_k}\right) c_{unit} \tag{A.22}$$

Equilibrium state BK-channel (-):

$$w_\infty = 0.5 \left(1 + \tanh\left(\frac{v_k + v_6}{v_4}\right)\right) \tag{A.23}$$

The time constant associated with the opening of the BK channel ($s^{-1}$):

$$\phi_n = \psi_n \cosh\left(\frac{v_k + v_6}{2v_4}\right) \tag{A.24}$$

Nernst potential for the BK channel (V):

$$E_{BK_k} = \frac{R_g T}{z_K \tilde{F}} \ln\left(\frac{K_p}{K_k}\right) \tag{A.25}$$

Nernst potential for the astrocytic $K^+$ channel (V):

$$E_{K_k} = \frac{R_g T}{z_K \tilde{F}} \ln\left(\frac{K_s}{K_k}\right) \tag{A.26}$$

Nernst potential for the astrocytic $Na^+$ channel (mV):

$$E_{Na_k} = \frac{R_g T}{z_{Na} \tilde{F}} \ln\left(\frac{Na_s}{Na_k}\right) \tag{A.27}$$

Nernst potential for the astrocytic $Cl^-$ channel (V):

$$E_{Cl_k} = \frac{R_g T}{z_{Cl} \tilde{F}} \ln\left(\frac{Cl_s}{Cl_k}\right) \tag{A.28}$$

Nernst potential for the astrocytic NBC channel (V):

$$E_{NBC_k} = \frac{R_g T}{z_{NBC} \tilde{F}} \ln\left(\frac{Na_s HCO_{3_s}{}^2}{Na_k HCO_{3_k}{}^2}\right) \tag{A.29}$$

| Parameter | Description | Value |
|---|---|---|
| $t_0$ | Start time of neuronal stimulation | 100 s |
| $t_1$ | End time of neuronal stimulation | 300 s |

| | | |
|---|---|---|
| $t_\beta$ | Time constant for $K(t)$ | 1 s |
| $\alpha_n$ | Beta distribution constant for $K(t)$ | 2 |
| $\beta_n$ | Beta distribution constant for $K(t)$ | 5 |
| $K_{input}$ | Scaling factor for $K(t)$ | $1.84 \times 10^{-4}$ μM m $s^{-1}$ |
| $\Delta t$ | Duration of initial input for $K(t)$ | 10 s |
| $L_p$ | Total water permeability per unit area of the astrocyte | $2.1 \times 10^{-9}$ $\mu M^{-1}$ m $s^{-1}$ |
| $X_k$ | Number of negatively charged impermeable ions in the astrocyte divided by the astrocyte area | $12.41 \times 10^{-3}$ μM m |
| $VR_{pk}$ | Volume ratio between PVS and astrocyte | 0.001 |
| $VR_{pi}$ | Volume ratio between PVS and smooth muscle cell (SMC) | 0.001 |
| $K_{decay_p}$ | Rate of decay of $K^+$ in PVS | 0.05 $s^{-1}$ |
| $K_{min_p}$ | Steady state value of $K^+$ in PVS | $3 \times 10^3$ μM |
| $g_{Na_k}$ | Specific ion conductance of $Na^+$ | 1.314 $\Omega^{-1}$ $m^{-2}$ |
| $g_{K_k}$ | Specific ion conductance of $K^+$ | 40 $\Omega^{-1}$ $m^{-2}$ |
| $g_{Cl_k}$ | Specific ion conductance of $Cl^-$ | $8.797 \times 10^{-1}$ $\Omega^{-1}$ $m^{-2}$ |
| $g_{NBC_k}$ | Specific ion conductance of the NBC co-transporter | $7.57 \times 10^{-1}$ $\Omega^{-1}$ $m^{-2}$ |
| $g_{BK_k}$ | Specific ion conductance of the BK channel | 1.16 $\Omega^{-1}$ $m^{-2}$ |
| $R_{tot}$ | Total volume area ratio of the astrocyte and SC | $8.79 \times 10^{-8}$ m |
| $J_{NaK_{max}}$ | Maximum flux through the $Na^+/K^+$ ATP-ase pump | $1.42 \times 10^{-3}$ μM m $s^{-1}$ |
| $K_{Na_k}$ | $Na^+/K^+$ ATP-ase pump constant | $10 \times 10^3$ μM |
| $K_{K_s}$ | $Na^+/K^+$ ATP-ase pump constant | $1.5 \times 10^3$ μM |
| $\psi_n$ | Characteristic time for the opening of the BK channel | 2.664 $s^{-1}$ |
| $v_6$ | Voltage associated with the opening of half the population | $22 \times 10^{-3}$ V |
| $v_4$ | A measure of the spread of $w_\infty$ | $14.5 \times 10^{-3}$ V |

Table 2: Parameters used in the astrocyte, SC and PVS compartments in the foundation model of Dormanns et al. [48].

### A.3.2 *SMC*

#### A.3.2.1 *ODEs*

Cytosolic $Ca^{2+}$ in the SMC (μM):

$$\frac{dCa_i}{dt} = J_{IP_{3i}} - J_{SR_{uptake_i}} + J_{CICR_i} - J_{extrusion_i} + J_{SR_{leak_i}} - J_{VOCC_i} + J_{Na/Ca_i} + 0.1J_{stretch_i} + J^{SMC-EC}_{Ca^{2+}-coupling_i} \tag{A.30}$$

$Ca^{2+}$ in the sarcoplasmic reticulum (SR) of the SMC (μM):

$$\frac{ds_i}{dt} = J_{SR_{uptake_i}} - J_{CICR_i} - J_{SR_{leak_i}} \tag{A.31}$$

Membrane potential of the SMC (mV):

$$\frac{dv_i}{dt} = \gamma_v(-J_{NaK_i} - J_{Cl_i} - 2J_{VOCC_i} - J_{Na/Ca_i} - J_{K_i} - J_{stretch_i} - J_{KIR_i}) + V^{SMC-EC}_{coupling_i} \tag{A.32}$$

Open state probability of $Ca^{2+}$-activated $K^+$ channels (-):

$$\frac{dw_i}{dt} = \lambda_i\,(K_{act_i} - w_i) \tag{A.33}$$

inositol trisphosphate ($IP_3$) concentration in the SMC (μM):

$$\frac{dIP3_i}{dt} = -J_{degrad_i} + J^{SMC-EC}_{IP_3-coupling_i} \tag{A.34}$$

$K^+$ concentration in the SMC (μM):

$$\frac{dK_i}{dt} = J_{NaK_i} - J_{KIR_i} - J_{K_i} \tag{A.35}$$

### A.3.2.2 *Algebraic Variables*

Release of $Ca^{2+}$ from $IP_3$ sensitive stores in the SMC (μM $s^{-1}$):

$$J_{IP3_i} = F_i \frac{IP3_i^2}{K_{ri}^2 + IP3_i^2} \tag{A.36}$$

Uptake of $Ca^{2+}$ into the SR (μM $s^{-1}$):

$$J_{SR_{uptake_i}} = B_i \frac{Ca_i^2}{c_{bi}^2 + Ca_i^2} \tag{A.37}$$

$Ca^{2+}$ induced $Ca^{2+}$ release (CICR) (μM $s^{-1}$):

$$J_{CICR_i} = C_i \frac{s_i^2}{s_{ci}^2 + s_i^2} \frac{Ca_i^4}{c_{ci}^4 + Ca_i^4} \tag{A.38}$$

$Ca^{2+}$ extrusion by $Ca^{2+}$-ATP-ase pumps ($\mu M\ s^{-1}$):

$$J_{extrusion_i} = D_i Ca_i \left(1 + \frac{v_i - v_d}{R_{di}}\right) \tag{A.39}$$

Leak current from the SR ($\mu M\ s^{-1}$):

$$J_{SR_{leak_i}} = L_i s_i \tag{A.40}$$

The flux of $Ca^{2+}$ through the voltage operated $Ca^{2+}$ channel (VOCC) which connects the SMC to the PVS ($\mu M\ s^{-1}$):

$$J_{VOCC_i} = G_{Cai} \frac{v_i - v_{Ca1}}{1 + \exp\left[-(v_i - v_{Ca2})/R_{Cai}\right]} \tag{A.41}$$

Flux of $Ca^{2+}$ exchanging with $Na^+$ in the $Na^+/Ca^{2+}$ exchange ($\mu M\ s^{-1}$):

$$J_{Na/Ca_i} = G_{Na/Ca_i} \frac{Ca_i}{Ca_i + c_{Na/Cai}} \left(v_i - v_{Na/Ca_i}\right) \tag{A.42}$$

$Ca^{2+}$ flux through the stretch-activated channels in the SMC ($\mu M\ s^{-1}$):

$$J_{stretch_i} = \frac{G_{stretch}}{1 + \exp\left(-\alpha_{stretch}\left(\frac{\Delta pR}{h} - \sigma_0\right)\right)} \left(v_i - E_{SAC}\right) \tag{A.43}$$

Flux through the $Na^+/K^+$ pump ($\mu M\ s^{-1}$):

$$J_{NaK_i} = F_{NaK} \tag{A.44}$$

$Cl^-$ flux through the $Cl^-$ channel ($\mu M\ s^{-1}$):

$$J_{Cl_i} = G_{Cli}\left(v_i - v_{Cli}\right) \tag{A.45}$$

$K^+$ flux through $K^+$ channel ($\mu M\ s^{-1}$):

$$J_{K_i} = G_{Ki} w_i \left(v_i - v_{K_i}\right) \tag{A.46}$$

$IP_3$ degradation ($\mu M\ s^{-1}$):

$$J_{degrad_i} = k_{di} IP3_i \tag{A.47}$$

Flux through inward rectifying $K^+$ (KIR) channels in the SMC ($\mu M\ s^{-1}$):

$$J_{KIR_i} = G_{KIR_i}(v_i - v_{KIR_i}) \tag{A.48}$$

Nernst potential of the KIR channel in the SMC (mV):

$$v_{KIR_i} = z_1 K_p - z_2 \tag{A.49}$$

Conductance of KIR channel ($\mu M\ mV^{-1}\ s^{-1}$):

$$G_{KIR_i} = F_{KIR_i} \exp(z_5 v_i + z_3 K_p - z_4) \tag{A.50}$$

Equilibrium distribution of open channel states for the SMC BK channel (-):

$$K_{act_i} = \frac{(Ca_i + c_{w,i})^2}{(Ca_i + c_{w,i})^2 + \alpha_{act_i} \exp(-([v_i - v_{Ca_{3i}}]/R_{Ki}))} \tag{A.51}$$

Heterocellular electrical coupling between SMCs and endothelial cells (ECs) ($mV\ s^{-1}$):

$$V^{SMC-EC}_{coupling_i} = -G_{coup}(v_i - v_j) \tag{A.52}$$

Heterocellular $IP_3$ coupling between SMCs and ECs ($\mu M\ s^{-1}$):

$$J^{SMC-EC}_{IP_3-coupling_i} = -P_{IP_3}(IP3_i - IP3_j) \tag{A.53}$$

$Ca^{2+}$ coupling between SMCs and ECs ($\mu M\ s^{-1}$):

$$J^{SMC-EC}_{Ca^{2+}-coupling_i} = -P_{Ca^{2+}}(Ca_i - Ca_j) \tag{A.54}$$

| Parameter | Description | Value |
|---|---|---|
| $\lambda_i$ | Rate constant for opening | 45 $s^{-1}$ |
| $F_i$ | Maximal rate of activation-dependent $Ca^{2+}$ influx | 0.23 $\mu M\ s^{-1}$ |
| $K_{ri}$ | Half-saturation constant for agonist-dependent $Ca^{2+}$ entry | 1 $\mu M$ |
| $B_i$ | SR uptake rate constant | 2.025 $\mu M\ s^{-1}$ |
| $c_{bi}$ | Half-point of the SR ATP-ase activation sigmoidal | 1 $\mu M$ |

| | | |
|---|---|---|
| $C_i$ | CICR rate constant | 55 $\mu M\ s^{-1}$ |
| $s_{ci}$ | Half-point of the CICR $Ca^{2+}$ efflux sigmoidal | 2 $\mu M$ |
| $c_{ci}$ | Half-point of the CICR activation sigmoidal | 0.9 $\mu M$ |
| $D_i$ | Rate constant for $Ca^{2+}$ extrusion by the ATP-ase pump | 0.24 $s^{-1}$ |
| $v_d$ | Intercept of voltage dependence of extrusion ATP-ase | $-100$ mV |
| $R_{di}$ | Slope of voltage dependence of extrusion ATP-ase | 250 mV |
| $L_i$ | Leak from SR rate constant | 0.025 $s^{-1}$ |
| $G_{Cai}$ | Whole-cell conductance for VOCCs | $1.29\times10^{-3}$ $\mu M\ mV^{-1}\ s^{-1}$ |
| $v_{Ca_{1i}}$ | Reversal potential for VOCCs | 100 mV |
| $v_{Ca_{2i}}$ | Half-point of the VOCC activation sigmoidal | $-24$ mV |
| $R_{Cai}$ | Maximum slope of the VOCC activation sigmoidal | 8.5 mV |
| $G_{Na/Cai}$ | Whole-cell conductance for $Na^+/Ca^{2+}$ exchange | $3.16\times10^{-3}$ $\mu M\ mV^{-1}\ s^{-1}$ |
| $c_{Na/Cai}$ | Half-point for activation of $Na^+/Ca^{2+}$ exchange by $Ca^{2+}$ | 0.5 $\mu M$ |
| $v_{Na/Cai}$ | Reversal potential for the $Na^+/Ca^{2+}$ exchanger | $-30$ mV |
| $G_{stretch}$ | Whole cell conductance for stretch activated channels (SACs) | $6.1\times10^{-3}$ $\mu M\ mV^{-1}\ s^{-1}$ |
| $\alpha_{stretch}$ | Slope of stress dependence of the SAC activation sigmoidal | $7.4\times10^{-3}$ $mmHg^{-1}$ |
| $\Delta p$ | Pressure difference over vessel | 30 mmHg |
| $\sigma_0$ | Half-point of the SAC activation sigmoidal | 500 mmHg |
| $E_{SAC}$ | Reversal potential for SACs | $-18$ mV |
| $F_{NaK}$ | Rate of the $K^+$ influx by the $Na^+/K^+$ pump | $4.32\times10^{-2}$ $\mu M\ s^{-1}$ |
| $G_{Cli}$ | Whole-cell conductance for $Cl^-$ current | $1.34\times10^{-3}$ $\mu M\ mV^{-1}\ s^{-1}$ |
| $v_{Cli}$ | Reversal potential for $Cl^-$ channels | $-25$ mV |
| $G_{Ki}$ | Whole-cell conductance for $K^+$ efflux | $4.46\times10^{-3}$ $\mu M\ mV^{-1}\ s^{-1}$ |
| $v_{K_i}$ | Nernst potential | $-94$ mV |
| $k_{di}$ | Rate constant of $IP_3$ degradation | 0.1 $s^{-1}$ |
| $F_{KIR_i}$ | Scaling factor of $K^+$ efflux through the KIR channel | 0.381 $\mu M\ mV^{-1}\ s^{-1}$ |
| $z_1$ | Model estimation for membrane voltage KIR channel | $4.5\times10^3$ mV $\mu M^{-1}$ |
| $z_2$ | Model estimation for membrane voltage KIR channel | 112 mV |
| $z_3$ | Model estimation for the KIR channel conductance | $4.2\times10^{-4}$ $\mu M^{-1}$ |
| $z_4$ | Model estimation for the KIR channel conductance | 12.6 |
| $z_5$ | Model estimation for the KIR channel conductance | $-7.4\times10^{-2}$ $mV^{-1}$ |
| $\alpha_{act_i}$ | Translation factor for $v_i$ dependence of $K_{act_i}$ sigmoidal | 0.13 $\mu M^2$ |
| $v_{Ca_{3i}}$ | Half-point for the $K_{act_i}$ activation sigmoidal | $-27$ mV |
| $R_{Ki}$ | Maximum slope of the $K_{act_i}$ activation sigmoidal | 12 mV |

| | | |
|---|---|---|
| $G_{coup}$ | Heterocellular electrical coupling coefficient | 0.5 $s^{-1}$ |
| $P_{IP_3}$ | Heterocellular $IP_3$ coupling coefficient | 0.05 $s^{-1}$ |
| $P_{Ca^{2+}}$ | Heterocellular $P_{Ca^{2+}}$ coupling coefficient | 0.05 $s^{-1}$ |

Table 3: Parameters used in the SMC compartment in the foundation model of Dormanns et al. [48].

### A.3.3 *EC*

#### A.3.3.1 *ODEs*

Cytosolic $Ca^{2+}$ concentration in the EC (µM):

$$\frac{dCa_j}{dt} = J_{IP_{3j}} - J_{ER_{uptake_j}} + J_{CICR_j} - J_{extrusion_j} + J_{ER_{leak_j}} + J_{cation_j} + J_{0_j} + J_{stretch_j} - J^{SMC-EC}_{Ca^{2+}-coupling_i} \tag{A.55}$$

$Ca^{2+}$ concentration in the endoplasmic reticulum (ER) of the EC (µM):

$$\frac{ds_j}{dt} = J_{ER_{uptake_j}} - J_{CICR_j} - J_{ER_{leak_j}} \tag{A.56}$$

Membrane potential of the EC (mV):

$$\frac{dv_j}{dt} = -\frac{1}{C_{m_j}}(I_{K_j} + I_{R_j}) - V^{SMC-EC}_{coupling_i} \tag{A.57}$$

$IP_3$ concentration of the EC (µM):

$$\frac{dIP3_j}{dt} = J_{PLC} - J_{degrad_j} - J^{SMC-EC}_{IP_3-coupling_i} \tag{A.58}$$

#### A.3.3.2 *Algebraic Variables*

Release of $Ca^{2+}$ from $IP_3$-sensitive stores in the EC (µM $s^{-1}$):

$$J_{IP_{3j}} = F_j \frac{IP3_j^2}{K_{rj}^2 + IP3_j^2} \tag{A.59}$$

Uptake of $Ca^{2+}$ into the ER (µM $s^{-1}$):

$$J_{ER_{uptake_j}} = B_j \frac{Ca_j^2}{c_{bj}^2 + Ca_j^2} \tag{A.60}$$

$Ca^{2+}$ induced $Ca^{2+}$ release (CICR) ($\mu M\ s^{-1}$):

$$J_{CICR_j} = C_j \frac{s_j^2}{s_{cj}^2 + s_j^2} \frac{Ca_j^4}{c_{cj}^4 + Ca_j^4} \tag{A.61}$$

$Ca^{2+}$ extrusion by $Ca^{2+}$-ATP-ase pumps ($\mu M\ s^{-1}$):

$$J_{extrusion_j} = D_j Ca_j \tag{A.62}$$

$Ca^{2+}$ flux through the stretch-activated channels in the EC ($\mu M\ s^{-1}$):

$$J_{stretch_j} = \frac{G_{stretch}}{1 + \exp\left(-\alpha_{stretch}\left(\frac{\Delta pR}{h} - \sigma_0\right)\right)} (v_j - E_{SAC}) \tag{A.63}$$

Leak current from the ER ($\mu M\ s^{-1}$):

$$J_{ER_{leak_j}} = L_j s_j \tag{A.64}$$

$Ca^{2+}$ influx through nonselective cation channels ($\mu M\ s^{-1}$):

$$J_{cation_j} = G_{cat_j}(E_{Ca_j} - v_j)\frac{1}{2}\left(1 + \tanh\left(\frac{\log_{10}(Ca_j/c_{log}) - m_{3_{cat_j}}}{m_{4_{cat_j}}}\right)\right) \tag{A.65}$$

$K^+$ current through the $BK_{Caj}$ channel and the $SK_{Caj}$ channel (fA):

$$I_{K_j} = G_{totj}(v_j - v_{Kj})\left(I_{BK_{Caj}} + I_{SK_{Caj}}\right) \tag{A.66}$$

$K^+$ efflux through the $BK_{Caj}$ channel (-):

$$I_{BK_{Caj}} = 0.2\left(1 + \tanh\left(\frac{(\log_{10}(Ca_j/c_{log}) - c)(v_j - b_j) - a_{1j}}{m_{3bj}(v_j + a_{2j}(\log_{10}(Ca_j/c_{log}) - c) - b_j)^2 + m_{4bj}}\right)\right) \tag{A.67}$$

$K^+$ efflux through the $SK_{Caj}$ channel (-):

$$I_{SK_{Caj}} = 0.3\left(1 + \tanh\left(\frac{\log_{10}(Ca_j/c_{log}) - m_{3sj}}{m_{4sj}}\right)\right) \tag{A.68}$$

Residual current regrouping $Cl^-$ and $Na^+$ current flux (fA):

$$I_{R_j} = G_{R_j}(v_j - v_{restj}) \tag{A.69}$$

$IP_3$ degradation ($\mu M\ s^{-1}$):

$$J_{degrad_j} = k_{dj} IP3_j \tag{A.70}$$

| Parameter | Description | Value |
|---|---|---|
| $J_{0_j}$ | Constant $Ca^{2+}$ influx | 0.029 $\mu M\ s^{-1}$ |
| $C_{m_j}$ | Membrane capacitance | 25.8 pF |
| $J_{PLC}$ | $IP_3$ production rate | 0.18 $\mu M\ s^{-1}$ |
| $F_j$ | Maximal rate of activation-dependent $Ca^{2+}$ influx | 0.23 $\mu M\ s^{-1}$ |
| $K_{rj}$ | Half-saturation constant for agonist-dependent $Ca^{2+}$ entry | 1 $\mu M$ |
| $B_j$ | ER uptake rate constant | 0.5 $\mu M\ s^{-1}$ |
| $c_{bj}$ | Half-point of the SR ATP-ase activation sigmoidal | 1 $\mu M$ |
| $C_j$ | CICR rate constant | 5 $\mu M\ s^{-1}$ |
| $s_{cj}$ | Half-point of the CICR $Ca^{2+}$ efflux sigmoidal | 2 $\mu M$ |
| $c_{cj}$ | Half-point of the CICR activation sigmoidal | 0.9 $\mu M$ |
| $D_j$ | Rate constant for $Ca^{2+}$ extrusion by the ATP-ase pump | 0.24 $s^{-1}$ |
| $L_j$ | Rate constant for $Ca^{2+}$ leak from the ER | 0.025 $s^{-1}$ |
| $G_{catj}$ | Whole-cell cation channel conductivity | $6.6\times10^{-4}$ $\mu M\ mV^{-1}\ s^{-1}$ |
| $E_{Caj}$ | $Ca^{2+}$ equilibrium potential | 50 mV |
| $c_{log}$ | Log constant | 1 $\mu M$ |
| $G_{totj}$ | Total $K^+$ channel conductivity | 6927 pS |
| $v_{Kj}$ | $K^+$ equilibrium potential | $-80$ mV |
| $m_{3_{catj}}$ | Model constant, further explanation see [111] | $-0.18$ |
| $m_{4_{catj}}$ | Model constant, further explanation see [111] | 0.37 |
| $c$ | Model constant, further explanation see [111] | $-0.4$ |
| $b_j$ | Model constant, further explanation see [111] | $-80.8$ mV |
| $a_{1j}$ | Model constant, further explanation see [111] | 53.3 mV |
| $a_{2j}$ | Model constant, further explanation see [111] | 53.3 mV |
| $m_{3bj}$ | Model constant, further explanation see [111] | $1.32\times10^{-3}$ $mV^{-1}$ |
| $m_{4bj}$ | Model constant, further explanation see [111] | 0.30 mV |
| $m_{3sj}$ | Model constant, further explanation see [111] | $-0.28$ |
| $m_{4sj}$ | Model constant, further explanation see [111] | 0.389 |
| $G_{R_j}$ | Residual current conductivity | 955 pS |
| $v_{restj}$ | Membrane resting potential | $-31.1$ mV |
| $k_{dj}$ | Rate constant of $IP_3$ degradation | 0.1 $s^{-1}$ |

Table 4: Parameters used in the EC compartment in the foundation model of Dormanns et al. [48].

### A.3.4 *Wall mechanics*

#### A.3.4.1 *ODEs*

Fraction of free phosphorylated cross-bridges (-):

$$\frac{d[Mp]}{dt} = K_4[AMp] + K_1[M] - (K_2 + K_3)[Mp] \tag{A.71}$$

Fraction of attached phosphorylated cross-bridges (-):

$$\frac{d[AMp]}{dt} = K_3[Mp] + K_6[AM] - (K_4 + K_5)[AMp] \tag{A.72}$$

Fraction of attached dephosphorylated cross-bridges (-):

$$\frac{d[AM]}{dt} = K_5[AMp] - (K_7 + K_6)[AM] \tag{A.73}$$

Vessel radius (μm):

$$\frac{dR}{dt} = \frac{R_{init}}{\eta}\left(\frac{RP_T}{h} - E\frac{R - R_0}{R_0}\right) \tag{A.74}$$

#### A.3.4.2 *Algebraic Variables*

Fraction of free non-phosphorylated cross-bridges (-):

$$[M] = 1 - [AM] - [AMp] - [Mp] \tag{A.75}$$

Rate constants for phosphorylation of M to Mp and of AM to AMp ($s^{-1}$):

$$K_1 = K_6 = \gamma_{cross} Ca_i^{n_{cross}} \tag{A.76}$$

Wall thickness of the vessel (μm):

$$h = 0.1R \tag{A.77}$$

Fraction of attached myosin cross-bridges (-):

$$F_r = [AM_p] + [AM] \tag{A.78}$$

Young's modulus (Pa):

$$E = E_{pas} + F_r\,(E_{act} - E_{pas}) \tag{A.79}$$

Initial radius (μm):

$$R_0 = R_{init} + F_r(\alpha_R - 1)R_{init} \tag{A.80}$$

| Parameter | Description | Value |
|---|---|---|
| $K_2$ | Rate constant for the dephosphorylation of Mp to M | 0.5 $s^{-1}$ |
| $K_3$ | Rate constant for attachment of phosphorylated crossbridges | 0.4 $s^{-1}$ |
| $K_4$ | Rate constant for detachment of phosphorylated crossbridges | 0.1 $s^{-1}$ |
| $K_5$ | Rate constant for the dephosphorylation of AMp to AM | 0.5 $s^{-1}$ |
| $K_7$ | Rate constant for detachment of dephosphorylated crossbridges | 0.1 $s^{-1}$ |
| $R_{init}$ | Vessel radius when passive and no stress is applied | 20 μm |
| $\eta$ | Viscosity | $10^4$ Pa s |
| $P_T$ | Transmural pressure | $4\times10^3$ Pa |
| $\gamma_{cross}$ | Sensitivity of the contractile apparatus to $Ca^{2+}$ | 17 $\mu M^{-3}s^{-1}$ |
| $n_{cross}$ | Fraction constant of the phosphorylation crossbridge | 3 |
| $E_{pas}$ | Young's moduli for the passive vessel | $66\times10^3$ Pa |
| $E_{act}$ | Young's moduli for the active vessel | $233\times10^3$ Pa |
| $\alpha_R$ | Scaling factor for initial radius | 0.6 |

Table 5: Parameters used in the wall mechanics submodule in the foundation model of Dormanns et al. [48].

## A.4 MODEL EXTENSION: EXTRACELLULAR DIFFUSION

This model extension is described in Chapter 3 and a schematic diagram can be found in Figure 8.

Extracellular $K^+$ concentration (μM):

$$\frac{dK_e}{dt} = J_{K_i} - J_{NaK_i} - J_{diff} \tag{A.81}$$

Diffusive flux between the extracellular space (ECS) and SC (μM $s^{-1}$):

$$J_{diff} = \frac{1}{\tau_s}\,(K_e - K_s) \tag{A.82}$$

### A.4.1 *Tissue slice model*

Extracellular $K^+$ in NVUs block with coordinates $i, j$ (μM):

$$\frac{dK_e^{i,j}}{dt} = J_{K_i}^{i,j} - J_{NaK_i}^{i,j} - J_{diff}^{i,j} - \frac{1}{\tau_e}\left(4K_e^{i,j} - K_e^{i-1,j} - K_e^{i+1,j} - K_e^{i,j-1} - K_e^{i,j+1}\right) \tag{A.83}$$

| Parameter | Description | Value |
|---|---|---|
| $\tau_s$ | Characteristic time for diffusion between the SC and ECS | 2.8 s |
| $\tau_e$ | Characteristic time for extracellular diffusion between adjacent NVU blocks | 4.3 s |

Table 6: Parameters used in the extracellular diffusion extension to the NVU model.

## A.5 MODEL EXTENSION: NITRIC OXIDE, ASTROCYTIC $Ca^{2+}$ DYNAMICS AND THE TRPV4 CHANNEL

This model extension is described in Chapter 4 and a schematic diagram can be found in Figure 14. The nitric oxide (NO) pathway is based on the work of Dormanns et al. [47].

### A.5.1 *NO pathway*

#### A.5.1.1 *Input to the model*

Glutamate concentration in the SC (μM):

$$Glu(t) = Glu_{max}\left[0.5\tanh\left(\frac{t-t_0}{\theta_L}\right) - 0.5\tanh\left(\frac{t-t_f}{\theta_R}\right)\right] \tag{A.84}$$

#### A.5.1.2 *ODEs*

$Ca^{2+}$ concentration in the neuron (μM):

$$\frac{dCa_n}{dt} = \frac{1}{1+\lambda_{buf}}\left(\frac{I_{Ca,tot}}{2FV_{spine}} - \kappa_{ex}(Ca_n - [Ca]_{rest})\right) \tag{A.85}$$

Activated neuronal NO synthase (nNOS) (μM):

$$\frac{d[nNOS]_n}{dt} = \frac{V_{max,nNOS}[CaM]_n}{K_{m,nNOS} + [CaM]_n} - \mu_{deact,n}[nNOS]_n \tag{A.86}$$

NO concentration in the neuron (μM):

$$\frac{dNO_n}{dt} = p_{NO,n} - c_{NO,n} + d_{NO,n} \tag{A.87}$$

NO concentration in the astrocyte (μM):

$$\frac{dNO_k}{dt} = p_{NO,k} - c_{NO,k} + d_{NO,k} \tag{A.88}$$

NO concentration in the SMC (μM):

$$\frac{dNO_i}{dt} = p_{NO,i} - c_{NO,i} + d_{NO,i} \tag{A.89}$$

Activated endothelial NO synthase (eNOS) (μM):

$$\frac{d[eNOS]_j}{dt} = \gamma_{eNOS}\frac{K_{dis}Ca_j}{K_{m,eNOS} + Ca_j} + (1 - \gamma_{eNOS})g_{max}F_{wss} - \mu_{deact,j}[eNOS]_j \tag{A.90}$$

NO concentration in the EC (μM):

$$\frac{dNO_j}{dt} = p_{NO,j} - c_{NO,j} + d_{NO,j} \tag{A.91}$$

Fraction of soluble guanylyl cyclase (sGC) in the basal state (-):

$$\frac{dE_b}{dt} = -k_1 E_b NO_i + k_{-1} E_{6c} + k_4 E_{5c} \tag{A.92}$$

Fraction of sGC in the intermediate form (-):

$$\frac{dE_{6c}}{dt} = k_1 E_b NO_i - (k_{-1} + k_2)E_{6c} - k_3 E_{6c} NO_i \tag{A.93}$$

Concentration of cyclic guanosine monophosphate (cGMP) in the SMC (μM):

$$\frac{dcGMP_i}{dt} = V_{max,sGC}E_{5c} - V_{max,pde}\frac{cGMP_i}{K_{m,pde} + cGMP_i} \tag{A.94}$$

### A.5.1.3 *Algebraic Variables*

Fraction of open NR2A N-methyl-D-aspartate (NMDA) receptors (-):

$$w_{NR2,A} = \frac{Glu(t)}{K_{m,A} + Glu(t)} \tag{A.95}$$

Fraction of open NR2B NMDA receptors (-):

$$w_{NR2,B} = \frac{Glu(t)}{K_{m,B} + Glu(t)} \tag{A.96}$$

Inward $Ca^{2+}$ current per open NMDA receptor (fA):

$$I_{Ca} = \frac{4\nu_n G_M (P_{Ca}/P_M)([Ca]_{ex}/[M])}{1 + \exp(\alpha_\nu(\nu_n + \beta_\nu))} \frac{\exp(2\nu_n/\phi))}{1 - \exp(2\nu_n/\phi))} \tag{A.97}$$

Total inward $Ca^{2+}$ current for all open NMDA receptors per synapse (fA):

$$I_{Ca,tot} = (n_{NR2,A} w_{NR2,A} + n_{NR2,B} w_{NR2,B}) I_{Ca} \tag{A.98}$$

$Ca^{2+}$-calmodulin complex concentration (μM):

$$[CaM]_n = \frac{Ca_n}{m_c} \tag{A.99}$$

Neuronal NO production flux (μM $s^{-1}$):

$$p_{NO,n} = V_{max,NO,n} [nNOS]_n \frac{[O_2]_n}{K_{m,O2,n} + [O_2]_n} \frac{[LArg]_n}{K_{m,LArg,n} + [LArg]_n} \tag{A.100}$$

Neuronal NO consumption flux (μM $s^{-1}$):

$$c_{NO,n} = k_{O2,n} [NO]_n^2 [O_2]_n \tag{A.101}$$

Neuronal NO diffusive flux (μM $s^{-1}$):

$$d_{NO,n} = \frac{[NO]_k - [NO]_n}{\tau_{nk}} \tag{A.102}$$

Time for NO to diffuse between the centres of the neuron and the astrocyte (s):

$$\tau_{nk} = \frac{x_{nk}^2}{2D_{c,NO}} \tag{A.103}$$

Astrocytic NO production flux ($\mu M\ s^{-1}$):

$$p_{NO,k} = 0 \tag{A.104}$$

Astrocytic NO consumption flux ($\mu M\ s^{-1}$):

$$c_{NO,k} = k_{O2,k}[NO]_k^2[O_2]_k \tag{A.105}$$

Astrocytic NO diffusive flux ($\mu M\ s^{-1}$):

$$d_{NO,k} = \frac{[NO]_n - [NO]_k}{\tau_{nk}} + \frac{[NO]_i - [NO]_k}{\tau_{ki}} \tag{A.106}$$

Time for NO to diffuse between the centres of the astrocyte and the SMC (s):

$$\tau_{ki} = \frac{x_{ki}^2}{2D_{c,NO}} \tag{A.107}$$

SMC NO production flux ($\mu M\ s^{-1}$):

$$p_{NO,i} = 0 \tag{A.108}$$

SMC NO consumption flux ($\mu M\ s^{-1}$):

$$c_{NO,i} = k_{dno}[NO]_i \tag{A.109}$$

SMC NO diffusive flux ($\mu M\ s^{-1}$):

$$d_{NO,i} = \frac{[NO]_k - [NO]_i}{\tau_{ki}} + \frac{[NO]_j - [NO]_i}{\tau_{ij}} \tag{A.110}$$

sGC kinetics rate constant ($s^{-1}$):

$$k_4 = C_4[cGMP]_i^2 \tag{A.111}$$

Fraction of sGC in the fully activated form (-):

$$E_{5c} = 1 - E_b - E_{6c} \tag{A.112}$$

Regulatory effect of cGMP on myosin dephosphorylation (-):

$$R_{cGMP} = \frac{[cGMP]_i^2}{K_{m,mlcp}^2 + [cGMP]_i^2} \tag{A.113}$$

Maximum cGMP production rate ($\mu M\ s^{-1}$):

$$V_{max,pde} = k_{pde}[cGMP]_i \tag{A.114}$$

Time for NO to diffuse between the centres of the SMC and the EC (s):

$$\tau_{ij} = \frac{x_{ij}^2}{2D_{c,NO}} \tag{A.115}$$

Fraction of the elastic strain energy stored within the membrane (-):

$$F_{wss} = \frac{1}{1 + \alpha_{wss}\exp(-W_{wss})} - \frac{1}{1 + \alpha_{wss}} \tag{A.116}$$

Strain energy density (-):

$$W_{wss} = W_0 \frac{(\tau_{wss} + \sqrt{16\delta_{wss}^2 + \tau_{wss}^2} - 4\delta_{wss})^2}{\tau_{wss} + \sqrt{16\delta_{wss}^2 + \tau_{wss}^2}} \tag{A.117}$$

Wall shear stress (Pa):

$$\tau_{wss} = \frac{R\Delta P}{2L} \tag{A.118}$$

EC NO production flux ($\mu M\ s^{-1}$):

$$p_{NO,j} = V_{max,NO,j}[eNOS]_j \frac{[O_2]_j}{K_{m,O2,j} + [O_2]_j} \frac{[LArg]_j}{K_{m,L\text{-}Arg,j} + [LArg]_j} \tag{A.119}$$

EC NO consumption flux ($\mu M\ s^{-1}$):

$$c_{NO,j} = k_{O2,j}[NO]_j^2[O_2]_j \tag{A.120}$$

EC NO diffusive flux ($\mu M\ s^{-1}$):

$$d_{NO,j} = \frac{[NO]_i - [NO]_j}{\tau_{ij}} - \frac{4D_{c,NO}[NO]_j}{r_l^2} \tag{A.121}$$

### A.5.1.4 *Modified equations*

Translation factor, regulatory effect of cGMP on the SMC BK channel open probability ($\mu M$):

$$c_{w,i} = \frac{\beta_{w,i}}{2}(1 + \tanh\left(\frac{cGMP_i - \alpha_{w,i}}{\epsilon_{w,i}}\right)) \tag{A.122}$$

Rate constants for dephosphorylation of Mp to M and of AMp to AM ($s^{-1}$):

$$K_2 = K_5 = \delta_K \left(k_{mlpc,b} + k_{mlpc,c} R_{cGMP}\right) \tag{A.123}$$

| Parameter | Description | Value |
|---|---|---|
| $[Glu]_{max}$ | Maximum glutamate concentration (one vesicle) | 1846 $\mu M$ |
| $\theta_L$ | Slope scaling factor for $Glu(t)$ | 1 s |
| $\theta_R$ | Slope scaling factor for $Glu(t)$ | 1 s |
| $\lambda_{buf}$ | Buffer capacity | 20 |
| $V_{spine}$ | Dendritic spine volume | $8 \times 10^{-5}$ pL |
| $\kappa_{ex}$ | Decay rate constant of internal $Ca^{2+}$ concentration | $1.6 \times 10^3\ s^{-1}$ |
| $[Ca]_{rest}$ | Resting internal $Ca^{2+}$ concentration | 0.1 $\mu M$ |
| $V_{max,nNOS}$ | Maximum nNOS activation rate | $25 \times 10^{-3}\ \mu M\ s^{-1}$ |
| $K_{m,nNOS}$ | Michaelis constant | $9.27 \times 10^{-2}\ \mu M$ |
| $\mu_{deact,n}$ | Rate constant at which nNOS is deactivated | $0.0167\ s^{-1}$ |
| $\gamma_{eNOS}$ | Relative strength of the $Ca^{2+}$ dependent pathway for eNOS activation | 0.1 |
| $K_{dis}$ | eNOS-caveolin disassociation rate | $0.09\ \mu M\ s^{-1}$ |
| $K_{m,eNOS}$ | Michaelis constant | 0.45 $\mu M$ |
| $g_{max}$ | Maximum wall-shear-stress-induced eNOS activation | $0.06\ \mu M\ s^{-1}$ |
| $\mu_{deact,j}$ | eNOS-caveolin association rate | $0.0167\ s^{-1}$ |
| $k_{-1}$ | sGC kinetics rate constant | $100\ s^{-1}$ |
| $k_1$ | sGC kinetics rate constant | $2 \times 10^3\ \mu M^{-1}\ s^{-1}$ |
| $k_2$ | sGC kinetics rate constant | $0.1\ s^{-1}$ |
| $k_3$ | sGC kinetics rate constant | $3\ \mu M^{-1}\ s^{-1}$ |
| $V_{max,sGC}$ | Maximal cGMP production rate | $0.8520\ \mu M\ s^{-1}$ |
| $K_{m,pde}$ | Michaelis constant | 2 $\mu M$ |

| | | |
|---|---|---|
| $K_{m,A}$ | Michaelis constant | 650 μM |
| $K_{m,B}$ | Michaelis constant | 2800 μM |
| $v_n$ | Neuronal membrane potential | −40 mV |
| $G_M$ | Conductance of NMDA receptor | 46 pS |
| $P_{Ca}/P_M$ | Ratio of $Ca^{2+}$ permeability to monovalent ion permeability | 3.6 |
| $[Ca]_{ex}$ | External $Ca^{2+}$ concentration | $2 \times 10^3$ μM |
| [M] | Concentration of monovalent ions | $1.3 \times 10^5$ μM |
| $\alpha_v$ | Voltage-dependent $Mg^{2+}$ block parameter | $-0.08$ $mV^{-1}$ |
| $\beta_v$ | Voltage-dependent $Mg^{2+}$ block parameter | 20 mV |
| $n_{NR2,A}$ | Average number of NR2A NMDA receptors | 0.63 |
| $n_{NR2,B}$ | Average number of NR2B NMDA receptors | 11 |
| $m_c$ | Number of $Ca^{2+}$ ions bound per calmodulin | 4 |
| $V_{max,NO,n}$ | Maximum catalytic rate of neuronal NO production | 4.22 $s^{-1}$ |
| $[O_2]_n$ | oxygen ($O_2$) concentration in the neuron | 200 μM |
| $K_{m,O2,n}$ | Michaelis constant for nNOS for $O_2$ | 243 μM |
| $[LArg]_n$ | L-Arg concentration in the neuron | 100 μM |
| $K_{m,LArg,n}$ | Michaelis constant for nNOS for LArg | 1.5 μM |
| $k_{O2,n}$ | $O_2$ reaction rate constant | $9.6 \times 10^{-6}$ $\mu M^{-2}$ $s^{-1}$ |
| $x_{nk}$ | Distance between centres of neuron and astrocyte | 25 μm |
| $D_{c,NO}$ | NO diffusion coefficient | 3300 $\mu m^2 s^{-1}$ |
| $k_{O2,k}$ | $O_2$ reaction rate constant | $9.6 \times 10^{-6} \mu M^{-2} s^{-1}$ |
| $[O_2]_k$ | $O_2$ concentration in the astrocyte | 200 μM |
| $x_{ki}$ | Distance between centres of astrocyte and SMC compartments | 25 μm |
| $k_{dno}$ | Constant reflecting the activity of various NO scavengers | 0.01 $s^{-1}$ |
| $C_4$ | sGC rate scaling constant | 0.011 $\mu M^{-2}$ $s^{-1}$ |
| $K_{m,mlcp}$ | Hill coefficient | 5.5 μM |
| $k_{pde}$ | Phosphodiesterase rate constant | 0.0195 $s^{-1}$ |
| $x_{ij}$ | Distance between centres of SMC and EC compartments | 3.75 μm |
| $\alpha_{wss}$ | Zero shear open channel constant | 2 |
| $W_0$ | Shear gating constant | 1.4 $Pa^{-1}$ |
| $\delta_{wss}$ | Membrane shear modulus | 2.86 Pa |
| $\Delta P/L$ | Pressure drop over length of arteriole | $9.1 \times 10^{-2}$ Pa $\mu m^{-1}$ |
| $V_{max,NO,j}$ | Maximum catalytic rate of NO production | 1.22 $s^{-1}$ |
| $[O_2]_j$ | $O_2$ concentration in the EC | 200 μM |
| $K_{m,O2,j}$ | Michaelis constant for eNOS for $O_2$ | 7.7 μM |
| $[LArg]_j$ | L-Arg concentration in the neuron | 100 μM |
| $K_{m,L\text{-}Arg,j}$ | Michaelis constant for L-Arg | 1.5 μM |

| | | |
|---|---|---|
| $k_{O2,j}$ | $O_2$ reaction rate constant | $9.6 \times 10^{-6}$ μM $^{-2}$ $s^{-1}$ |
| $r_l$ | Constant of lumen radius | 25 μm |
| $\beta_{w,i}$ | Constant to fit data | 1 μM |
| $\alpha_{w,i}$ | Constant to fit data | 10.75 μM |
| $\epsilon_{w,i}$ | Constant to fit data | 0.668 μM |
| $\delta_K$ | Constant to fit data | 58.14 |
| $k_{mlpc,b}$ | Basal MLC dephosphorylation rate constant | $0.86 \times 10^{-2}$ $s^{-1}$ |
| $k_{mlpc,c}$ | First-order rate constant for cGMP regulated MLC dephosphorylation | $3.27 \times 10^{-2}$ $s^{-1}$ |

Table 7: Parameters used in the NO extension to the NVU model.

### A.5.2 *Astrocytic $Ca^{2+}$ Pathway and TRPV4 channel*

#### A.5.2.1 *ODEs*

The astrocytic cytosolic $Ca^{2+}$ concentration (μM):

$$\frac{dCa_k}{dt} = B_{cyt}\left(J_{IP3_k} - J_{pump_k} + J_{ERleak_k} - \frac{J_{TRPV_k}}{r_{buff}}\right) \tag{A.124}$$

The astrocytic $IP_3$ concentration (μM):

$$\frac{dIP3_k}{dt} = r_h G - k_{deg}\ IP3_k \tag{A.125}$$

The astrocytic epoxyeicosatrienoic acid (EET) concentration (μM):

$$\frac{deet_k}{dt} = V_{eet}\max(Ca_k - c_{k_{min}}, 0) - k_{eet}eet_k \tag{A.126}$$

The $Ca^{2+}$ concentration in the astrocytic ER (μM):

$$\frac{ds_k}{dt} = \frac{-B_{cyt}}{VR_{ERcyt}}\left(J_{IP3_k} - J_{pump_k} + J_{ERleak_k}\right) \tag{A.127}$$

The inactivation variable $h_k$ of the astrocytic $IP_3R$ channel (-):

$$\frac{dh_k}{dt} = k_{on}\left[K_{inh} - (Ca_k + K_{inh})h_k\right] \tag{A.128}$$

$Ca^{2+}$ concentration in the PVS (μM):

$$\frac{dCa_p}{dt} = \frac{J_{TRPV_k}}{VR_{pk}} + \frac{J_{VOCC_i}}{VR_{pi}} - Ca_{decay_p}(Ca_p - Ca_{min_p}) \tag{A.129}$$

The open probability of the transient receptor potential vanniloid-related 4 (TRPV4) channel (-):

$$\frac{dm_k}{dt} = \frac{m_{\infty_k} - m_k}{t_{TRPV_k}} \tag{A.130}$$

### A.5.2.2 *Algebraic Variables*

The ratio ρ of bound to unbound metabotropic receptors on the astrocytic process adjacent to the SC (-):

$$\rho = \rho_{min} + \frac{\rho_{max} - \rho_{min}}{Glu_{max}} Glu(t) \tag{A.131}$$

The ratio G of active to total G-protein due to metabotropic glutamate receptor (mGluR) binding on the astrocyte endfoot surround the SC (-):

$$G = \frac{\rho + \delta_G}{K_G + \rho + \delta_G} \tag{A.132}$$

Fast $Ca^{2+}$ buffering is described within the steady state approximation (-):

$$B_{cyt} = \left(1 + BK_{end} + \frac{K_{ex}B_{ex}}{(K_{ex} + Ca_k)^2}\right)^{-1} \tag{A.133}$$

The flux of $Ca^{2+}$ through the $IP_3R$ channel (μM $s^{-1}$):

$$J_{IP3_k} = J_{max}\left[\left(\frac{IP3_k}{IP3_k + K_i}\right)\left(\frac{Ca_k}{Ca_k + K_{act_k}}\right)h_k\right]^3\left(1 - \frac{Ca_k}{s_k}\right) \tag{A.134}$$

The flux of $Ca^{2+}$ through the uptake pump (μM $s^{-1}$):

$$J_{pump_k} = V_{max}\frac{Ca_k^2}{Ca_k^2 + k_{pump}^2} \tag{A.135}$$

The flux of $Ca^{2+}$ through the leak channel (μM $s^{-1}$):

$$J_{ERleak_k} = P_L\left(1 - \frac{Ca_k}{s_k}\right) \tag{A.136}$$

The flux of $Ca^{2+}$ through the TRPV4 channel ($\mu M\ s^{-1}$):

$$J_{TRPV_k} = G_{TRPV_k} m_k (v_k - E_{TRPV_k}) c_{unit} \tag{A.137}$$

The Nernst potential of the TRPV4 channel (V):

$$E_{TRPV_k} = \frac{R_g T}{z_{Ca} \tilde{F}} \log\left(\frac{Ca_p}{Ca_k}\right) \tag{A.138}$$

The equilibrium state of the TRPV4 channel (-):

$$m_{\infty_k} = \Gamma_m \left[\frac{1}{1 + H_{Ca_k}} \left(H_{Ca_k} + \tanh\left(\frac{v_k - v_{1,TRPV}}{v_{2,TRPV}}\right)\right)\right] \tag{A.139}$$

The material strain gating term (-):

$$\Gamma_m = \frac{1}{1 + \exp\left(-\frac{\eta - \eta_0}{\kappa_k}\right)} \tag{A.140}$$

The strain on the perivascular endfoot of the astrocyte (-)

$$\eta = \frac{R - R_{init}}{R_{init}} \tag{A.141}$$

The $Ca^{2+}$ inhibitory term (-)

$$H_{Ca_k} = \frac{Ca_k}{\gamma_{Cai}} + \frac{Ca_p}{\gamma_{Cae}} \tag{A.142}$$

The voltage associated with half open probability of the BK channel (mV):

$$v_3 = -\frac{v_5}{2} \tanh\left(\frac{Ca_k - Ca_3}{Ca_4}\right) + v_6 \tag{A.143}$$

### A.5.2.3 *Modified Equations*

Membrane voltage of the astrocyte (V):

$$v_k = \frac{g_{Na_k} E_{Na_k} + g_{K_k} E_{K_k} + g_{Cl_k} E_{Cl_k} + g_{NBC_k} E_{NBC_k} + g_{BK_k} w_k E_{BK_k} + g_{TRPV_k} m_k E_{TRPV_k} - J_{NaK_k} \tilde{F} / c_{unit}}{g_{Na_k} + g_{K_k} + g_{Cl_k} + g_{NBC_k} + g_{BK_k} w_k + g_{TRPV_k} m_k} \tag{A.144}$$

The time constant associated with the opening of the BK channel ($s^{-1}$):

$$\phi_n = \psi_n \cosh\left(\frac{v_k - v_3}{2 v_4}\right) \tag{A.145}$$

The equilibrium state of the BK channel (-):

$$w_\infty = \frac{1}{2}\left(1 + \tanh\left(\frac{v_k + eet_{shift}eet_k - v_3}{v_4}\right)\right) \tag{A.146}$$

| Parameter | Description | Value |
|---|---|---|
| $r_{buff}$ | Rate of $Ca^{2+}$ buffering at the endfoot compared to the astrocyte body | 0.05 |
| $r_h$ | Maximum rate of $IP_3$ production in astrocyte due to glutamate receptors | 4.8 $\mu M\ s^{-1}$ |
| $k_{deg}$ | Rate constant for $IP_3$ degradation in astrocyte | 1.25 $s^{-1}$ |
| $V_{eet}$ | EET production rate | 72 $s^{-1}$ |
| $c_{k_{min}}$ | Minimum $Ca^{2+}$ concentration required for EET production | 0.1 $\mu M$ |
| $k_{eet}$ | EET degradation rate | 7.2 $s^{-1}$ |
| $VR_{ERcyt}$ | Volume ratio between ER and astrocytic cytosol | 0.185 |
| $k_{on}$ | Rate of $Ca^{2+}$ binding to the inhibitory site on the $IP_3R$ | 2 $\mu M^{-1}\ s^{-1}$ |
| $K_{inh}$ | Disassociation constant of $IP_3R$ | 0.1 $\mu M$ |
| $Ca_{decay_p}$ | Rate of decay of $Ca^{2+}$ in PVS | 0.5 $s^{-1}$ |
| $Ca_{min_p}$ | Steady state value of $Ca^{2+}$ in PVS | $2 \times 10^3$ $\mu M$ |
| $t_{TRPV_k}$ | Characteristic time constant for $m_k$ | 0.9 s |
| $\rho_{min}$ | Minimum ratio of bound to unbound $IP_3$ receptors | 0.1 |
| $\rho_{max}$ | Maximum ratio of bound to unbound $IP_3$ receptors | 0.7 |
| $\delta_G$ | Ratio of the activities of the unbound and bound receptors | $1.235 \times 10^{-2}$ |
| $K_G$ | G-protein disassociation constant | 8.82 |
| $BK_{end}$ | Ratio of endogenous buffer concentration to disassociation constant | 40 |
| $K_{ex}$ | Disassociation constant of exogenous buffer | 0.26 $\mu M$ |
| $B_{ex}$ | Concentration of exogenous buffer | 11.35 $\mu M$ |
| $J_{max}$ | Maximum rate of $Ca^{2+}$ through the $IP_3$ mediated channel | 2880 $\mu M\ s^{-1}$ |
| $K_i$ | Disassociation constant for $IP_3$ binding to an $IP_3R$ | 0.03 $\mu M$ |
| $K_{act_k}$ | Disassociation constant for $Ca^{2+}$ binding to an activation site on an $IP_3R$ | 0.17 $\mu M$ |
| $V_{max}$ | Maximum rate of $Ca^{2+}$ uptake pump on the ER | 20 $\mu M\ s^{-1}$ |
| $k_{pump}$ | $Ca^{2+}$ uptake pump disassociation constant | 0.24 $\mu M$ |
| $P_L$ | ER leak channel steady state balance constant | 0.0804 $\mu M\ s^{-1}$ |
| $G_{TRPV_k}$ | TRPV4 whole cell conductance | $3.15 \times 10^{-4}$ $\mu M\ mV^{-1}\ s^{-1}$ |

| | | |
|---|---|---|
| $v_{1,TRPV}$ | TRPV4 channel voltage gating constant | 0.12 V |
| $v_{2,TRPV}$ | TRPV4 channel voltage gating constant | 0.013 V |
| $\eta_0$ | Strain required for half activation of the TRPV4 channel | 0.1 |
| $\kappa_k$ | TRPV4 channel strain constant | 0.1 |
| $\gamma_{Cai}$ | $Ca^{2+}$ concentration constant | 0.01 μM |
| $\gamma_{Cae}$ | $Ca^{2+}$ concentration constant | 200 μM |
| $Ca_3$ | BK open probability $Ca^{2+}$ constant | 0.4 μM |
| $Ca_4$ | BK open probability $Ca^{2+}$ constant | 0.35 μM |
| $g_{TRPV_k}$ | TRPV4 channel conductance per unit area | $1.35 \times 10^{-2}$ S $m^2$ |
| $v_4$ | Measure of the spread of $w_\infty$ (*) | $8\times10^{-3}$ V |
| $v_5$ | Determines the range of the shift of $w_\infty$ as $Ca^{2+}$ varies (*) | $15\times10^{-3}$ V |
| $v_6$ | Shifts the range of $w_\infty$ (*) | $-55 \times 10^{-3}$ V |
| $eet_{shift}$ | Describes the EET dependent voltage shift | $2\times10^{-3}$ μM $^{-1}$ |

Table 8: Parameters used in the astrocytic $Ca^{2+}$ and TRPV4 channel extension to the NVU model, where an asterisk (*) denotes a parameter that has changed in value from the previous model version.

### A.5.3 *Other modified equations*

Cytosolic $Ca^{2+}$ in the SMC (μM):

$$\frac{dCa_i}{dt} = J_{IP_{3i}} - J_{SR_{uptake_i}} + J_{CICR_i} - J_{extrusion_i} + J_{SR_{leak_i}} - J_{VOCC_i} + J_{Na/Ca_i} - 0.1J_{stretch_i} + J^{SMC-EC}_{Ca^{2+}-coupling_i} \tag{A.147}$$

Cytosolic $Ca^{2+}$ concentration in the EC (μM):

$$\frac{dCa_j}{dt} = J_{IP_{3j}} - J_{ER_{uptake_j}} + J_{CICR_j} - J_{extrusion_j} + J_{ER_{leak_j}} + J_{cation_j} + J_{0_j} - J_{stretch_j} - J^{SMC-EC}_{Ca^{2+}-coupling_i} \tag{A.148}$$

| | | |
|---|---|---|
| $J_{PLC}$ | $IP_3$ production rate (*) | 0.11 μM $s^{-1}$ |

## A.6 MODEL EXTENSION: NEURON DYNAMICS AND THE BOLD SIGNAL

This model extension is described in Chapter 5 and a schematic diagram can be found in Figure 22. The neuron dynamics and blood-oxygen-level dependent (BOLD) signal submodel is based on

the work of Mathias et al. [122]. The flux $J_{diff}$ and the input functions $K(t)$ and $Glu(t)$ from the previous model version have been removed.

### A.6.1 *Neuron and Extracellular Space*

#### A.6.1.1 *Input to the model*

The input current to the soma (mA cm$^{-2}$):

$$I_{input} = \begin{cases} I_{strength}, & \text{for } t_0 \leqslant t \leqslant t_1 \\ 0 & \text{otherwise} \end{cases} \tag{A.149}$$

#### A.6.1.2 *ODEs*

The membrane potential of the soma/axon ($v_{sa}$) and dendrite ($v_d$) (mV):

$$C_m \frac{dv_{sa}}{dt} = -I_{tot_{sa}} + \frac{1}{2R_a\delta_d^2}(v_d - v_{sa}) + I_{input} \tag{A.150}$$

$$C_m \frac{dv_d}{dt} = -I_{tot_d} + \frac{1}{2R_a\delta_d^2}(v_{sa} - v_d) \tag{A.151}$$

The ion concentrations ($K^+$ and $Na^+$) in the soma/axon (mM):

$$\frac{dK_{sa}}{dt} = -\frac{A_s}{FV_s} I_{K,tot_{sa}} + \frac{D_{K,n}(V_d + V_s)}{2\delta_d^2 V_s}(K_d - K_{sa}) \tag{A.152}$$

$$\frac{dNa_{sa}}{dt} = -\frac{A_s}{FV_s} I_{Na,tot_{sa}} + \frac{D_{Na,n}(V_d + V_s)}{2\delta_d^2 V_s}(Na_d - Na_{sa}) \tag{A.153}$$

The ion concentrations ($K^+$ and $Na^+$) in the dendrite (mM):

$$\frac{dK_d}{dt} = -\frac{A_d}{FV_d} I_{K,tot_d} + \frac{D_{K,n}(V_d + V_s)}{2\delta_d^2 V_d}(K_{sa} - K_d) \tag{A.154}$$

$$\frac{dNa_d}{dt} = -\frac{A_d}{FV_d} I_{Na,tot_d} + \frac{D_{Na,n}(v_d + V_s)}{2\delta_d^2 V_d}(Na_{sa} - Na_d) \tag{A.155}$$

The $Na^+$ ion concentration in the ECS (mM):

$$\frac{dNa_e}{dt} = \frac{1}{Ff_e}\left(\frac{A_s I_{Na,tot_{sa}}}{V_s} + \frac{A_d I_{Na,tot_d}}{v_d}\right) \tag{A.156}$$

The buffer concentration in the ECS ($Buff_e$) (mM):

$$\frac{dBuff_e}{dt} = \mu(B_0 - Buff_e)\frac{K_e}{1+\exp\left(\frac{-(K_e-5.5)}{1.09}\right)} - \mu Buff_e \tag{A.157}$$

Activation gating variable $m_*$ (for $m_1$ to $m_8$) (-):

$$\frac{dm_*}{dt} = (\alpha_{m_*}(1-m_*) - \beta_{m_*}m_*) \tag{A.158}$$

Deactivation gating variable $h_*$ (for $h_1$ to $h_6$) (-):

$$\frac{dh_*}{dt} = (\alpha_{h_*}(1-h_*) - \beta_{h_*}h_*) \tag{A.159}$$

The tissue $O_2$ concentration (mM):

$$\frac{dO_2}{dt} = J_{O_2\,vascular} - J_{O_2\,background} - J_{O_2\,pump} \tag{A.160}$$

### A.6.1.3 *Algebraic Variables*

Total current of ions in soma/axon (sa) or dendrite (d) (mA $cm^{-2}$):

$$I_{tot_*} = I_{K,tot_*} + I_{Na,tot_*} + I_{leak_*} \tag{A.161}$$

Total current of $K^+$ in soma/axon (mA $cm^{-2}$):

$$I_{K,tot_{sa}} = I_{KDR_{sa}} + I_{KA_{sa}} + I_{K,leak_{sa}} + I_{pump,K_{sa}} \tag{A.162}$$

Total current of $K^+$ in dendrite (mA $cm^{-2}$):

$$I_{K,tot_d} = I_{KDR_d} + I_{KA_d} + I_{K,leak_d} + I_{pump,K_d} + I_{NMDA,K_d} \tag{A.163}$$

Total current of $Na^+$ in soma/axon (mA $cm^{-2}$):

$$I_{Na,tot_{sa}} = I_{NaP_{sa}} + I_{NaT_{sa}} + I_{Na,leak_{sa}} + I_{pump,Na_{sa}} \tag{A.164}$$

Total current of $Na^+$ in dendrite (mA $cm^{-2}$):

$$I_{Na,tot_d} = I_{NaP_d} + I_{Na,leak_d} + I_{pump,Na_d} + I_{NMDA,Na_d} \tag{A.165}$$

$K^+$ current through $Na^+/K^+$ ATP-ase pump in the soma/axon (sa) or dendrite (d) (mA $cm^{-2}$):

$$I_{pump,K_*} = -2\, I_{pump_*} \tag{A.166}$$

$Na^+$ current through $Na^+/K^+$ ATP-ase pump in soma/axon (sa) or dendrite (d) (mA $cm^{-2}$):

$$I_{pump,Na_*} = 3\, I_{pump_*} \tag{A.167}$$

$Na^+/K^+$ ATP-ase pump flux in soma/axon (sa) or dendrite (d) (mA $cm^{-2}$):

$$I_{pump_*} = I_{max} J_{pump1_*} J_{pump2}(O_2) \tag{A.168}$$

Oxygen independent term of the ATP-ase pump in both the soma/axon (sa) or dendrite (d) (-):

$$J_{pump1_*} = \left(1 + \frac{K_{e,0}}{K_e}\right)^{-2} \left(1 + \frac{Na_{*,0}}{Na_*}\right)^{-3} \tag{A.169}$$

Oxygen dependent term of the ATP-ase pump (-):

$$J_{pump2}(O_2) = 2\left(1 + \frac{O2_0}{(1-\alpha_{O2})\, O_2 + \alpha_{O2}\, O2_0}\right)^{-1} \tag{A.170}$$

The vascular supply of $O_2$ (mM $s^{-1}$):

$$J_{O_2\, vascular} = J\frac{O2_b - O_2}{O2_b - O2_0} \tag{A.171}$$

The background $O_2$ consumption (mM $s^{-1}$):

$$J_{O_2\, background} = J_0 P_{O2}(1 - \gamma_{O2}) \tag{A.172}$$

The tissue $O_2$ consumption due to the ATP-ase pump (mM $s^{-1}$):

$$J_{O_2\, pump} = J_0 P_{O2} \gamma_{O2} \frac{J_{pump1_{sa}} + J_{pump1_d}}{J_{pump1_{sa_0}} + J_{pump1_{d_0}}} \tag{A.173}$$

The change in $O_2$ concentration due to cerebral blood flow (CBF) (mM $s^{-1}$):

$$J = J_0 \frac{CBF}{CBF_{init}} \tag{A.174}$$

The CBF (-):

$$CBF = CBF_{init} \frac{R^4}{R^4_{init}} \tag{A.175}$$

The normalised pump rate (-):

$$P_{O2} = \frac{J_{pump2}(O_2) - J_{pump2}(0)}{J_{pump2}(O2_0) - J_{pump2}(0)} \tag{A.176}$$

Leak currents of $K^+$, $Na^+$ and general leak in the soma/axon or dendrite (mA $cm^{-2}$):

$$I_{K,leak_*} = g_{K,leak_*}(v_* - E_{K_*}) \tag{A.177}$$

$$I_{Na,leak_*} = g_{Na,leak_*}(v_* - E_{Na_*}) \tag{A.178}$$

$$I_{leak_*} = g_{leak_*}(v_* - E_{leak_*}) \tag{A.179}$$

Nernst potential for $K^+$ and $Na^+$ in the soma/axon (sa) or dendrite (d) (mV):

$$E_{K_*} = \frac{\phi}{z_K} \ln\left(\frac{K_e}{K_*}\right) \tag{A.180}$$

$$E_{Na_*} = \frac{\phi}{z_{Na}} \ln\left(\frac{Na_e}{Na_*}\right) \tag{A.181}$$

$K^+$ current through delayed rectifier $K^+$ (KDR) channel in the soma/axon (mA $cm^{-2}$):

$$I_{KDR_{sa}} = m_2^2 \, \frac{g_{KDR} F v_{sa} \left(K_{sa} - \exp\left(\frac{-v_{sa}}{\phi}\right) K_e\right)}{\phi \left(1 - \exp\left(\frac{-v_{sa}}{\phi}\right)\right)} \tag{A.182}$$

$K^+$ current through transient $K^+$ (KA) channel in the soma/axon (mA $cm^{-2}$):

$$I_{KA_{sa}} = m_3^2 \, h_2 \, \frac{g_{KA} F v_{sa} \left(K_{sa} - \exp\left(\frac{-v_{sa}}{\phi}\right) K_e\right)}{\phi \left(1 - \exp\left(\frac{-v_{sa}}{\phi}\right)\right)} \tag{A.183}$$

$K^+$ current through KDR channel in the dendrite (mA $cm^{-2}$):

$$I_{KDR_d} = m_6^2 \, \frac{g_{KDR} F v_d \left(K_d - \exp\left(\frac{-v_d}{\phi}\right) K_e\right)}{\phi \left(1 - \exp\left(\frac{-v_d}{\phi}\right)\right)} \tag{A.184}$$

$K^+$ current through KA channel in the dendrite (mA $cm^{-2}$):

$$I_{KA_d} = m_7^2 \, h_5 \, \frac{g_{KA} F v_d \left(K_d - \exp\left(\frac{-v_d}{\phi}\right) K_e\right)}{\phi \left(1 - \exp\left(\frac{-v_d}{\phi}\right)\right)} \tag{A.185}$$

$K^+$ current through NMDA channel in the dendrite (mA $cm^{-2}$):

$$I_{NMDA,K_d} = m_5 \, h_4 \, \frac{g_{NMDA} F v_d \left(K_d - \exp\left(\frac{-v_d}{\phi}\right) K_e\right)}{\phi \left(1 - \exp\left(\frac{-v_d}{\phi}\right)\right) \left(1 + 0.33 \, [Mg]_0 \exp(-0.07 v_d - 0.7)\right)} \tag{A.186}$$

$Na^+$ current through persistent $Na^+$ (NaP) channel in soma/axon (mA $cm^{-2}$):

$$I_{NaP,Na_{sa}} = m_1^2 \, h_1 \, \frac{g_{NaP} F v_{sa} \left(Na_{sa} - \exp\left(\frac{-v_{sa}}{\phi}\right) Na_e\right)}{\phi \left(1 - \exp\left(\frac{-v_{sa}}{\phi}\right)\right)} \tag{A.187}$$

$Na^+$ current through transient $Na^+$ (NaT) channel in soma/axon (mA $cm^{-2}$):

$$I_{NaT,Na_{sa}} = m_8^3 \, h_6 \, \frac{g_{NaT} F v_{sa} \left(Na_{sa} - \exp\left(\frac{-v_{sa}}{\phi}\right) Na_e\right)}{\phi \left(1 - \exp\left(\frac{-v_{sa}}{\phi}\right)\right)} \tag{A.188}$$

$Na^+$ current through NaP channel in dendrite (mA $cm^{-2}$):

$$I_{NaP,Na_d} = m_4^2 \, h_3 \, \frac{g_{NaP} F v_d \left(Na_d - \exp\left(\frac{-v_d}{\phi}\right) Na_e\right)}{\phi \left(1 - \exp\left(\frac{-v_d}{\phi}\right)\right)} \tag{A.189}$$

$Na^+$ current through NMDA channel in dendrite (mA $cm^{-2}$):

$$I_{NMDA,Na_d} = m_5 \, h_4 \, \frac{g_{NMDA} F v_d \left(Na_d - \exp\left(\frac{-v_d}{\phi}\right) Na_e\right)}{\phi \left(1 - \exp\left(\frac{-v_d}{\phi}\right)\right) \left(1 + 0.33 \, [Mg]_0 \exp(-0.07 v_d - 0.7)\right)} \tag{A.190}$$

Rate functions for the activation ($m$) gating variables ($s^{-1}$):

$$\alpha_{m_1} = \frac{1000}{6} \frac{1}{1 + \exp(-(0.143 v_{sa} + 5.67))} \tag{A.191}$$

$$\beta_{m_1} = \frac{1000}{6} - \alpha_{m_1} \tag{A.192}$$

$$\alpha_{m_2} = 16\frac{v_{sa} + 34.9}{1 - \exp(-(0.2v_{sa} + 6.98))} \tag{A.193}$$

$$\beta_{m_2} = 250\exp(-(0.025v_{sa} + 1.25)) \tag{A.194}$$

$$\alpha_{m_3} = 20\frac{v_{sa} + 56.9}{1 - \exp(-(0.1v_{sa} + 5.69))} \tag{A.195}$$

$$\beta_{m_3} = 17.5\frac{v_{sa} + 29.9}{\exp(0.1v_{sa} + 2.99) - 1} \tag{A.196}$$

$$\alpha_{m_4} = \frac{1000}{6}\frac{1}{1 + \exp(-(0.143v_d + 5.67))} \tag{A.197}$$

$$\beta_{m_4} = \frac{1000}{6} - \alpha_{m_4} \tag{A.198}$$

$$\alpha_{m_5} = 500\frac{1}{1 + \exp(\frac{13.5 - K_e}{1.42})} \tag{A.199}$$

$$\beta_{m_5} = 500 - \alpha_{m_5} \tag{A.200}$$

$$\alpha_{m_6} = 16\frac{v_d + 34.9}{1 - \exp(-(0.2v_d + 6.98))} \tag{A.201}$$

$$\beta_{m_6} = 250\exp(-(0.025v_d + 1.25)) \tag{A.202}$$

$$\alpha_{m_7} = 20\frac{v_d + 56.9}{1 - \exp(-(0.1v_d + 5.69))} \tag{A.203}$$

$$\beta_{m_7} = 17.5\frac{v_d + 29.9}{\exp(0.1v_d + 2.99) - 1} \tag{A.204}$$

$$\alpha_{m_8} = 320\frac{-v_{sa} - 51.9}{\exp(-(0.25v_{sa} + 12.975)) - 1} \tag{A.205}$$

$$\beta_{m_8} = 280\frac{v_{sa} + 24.89}{\exp(0.2v_{sa} + 4.978) - 1} \tag{A.206}$$

Rate functions for the deactivation ($h$) gating variables ($s^{-1}$):

$$\alpha_{h_1} = 5.12 \times 10^{-5}\exp(-(0.056v_{sa} + 2.94)) \tag{A.207}$$

$$\beta_{h_1} = 1.6 \times 10^{-3}\frac{1}{1 + \exp(-(0.2v_{sa} + 8))} \tag{A.208}$$

$$\alpha_{h_2} = 16\exp(-(0.056v_{sa} + 4.61)) \tag{A.209}$$

$$\beta_{h_2} = 500\frac{1}{1 + \exp(-(0.2v_{sa} + 11.98))} \tag{A.210}$$

$$\alpha_{h_3} = 5.12 \times 10^{-5}\exp(-(0.056v_d + 2.94)) \tag{A.211}$$

$$\beta_{h_3} = 1.6 \times 10^{-3}\frac{1}{1 + \exp(-(0.2v_d + 8))} \tag{A.212}$$

$$\alpha_{h_4} = 0.5\frac{1}{\left(1 + \exp\left(\frac{K_e - 6.75}{0.71}\right)\right)} \tag{A.213}$$

$$\beta_{h_4} = 0.5 - \alpha_{h_4} \tag{A.214}$$

$$\alpha_{h_5} = 16\exp(-(0.056v_d + 4.61)) \tag{A.215}$$

$$\beta_{h_5} = 500\frac{1}{1+\exp(-(0.2v_d + 11.98))} \tag{A.216}$$

$$\alpha_{h_6} = 128\exp(-(0.056v_{sa} + 2.94)) \tag{A.217}$$

$$\beta_{h_6} = 4\times10^3\frac{1}{1+\exp(-(0.2v_{sa} + 6))} \tag{A.218}$$

The flux of $K^+$ into the SC based on the extracellular $K^+$ ($\mu$M m $s^{-1}$):

$$J_{NEtoSC} = c_{unit}k_{syn}R_s\frac{dK_e}{dt} \tag{A.219}$$

### A.6.1.4 *Modified equations*

The $K^+$ concentration in the ECS (mM):

$$\frac{dK_e}{dt} = \frac{1}{Ff_e}\left(\frac{A_s I_{K,tot_{sa}}}{V_s} + \frac{A_d I_{K,tot_d}}{V_d}\right) - \frac{dBuff_e}{dt} \tag{A.220}$$

The number of $K^+$ ions per unit area in the SC ($\mu$M m):

$$\frac{dN_{K_s}}{dt} = J_{K_k} - 2J_{NaK_k} - J_{NKCC1_k} - J_{KCC1_k} + J_{NEtoSC} \tag{A.221}$$

The number of $Na^+$ ions per unit area in the SC ($\mu$M m):

$$\frac{dN_{Na_s}}{dt} = J_{Na_k} + 3J_{NaK_k} - J_{NKCC1_k} - J_{NBC_k} - J_{NEtoSC} \tag{A.222}$$

The glutamate concentration in the SC ($\mu$M):

$$Glu = \frac{Glu_{max}}{2}\left(1 + \tanh\left(\frac{K_e - K_{e_{switch}}}{Glu_{slope}}\right)\right) \tag{A.223}$$

$O_2$ concentration in the EC ($\mu$M):

$$[O_2]_j = c_{unit}\,O_2 \tag{A.224}$$

| Parameter | Description | Value |
|---|---|---|
| $I_{strength}$ | Amplitude of input current | 0.022 mA $cm^{-2}$ |
| $t_0$ | Start time of input current (*) | 0 s |
| $t_1$ | Final time of input current (*) | 20 s |
| $C_m$ | Membrane capacitance | $7.5\times10^{-7}$ S $cm^{-2}$ s |

| | | |
|---|---|---|
| $R_a$ | Input resistance of dendritic tree | $1.83\times10^{5}$ Ω |
| $\delta_d$ | Half length of dendrite | $4.5\times10^{-2}$ cm |
| $A_s$ | Soma/axon surface area | $1.586\times10^{-5}$ cm$^2$ |
| $A_d$ | Dendrite surface area | $2.6732\times10^{-4}$ cm$^2$ |
| $V_s$ | Soma/axon volume | $2.16\times10^{-9}$ cm$^3$ |
| $V_d$ | Dendrite volume | $5.614\times10^{-9}$ cm$^3$ |
| $f_e$ | ECS to neuron volume ratio | 0.15 |
| $D_{Na,n}$ | Intracellular diffusion rate of $Na^+$ | $1.33\times10^{-5}$ cm$^2$ s$^{-1}$ |
| $D_{K,n}$ | Intracellular diffusion rate of $K^+$ | $1.96\times10^{-5}$ cm$^2$ s$^{-1}$ |
| $\mu$ | Buffer rate | $8\times10^{-4}$ ms$^{-1}$ |
| $B_0$ | Effective total buffer concentration | 500 mM |
| $I_{max}$ | Maximum rate of $Na^+/K^+$ ATP-ase pump | 0.078 mA cm$^{-2}$ |
| $K_{e,0}$ | Equilibrium $K_e$ | 2.9 mM |
| $Na_{sa,0}$ | Equilibrium $Na_{sa}$ | 10 mM |
| $Na_{d,0}$ | Equilibrium $Na_d$ | 10 mM |
| $O2_b$ | Blood $O_2$ level | 0.04 mM |
| $O2_0$ | Equilibrium tissue $O_2$ level | 0.02 mM |
| $\alpha_{O2}$ | Fraction of $O_2$ independent ATP production | 0.05 |
| $J_0$ | Equilibrium change in $O_2$ concentration due to CBF | 0.032 mM s$^{-1}$ |
| $\gamma_{O2}$ | Fraction of the total $O_2$ consumption at steady state | 0.1 |
| $J_{pump1_{sa_0}}$ | Steady state pump rate in the soma/axon | 0.0312 |
| $J_{pump1_{d_0}}$ | Steady state pump rate in the dendrite | 0.0312 |
| $CBF_{init}$ | Equilibrium CBF | 0.032 |
| $J_{pump2}(0)$ | Pump rate when $O_2$ concentration is 0 | 0.0952 |
| $J_{pump2}(O2_0)$ | Pump rate when $O_2$ is at equilibrium | 1 |
| $g_{K,leak_{sa}}$ | Conductance of $K^+$ leak channel on soma/axon | $2.1989\times10^{-4}$ S cm$^{-2}$ |
| $g_{Na,leak_{sa}}$ | Conductance of $Na^+$ leak channel on soma/axon | $6.2378\times10^{-5}$ S cm$^{-2}$ |
| $g_{leak_{sa}}$ | Conductance of general leak channel on soma/axon | $6.2378\times10^{-4}$ S cm$^{-2}$ |
| $g_{K,leak_d}$ | Conductance of $K^+$ leak channel on dendrite | $2.1987\times10^{-4}$ S cm$^{-2}$ |
| $g_{Na,leak_d}$ | Conductance of $Na^+$ leak channel on dendrite | $6.2961\times10^{-5}$ S cm$^{-2}$ |
| $g_{leak_d}$ | Conductance of general leak channel on dendrite | $6.2961\times10^{-4}$ S cm$^{-2}$ |
| $E_{leak_{sa}}$ | Nernst potential for general leak in the soma/axon | −70 mV |
| $E_{leak_d}$ | Nernst potential for general leak in the dendrite | −70 mV |
| $g_{KDR}$ | KDR channel conductance | $10^{-4}$ S cm$^{-2}$ |
| $g_{KA}$ | KA channel conductance | $10^{-5}$ S cm$^{-2}$ |
| $g_{NMDA}$ | NMDA channel conductance | $10^{-5}$ S cm$^{-2}$ |
| $g_{NaP}$ | NaP channel conductance | $2\times10^{-6}$ S cm$^{-2}$ |

| | | |
|---|---|---|
| $g_{NaT}$ | NaT channel conductance | $10^{-5}$ S cm$^{-2}$ |
| $[Mg]_0$ | Equilibrium magnesium | 1.2 mM L$^{-1}$ |
| $k_{syn}$ | The number of active synapses per astrocytic process | 11.5 |
| $K_{e_{switch}}$ | Threshold past which glutamate is released | 5.5 mM |
| $Glu_{slope}$ | Slope of glutamate sigmoidal | 0.1 mM |

Table 9: Parameters used in the neuron and extracellular space extension to the NVU model, where an asterisk $(*)$ denotes a parameter that has changed in value from the previous model version.

### A.6.2 *BOLD response*

#### A.6.2.1 *ODEs*

The non dimensional cerebral blood volume (CBV) (-):

$$\frac{dCBV}{dt} = \frac{1}{\tau_{MTT} + \tau_{TAT}} \left( \frac{CBF}{CBF_{init}} - CBV^d \right) \tag{A.225}$$

The non dimensional deoxyhemoglobin (HbR) concentration (-):

$$\frac{dHbR}{dt} = \frac{1}{\tau_{MTT}} \left( \frac{CMRO_2}{CMRO_{2_0}} - \frac{HbR}{CBV} f_{out} \right) \tag{A.226}$$

#### A.6.2.2 *Algebraic Variables*

The non dimensional normalised total hemoglobin (HbT) concentration (-):

$$HbT_N = \frac{CBF_N HbR_N}{CMRO_{2_N}} \tag{A.227}$$

where the normalised CBF is given by $CBF_N = CBF/CBF(0)$ and $CBF(0)$ is the steady state value, similarly for HbR and $CMRO_{2_N}$.

The non dimensional normalised oxyhemoglobin (HbO) concentration (-):

$$HbO_N = HbT_N - HbR_N + 1 \tag{A.228}$$

The time dependent outflow from the venous compartment (-):

$$f_{out} = CBV^d + \tau_{TAT} \frac{dCBV}{dt} \tag{A.229}$$

The cerebral metabolic rate of $O_2$ consumption (mM $s^{-1}$):

$$CMRO_2 = J_{O_2\,background} + J_{O_2\,pump} \tag{A.230}$$

The equilibrium value of $CMRO_2$ (mM $s^{-1}$):

$$CMRO_{2_0} = J_0 P_{02} \tag{A.231}$$

The $O_2$ extraction fraction (-):

$$E = E_0 \frac{CMRO_2}{J} \tag{A.232}$$

The BOLD signal change from its steady state value (-):

$$\Delta BOLD \approx V_0 \left(a_1 \left[1 - HbR_N\right] + a_2 \left[CBV_N - 1\right]\right) \tag{A.233}$$

| Parameter | Description | Value |
|---|---|---|
| $\tau_{MTT}$ | Mean transit time | 3 s |
| $\tau_{TAT}$ | Transient adjustment time constant | 20 s |
| $d$ | Empirical relation between CBF and CBV | 2.5 |
| $E_0$ | Baseline $O_2$ extraction fraction | 0.4 |
| $V_0$ | Resting venous blood volume fraction | 0.03 |
| $a_1$ | Weight for HbR change | 3.4 |
| $a_2$ | Weight for CBV change | 1 |

Table 10: Parameters used in the BOLD signal extension to the NVU model.

### A.6.3 *Other modified equations*

Fraction of free phosphorylated cross-bridges (-):

$$\frac{d[Mp]}{dt} = \chi_w \left(K_4[AMp] + K_1[M] - (K_2 + K_3)[Mp]\right) \tag{A.234}$$

Fraction of attached phosphorylated cross-bridges (-):

$$\frac{d[AMp]}{dt} = \chi_w \left(K_3[Mp] + K_6[AM] - (K_4 + K_5)[AMp]\right) \tag{A.235}$$

Fraction of attached dephosphorylated cross-bridges (-):

$$\frac{d[AM]}{dt} = \chi_w \left(K_5[AMp] - (K_7 + K_6)[AM]\right) \tag{A.236}$$

| | | |
|---|---|---|
| $\chi_w$ | Scaling constant for wall mechanics | 1.7 |
| $K_{decay_p}$ | Rate of decay of $K^+$ in PVS (*) | 0.15 $s^{-1}$ |

## A.7 MODEL EXTENSION: EXTRACELLULAR ELECTRODIFFUSION AND ASTROCYTIC GAP JUNCTIONS

This model extension is described in Chapter 6 and schematic diagrams can be found in Figures 22 and 28. The following variables from the previous model version have been removed: $R_k, N_{K_k}, N_{Na_k}, N_{HCO3_k}, N_{Cl_k}, N_{K_s}, N_{Na_s}, N_{HCO3_s}$, and $N_{Cl_s}$.

### A.7.1 *Modified equations*

#### A.7.1.1 *ODEs*

$K^+$ concentration in the SC (µM):

$$\frac{dK_s}{dt} = \frac{1}{VR_{sk}} \left(J_{K_k} - 2J_{NaK_k} - J_{NKCC1_k} - J_{KCC1_k}\right) + J_{NEtoSC} \tag{A.237}$$

$Na^+$ concentration in the SC (µM):

$$\frac{dNa_s}{dt} = \frac{1}{VR_{sk}} \left(J_{Na_k} + 3 * J_{NaK_k} - J_{NKCC1_k} - J_{NBC_k}\right) - J_{NEtoSC} \tag{A.238}$$

$HCO_3^-$ concentration in the SC (µM):

$$\frac{dHCO_{3_s}}{dt} = \frac{1}{VR_{sk}} \left(-2J_{NBC_k}\right) \tag{A.239}$$

$K^+$ concentration in the astrocyte (μM):

$$\frac{dK_k}{dt} = -J_{K_k} + 2J_{NaK_k} + J_{NKCC1_k} + J_{KCC1_k} - J_{BK_k} \tag{A.240}$$

$Na^+$ concentration in the astrocyte (μM):

$$\frac{dNa_k}{dt} = -J_{Na_k} - 3J_{NaK_k} + J_{NKCC1_k} + J_{NBC_k} \tag{A.241}$$

$HCO_3^-$ concentration in the astrocyte (μM):

$$\frac{dHCO3_k}{dt} = 2J_{NBC_k} \tag{A.242}$$

$Cl^-$ concentration in the astrocyte (μM):

$$\frac{dCl_k}{dt} = \frac{dNa_k}{dt} + \frac{dK_k}{dt} - \frac{dHCO3_k}{dt} + 2\frac{dCa_k}{dt} \tag{A.243}$$

Membrane potential of the astrocyte (mV):

$$\frac{dv_k}{dt} = \gamma_v(-J_{BK_k} - J_{K_k} - J_{Cl_k} - J_{NBC_k} - J_{Na_k} - J_{NaK_k} - 2J_{TRPV_k}) \tag{A.244}$$

$K^+$ concentration in the PVS (μM):

$$\frac{dK_p}{dt} = \frac{J_{BK_k}}{VR_{pk}} + \frac{J_{KIR_i}}{VR_{pi}} - K_{decay_p}(K_p - K_{min_p}) \tag{A.245}$$

### A.7.1.2 *Algebraic Variables*

$Cl^-$ concentration in the SC (μM):

$$Cl_s = Na_s + K_s - HCO3_s \tag{A.246}$$

The flux of $K^+$ into the SC based on the extracellular $K^+$ ($\mu Ms^{-1}$):

$$J_{NEtoSC} = c_{unit} k_{syn} \frac{dK_e}{dt} \tag{A.247}$$

$Cl^-$ flux through the $Cl^-$ channel ($\mu M\ s^{-1}$):

$$J_{Cl_k} = G_{Cl_k}(v_k - E_{Cl_k}) \tag{A.248}$$

$K^+$ flux through the $K^+$ channel ($\mu M\ s^{-1}$):

$$J_{K_k} = G_{K_k}(v_k - E_{K_k}) \tag{A.249}$$

$Na^+$ flux through the $Na^+$ channel ($\mu M\ s^{-1}$):

$$J_{Na_k} = G_{Na_k}(v_k - E_{Na_k}) \tag{A.250}$$

$Na^+$ and $HCO_3^-$ flux through the NBC channel ($\mu M\ s^{-1}$):

$$J_{NBC_k} = G_{NBC_k}(v_k - E_{NBC_k}) \tag{A.251}$$

$Cl^-$ and $K^+$ flux through the KCC1 channel ($\mu M\ s^{-1}$):

$$J_{KCC1_k} = G_{KCC1_k}\phi \ln\left(\frac{K_s Cl_s}{K_k Cl_k}\right) \tag{A.252}$$

$Na^+$, $K^+$ and $Cl^-$ flux through the NKCC1 channel ($\mu M\ s^{-1}$):

$$J_{NKCC1_k} = G_{NKCC1_k}\phi \ln\left(\frac{Na_s K_s {Cl_s}^2}{Na_k K_k {Cl_k}^2}\right) \tag{A.253}$$

$K^+$ flux through the BK channel ($\mu M\ s^{-1}$):

$$J_{BK_k} = G_{BK_k} w_k (v_k - E_{BK_k}) \tag{A.254}$$

The flux of $Ca^{2+}$ through the TRPV4 channel ($\mu M\ s^{-1}$):

$$J_{TRPV_k} = G_{TRPV_k} m_k (v_k - E_{TRPV_k}) \tag{A.255}$$

Nernst potential for the $K^+$ channel (mV):

$$E_{K_k} = \frac{\phi}{z_K} \ln\left(\frac{K_s}{K_k}\right) \tag{A.256}$$

Nernst potential for the $Na^+$ channel (mV):

$$E_{Na_k} = \frac{\phi}{z_{Na}} \ln\left(\frac{Na_s}{Na_k}\right) \tag{A.257}$$

Nernst potential for the $Cl^-$ channel (mV):

$$E_{Cl_k} = \frac{\phi}{z_{Cl}} \ln\left(\frac{Cl_s}{Cl_k}\right) \tag{A.258}$$

Nernst potential for the NBC channel (mV):

$$E_{NBC_k} = \frac{\phi}{z_{NBC}} \ln\left(\frac{Na_s HCO_{3_s}{}^2}{Na_k HCO_{3_k}{}^2}\right) \tag{A.259}$$

Nernst potential for the BK channel (mV):

$$E_{BK_k} = \frac{\phi}{z_K} \ln\left(\frac{K_p}{K_k}\right) \tag{A.260}$$

The Nernst potential of the TRPV4 channel (mV):

$$E_{TRPV_k} = \frac{\phi}{z_{Ca}} \ln\left(\frac{Ca_p}{Ca_k}\right) \tag{A.261}$$

| | | |
|---|---|---|
| $VR_{sk}$ | Volume ratio between the SC and astrocyte | 0.465 |
| $G_{K_k}$ | Whole cell conductance of $K^+$ | 6908 μM $mV^{-1}$ $s^{-1}$ |
| $G_{Na_k}$ | Whole cell conductance of $Na^+$ | 227 μM $mV^{-1}$ $s^{-1}$ |
| $G_{NBC_k}$ | Whole cell conductance of the NBC cotransporter | 131 μM $mV^{-1}$ $s^{-1}$ |
| $G_{KCC1_k}$ | Whole cell conductance of the KCC1 cotransporter | 1.73 μM $mV^{-1}$ $s^{-1}$ |
| $G_{NKCC1_k}$ | Whole cell conductance of the NKCC1 cotransporter | 9.57 μM $mV^{-1}$ $s^{-1}$ |
| $G_{BK_k}$ | Whole cell conductance of the BK channel | 10.3 μM $mV^{-1}$ $s^{-1}$ |
| $G_{Cl_k}$ | Whole cell conductance of $Cl^-$ | 152 μM $mV^{-1}$ $s^{-1}$ |
| $J_{NaK_{max}}$ | Maximum flux through the $Na^+/K^+$ ATP-ase pump (*) | $2.37\times10^4$ μM $s^{-1}$ |
| $eet_{shift}$ | Describes the EET dependent voltage shift (*) | 2 mV μM $^{-1}$ |
| $v_4$ | Measure of the spread of $w_\infty$ (*) | 8 mV |
| $v_5$ | Determines the range of the shift of $w_\infty$ as $Ca^{2+}$ varies (*) | 15 mV |
| $v_6$ | Shifts the range of $w_\infty$ (*) | −55 mV |
| $v_{1,TRPV}$ | TRPV4 channel voltage gating constant (*) | 120 mV |
| $v_{2,TRPV}$ | TRPV4 channel voltage gating constant (*) | 13 mV |

### A.7.2 *Tissue slice model*

#### A.7.2.1 *ODEs*

$K^+$ concentration in the astrocyte of NVU block $i$ with four neighbours $j$ (μM):

$$\frac{dK_k^i}{dt} = -\frac{1}{\Delta x}\sum_j J_{K,i\to j} - J_{K_k}^i + 2J_{NaK_k}^i + J_{NKCC1_k}^i + J_{KCC1_k}^i \tag{A.262}$$

Membrane potential in the astrocyte of NVU block $i$ with four neighbours $j$ (mV):

$$\frac{dv_k^i}{dt} = \gamma_v\left[-\frac{1}{\Delta x}\sum_j z_K J_{K,i\to j} - J_{BK_k}^i - J_{K_k}^i - J_{Cl_k}^i - J_{NBC_k}^i - J_{Na_k}^i - J_{NaK_k}^i - 2J_{TRPV_k}^i\right] \tag{A.263}$$

$K^+$ concentration in the ECS of NVU block $i$ with four neighbours $j$ (mM):

$$\frac{dK_e^i}{dt} = -\frac{1}{\Delta x}\sum_j J_{K,i\to j}^e + \frac{1}{Ff_e}\left(\frac{A_s I_{K,tot_{sa}}^i}{V_s} + \frac{A_d I_{K,tot_d}^i}{V_d}\right) - \frac{dBuff_e^i}{dt} \tag{A.264}$$

$Na^+$ concentration in the ECS of NVU block $i$ with four neighbours $j$ (mM):

$$\frac{dNa_e^i}{dt} = -\frac{1}{\Delta x}\sum_j J_{Na,i\to j}^e + \frac{1}{Ff_e}\left(\frac{A_s I_{Na,tot_{sa}}^i}{V_s} + \frac{A_d I_{Na,tot_d}^i}{V_d}\right) \tag{A.265}$$

#### A.7.2.2 *Algebraic Variables*

Gap junction flux of $K_k$ from NVU block $i$ to neighbour $j$ (μMm $s^{-1}$):

$$J_{K,i\to j} = -\frac{D_{gap}}{\Delta x}\left((K_k^j - K_K^i) + \frac{z_K F}{RT}\frac{K_k^i + K_k^j}{2}(v_k^j - v_k^i)\right) \tag{A.266}$$

Extracellular electrodiffusive flux of $K_e$ and $Na_e$ from NVU block $i$ to neighbour $j$ (mMm $s^{-1}$):

$$J^e_{K,i\to j} = -\frac{D_{K,e}}{\Delta x}\left[(K^j_e - K^i_e) - z_K\left(\frac{K^i_e + K^j_e}{2}\right)\left(\frac{z_K D_{K,e}(K^j_e - K^i_e) + z_{Na} D_{Na,e}(Na^j_e - Na^i_e)}{z_K^2 D_{K,e}\frac{K^i_e + K^j_e}{2} + z_{Na}^2 D_{Na,e}\frac{Na^i_e + Na^j_e}{2}}\right)\right] \tag{A.267}$$

$$J^e_{Na,i\to j} = -\frac{D_{Na,e}}{\Delta x}\left[(Na^j_e - Na^i_e) - z_{Na}\left(\frac{Na^i_e + Na^j_e}{2}\right)\left(\frac{z_K D_{K,e}(K^j_e - K^i_e) + z_{Na} D_{Na,e}(Na^j_e - Na^i_e)}{z_K^2 D_{K,e}\frac{K^i_e + K^j_e}{2} + z_{Na}^2 D_{Na,e}\frac{Na^i_e + Na^j_e}{2}}\right)\right] \tag{A.268}$$

| Parameter | Description | Value |
|---|---|---|
| $D_{gap}$ | Astrocytic gap junction diffusion coefficient | $3.1 \times 10^{-9}$ m$^2$ s$^{-1}$ |
| $\Delta x^2$ | Width of one NVU block | $1.24 \times 10^{-4}$ m |
| $D_{K,e}$ | Extracellular $K^+$ diffusion coefficient | $3.8 \times 10^{-9}$ m$^2$ s$^{-1}$ |
| $D_{Na,e}$ | Extracellular $Na^+$ diffusion coefficient | $2.5 \times 10^{-9}$ m$^2$ s$^{-1}$ |

Table 11: Parameters of the astrocytic gap junction and extracellular electrodiffusion extension in the large scale tissue slice model.

# BIBLIOGRAPHY


[1] **Aalkjaer, C. and Nilsson, H.** (**2005**): Vasomotion: cellular background for the oscillator and for the synchronization of smooth muscle cells., British journal of pharmacology, Vol. 144, No. 5 pp. 605–616. (Cited on page 87.)

[2] **Abbena, E.; Salamon, S. and Gray, A.** (**1996**): Modern differential geometry of curves and surfaces with Mathematica, CRC Press. (Cited on page 119.)

[3] **Aksenov, D. P.; Li, L.; Miller, M. J.; Iordanescu, G. and Wyrwicz, A. M.** (**2015**): Effects of Anesthesia on BOLD Signal and Neuronal Activity in the Somatosensory Cortex, Journal of Cerebral Blood Flow & Metabolism, Vol. 35, No. 11 pp. 1819–1826. (Cited on page 131.)

[4] **Almeida, A. C. G.; Texeira, H. Z.; Duarte, M. A. and Infantosi, A. F. C.** (**2004**): Modeling Extracellular Space Electrodiffusion during Leão's Spreading Depression, IEEE Transactions on Biomedical Engineering, Vol. 51, No. 3 pp. 450–458. (Cited on page 81.)

[5] **Attwell, D.; Buchan, A. M.; Charpak, S.; Lauritzen, M.; MacVicar, B. a. and Newman, E. a.** (**2010**): Glial and neuronal control of brain blood flow., Nature, Vol. 468, No. 7321 pp. 232–243. (Cited on pages xiv, 5, 6, 14, 33, 34, 37, 59, 67, and 130.)

[6] **Ayata, C. and Lauritzen, M.** (**2015**): Spreading Depression, Spreading Depolarizations, and the Cerebral Vasculature, Physiological Reviews, Vol. 95, No. 3 pp. 953–993. (Cited on pages 76, 84, 98, 125, and 135.)

[7] **Bazargani, N. and Attwell, D.** (**2016**): Astrocyte calcium signaling: the third wave., Nature neuroscience, Vol. 19, No. 2 pp. 182–9. (Cited on pages 7 and 33.)

[8] **Bellot-Saez, A.; Kékesi, O.; Morley, J. W. and Buskila, Y.** (**2017**): Astrocytic modulation of neuronal excitability through K+ spatial buffering, Neuroscience and Biobehavioral Reviews, Vol. 77 pp. 87–97. (Cited on page 136.)

[9] **Benfenati, V.; Amiry-Moghaddam, M.; Caprini, M.; Mylonakou, M. N.; Rapisarda, C.; Ottersen, O. P. and Ferroni, S.** (**2007**): Expression and functional characterization of transient receptor potential vanilloid-related channel 4 (TRPV4) in rat cortical astrocytes., Neuroscience, Vol. 148, No. 4 pp. 876–892. (Cited on page 33.)

[10] **Bennett, M. R.; Farnell, L. and Gibson, W. G.** (**2008**): A quantitative model of cortical spreading depression due to purinergic and gap-junction transmission in astrocyte networks, Biophysical journal, Vol. 95, No. 12 pp. 5648–5660. (Cited on page 33.)

[11] **Bennett, M. R.; Farnell, L. and Gibson, W. G.** (**2008**): Origins of blood volume change due to glutamatergic synaptic activity at astrocytes abutting on arteriolar smooth muscle cells, Journal of theoretical biology, Vol. 250, No. 1 pp. 172–185. (Cited on pages 39 and 130.)

[12] **Bevan, J. A.; Dodge, J.; Walters, C. L.; Wellman, T. and Bevan, R. D.** (**1999**): As human pial arteries (internal diameter 200 - 1000 um) get smaller, their wall thickness and capacity to develop tension relative to their diameter increase, Life Sciences, Vol. 65, No. 11 pp. 1153–1161. (Cited on page 3.)

[13] **Boas, D. A.; Strangman, G.; Culver, J. P.; Hoge, R. D.; Jasdzewski, G.; Poldrack, R. A.; Rosen, B. R. and Mandeville, J. B.** (**2003**): Can the cerebral metabolic rate of oxygen be estimated with near-infrared spectroscopy?, Physics in Medicine and Biology, Vol. 48, No. 15 pp. 2405–2418. (Cited on pages 66, 70, and 71.)

[14] **Bogdanov, V. B.; Middleton, N. A.; Theriot, J. J.; Parker, P. D.; Abdullah, O. M.; Ju, Y. S.; Hartings, J. A. and Brennan, K. C.** (**2016**): Susceptibility of Primary Sensory Cortex to Spreading Depolarizations, Journal of Neuroscience, Vol. 36, No. 17 pp. 4733–4743. (Cited on page 7.)

[15] **Bonder, D. E. and McCarthy, K. D.** (**2014**): Astrocytic Gq-GPCR-linked IP3R-dependent Ca2+ signaling does not mediate neurovascular coupling in mouse visual cortex in vivo., Journal of Neuroscience, Vol. 34, No. 39 pp. 13139–13150. (Cited on page 33.)

[16] **Brown, R. G. and David, T.** (**2013**): Modelling and simulation of cerebral autoregulation and functional hyperaemia in a large-scale vascular tree pp. 1–28. (Cited on pages 19 and 20.)

[17] **Bulicek, M.; Malek, J. and Rajagopal, K. R.** (**2012**): On Kelvin-Voigt model and its generalizations, Evolution Equations and Control Theory, Vol. 1, No. 1 pp. 17–42. (Cited on page 13.)

[18] **Bures, J.; Buresova, O. and Krivanek, J.** (**1974**): The mechanism and applications of Leao's spreading depression of electroencephalographic activity, Academic Press. (Cited on pages 7 and 97.)

[19] **Buxton, R. B.; Uludag, K.; Dubowitz, D. J. and Liu, T. T.** (**2004**): Modeling the hemodynamic response to brain activation, NeuroImage, Vol. 23, No. SUPPL. 1 pp. 220–233. (Cited on pages 57, 64, and 102.)

[20] **Buxton, R. B.; Wong, E. C. and Frank, L. R.** (**1998**): Dynamics of blood flow and oxygenation changes during brain activation: the balloon model., Magnetic Resonance Med., Vol. 39, No. 6 pp. 855–864. (Cited on page 64.)

[21] **Cahoy, J. D.; Emery, B.; Kaushal, A.; Foo, L. C.; Zamanian, J. L.; Christopherson, K. S.; Xing, Y.; Lubischer, J. L.; Krieg, P. A.; Krupenko, S. A.; Thompson, W. J. and Barres, B. A.** (**2008**): A transcriptome database for astrocytes, neurons, and oligodendrocytes: a new resource for understanding brain development and function, Journal of Neuroscience, Vol. 28, No. 1 pp. 264–278. (Cited on page 33.)

[22] **Cameron, I. R. and Caronna, J.** (**1976**): The effect of local changes in potassium and bicarbonate concentration on hypothalamic blood flow in the rabbit., The Journal of physiology, Vol. 262, No. 2 pp. 415–430. (Cited on pages 76 and 98.)

[23] **Cao, R.** (**2011**): The Hemo-Neural Hypothesis: Effects of Vasodilation on Astrocytes in Mammalian Neocortex, phdthesis, Massachusetts Institute of Technology. (Cited on page 33.)

[24] **Chakravarty, S. and Sannigrahi, A. K.** (**1999**): A nonlinear mathematical model of blood flow in a constricted artery experiencing body acceleration, Mathematical and Computer Modelling, Vol. 29, No. 8 pp. 9–25. (Cited on page 11.)

[25] **Champneys, A. R.; Kuznetsov, Y. A.; Paffenroth, R. C.; Fairgrieve, T. F.; Oldeman, B. E. and Wang, X.** (**2002**): AUTO 2000: Continuation And Bifurcation Software For Ordinary Differential Equations, technical report. (Cited on pages xvi and 86.)

[26] **Chang, J. C.; Brennan, K. C.; He, D.; Huang, H.; Miura, R. M.; Wilson, P. L. and Wylie, J. J.** (**2013**): A mathematical model of the metabolic and perfusion effects on cortical spreading depression., PloS One, Vol. 8, No. 8 p. e70469. (Cited on pages 5, 12, 13, 21, 58, 66, 77, and 98.)

[27] **Charles, A. C. and Baca, S. M.** (**2013**): Cortical spreading depression and migraine, Nature Reviews Neurology, Vol. 9, No. 11 pp. 637–644. (Cited on pages 7, 76, and 101.)

[28] **Chen, B. R.; Bouchard, M. B.; McCaslin, A. F. H.; Burgess, S. A. and Hillman, E. M. C.** (**2011**): High-speed vascular dynamics of the hemodynamic response, Cell, Vol. 54, No. 2 pp. 1021–1030. (Cited on page 54.)

[29] **Chen, Q. S.; Kagan, B. L.; Hirakura, Y. and Xie, C. W.** (**2000**): Impairment of hippocampal long-term potentiation by Alzheimer amyloid beta-peptides., Journal of neuroscience research, Vol. 60, No. 1 pp. 65–72. (Cited on page 101.)

[30] **Chen, S.; Feng, Z.; Li, P.; Jacques, S. L.; Zeng, S. and Luo, Q.** (**2006**): In vivo optical reflectance imaging of spreading depression waves in rat brain with and without focal cerebral ischemia, Journal of Biomedical Optics, Vol. 11, No. 3 p. 034002. (Cited on pages xviii, 7, 10, 76, 96, 99, and 125.)

[31] **Chen, Y. and Swanson, R. A.** (**2003**): Astrocytes and brain injury, Journal of Cerebral Blood Flow & Metabolism, Vol. 23, No. 2 pp. 137–149. (Cited on page 76.)

[32] **Chew, S. S. L.; Johnson, C. S.; Green, C. R. and Danesh-Meyer, H. V.** (**2010**): Role of connexin43 in central nervous system injury., Experimental neurology, Vol. 225, No. 2 pp. 250–261. (Cited on page 76.)

[33] **Chung, S. H.; Andersen, O. S. and Krishnamurthy, V. V.** (**2007**): Biological Membrane Ion Channels: Dynamics, Structure, and Applications, Springer Science & Business Media. (Cited on pages 14 and 35.)

[34] **Cloutier, M.; Bolger, F. B.; Lowry, J. P. and Wellstead, P.** (**2009**): An integrative dynamic model of brain energy metabolism using in vivo neurochemical measurements, Journal of Computational Neuroscience, Vol. 27, No. 3 pp. 391–414. (Cited on page 63.)

[35] **Conte, C.; Lee, R.; Sarkar, M. and Terman, D.** (**2018**): A mathematical model of recurrent spreading depolarizations, Journal of Computational Neuroscience, Vol. 44 pp. 203–217. (Cited on pages 12, 13, and 77.)

[36] **Cox, D. H.** (**2014**): Modeling a Ca2+ channel/BKCa channel complex at the single-complex level, Biophysical Journal, Vol. 107, No. 12 pp. 2797–2814. (Cited on page 42.)

[37] **Dahlem, M. and Müller, S.** (**2004**): Reaction-diffusion waves in neuronal tissue and the window of cortical excitability, Annalen der Physik, Vol. 13, No. 78 pp. 442–449. (Cited on pages 101 and 125.)

[38] **Dahlem, M. A. and Chronicle, E. P.** (**2004**): A computational perspective on migraine aura, Progress in Neurobiology, Vol. 74, No. 6 pp. 351–361. (Cited on pages 101 and 125.)

[39] **Dahlem, M. A. and Hadjikhani, N.** (**2009**): Migraine aura: Retracting particle-like waves in weakly susceptible cortex, PLoS ONE, Vol. 4, No. 4. (Cited on pages 101 and 125.)

[40] **Dahlem, M. A.; Schmidt, B.; Bojak, I.; Boie, S.; Kneer, F.; Hadjikhani, N. and Kurths, J.** (**2015**): Cortical hot spots and labyrinths: why cortical neuromodulation for episodic migraine with aura should be personalized, Frontiers in Computational Neuroscience, Vol. 9, No. March pp. 1–13. (Cited on pages xviii, 101, 102, 103, 119, 124, and 136.)

[41] **Dallérac, G.; Chever, O. and Rouach, N.** (**2013**): How do astrocytes shape synaptic transmission? Insights from electrophysiology., Frontiers in cellular neuroscience, Vol. 7, No. October p. 159. (Cited on page 136.)

[42] **De Martino, F.; Esposito, F.; van de Moortele, P.-F.; Harel, N.; Formisano, E.; Goebel, R.; Ugurbil, K. and Yacoub, E.** (**2011**): Whole brain high-resolution functional imaging at ultra high magnetic fields: an application to the analysis of resting state networks, Neuroimage, Vol. 57, No. 3 pp. 1031–1044. (Cited on page 136.)

[43] **D'Esposito, M.; Deouell, L. Y. and Gazzaley, A.** (**2003**): Alterations in the BOLD fMRI signal with ageing and disease: a challenge for neuroimaging, Nature reviews. Neuroscience, Vol. 4, No. 11 pp. 863–872. (Cited on page 127.)

[44] **Donk, L. V. D. and Kock, E. G. J. D.** (**2013**): Bluefern Supercomputing Unit, University of Canterbury, Eindhoven University of Technology. (Cited on page 13.)

[45] **Dormanns, K.** (**2015**): Computational models of neurovascular coupling, Phd thesis, University of Canterbury. (Cited on pages ix and 16.)

[46] **Dormanns, K.; Brown, R. G. and David, T.** (**2015**): Neurovascular coupling: a parallel implementation, Frontiers in computational neuroscience, Vol. 9, No. September pp. 1–17. (Cited on pages x, 9, 16, 17, 19, 20, 21, 23, and 129.)

[47] **Dormanns, K.; Brown, R. G. and David, T.** (**2016**): The role of nitric oxide in neurovascular coupling, Journal of theoretical biology, Vol. 394 pp. 1–17. (Cited on pages ii, 6, 37, 45, 52, 77, 128, and 153.)

[48] **Dormanns, K.; van Disseldorp, E. M. J.; Brown, R. G. and David, T.** (**2015**): Neurovascular coupling and the influence of luminal agonists via the endothelium, Journal of Theoretical Biology, Vol. 364 pp. 49–70. (Cited on pages ix, xxiii, 9, 13, 14, 15, 16, 21, 26, 29, 33, 34, 40, 41, 80, 128, 129, 138, 139, 143, 148, 150, and 152.)

[49] **Dreier, J. P.** (**2011**): The role of spreading depression, spreading depolarization and spreading ischemia in neurological disease., Nature medicine, Vol. 17, No. 4 pp. 439–447. (Cited on pages 7 and 76.)

[50] **Drewes, L. R.** (**2012**): Making connexons in the neurovascular unit, Journal of Cerebral Blood Flow & Metabolism, Vol. 32, No. 8 p. 1455. (Cited on page 5.)

[51] **Du, T.; Hu, D. and Cai, D.** (**2015**): Outflow Boundary Conditions for Blood Flow in Arterial Trees, PLoS ONE, Vol. 10, No. 5 p. e0128597. (Cited on pages 50 and 51.)

[52] **Dunn, K. M.; Hill-Eubanks, D. C.; Liedtke, W. B. and Nelson, M. T.** (**2013**): TRPV4 channels stimulate Ca2+-induced Ca2+ release in astrocytic endfeet and amplify neurovascular coupling responses., Proceedings of the National Academy of Sciences, Vol. 110, No. 15 pp. 6157–6162. (Cited on pages 33, 50, and 55.)

[53] **Edwards, F. R.; Hirst, G. D. S. and Silverberg, G. D.** (**1988**): Inward Rectification in Rat Cerebral Arterioles; Involvement of Potassium Ions in Autoregukation, Journal of Physiology, Vol. 404, No. 1 pp. 455–466. (Cited on pages 76 and 98.)

[54] **Enger, R.; Tang, W.; Vindedal, G. F.; Jensen, V.; Helm, P. J.; Sprengel, R.; Looger, L. L.; Nagelhus, E. A.; Johannes Helm, P.; Sprengel, R.; Looger, L. L. and Nagelhus, E. A.** (**2015**): Dynamics of ionic shifts in cortical spreading depression, Cerebral Cortex, Vol. 25, No. 11 pp. 4469–4476. (Cited on pages 7 and 76.)

[55] **Fang, X.; Weintraub, N. L.; Stoll, L. L. and Spector, A. a.** (**1999**): Epoxyeicosatrienoic Acids Increase Intracellular Calcium Concentration in Vascular Smooth Muscle Cells, Hypertension, Vol. 34, No. 6 p. 1242. (Cited on page 130.)

[56] **Farr, H. and David, T.** (**2011**): Models of neurovascular coupling via potassium and EET signalling., Journal of theoretical biology, Vol. 286, No. 1 pp. 13–23. (Cited on pages 13, 33, 38, 40, 41, 128, 138, and 139.)

[57] **Filosa, J. A. and Blanco, V. M.** (**2007**): Neurovascular coupling in the mammalian brain., Experimental physiology, Vol. 92, No. 4 pp. 641–646. (Cited on page 74.)

[58] **Filosa, J. A.; Bonev, A. D. and Nelson, M. T.** (**2004**): Calcium Dynamics in Cortical Astrocytes and Arterioles During Neurovascular Coupling, Circulation research, Vol. 95, No. 10 pp. e73–e81. (Cited on page 33.)

[59] **Filosa, J. A.; Bonev, A. D.; Straub, S. V.; Meredith, A. L.; Wilkerson, M. K.; Aldrich, R. W. and Nelson, M. T.** (**2006**): Local potassium signaling couples neuronal activity to vasodilation in the brain, Nature neuroscience, Vol. 9, No. 11 pp. 1397–1403. (Cited on pages xiv, 6, 14, 33, 37, 55, 59, and 67.)

[60] **Fink, C. C.; Slepchenko, B. and Loew, L. M.** (**1999**): Determination of time-dependent inositol-1,4,5-trisphosphate concentrations during calcium release in a smooth muscle cell., Biophysical journal, Vol. 77, No. 1 pp. 617–628. (Cited on page 39.)

[61] **Förstermann, U.** (**2006**): Janus-faced role of endothelial NO synthase in vascular disease: uncoupling of oxygen reduction from NO synthesis and its pharmacological reversal, Biological chemistry, Vol. 387, No. 12 pp. 1521–1533. (Cited on page 37.)

[62] **Fox, P. T. and Raichle, M. E.** (**1986**): Focal physiological uncoupling of cerebral blood flow and oxidative metabolism during somatosensory stimulation in human subjects., Proceedings of the National Academy of Sciences of the United States of America, Vol. 83 pp. 1140–1144. (Cited on pages 57, 64, and 113.)

[63] **Fujii, Y.; Maekawa, S. and Morita, M.** (**2017**): Astrocyte calcium waves propagate proximally by gap junction and distally by extracellular diffusion of ATP released from volume-regulated anion channels, Scientific Reports, Vol. 7, No. 1 p. 13115. (Cited on page 78.)

[64] **Fujita, S.; Mizoguchi, N.; Aoki, R.; Cui, Y.; Koshikawa, N. and Kobayashi, M.** (**2015**): Cytoarchitecture-dependent decrease in propagation velocity of cortical spreading depression in the rat insular cortex revealed by optical imaging, Cerebral Cortex, Vol. 26, No. 4 pp. 1580–1589. (Cited on page 96.)

[65] **Fung, Y. C.** (**1997**): Biomechanics: Circulation, 2nd Edn., Springer-Verlag, New York. (Cited on pages 16 and 17.)

[66] **Gao, Y. R.; Ma, Y.; Zhang, Q.; Winder, A. T.; Liang, Z.; Antinori, L.; Drew, P. J. and Zhang, N.** (**2017**): Time to wake up: Studying neurovascular coupling and brain-wide circuit function in the un-anesthetized animal, NeuroImage, Vol. 153, No. April 2016 pp. 382–398. (Cited on page 10.)

[67] **Garcia, N. and Stoll, E.** (**1984**): Monte Carlo Calculation for Electromagnetic-Wave Scattering from Random Rough Surfaces, Physical Review Letters, Vol. 52, No. 20 pp. 1798–1801. (Cited on page 119.)

[68] **Girouard, H.; Bonev, A. D.; Hannah, R. M.; Meredith, A.; Aldrich, R. W. and Nelson, M. T.** (**2010**): Astrocytic endfoot Ca2+ and BK channels determine both arteriolar dilation and constriction., Proceedings of the National Academy of Sciences of the United States of America, Vol. 107, No. 8 pp. 3811–3816. (Cited on pages xii, 33, 35, 46, 50, 52, 53, and 55.)

[69] **Girouard, H. and Iadecola, C.** (**2006**): Neurovascular coupling in the normal brain and in hypertension, stroke, and Alzheimer disease., Journal of Applied Physiology, Vol. 100, No. 1 pp. 328–335. (Cited on pages 7 and 76.)

[70] **Glaser, R.** (**2001**): Biophysics, Springer-Verlag, Berlin, Germany. (Cited on pages 79 and 107.)

[71] **Goldbeter, A.; Dupont, G. and Berridge, M. J.** (**1990**): Minimal model for signal-induced Ca2+ oscillations and for their frequency encoding through protein phosphorylation., Proceedings of the National Academy of Sciences, Vol. 87, No. 4 pp. 1461–1465. (Cited on page 101.)

[72] **Golding, E. M.; Steenberg, M. L.; Johnson, T. D. and Bryan, R. M.** (**2000**): The effects of potassium on the rat middle cerebral artery, Brain research, Vol. 880, No. 1 pp. 159–166. (Cited on pages 76 and 98.)

[73] **Golubitsky, M.; Knobloch, E. and Stewart, I.** (**2000**): Target Patterns and Spirals in Planar Reaction-Diffusion Systems, J. Nonlin. Sci., Vol. 10 pp. 333–354. (Cited on page 120.)

[74] **Gonzalez-Fernandez, J. M. and Ermentrout, B.** (**1994**): On the origin and dynamics of the vasomotion of small arteries, Mathematical biosciences, Vol. 119, No. 2 pp. 127–167. (Cited on page 41.)

[75] **Gordon, G. R. J.; Choi, H. B.; Rungta, R. L.; Ellis-Davies, G. C. R. and MacVicar, B. A.** (**2008**): Brain metabolism dictates the polarity of astrocyte control over arterioles., Nature, Vol. 456, No. 7223 pp. 745–749. (Cited on page 55.)

[76] **Gordon, G. R. J.; Howarth, C. and MacVicar, B. a.** (**2011**): Bidirectional control of arteriole diameter by astrocytes., Experimental physiology, Vol. 96, No. 4 pp. 393–399. (Cited on page 55.)

[77] **Gorelova, N. A.** (**1983**): Spiral Waves of Spreading Depression in the Isolated Chicken Retina, Vol. 14, No. 5 pp. 353–363. (Cited on page 101.)

[78] **Gropp, W.; Hoefler, T.; Thakur, R. and Lusk, E.** (**2014**): Using Advanced MPI: Modern Features of the Message-Passing Interface, MIT Press. (Cited on pages 25 and 109.)

[79] **Haddock, R. E. and Hill, C. E.** (**2005**): Rhythmicity in arterial smooth muscle, The Journal of physiology, Vol. 566, No. 3 pp. 645–656. (Cited on pages 87 and 88.)

[80] **Hai, C. M. and Murphy, R. A.** (**1988**): Cross-bridge phosphorylation and regulation of latch state in smooth muscle, American Journal of Physiology - Cell Physiology, Vol. 254, No. 1 pp. C99—-C106. (Cited on pages 4, 13, and 74.)

[81] **Hall, C. N.; Reynell, C.; Gesslein, B.; Hamilton, N. B.; Mishra, A.; Sutherland, B. A.; O'Farrell, F. M.; Buchan, A. M.; Lauritzen, M. and Attwell, D.** (**2014**): Capillary pericytes regulate cerebral blood flow in health and disease., Nature, Vol. 508, No. 7494 pp. 55–60. (Cited on page 6.)

[82] **Halnes, G.; Østby, I.; Pettersen, K. H.; Omholt, S. W. and Einevoll, G. T.** (**2013**): Electrodiffusive Model for Astrocytic and Neuronal Ion Concentration Dynamics, PLoS Computational Biology, Vol. 9, No. 12. (Cited on page 11.)

[83] **Hamel, E.** (**2006**): Perivascular nerves and the regulation of cerebrovascular tone, Journal of applied physiology, Vol. 100, No. 3 pp. 1059–1064. (Cited on page 5.)

[84] **Hamilton, N. B.; Attwell, D. and Hall, C. N.** (**2010**): Pericyte-mediated regulation of capillary diameter: a component of neurovascular coupling in health and disease., Frontiers in neuroenergetics, Vol. 2, No. May pp. 1–14. (Cited on page 23.)

[85] **Heinrich, R. and Schuster, S.** (**1996**): The regulation of cellular systems, Springer Science & Business Media. (Cited on page 63.)

[86] **Higashi, K.; Fujita, A.; Inanobe, A.; Tanemoto, M.; Doi, K.; Kubo, T. and Kurachi, Y.** (**2001**): An inwardly rectifying K(+) channel, Kir4.1, expressed in astrocytes surrounds synapses and blood vessels in brain., American journal of physiology. Cell physiology, Vol. 281 pp. C922–C931. (Cited on page 136.)

[87] **Higashimori, H.; Blanco, V. M.; Tuniki, V. R.; Falck, J. R. and Filosa, J. A.** (**2010**): Role of epoxyeicosatrienoic acids as autocrine metabolites in glutamate-mediated K+ signaling in perivascular astrocytes, American Journal of Physiology-Cell Physiology, Vol. 299, No. 5 pp. C1068–C1078. (Cited on pages 33 and 34.)

[88] **Hill, C. E.; Eade, J. and Sandow, S. L.** (**1999**): Mechanisms underlying spontaneous rhythmical contractions in irideal arterioles of the rat, Journal of Physiology, Vol. 521, No. 2 pp. 507–516. (Cited on page 88.)

[89] **Hill, R. A.; Tong, L.; Yuan, P.; Murikinati, S.; Gupta, S. and Grutzendler, J.** (**2015**): Regional Blood Flow in the Normal and Ischemic Brain Is Controlled by Arteriolar Smooth Muscle Cell Contractility and Not by Capillary Pericytes, Neuron, Vol. 87, No. 1 pp. 95–110. (Cited on page 6.)

[90] **Hoge, R. D.; Atkinson, J.; Gill, B.; Crelier, G. R.; Marrett, S. and Pike, G. B.** (**1999**): Linear coupling between cerebral blood flow and oxygen consumption in activated human cortex., Proceedings of the National Academy of Sciences of the United States of America, Vol. 96 pp. 9403–9408. (Cited on page 64.)

[91] **Hong, K.-S. and Zafar, A.** (**2018**): Existence of Initial Dip for BCI: An Illusion or Reality, Frontiers in Neurorobotics, Vol. 12 p. 69. (Cited on page 64.)

[92] **Hu, X. and Yacoub, E.** (**2012**): The story of the initial dip in fMRI. (Cited on page 64.)

[93] **Huang, X.; Xu, W.; Liang, J.; Takagaki, K.; Gao, X. and Wu, J.-Y.** (**2010**): Spiral wave dynamics in neocortex, Neuron, Vol. 68, No. 5 pp. 978–90. (Cited on page 120.)

[94] **Huguet, G.; Joglekar, A.; Messi, L. M.; Buckalew, R.; Wong, S. and Terman, D.** (**2016**): Neuroprotective Role of Gap Junctions in a Neuron Astrocyte Network Model, Biophysical journal, Vol. 111, No. 2 pp. 452–462. (Cited on pages 7, 12, 13, 76, and 77.)

[95] **Iadecola, C.** (**2004**): Neurovascular regulation in the normal brain and in Alzheimer's disease, Nature Reviews. Neuroscience, Vol. 5, No. 5 pp. 347–360. (Cited on pages 5 and 127.)

[96] **Iadecola, C.** (**2017**): The Neurovascular Unit Coming of Age: A Journey through Neurovascular Coupling in Health and Disease, Neuron, Vol. 96, No. 1 pp. 17–42. (Cited on page 7.)

[97] **Jacobsen, J. C. B.; Aalkjaer, C.; Nilsson, H.; Matchkov, V. V.; Freiberg, J. and Holstein-Rathlou, N.-H.** (**2007**): A model of smooth muscle cell synchronization in the arterial wall., American journal of physiology. Heart and circulatory physiology, Vol. 293, No. March 2007 pp. H229–H237. (Cited on pages 78 and 79.)

[98] **Jing, J.; Aitken, P. G. and Somjen, G. G.** (**1994**): Interstitial volume changes during spreading depression (SD) and SD-like hypoxic depolarization in hippocampal tissue slices, Journal of Neurophysiology, Vol. 71, No. 6 pp. 2548–2551. (Cited on page 135.)

[99] **Kager, H.; Wadman, W. J. and Somjen, G. G.** (**2000**): Simulated Seizures and Spreading Depression in a Neuron Model Incorporating Interstitial Space and Ion Concentrations, Journal of neurophysiology, Vol. 84, No. 1 pp. 495–512. (Cited on pages 5, 12, 21, 58, 66, 83, 84, 90, and 135.)

[100] **Keener, J. P. and Tyson, J. J.** (**1986**): Spiral waves in the Belousov-Zhabotinskii reaction, Physica D: Nonlinear Phenomena, Vol. 21, No. 2 pp. 307–324. (Cited on page 101.)

[101] **Keizer, J. and De Young, G. W.** (**1992**): Two roles of Ca2+ in agonist stimulated Ca2+ oscillations, Biophysical journal, Vol. 61, No. 3 pp. 649–660. (Cited on page 14.)

[102] **Kenny, A.; David, P. T. and Plank, M. J.** (**2016**): Calcium Dynamics and Wave Propagation in Coupled Cells, Master's thesis, University of Canterbury. (Cited on page 101.)

[103] **Kenny, A.; Plank, M. J. and David, T.** (**2019**): The effects of cerebral curvature on cortical spreading depression, Journal of Theoretical Biology, Vol. 472 pp. 11–26. (Cited on page 103.)

[104] **Kenny, A.; Plank, M. J. M. and David, T.** (**2018**): Macro scale modelling of cortical spreading depression and the role of astrocytic gap junctions, Journal of Theoretical Biology, Vol. 458 pp. 78–91. (Cited on page 103.)

[105] **Kenny, A.; Plank, M. J. M. and David, T.** (**2018**): The role of astrocytic calcium and TRPV4 channels in neurovascular coupling, Journal of Computational Neuroscience, Vol. 44, No. 1 pp. 97–114. (Cited on pages 77 and 95.)

[106] **Kenny, A.; Zakkaroff, C.; Plank, M. J. M. and David, T.** (**2018**): Massively parallel simulations of neurovascular coupling with extracellular diffusion, Journal of Computational Science, Vol. 24 pp. 116–124. (Cited on page 79.)

[107] **Kimelberg, H. K.** (**2004**): The problem of astrocyte identity., Neurochemistry international, Vol. 45, No. 2-3 pp. 191–202. (Cited on page 3.)

[108] **Kneer, F.; Schöll, E. and Dahlem, M. A.** (**2014**): Nucleation of reaction-diffusion waves on curved surfaces, New Journal of Physics, Vol. 16. (Cited on pages xviii, 13, 93, 101, 104, 106, 107, and 115.)

[109] **Kochunov, P.; Mangin, J. F.; Coyle, T.; Lancaster, J.; Thompson, P.; Rivière, D.; Cointepas, Y.; Régis, J.; Schlosser, A.; Royall, D. R.; Zilles, K.; Mazziotta, J.; Toga, A. and Fox, P. T.** (**2005**): Age-related morphology trends of cortical sulci, Human Brain Mapping, Vol. 26, No. 3 pp. 210–220. (Cited on page 115.)

[110] **Koenigsberger, M.; Sauser, R.; Bény, J.-L. and Meister, J.-J.** (**2005**): Role of the endothelium on arterial vasomotion., Biophysical journal, Vol. 88, No. 6 pp. 3845–3854. (Cited on page 23.)

[111] **Koenigsberger, M.; Sauser, R.; Bény, J.-L. and Meister, J.-J.** (**2006**): Effects of arterial wall stress on vasomotion, Biophysical journal, Vol. 91, No. September pp. 1663–1674. (Cited on pages 13, 44, 80, and 150.)

[112] **Ku, D. N.** (**1997**): Blood Flow in Arteries, Annual Review of Fluid Mechanics, Vol. 29, No. 1 pp. 399–434. (Cited on page 17.)

[113] **Kuschinsky, W.; Wahl, M.; Bosse, O. and Thurau, K.** (**1972**): Perivascular Potassium and pH as Determinants of Local Pial Arterial Diameter in Cats A MICROAPPLICATION STUDY, Circulation Research, Vol. 31, No. 2 pp. 240–247. (Cited on pages 76 and 98.)

[114] **Lauritzen, M.; Dreier, J. P.; Fabricius, M.; Hartings, J. A.; Graf, R. and Strong, A. J.** (**2011**): Clinical relevance of cortical spreading depression in neurological disorders: migraine, malignant stroke, subarachnoid and intracranial hemorrhage, and traumatic brain injury, Journal of Cerebral Blood Flow & Metabolism, Vol. 31, No. 1 pp. 17–35. (Cited on pages 7 and 76.)

[115] **Leâo, A. A. P.** (**1944**): Spreading depression of activity in the cerebral cortex, Journal of neurophysiology, Vol. 7, No. 6 pp. 359–390. (Cited on pages 7, 76, and 77.)

[116] **Lin, J. H. C.; Weigel, H.; Cotrina, M. L.; Liu, S.; Bueno, E.; Hansen, A. J.; Hansen, T. W.; Goldman, S. and Nedergaard, M.** (**1998**): Gap-junction-mediated propagation and amplification of cell injury, Nature neuroscience, Vol. 1, No. 6 p. 494. (Cited on page 77.)

[117] **Lourenço, C. F.; Barbosa, R. M. and Laranjinha, J.** (**2014**): Nitric Oxide-Mediated Neurovascular Coupling Is Impaired in the Triple-Transgenic Mouse Model of Alzheimer's Disease Due to Cerebrovascular Dysfunction, Free Radical Biology and Medicine, Vol. 76 p. S25. (Cited on page 127.)

[118] **Ma, B.; Buckalew, R.; Du, Y.; Kiyoshi, C. M.; Alford, C. C.; Wang, W.; Mctigue, D. M.; Enyeart, J. J.; Terman, D. and Zhou, M.** (**2016**): Gap Junction Coupling Confers Isopotentiality on Astrocyte Syncytium, Glia, Vol. 64, No. 2 pp. 214–226. (Cited on page 77.)

[119] **Marcus, G. F. and Freeman, J.** (**2003**): Neuroscience in Medicine, Vol. 47, Springer Science & Business Media. (Cited on page 3.)

[120] **Martínez, M.; Martínez, N. A. and Silva, W. I.** (**2017**): Measurement of the Intracellular Calcium Concentration with Fura-2 AM Using a Fluorescence Plate Reader, Bio-protocol, Vol. 7, No. 14 p. e2411. (Cited on page 10.)

[121] **Mathias, E.; Kenny, A.; Plank, M. J. and David, T.** (**2018**): Integrated models of neurovascular coupling and BOLD signals: Responses for varying neural activations, NeuroImage, Vol. 174, No. March pp. 69–86. (Cited on pages 58, 66, 81, 90, 97, and 103.)

[122] **Mathias, E. J.; Plank, M. J. and David, T.** (**2017**): A model of neurovascular coupling and the BOLD response: PART I, Computer Methods in Biomechanics and Biomedical Engineering, Vol. 20, No. 5 pp. 508–518. (Cited on pages 57, 58, 64, 66, and 165.)

[123] **McCarron, J. G. and Halpern, W.** (**1990**): Potassium dilates rat cerebral arteries by two independent mechanisms, American Journal of Physiology-Heart and Circulatory Physiology, Vol. 259, No. 3 pp. H902—-H908. (Cited on pages 76 and 98.)

[124] **Meeks, J. P. and Mennerick, S.** (**2007**): Astrocyte Membrane Responses and Potassium Accumulation During Neuronal Activity, Hippocampus, Vol. 17 pp. 1100–1108. (Cited on page 42.)

[125] **Metea, M. R. and Newman, E. A.** (**2006**): Glial cells dilate and constrict blood vessels: a mechanism of neurovascular coupling., Journal of Neuroscience, Vol. 26, No. 11 pp. 2862–2870. (Cited on pages 34, 71, 74, and 130.)

[126] **Mishra, A.; Reynolds, J. P.; Chen, Y.; Gourine, A. V.; Rusakov, D. A. and Attwell, D.** (**2016**): Astrocytes mediate neurovascular signaling to capillary pericytes but not to arterioles, Nature Publishing Group, Vol. 19, No. October pp. 1619–1627. (Cited on page 131.)

[127] **Moore, C. I. and Cao, R.** (**2008**): The hemo-neural hypothesis: on the role of blood flow in information processing., Journal of neurophysiology, Vol. 99, No. 5 pp. 2035–2047. (Cited on page 33.)

[128] **Morin, C.; Sirois, M.; Echave, V.; Gomes, M. M. and Rousseau, E.** (**2007**): Epoxyeicosatrienoic acid relaxing effects involve Ca2+ activated K+ channel activation and CPI-17 dephosphorylation in human bronchi, American Journal of Respiratory Cell and Molecular Biology, Vol. 36, No. 5 pp. 633–641. (Cited on page 130.)

[129] **Mulligan, S. J. and MacVicar, B. A.** (**2004**): Calcium transients in astrocyte endfeet cause cerebrovascular constrictions, Nature, Vol. 431, No. 7005 pp. 195–199. (Cited on page 130.)

[130] **Nakahata, K.; Kinoshita, H.; Tokinaga, Y.; Ishida, Y.; Kimoto, Y.; Dojo, M.; Mizumoto, K.; Ogawa, K. and Hatano, Y.** (**2006**): Vasodilation mediated by inward rectifier K+ channels in cerebral microvessels of hypertensive and normotensive rats, Anesthesia & Analgesia, Vol. 102, No. 2 pp. 571–576. (Cited on pages xiv, 6, 14, 37, 59, and 67.)

[131] **Nakase, T.; Fushiki, S.; Söhl, G.; Theis, M.; Willecke, K. and Naus, C. C.** (**2003**): Neuroprotective Role of Astrocytic Gap Junctions in Ischemic Stroke, Cell Communication & Adhesion, Vol. 10, No. 4-6 pp. 413–417. (Cited on pages 77, 96, and 99.)

[132] **Newman, E. A.** (**1984**): Regional specialization of retinal glial cell membrane, Nature, Vol. 309, No. 5964 pp. 155–157. (Cited on page 66.)

[133] **Nizar, K.; Uhlirova, H.; Tian, P.; Saisan, P. A.; Cheng, Q.; Reznichenko, L.; Weldy, K. L.; Steed, T. C.; Sridhar, V. B.; MacDonald, C. L.; Cui, J.; Gratiy, S. L.; Sakadzic, S.; Boas, D. A.; Beka, T. I.; Einevoll, G. T.; Chen, J.; Masliah, E.; Dale, A. M.; Silva, G. A. and Devor, A.** (**2013**): In vivo Stimulus-Induced Vasodilation Occurs without IP3 Receptor Activation and May Precede Astrocytic Calcium Increase, Journal of Neuroscience, Vol. 33, No. 19 pp. 8411–8422. (Cited on page 33.)

[134] **Obata, T.; Liu, T. T.; Miller, K. L.; Luh, W. M.; Wong, E. C.; Frank, L. R. and Buxton, R. B.** (**2004**): Discrepancies between BOLD and flow dynamics in primary and supplementary motor areas: Application of the balloon model to the interpretation of BOLD transients, NeuroImage, Vol. 21 pp. 144–153. (Cited on page 65.)

[135] **O'Connell, R. and Mori, Y.** (**2016**): Effects of Glia in a Triphasic Continuum Model of Cortical Spreading Depression, Bulletin of Mathematical Biology, Vol. 78, No. 10 pp. 1943–1967. (Cited on pages 13 and 77.)

[136] **Ogawa, S.; Lee, T. M.; Kay, A. R. and Tank, D. W.** (**1990**): Brain magnetic resonance imaging with contrast dependent on blood oxygenation., Proceedings of the National Academy of Sciences of the United States of America, Vol. 87, No. 24 pp. 9868–9872. (Cited on pages 57 and 102.)

[137] **Østby, I.; Øyehaug, L.; Einevoll, G. T.; Nagelhus, E. A.; Plahte, E.; Zeuthen, T.; Lloyd, C. M.; Ottersen, O. P. and Omholt, S. W.** (**2009**): Astrocytic Mechanisms Explaining Neural-Activity-Induced Shrinkage of Extraneuronal Space, PLoS Computational Biology, Vol. 5, No. 1 p. e1000272. (Cited on pages 12, 13, 25, and 80.)

[138] **Otsu, Y.; Couchman, K.; Lyons, D. G.; Collot, M.; Agarwal, A.; Mallet, J.-M.; Pfrieger, F. W.; Bergles, D. E. and Charpak, S.** (**2015**): Calcium dynamics in astrocyte processes during neurovascular coupling., Nature neuroscience, Vol. 18, No. 2 pp. 210–218. (Cited on page 55.)

[139] **Ottesen, J. T.; Olufsen, M. S. and Larsen, J. K.** (**2004**): Applied mathematical models in human physiology, Society for Industrial and Applied Mathematics. (Cited on page 17.)

[140] **Øyehaug, L.; Østby, I.; Lloyd, C. M.; Omholt, S. W. and Einevoll, G. T.** (**2012**): Dependence of spontaneous neuronal firing and depolarisation block on astroglial membrane transport mechanisms, Journal of Computational Neuroscience, Vol. 32 pp. 147–165. (Cited on pages 12 and 77.)

[141] **Pappano, A. J. and Gil Wier, W.** (**2013**): The Microcirculation and Lymphatics, in **Pappano, A. J. and Wier, W. G.** (Ed.), Cardiovascular Physiology, Philadelphia, pp. 153–170. (Cited on pages 3 and 4.)

[142] **Parthimos, D.; Edwards, D. H. and Griffith, T. M.** (**1999**): Minimal model of arterial chaos generated by coupled intracellular and membrane Ca2+ oscillators., The American journal of physiology, Vol. 277, No. 3 pp. H1119–H1144. (Cited on pages 23 and 80.)

[143] **Parys, B.; Cote, A.; Gallo, V.; De Koninck, P. and Sik, A.** (**2010**): Intercellular calcium signaling between astrocytes and oligodendrocytes via gap junctions in culture., Neuroscience, Vol. 167, No. 4 pp. 1032–1043. (Cited on page 78.)

[144] **Peterka, D. S.; Takahashi, H. and Yuste, R.** (**2011**): Imaging voltage in neurons, Neuron, Vol. 69, No. 1 pp. 9–21. (Cited on page 10.)

[145] **Pfister, S. L.; Gauthier, K. M. and Campbell, W. B.** (**2010**): Vascular Pharmacology of Epoxyeicosatrienoic Acids, Advances in Pharmacology, Vol. 60, No. C pp. 27–59. (Cited on page 130.)

[146] **Pietrobon, D. and Moskowitz, M. A.** (**2014**): Chaos and commotion in the wake of cortical spreading depression and spreading depolarizations., Nature Reviews. Neuroscience, Vol. 15, No. 6 pp. 379–393. (Cited on page 7.)

[147] **Poolos, N. P. and Kocsis, J. D.** (**1990**): Elevated extracellular potassium concentration enhances synaptic activation of N-methyl-d-aspartate receptors in hippocampus, Brain Research, Vol. 508, No. 1 pp. 7–12. (Cited on page 84.)

[148] **Purves, D.; Augustine, G. J.; Fitzpatrick, D.; Hall, W. C.; LaMantia, A. S.; McNamara, J. O. and White, L. E.** (**2008**): Neuroscience, De Boeck, Sinauer, Sunderland. (Cited on page 3.)

[149] **Rakic, P.** (**2009**): Evolution of the neocortex: Perspective from developmental biology, Nat Rev Neurosci, Vol. 10, No. 10 pp. 724–735. (Cited on pages 1 and 125.)

[150] **Rimmele, T. S. and Chatton, J.-Y.** (**2014**): A Novel Optical Intracellular Imaging Approach for Potassium Dynamics in Astrocytes, PLoS ONE, Vol. 9, No. 10 p. e109243. (Cited on page 10.)

[151] **Rovegno, M. and Sáez, J. C.** (**2018**): Role of astrocyte connexin hemichannels in cortical spreading depression, Biochimica et Biophysica Acta - Biomembranes, Vol. 1860, No. 1 pp. 216–223. (Cited on page 136.)

[152] **Roy, C. S. and Sherrington, C. S.** (**1890**): On the regulation of the blood-supply of the brain, The Journal of physiology, Vol. 11, No. 1-2 p. 85. (Cited on page 5.)

[153] **Santos, E.; Schöll, M.; Sánchez-Porras, R.; Dahlem, M. A.; Silos, H.; Unterberg, A.; Dickhaus, H. and Sakowitz, O. W.** (**2014**): Radial, spiral and reverberating waves of spreading depolarization occur in the gyrencephalic brain, NeuroImage, Vol. 99 pp. 244–255. (Cited on pages 101, 120, and 125.)

[154] **Shanks, N.; Greek, R. and Greek, J.** (**2009**): Are animal models predictive for humans?, Philosophy, Ethics, and Humanities in Medicine, Vol. 4 p. 2. (Cited on page 10.)

[155] **Straub, S. V.; Bonev, A. D.; Wilkerson, M. K. and Nelson, M. T.** (**2006**): Dynamic inositol trisphosphate-mediated calcium signals within astrocytic endfeet underlie vasodilation of cerebral arterioles., The Journal of general physiology, Vol. 128, No. 6 pp. 659–669. (Cited on page 33.)

[156] **Sun, T. and Hevner, R. F.** (**2014**): Growth and folding of the mammalian cerebral cortex: from molecules to malformations, Nat Rev, Vol. 15, No. 4 pp. 217–232. (Cited on pages 1 and 125.)

[157] **Sykova, E. and Nicholson, C.** (**2008**): Diffusion in brain extracellular space, Physiological reviews, Vol. 88, No. 4 pp. 1277–1340. (Cited on pages 22 and 82.)

[158] **Takano, T. and Nedergaard, M.** (**2009**): Deciphering migraine., The Journal of clinical investigation, Vol. 119, No. 1 pp. 16–9. (Cited on pages 7 and 76.)

[159] **Takata, N.; Nagai, T.; Ozawa, K.; Oe, Y.; Mikoshiba, K. and Hirase, H.** (**2013**): Cerebral Blood Flow Modulation by Basal Forebrain or Whisker Stimulation Can Occur Independently of Large Cytosolic Ca2+ Signaling in Astrocytes, PLoS ONE, Vol. 8, No. 6 pp. 4–9. (Cited on page 33.)

[160] **Takuwa, H.; Autio, J.; Nakayama, H.; Matsuura, T.; Obata, T.; Okada, E.; Masamoto, K. and Kanno, I.** (**2011**): Reproducibility and variance of a stimulation-induced hemodynamic response in barrel cortex of awake behaving mice, Brain Research, Vol. 1369 pp. 103–111. (Cited on page 74.)

[161] **Tomita, Y.; Tomita, M.; Schiszler, I.; Amano, T.; Tanahashi, N.; Kobari, M.; Takeda, H.; Ohtomo, M. and Fukuuchi, Y.** (**2002**): Repetitive concentric wave-ring spread of oligemia/hyperemia in the sensorimotor cortex accompanying K(+)-induced spreading depression in rats and cats., Neuroscience letters, Vol. 322 pp. 157–160. (Cited on pages 7, 76, 99, 101, and 125.)

[162] **Toussay, X.; Basu, K.; Lacoste, B. and Hamel, E.** (**2013**): Locus Coeruleus Stimulation Recruits a Broad Cortical Neuronal Network and Increases Cortical Perfusion, Journal of Neuroscience, Vol. 33, No. 8 pp. 3390–3401. (Cited on page 72.)

[163] **Tuckwell, H. C. and Miura, R. M.** (**1978**): A mathematical model for spreading cortical depression, Biophys J., Vol. 23, No. 2 pp. 257–276. (Cited on page 82.)

[164] **Vargová, L. and Syková, E.** (**2008**): Extracellular space diffusion and extrasynaptic transmission., Physiological research / Academia Scientiarum Bohemoslovaca, Vol. 57 Suppl 3. (Cited on pages 5 and 21.)

[165] **Wallraff, A.** (**2006**): The Impact of Astrocytic Gap Junctional Coupling on Potassium Buffering in the Hippocampus, Journal of Neuroscience, Vol. 26, No. 20 pp. 5438–5447. (Cited on pages 76 and 98.)

[166] **Wang, B.; Chen, Q. H.; Brenner, R.; Health, T.; Antonio, S. and Antonio, S.** (**2009**): Proepileptic Effects of BK Channel Gene Mutations, in Encyclopedia of basic epilepsy research, Academic Press, pp. 662–669. (Cited on page 42.)

[167] **Wang, I.; Politi, A. Z.; Tania, N.; Yan, B.; Sanderson, M. J. and Sneyd, J.** (**2008**): A mathematical model of airway and pulmonary arteriole smooth muscle., Biophysical journal, Vol. 94, No. 6 pp. 2053–2064. (Cited on page 3.)

[168] **Wang, Y.; Necus, J.; Kaiser, M. and Mota, B.** (**2016**): Universality in human cortical folding in health and disease, Proceedings of the National Academy of Sciences, Vol. 113, No. 45 pp. 12820–12825. (Cited on pages 136 and 137.)

[169] **Wilson, H. R. and Cowan, J. D.** (**1972**): Excitatory and inhibitory interactions in localized populations of model neurons., Biophysical Journal, Vol. 12 pp. 1–24. (Cited on page 135.)

[170] **Witthoft, A.; Filosa, J. A. and Karniadakis, G. E.** (**2013**): Potassium buffering in the neurovascular unit: models and sensitivity analysis, Biophysical Journal, Vol. 105, No. 9 pp. 2046–2054. (Cited on pages 44 and 128.)

[171] **Witthoft, A.; Karniadakis, G. E. and Em Karniadakis, G.** (**2012**): A bidirectional model for communication in the neurovascular unit., Journal of theoretical biology, Vol. 311 pp. 80–93. (Cited on pages 22, 33, 34, 43, and 80.)

[172] **Zamir, M. and Budwig, R. S.** (**2002**): Physics of Pulsatile Flow, Vol. 55, AIP Press, New York, NY. (Cited on page 63.)

[173] **Zhao, L. and Brinton, R. D.** (**2002**): Vasopressin-induced cytoplasmic and nuclear calcium signaling in cultured cortical astrocytes, Brain research, Vol. 943, No. 1 pp. 117–131. (Cited on page 50.)

[174] **Zheng, Y.; Pan, Y.; Harris, S.; Billings, S.; Coca, D.; Berwick, J.; Jones, M.; Kennerley, A.; Johnston, D.; Martin, C.; Devonshire, I. M. and Mayhew, J.** (**2010**): A dynamic model of neurovascular coupling: Implications for blood vessel dilation and constriction, NeuroImage, Vol. 52, No. 3 pp. 1135–1147. (Cited on pages xiv, xv, 58, 67, 68, 69, 70, 71, 73, 74, and 128.)

[175] **Zlokovic, B. V.** (**2005**): Neurovascular mechanisms of Alzheimer's neurodegeneration, Trends in Neurosciences, Vol. 28, No. 4 pp. 202–208. (Cited on pages 4, 7, and 127.)

[176] **Zlokovic, B. V.** (**2011**): Neurovascular pathways to neurodegeneration in Alzheimer's disease and other disorders., Nature reviews. Neuroscience, Vol. 12, No. 12 pp. 723–738. (Cited on pages ix, 1, 4, and 7.)

[177] **Zonta, M.; Angulo, M. C.; Gobbo, S.; Rosengarten, B.; Hossmann, K.-A.; Pozzan, T. and Carmignoto, G.** (**2003**): Neuron-to-Astrocyte signaling is central to the dynamic control of brain microcirculation, Nature neuroscience, Vol. 6, No. 1 pp. 43–50. (Cited on page 33.)

[178] **Zykov, V. S.; Oikawa, N. and Bodenschatz, E.** (**2011**): Selection of Spiral Waves in Excitable Media with a Phase Wave at the Wave Back, Phys. Rev. Lett., Vol. 107, No. 25 p. 254101. (Cited on page 101.)

# DECLARATION

I declare that this dissertation is my own unaided work. It is being submitted for the degree of Doctor of Philosophy at the University of Canterbury. It has not been submitted for any other degree or examination in any other University.

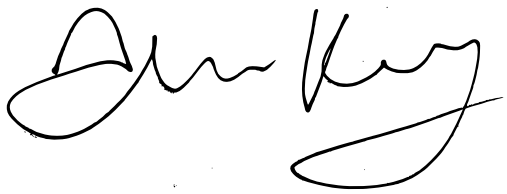

Allanah Kenny